PINNING ENHANCEMENT FOR $YBa_2Cu_3O_{7-\delta}$ (YBCO) AND IRON CHALCOGENIDE THIN FILMS

A Dissertation

by

JIJIE HUANG

Submitted to the Office of Graduate and Professional Studies of
Texas A&M University
in partial fulfillment of the requirements for the degree of

DOCTOR OF PHILOSOPHY

Chair of Committee,	Haiyan Wang
Co-Chair of Committee,	Xiaofeng Qian
Committee Members,	Jun Kameoka
	Xinghang Zhang
Head of Department,	Ibrahim Karaman

December 2016

Major Subject: Materials Science and Engineering

ABSTRACT

Over the past two decades, $YBa_2Cu_3O_{7-\delta}$ (YBCO) has aroused great research interests, owing to its high transition temperature ($\boldsymbol{T_c}$) of above 90 K and some other advantages. However, most of the practical applications of YBCO coated conductors require high electrical current transport properties under magnetic field with little or even no losses, which means high in-field critical current density ($\boldsymbol{J_c}$) is needed. Therefore, tremendous research has been focused on $\boldsymbol{J_c}$ improvement for YBCO thin films. One effective way is to introduce defects by designed nanostructure landscapes, so far, 0-D nanoparticles, 1-D nanopillars and 2-D nanolayers have been reported for effective defect pinning enhancement. Magnetic pinning is another method to enhance the $\boldsymbol{J_c}$ values for YBCO thin films, by the interaction between the fluxons and the magnetic inclusions.

However, there are very limited reports on the combination of defect and magnetic pinning together to further improve the $\boldsymbol{J_c}$ values. In this thesis, both defect and magnetic pinning are introduced by incorporating designed vertically aligned nanocomposite (VAN) layers, which include magnetic portion. $(CoFe_2O_4)_x(CeO_2)_{1-x}$ and $(La_{0.67}Sr_{0.33}MnO_3)_x(CeO_2)_{1-x}$ are introduced as either cap layer or buffer layer into YBCO thin films for the pinning enhancement, as $CoFe_2O_4$ and $La_{0.67}Sr_{0.33}MnO_3$ are both magnetic materials. Furthermore, VAN/YBCO mulitlayers are also successfully grown for effective pinning enhancement. By these doping methods and designed architectures, both magnetic and defect pinning are involved, and the superconducting properties are improved.

On another side, several iron based superconductors have been discovered, and FeSe with the simplest structure and a transition temperature ($\boldsymbol{T_c}$) around 8 K arouses much research interest. Up to date, most of the research efforts in this field are to improve the ***Tc*** value of iron chalcogenide thin films. In this thesis, the pinning effects are studied for the superconducting $FeSe_xTe_{1-x}$ thin films by nanoinclusions, such as CeO_2 nanolayer, which was proved to be able to create effective defect pinning centers for $FeSe_xTe_{1-x}$ thin films. In addition, $(CoFe_2O_4)_{0.1}(CeO_2)_{0.9}$ VAN layer is also incorporated for both defect and magnetic pinning. Last but not the least, $FeSe_xTe_{1-x}$ thin films have been deposited on various kinds of substrates, including single crystal STO, amorphous glass, Si with or without a SiO_x protection layer, and even metal substrate without a complicated set of buffer layers. Surprisingly, the $FeSe_xTe_{1-x}$ thin films can be grown along the c-direction on all the different substrates, even on amorphous glass and metal substrates, which demonstrates a very simplified and cost-effective approach of this Fe-based coated conductor for potential high field applications.

DEDICATION

I dedicate this to my parents.

ACKNOWLEDGMENTS

I would like to express my deepest appreciation to my research advisor, Dr. Haiyan Wang. During my Ph.D. period in her group, Dr. Wang was always willing to guide me to the right research direction and give great advice on how to do research. I can always feel her enthusiasm on doing research, which led me to become a true researcher. Dr. Wang always tried her best to provide all the workable experimental tools, and I very much appreciate the good equipment training in the group. Furthermore, I am so impressed by her wide knowledge in Materials Science and Electrical Engineering, I learned so much from her. Her nice personality made the group like a family, I feel so happy to have worked in such a group. I really appreciate all of her help, in both academic advice and personal life.

I would also like to thank my thesis committee, Dr. Xiaofeng Qian, Dr. Jun Kameoka, and Dr. Xinghang Zhang for their valuable suggestions and guidance on my research. I truly appreciate their willingness to be my thesis committee members and time to attend my prelim and final defense.

I also want to thank all my colleagues in Dr. Haiyan Wang's Functional Thin Film Group, including the alumni (Dr. Li Chen, Dr. Chen-Fong Tsai, Dr. Aiping Chen, Dr. Qing Su, Dr. Wenrui Zhang, Dr. Fauzia Khatkhatay, Dr. Liang Jiao, Dr. Clement Jacob) and the current members (Jie Jian, Leigang Li, Meng Fan, Han Wang, Zhimin Qi, Xingyao Gao, Bruce Zhang, Xuejing Wang, Xing Sun). I feel so lucky to have worked with so many great young researchers, all of them helped me a lot during my Ph.D life.

I also want to thank all my friends in the US, including Dan Zhang, Hong Li, Fanglue Wu, Yuan Yue, Dali Huang, Hua Wang and so many others. All of them helped me a lot and gave me a wonderful life in a foreign country.

Last but not least, I would like to thank my beloved family: my father, my mother and my brother. I could not have finished my Ph.D. study without their encouragement and support in my life. They are always the most important people in my life.

NOMENCLATURE

HTS	High Temperature Superconductor
STM	Scanning Tunneling Microscope
SQUID	Superconducting Quantum Interference Device
D-SMES	Distributed Superconducting Magnetic Energy Storage System
RABiTS	Rolling-Assisted-Biaxially-Textured-Substrates
IBAD	Ion-Beam-Assisted Deposition
MOCVD	Metal-organic Chemical Vapor Deposition
PLD	Pulsed Laser Deposition
PVD	Physical Vapor Deposition
MOD	Metal-organic Deposition
TFA	Trifluoroacetate
SEM	Scanning Electron Microscopy
TEM	Transmission Electron Microscopy
HRTEM	High Resolution Transmission Electron Microscopy
XRD	X-ray Diffraction
SAED	Selected Area Electron Diffraction
FFT	Fast Fourier Transformation
STEM	Scanning Transmission Electron Microscopy
AFM	Atomic Force Microscopy
EDS	Energy-dispersive Spectrometry
ADF	Annular Dark-field Imaging

EELS	Electron Energy Loss Spectroscopy
STEM	Scanning Transmission Electron Microscopy
PPMS	Physical Property Measurement System
VSM	Vibrating Sample Magnetometer
VAN	Vertically Aligned Nanocomposite
PIT	Powder-In-Tube
CC	Coated Conductor
XTEM	Cross-sectional Transmission Electron Microscopy

TABLE OF CONTENTS

Page

LIST OF FIGURES

LIST OF TABLES

Page

CHAPTER I

INTRODUCTION

1.1 Overview of superconductivity

Superconductor is a kind of material that exhibits zero (dc) electrical resistivity and expulses magnetic field (Messiner effect) when being cooled down to a particular temperature (which is called critical temperature, T_c). [1] Superconductivity was first discovered in mercury by Kamerlingh Onnes in 1911 and later found in other elements, as well as alloys, and compounds. The sudden drop of the resistance occurs when the temperature is lowered down to a certain point, which is called critical temperature (T_c), as shown in Figure 1.1(a). [2] In 1933, Meissner and Ochsenfeld found that superconductors completely expel magnetic field while temperature was cooled down to or below T_c, which refers to perfect diamagnetism or so-called Meissner effect, as illustrated in Figure 1.1(b). [2]

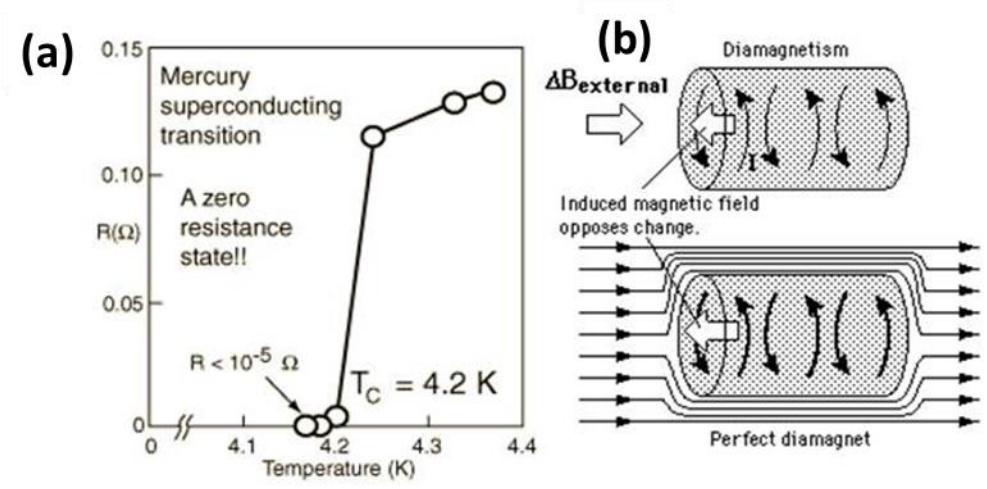

Figure 1.1 (a) Resistance-temperature plot to show superconducting transition temperature; (b) Schematic illustration of Meissner effect. [2]

1.1.1 Brief history of superconductor

As mentioned, superconductivity was first found in 1911 by Kamerlingh Onnes. However, there was a big step before that, which was the successful operation of the liquefier of helium. Helium has a boiling point of around 4.2 K at atmospheric pressure condition. And the temperature can further drop to 1.7 K with reduced pressure, which assured sufficient cooling to reach mercury's $\boldsymbol{T_c}$ for the later discovery. [3] Actually, platinum was the first material Onnes tested and no superconducting exhibited. Then, mercury was selected for the next test material, surprisingly, the resistance suddenly disappeared below 4.2 K. [4] After that, Onnes tested more metallic elements following this initial work, for example, indium, tin and lead showed superconductivity at 3.4, 3.7 and 7.2 K, respectively. Furthermore, during the next several decades, other metallic elements and even alloys were measured to be superconducting, for instance, Nb_3Sn exhibited superconductivity with a $\boldsymbol{T_c}$ of 17.9 K. Because of these exciting works, Onnes was awarded the Nobel Prize in physics in the year of 1913.

The next important time point for the development of superconductor was 1933, when Meissner effect was discovered. In 1933, Walter Meissner and Robert Ochsenfeld found that superconductor could expel magnetic flux. This finding was really exciting, as it was the very first time people considering superconductivity as a magnetic phenomenon. [5] However, Meissner effect could not be seen when temperature or applied magnetic field was beyond its critical values. There was more progress for superconductivity after this breakthrough. For example, Fritz and Heinz London demonstrated that although magnetic flux was expelled from the matrix of a

superconductor, it could still penetrate into a small distance from the surface, which was considered as penetration depth. To explain Meissner effect, they modified the classical Maxwell equations.

In 1934, another critical development was made by Gorter, who proposed that a superconductor contained a mixture of superconducting electrons (superelectrons) and normal electrons. When temperature is at onset of $\boldsymbol{T_c}$, no superelectron appears, and 100% superelectrons contribute when temperature lowers to 0 K. This theory is called "two-fluid" model, which is still very useful for modeling superconductor behavior. The next critical point was the demonstration of Type I and Type-II in 1936. Lev Shubnikov indicated that much higher magnetic field was required for superconducting alloys like Pb-Bi to lose its superconductivity, compared to pure metal elements. [6] These alloys were categorized as Type-II superconductor, while the pure metal elements were called Type I superconductor.

For the superconductivity theory, in 1950, Vitaly Ginzburg and Lev Landau introduced the concept of coherent length by extending London theory. The coherent length was defined as the length over which density of superelectrons change, which was further proved experimentally by Brian Pippard in 1953. Then in 1956, Leon Cooper observed the interaction between electrons and lattice vibrations in superconductor and indicated that superconductivity was correlative with pairs of electrons traveling through the lattice, which was known as the "Cooper Pairs". Based on the demonstration of "Cooper Pairs", John Bardeen, Leon Cooper and Robert Schrieffer developed a comprehensive theory of superconductivity in 1957, which is the famous BCS theory. [7]

In the same year of 1957, Alexei Abrikosov proposed a mixed state in Type-II superconductor, where both superconducting and normal states appear. And, he also suggested that the magnetic flux in the superconductor formed a regular array of quantum vortices. [8]

Time came to the 1980s, Alex Muller and George Bednorz at IBM laboratory in Zurich Switzerland were focusing their work on perovskites, which have many important properties, such as ferroelectrics, piezoelectrics, multiferroics and so on. In 1986, Muller and Bednorz prepared some solid solutions of barium-doped lanthanum cuprates (Ba-La-Cu-O system), and found that a sharp resistance droped at 11 K. Then, the samples were further optimized to achieve $\boldsymbol{T_c}$ of 30 K, which was a record at that time. [9] They received the Nobel Prize in the next year 1987. This result was confirmed by Kitazawa in Dec. 1986. At the same time, Paul Chu from University of Houston reported an increase of $\boldsymbol{T_c}$ to 40 K and it could even reach to 52 K by applying pressure. The breakthrough of searching for high temperature superconductor occurred in 1987, when Paul C. W. Chu and M. K. Wu substituted Yttrium for Lanthanum to produce Y-Ba-Cu-O and saw evidence of superconductivity up to 93 K, which was higher than the sublimation temperature of liquid nitrogen. [10] After that, tremendous research interests were focused on searching for superconductors with higher $\boldsymbol{T_c}$ value. In 1988, A. Maeda *et al*. added Ca and obtained $\boldsymbol{T_c}$ up to 110 K in Bi-Sr-Ca-Cu-O system with the compound formulation of 2201, 2212 and 2223. [11] In the same year, Z. Z. Sheng and A. M. Hermann explored superconducting property in Tl-Ba-Ca-Cu-O at 125 K in compounds of formulation 2212, 2223 and 1223. [12] Later in 1993, A. Schilling, M.

Cantoni, J. D. Guo, and H. R. Ott reported T_c up to 135 K in $HgBa_2Ca_2Cu_3O_x$, [13] and C. W. Chu *et al*. further raised this value to 150 K by applying pressure of 150 kBar. [14]

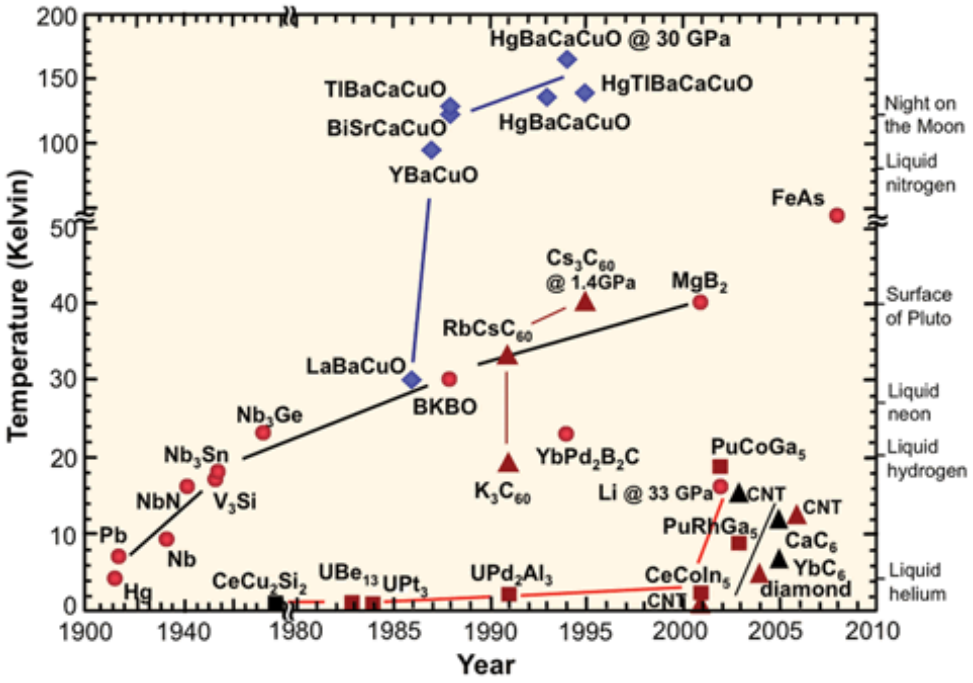

Figure 1.2 The discovery and development for superconductors.

Besides the work on searching for more high temperature superconductors with higher T_c, other research efforts were focusing on searching for new superconductors. For example, the discovery of MgB_2 in 2001 brought much excitement as its T_c value reached to 39 K, which also exceeded the limit predicted by BCS theory. [15] Another good example was the discovery of iron-based superconductors, which was first found in LaOFeP with T_c ~ 4 K in 2006. [16] Researchers all over the world are still working on this exciting field, to find more new superconductors and developing superconductor

with better superconducting properties. Figure 1.2 presents the discovery and development in the research field of superconductor since its first discovery, as well as their corresponding critical temperatures.

1.1.2 Two categories of superconductors

Generally, superconductors can be divided into two categories, named as "Type I" and "Type-II" superconductors. Generally speaking, "Type I" superconductors must exclude essentially all of the applied magnetic field to maintain its superconductivity. This means that there is only one critical field ($\boldsymbol{H_c}$: the maximum field a type-I superconductor remains superconducting) value at a specific temperature under $\boldsymbol{T_c}$ for "Type I" superconductors, above which is the normal state and below is the superconducting state. The magnetization (**M**) is with the same value of the applied magnetic field ($\boldsymbol{H_e}$) of opposite direction, when the applied field is under critical field $\boldsymbol{H_c}$, as described in the following Equation 1.1.

$$\boldsymbol{M = -H_e} \quad \text{(Equation 1.1)}$$

This equation sustains only when the applied field $\boldsymbol{H_e}$ is lower than critical field $\boldsymbol{H_c}$. When the external field increases to above its critical field, the superconducting state will be destroyed into normal state, and magnetization abruptly drops to 0, as illustrated in Figure 1.3(a). Moreover, critical field $\boldsymbol{H_c}$ for "Type I" superconductors varies while changing temperature, and this correlation can be described as the following equation.

$$\boldsymbol{H_c(T) = H_c(0)\left[1 - \left(\frac{T}{T_c}\right)^2\right]} \quad \text{(Equation 1.2)}$$

Most pure metals belong to “Type I” superconductor, Table 1.1 lists the “Type I” superconductors with their corresponding $\boldsymbol{T_c}$ and $\boldsymbol{H_c}(0)$ values.

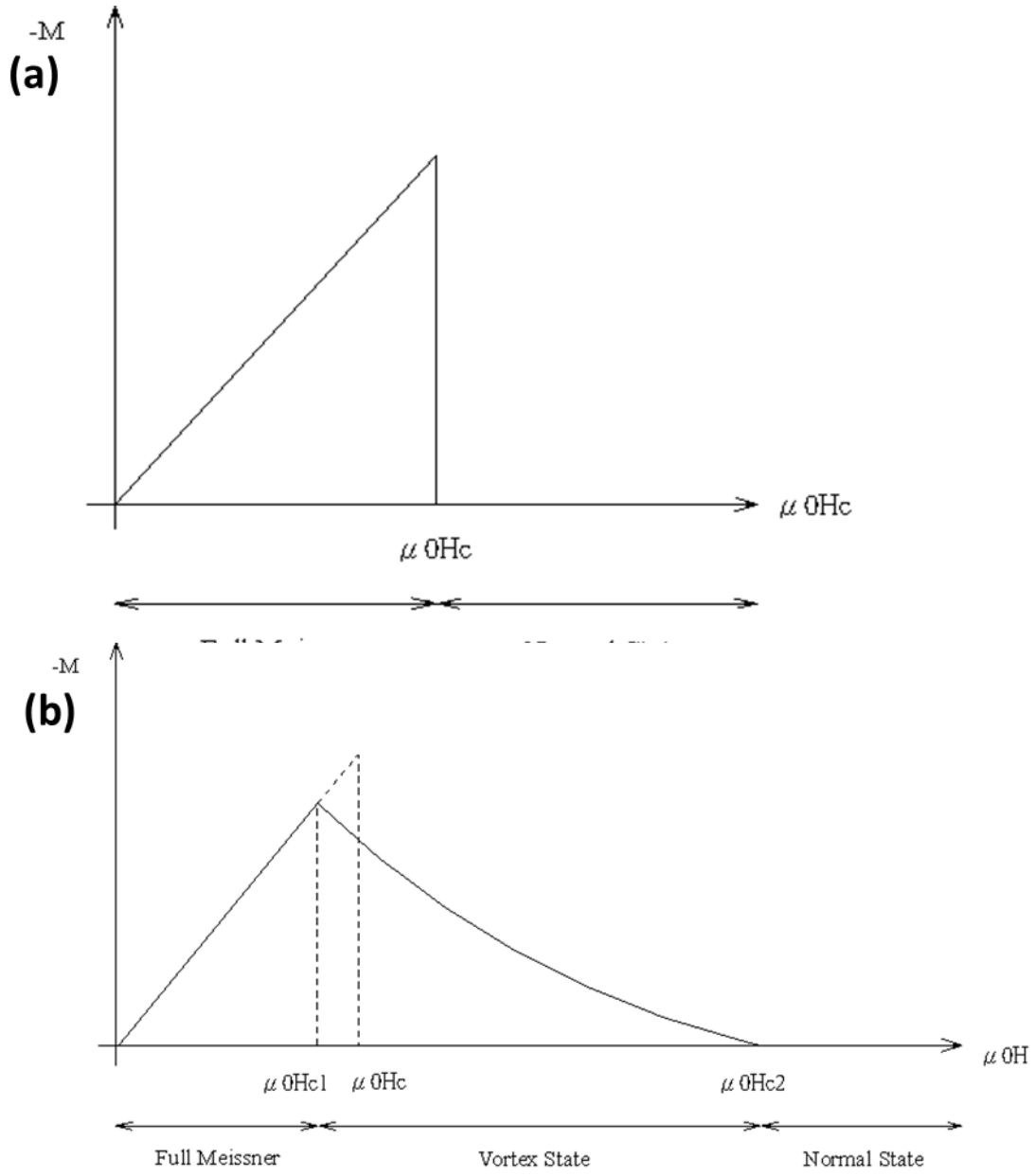

Figure 1.3 Magnetization curve of type I (a) and type II (b) superconductor. [2]

Table 1.1 List of some "Type I" superconductors with their corresponding T_c and $H_c(0)$ values.

Element	T_c (K)	$H_c(0)$ (Oe)
Aluminum (Al)	1.175	99
Americium (Am)	0.6	-
Beryllium (Be)	0.02	-
Cadmium (Cd)	0.52	30
Gallium (Ga)	1.1	51
Hafnium (Hf)	0.13	-
Indium (In)	3.4	293
Iridium (Ir)	0.11	~20
Lanthanum-α (La)	4.88	-
Lanthanum-β (La)	6.0	1600
Lead (Pb)	7.2	803
Lithium (Li)	0.0004	-
Mercury-α (Hg)	4.15	411
Mercury-β (Hg)	3.95	340
Molybdenum (Mo)	0.915	-
Niobium (Nb)	9.46	1944
Osmium (Os)	0.66	65
Palladium (Pd)	3.3	-
Platinum (Pt)	0.002	-
Protactinium (Pa)	1.4	-
Rhenium (Re)	1.7	198
Rhodium (Rh)	0.0003	-
Ruthenium (Ru)	0.49	66
Tantalum (Ta)	4.48	830
Technetium (Tc)	7.75	1410
Thallium (Tl)	2.38	171
Thorium (Th)	1.38	162
Tin (Sn)	3.72	309
Titanium (Ti)	0.4	100
Tungsten (W)	0.012	1070
Uranium-α (U)	0.68	~2000
Uranium-β (U)	1.80	-
Vanadium (V)	5.414	1370
Zinc (Zn)	0.875	53
Zirconium (Zr)	0.6	47

For "Type II" superconductors, instead of completely expel applied magnetic fields, the fields can be confined into a normal-state flux tube inside the material called

"vortices". This suggests that "Type II" superconductors contain both normal-state phase (vortices) and superconducting phase (the matrix), which is the mixed state. And it has two $\boldsymbol{H_c}$ values (lower critical field $\boldsymbol{H_{c1}}$ and upper critical field $\boldsymbol{H_{c2}}$), below $\boldsymbol{H_{c1}}$, between $\boldsymbol{H_{c1}}$ and $\boldsymbol{H_{c2}}$ and above $\boldsymbol{H_{c2}}$ correspond to superconducting state, mixed state and normal state, respectively. The magnetization curve of "Type II" superconductors can be observed in Figure 1.3(b), and alloys and impure metals belong to this category. As mentioned, while in mixed state, both superconducting and normal phases appear. Basically, to maximize negative surface energy, the ratio of surface to volume of the normal phase needs to be maximum. Therefore, the normal materials in the superconductor will be shaped as cylinders, and these cylinders are parallel to the applied magnetic field. There is a magnetic flux in every normal core, which is in the same direction of the magnetic field and is generated by current circulating the core in the direction opposite to the diamagnetic shielding current. In addition, the vortices current circulating around a normal core is affected by the magnetic field generated from vortex current encircling another core, which results in the repelling of the normal cores from each other. Because of this interaction, the normal cores always arrange themselves in a triangular or hexagonal periodic lattice. Figure 1.4 presents triangular vortex lattice in $NbSe_2$ by scanning tunneling microscope (STM) imaging. Normally, "Type II" superconductors obtain better superconducting properties than "Type I" superconductors, which is believed to be caused by the layered crystal structure in "Type II" superconductors. For example, the high temperature superconductors YBCO and MgB_2 are both "Type II" superconductors.

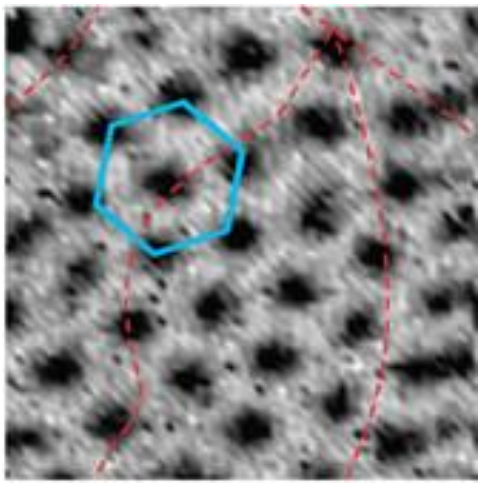

Figure 1.4 Triangular vortex lattice in $NbSe_2$ demonstrated by STM imaging. [17] Reprinted with permission from "I. Guillamon, H. Suderow, A. Fernandez-Pacheco, J. Sese, R. Cordoba, J. M. De Teresa, M. R. Ibarra, and S. Vieira, Nat. Phys. **5**, 651 (2009)."

1.1.3 Applications of superconductors

Generally speaking, the applications of superconductor can be divided into two categories. The first one is that of lower-power electronic application. For this kind of application, superconductors are always made into thin film form on dielectric substrates, and then Josephson junctions are fabricated based on this. These Josephson junctions can be used for superconducting quantum interference device (SQUID) and other applications related to analog or digital circuitry. The current density can be very high, as a general low-power electronic conductor can only carry current in the order of few mA. Table 1.2 summaries the requirements of magnetic field and current density for some typical applications. The second category is using bulk superconducting materials to form large cross-sectional conductors. The conductors normally carry a high current density and often be used in high magnetic field environment.

Table 1.2 Requirements of current density (***J***) and magnetic field (***H***) for some typical applications of superconductors. [3]

Application	***H* (T)**	***J* (A/cm2)**
Interconnects	0.1	5×10^6
AC Transmission Lines	0.2	10^5-10^6
Power Transformers	0.3-3	10^5
DC Transmission Lines	0.2	2×10^4
SQUIDs	0.1	2×10^2
SQMEs (Energy Storage)	2.5-5	5×10^5
Motors, Generators	2.5-5	4×10^4-10^5
Magnetic Separation	2-5	3×10^4
MAGLEV	5-6	4×10^4
Fusion	10-15	10^5
Fault Current Limiters	> 5	> 10^5

Compared to conventional cables, high temperature superconductor (HTS) conductors can carry 5 to 10 times more current capacity. It can be used in existing underground conduits, which can save trenching costs. In addition, the coolant for HTS is liquid nitrogen, which is dielectric and eliminates the possibility of oil fires and corresponding environmental hazards. Furthermore, compared to the size and weight of conventional equipment, HTS generators, motors and transformers are 50% smaller. Therefore, HTS cables are very promising to be used in Navy, and it can also provide premium power for military applications.

Currently, the most used HTS materials are BSCCO and YBCO, which have been fabricated into coated conductors. People are mostly working on scaling up the HTS coated conductors and increasing the current density ($\boldsymbol{J_c}$) to satisfy the commercial requirements. For example, SuperPower© has successfully fabricated 10 km of superconducting YBCO wire for a power grid system in Albany, New York, as shown in

Figure 1.5(b). However, it costs much more compared to conventional copper wires. Moreover, in 2000, American Superconductor© installed a distributed superconducting magnetic energy storage system (D-SMES) in Wisconsin. Each D-SMES units can storage over 3 million watts to stabilize line voltage during a disturbance in the power grid. Figure 1.5 presents some real images of the applications, including HTS power transmission cable, superconducting power grid and superconducting magnetic energy storage.

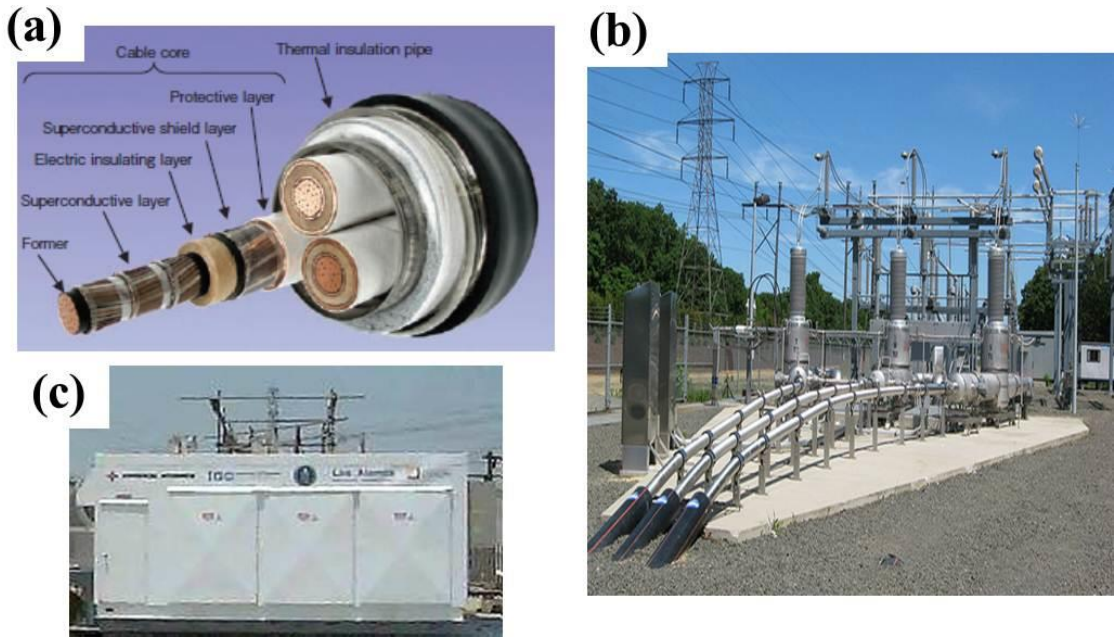

Figure 1.5 (a) HTS power transmission cable, (b) superconducting power grid in Albany, New York, and (c) superconducting magnetic energy storage. [18]

1.1.4 Flux pinning of superconductors

There are three parameters needed to be satisfied to become superconducting, as shown in Figure 1.6. Critical temperature $\boldsymbol{T_c}$ and critical field $\boldsymbol{H_c}$ have been mentioned previously, the third one is the critical direct-current density $\boldsymbol{J_c}$. When the current density in superconductor exceeds some value, it causes the material to "quench" and lose its superconducting properties, this value is $\boldsymbol{J_c}$. In order to improve the performance of superconductors, $\boldsymbol{J_c}$ value needs to be enhanced to carry more current, especially under external magnetic field. In fact, $\boldsymbol{T_c}$ and $\boldsymbol{H_c}$ are more or less considered as intrinsic properties of the specific material, however, $\boldsymbol{J_c}$ is largely related to the microstructure of the sample and can be varied a lot with different material processing techniques.

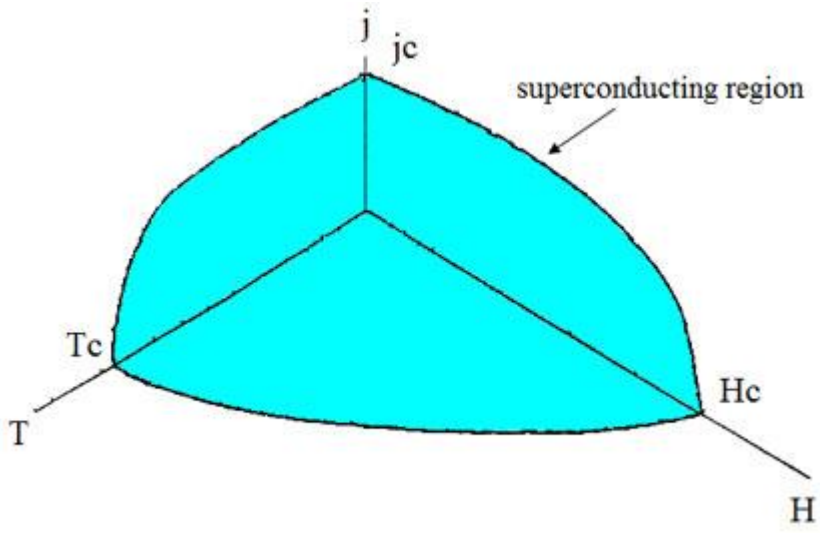

Figure 1.6 The most important parameters for superconductor.

As introduced in the previous section, the vortex or fluxon lattice forms a triangular array to achieve the lowest energy state, and each vortex has a single fluxon $\boldsymbol{\Phi_0}$ passing through it. The vortices are surrounded by the matrix with current flowing, thus an electromagnetic force (Lorentz force, $\boldsymbol{F_L}$) exists. The normal cores (vortices) are pinned in the materials by a pinning force $\boldsymbol{F_p}$. If $\boldsymbol{F_L}$ exceeds $\boldsymbol{F_p}$, the flux lattice begins to move, as shown in Figure 1.7. In order to maintain its motion, energy has to be supplied and it comes from the transport current. This dissipation of energy leads to resistance. Impurities and defects (pinning centers) can help to stabilize or pin the fluxons to increase fluxon stability and critical current density, which refers to flux pinning property.

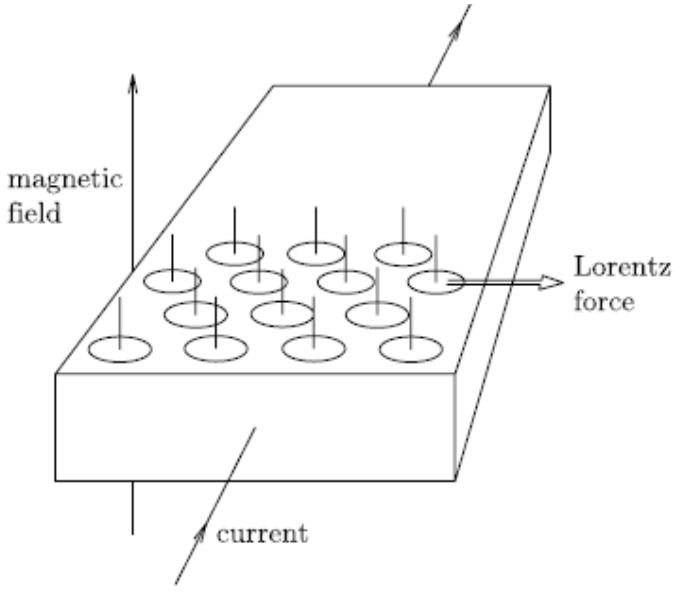

Figure 1.7 The Lorenz force acting on a current-carrying superconductor under magnetic field. [19]

Pinning has to be maximized in order to achieve $\boldsymbol{J_c}$ values close to depairing $\boldsymbol{J_c}$. Therefore, pinning force should be large enough to pin the vortices. Pinning force is determined by several factors, including the superconducting nature of pinning centers, size and spacing of pinning centers compared to penetration depth, as well as the rigidity of flux lattice. When it reaches to the critical current density $\boldsymbol{J_c}$, the Lorentz force $\boldsymbol{F_L}=\boldsymbol{J_cB}$ acting on the flux lines in a unit volume will be balanced by the pinning force, therefore:

$$\boldsymbol{J_c} = \frac{\boldsymbol{F_p}}{\boldsymbol{B}} \text{ (Equation 1.3)}$$

So, stronger the pinning force, higher the critical current density, and imperfect samples may exhibit higher $\boldsymbol{J_c}$ values.

1.2 High temperature superconductor: YBCO

1.2.1 Introduction of YBCO

In 1987, Chu and Wu produced a new perovskite ceramic type-II superconductor- $YBa_2Cu_3O_{7-\delta}$ (YBCO), with a much raised $\boldsymbol{T_c}$ value of above 90 K. [10] The discovery of YBCO brought great excitement within the scientific community since it was the first superconductor found with $\boldsymbol{T_c}$ above the boiling point of liquid nitrogen (~77 K). Liquid nitrogen is much easier to be handled and much more cost-effective compared to liquid Helium, which makes it more promising for practical applications. Its lattice structure is shown in Figure 1.8. The δ value refers to the oxygen deficiency in $YBa_2Cu_3O_{7-\delta}$ cuprate. The larger value of δ indicates a stronger oxygen deficiency.

When $\delta = 1$, the O(1) sites are vacant and the structure is tetragonal with lattice parameters of a = 3.87 Å and c = 11.77 Å, which YBCO phase is an insulator and does not become superconducting. For $\delta < 0.65$, Cu-O chains along the b axis are formed and cause an extension of the b axis. It changes its structure to orthorhombic with lattice parameters of a = 3.82 Å, b = 3.89 Å, and c = 11.68 Å and becomes superconducting. [20]

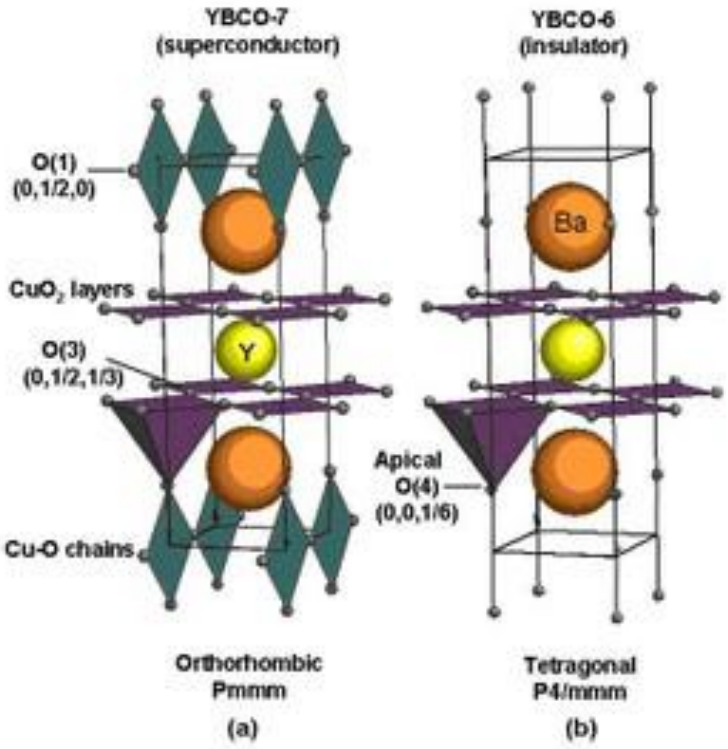

Figure 1.8 Unit-cell of (a) superconducting orthorhombic $YBa_2Cu_3O_7$ and (b) tetragonal $YBa_2Cu_3O_6$. [20]

1.2.2 Synthesis methods for YBCO

For the thin film form of YBCO, tremendous research progress has been achieved to satisfy the requirements on the epitaxial growth of the YBCO thin film coated conductors on flexible metal substrates, and then to solve critical problems that limit the property of YBCO-based coated conductors. To achieve the epitaxial growth of YBCO thin films on metal substrates, complex templates are needed. The two major methods are (1) involve a textured metal substrate to start with, i.e., rolling-assisted biaxially textured substrates (RABiTS) [21-24] and (2) build an epitaxial template on amorphous buffered metal substrates called ion-beam-assisted deposition (IBAD) substrates. [25-29] Furthermore, several film growth techniques have been successfully proposed for the growth of YBCO thin films with high epitaxial quality.

1.2.2.1 Metal-organic chemical vapor deposition (MOCVD)

Metal-organic chemical vapor deposition (MOCVD) is a chemical vapour deposition method used to produce single or polycrystalline thin films. MOCVD method has been used to deposit YBCO thin film shortly after it has been discovered. [30-32] However, it is difficult to use an oxide compound composed of multiple heavy-metal elements to grow YBCO. [33] The lack of gas-phase or liquid-phase metalorganic precursors for the heavy-metal elements hinders the further application of MOCVD for HTS YBCO growth. The commonly used precursors for YBCO growth is named thd precursors (2,2,6,6,-tetramethyl- 3,5-heptanedionate) of Y, Ba, and Cu, which presents a high melting point and a low vapor pressure. Although it is difficult to control the vapor-

phase composition during the whole process, various different precursors and corresponding precursor delivery approaches have been proposed and tested. [34-39]

For instance, Busch *et al*. used the precursors of $Ba(tdfnd)_2$·tetraglyme, $Y(thd)_3$·4tBuPyNO, and $Cu(tdfnd)_2$·H_2O for the MOCVD growth of YBCO film. [36] All these precursors were evaporated from the liquid material and the reproducibility of the film composition was good. However, water vapor was required to be added into these fluorinated precursors to avoid the formation of BaF_2, which caused the problems associated with the removal of HF. In another side, Richards *et al*. used a fluorinated barium precursor, $Ba(tdfnd)_2$·tetraglyme (tdfnd: tetradecafluorononanedione), which was stable at its operating vaporization temperature (~145 °C). [38] The $\boldsymbol{J_c}$ value at 77 K of the YBCO film made by this precursor is ~5 MA/cm^2, which was also reproducible. However, the addition of water vapor in the deposition process was needed for the fluorinated precursors, to avoid the generation of BaF_2, which consequently resulted in problems associated with the removal of HF. Furthermore, liquid-state nonfluorinated sources of $Y(thd)_3$·4tBuPyNO, $Ba(thd)_2$·2tetraene, and $Cu(thd)_2$ were reported to produce high-crystalline-quality YBCO films, by Nagai et al. [35] Other adducts, such as triglyme and phenanthroline, have been used to stabilize the Ba-thd precursor.

1.2.2.2 Magnetron sputtering

Magnetron sputtering is a physical vapor deposition (PVD) method of this film deposition by sputtering. Magnetron sputtering is very widely used for thin film deposition, including metal thin films, [40-44] oxide thin films, [45-50] as well as nitride

thin films. [51-55] This technique has several advantages, such as low temperature processing, film composition is almost the same as the target, as well as high film quality due to its high kinetic energy involved. Therefore, sputtering has been applied for YBCO thin film deposition soon after it has been discovered. [56-60] However, in the early stage of this method for producing YBCO films, the superconducting properties of these films are not as good as expected.

For example, Yin *et al*. deposited YBCO thin film on polycrystalline metal substrates with yttrium-stabilized zirconia (YSZ) and silver buffer layers. [57] Unfortunately, the films were grown along c-direction with random rotation in a-b plane, which depresses it critical temperature $\boldsymbol{T_c}$ to 81 K and critical current density $\boldsymbol{J_c}$ to as low as ~10^4 A/cm^2 at 40 K. Later on, more work has been done to optimize the sputtered YBCO film. Pan *et al*. deposited YBCO films by off-axis DC magnetron sputtering on CeO_2 buffered r-cut sapphire substrates. [60] Rows of growth-induced out-of-plane edge dislocations were observed to form low-angle boundaries, which were believed to be the most important role to achieve a high $\boldsymbol{J_c}$ of $\geq 2\times10^6$ A/cm^2.

1.2.2.3 Pulsed laser deposition (PLD)

Pulsed laser deposition (PLD) is also a physical vapor deposition (PVD) process, a high-power pulsed laser beam will be focused into a pre-pumped vacuum chamber to strike a target of the material that is to be deposited. Then, the material from the target will be vaporized to form a plasma plume and be deposited as a thin film on certain substrates. During the process, one inflows gas like oxygen, argon, nitrogen, or deposit

in vacuum condition. Almost all metals and complex ceramic materials can be grown by this method, therefore, PLD becomes one of the most popular in thin film research area. [61-65] PLD is suitable for the complex oxide material growth, thus, a large amount of work has been done for the PLD grown YBCO thin films. [66-70]

Early in 1996, Lorenz *et al*. reported PLD deposited YBCO thin films on sapphire substrates with CeO_2 buffer layers. [66] The thickness of the films was in the range of 350-500 nm, and the $\boldsymbol{J_c}$ values were 3×10^6 A/cm^2-5×10^6 A/cm^2. The YBCO films in this study were also homogeneous and reproducible. Because of the advantages of PLD to grow YBCO superconducting thin films, it has been used a lot later in this research field. For example, Campbell *et al*. reported Y_2O_3/YBCO multilayer grown by PLD method on $SrTiO_3$ (STO) and $LaAlO_3$ (LAO) substrates, the thickness of each layer was varied and controlled by deposition time. [68] The goal of this study is also to explore the potential flux pinning effect provided by the added Y_2O_3 nanolayers. The results showed that the $\boldsymbol{J_c}$ values in this study ranged 3-5 MA/cm^2. In addition, by modifying the target, nanoinclusions can be incorporated into YBCO film. Mele *et al*. used a unique YBCO target with a thin YSZ sector on top to grow mixed YBCO + YSZ thin film. [69] The $\boldsymbol{J_c}$ value of this film was enhanced to 1.95 MA/cm^2, compared to 1.46 MA/cm^2 of the pure YBCO film.

1.2.2.4 Metal-organic deposition (MOD)

Some other researchers also used the method of metal-organic deposition to grow YBCO thin films. [71-74] For example, Verebelyi *et al*. developed a commercial web-

coating process with metal-organic deposition method using a trifluoroacetate (TFA)-based precursor, to coat a single layer of YBCO precursor on CeO_2 buffered wires. [73] By this method, a long wire with 8 m could be coated with uniform YBCO, and its critical current performance was enhanced to 132 A/cm width.

1.2.3 Flux pinning for YBCO

1.2.3.1 Defect pinning

Most of the applications of superconductor require high critical current density $\boldsymbol{J_c}$ to carry more current in applied magnetic field, especially the HTS coated conductor. $\boldsymbol{J_c}$ is the maximum current density that can be carried by a superconductor without breaking the superconducting state. $\boldsymbol{J_c}$ translates into a critical current $\boldsymbol{I_c}$ for a wire with certain cross section area. Therefore, increase $\boldsymbol{J_c}$ value under high magnetic field becomes one of the most critical research fields in superconductor. It is also important to scale up the coated conductor to longer length with similar $\boldsymbol{J_c}$ value along all the length, and keep the $\boldsymbol{T_c}$ value almost the same (normally ~90 K).

1.2.3.1.a Material imperfections

There are several important parameters that can affect the performance of $\boldsymbol{J_c}$, including material imperfections, weak-link effect and flux pinning effect. [75, 76] Material imperfections are the defects naturally generated during the growth process of the material or the post-treatment, such as ion radiation and heat annealing. Different intrinsic defects can be found in YBCO thin films, as shown in Figure 1.9, [75] such as

preciptates, twin boundaries, threading dislocations, voids and so on. Among all of them, some may deteriorate the superconducting properties of YBCO, like cracks and voids, as they may impede the supercurrent flowing. These harmful cracks and voids can be avoided by optimizing the growth procedure. In another side, other defects like twin boundaries, misfit dislocations, threading dislocations and point defects can serve as pinning centers to improve the superconducting performance. Therefore, introducing more artificial dislocations or point defects is one of the most effective ways to enhance superconducting properties.

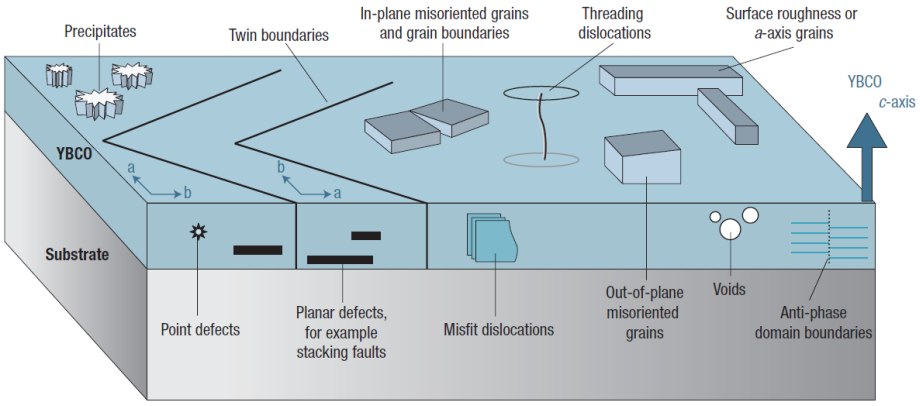

Figure 1.9 Schematic illustration of different intrinsic defects in YBCO thin film. [75] Reprinted with permission from "S. R. Foltyn, L. Civale, J. L. Macmanus-Driscoll, Q. X. Jia, B. Maiorov, H. Wang, and M. Maley, Nat. Mater. **6**, 631 (2007)."

1.2.3.1.b Weak-link effect

Weak-link effect is caused by the mis-orientation between adjacent grains, which results in an exponential degradation of $\boldsymbol{J_c}$, as shown in Figure 1.10. To achieve good superconducting performance of YBCO thin films, it not only requires the high crystallinity along the c-direction, but also needs the perfect in-plane alignment.

Therefore, it is desirable to use single-crystal substrates with perfect lattice matching with YBCO, to achieve high quality YBCO thin films. For the coated conductors, YBCO is deposited on metal substrates. Therefore, the ion-beam-assisted deposition (IBAD) and the Rolling Assisted Biaxial Textured (RABiT) techniques have been developed to create templates for the YBCO growth.

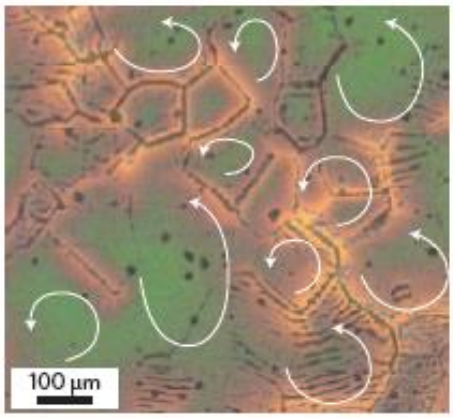

Figure 1.10 Magnetic granularity in an in-plane mis-oriented YBCO thin film. [77] Reprinted with permission from "A. Gurevich, Nat. Mater. 10, 255 (2011)."

1.2.3.1.c Flux pinning effect

Flux pinning effect is probably the most important factor for superconducting property enhancement. As discussed in previous section, magnetic field exists as the form of vortices or fluxons inside Type II superconductors such as YBCO, and there is one unit magnetic flux or flux quantum within one vortice. [2] A lateral force will be generated on the vortices, by the applied electric current on the superconductor, which is called the Lorentz force. This force leads the vortex motion and causes dissipated energy, thereby electrical resistance appears in the superconductor. Thus, a pinning force larger

than the Lorentz force is needed to keep the vortices immobilized. Pinning force arises from some kinds of the material imperfections and artificial defects.

Depends on the orientation and distribution in the YBCO matrix, these effective pinning defects can be categorized as correlated pinning and uncorrelated (random) pinning defects. [75] Correlated pinning is generated from parallel arrays of planar and linear defects, which will be more effective when the applied magnetic field is in the same direction of these defects. Figure 1.11 shows the normalized $\boldsymbol{J_c}$ values in depend on the angle between applied field (H) and c-axis. Obvious, peaks can be observed at angle of 90°, which indicates defects appearing along this direction. Screw dislocations, edge dislocations threading dislocations, and misfit dislocations generate stronger pinning effect along c-direction, while twin boundaries, in-plane grain boundaries, anti-phase domain boundaries, and stacking faults are more effective in the a-b plane.

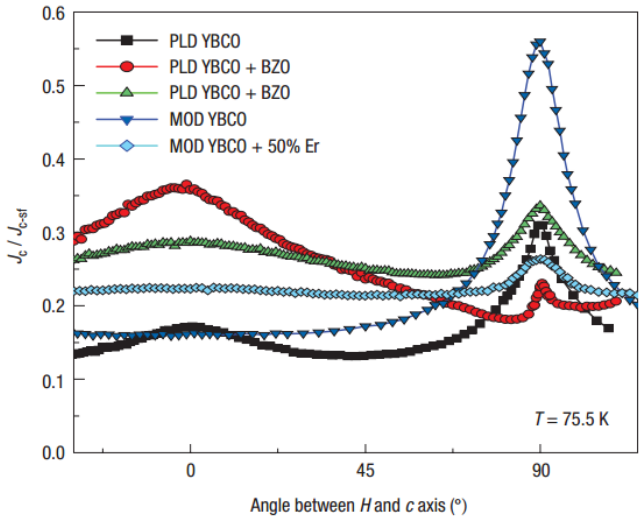

Figure 1.11 Normalized $\boldsymbol{J_c}$ values in depend on the angle between applied field (H) and c-axis. [75] Reprinted with permission from "S. R. Foltyn, L. Civale, J. L. Macmanus-Driscoll, Q. X. Jia, B. Maiorov, H. Wang, and M. Maley, Nat. Mater. **6**, 631 (2007)."

Uncorrelated (random) pinning results from randomly distributes defects, such as atomic vacancies and oxygen vacancies, which provide uniformly distributed pinning effect in all orientations. The atomic size vacancies are potential pinning centers due to the small ξ of YBCO thin films. In addition, large point defects such as precipitates and normal metallic secondary-phase inclusions can also work as strong pinning centers in YBCO films.

1.2.3.1.d 0-D nanoparticles for flux pinning

In order to improve the superconducting performance of YBCO, defects are introduced into YBCO artificially by researchers. In the early days, people were trying to create high density defects in YBCO matrix by particle irradiation, to enhance its $\boldsymbol{J_c}$ value. In such process, randomly distributed uncorrelated defects can be generated by high energy radiation with particles like electrons, protons, and fast neutrons. [78-80] However, there are disadvantages for this method, first, it is difficult to control the distribution of the defects in the sample, which are always randomly distributed. Furthermore, the irradiation may cause damage to the film and deteriorate the film crystallinity. Therefore, it is important to develop more ideal ways to create artificial pinning defects, without degrading the film quality.

Introducing a secondary phase into YBCO thin film could be a more promising approach. Depending on the architecture of the dopants, the introduced pinning centers can be obtained from 0-D nanoparticles, 1-D nanocolumns and 2-D nanolayers. Besides, defects will also be generated simultaneously in the area close to the interface of the dopants and YBCO matrix, which can provide more pinning effect. The selected dopant material should

be chemically and thermodynamically stable with YBCO matrix, moreover, no chemical compound or solid solution should be formed during the high temperature deposition process.

First, let's see what kind of nanoparticles been incorporated into YBCO matrix for pinning enhancement. The very first nanoparticle doping YBCO was reported by T. Haugan in 2004. [81] In such study, YBa_2CuO_5 (YBCO 211) was incorporated into YBCO 123 matrix to form uniform distributed nanoparticles. What is interesting in this study is that these YBCO 211 nanoparticles were generated by depositing (211/123)×N multilayers (N up to 100). The multilayers were produced using PLD method by ablation of separate 123 and 211 composition targets. Because of the island-growth mode in YBCO and each layer was ultrathin, YBCO 211 nanoparticles were actually formed, as shown in Figure 1.12. From the plan-view SEM image in Figure 1.12(a), the density of YBCO 211 nanoparticle could be estimated to be $1\text{-}1.3\times10^{11}$ cm^{-2}, with the size of ~15 nm. However, from the cross-sectional TEM image in Figure 1.12(b), the particle size was around half compared to what had been seen on the surface, which was believed to be caused by coalescence and ripening while holding the temperature higher than 700°C. Consequently, the pinning enhancement of these YBCO 211 nanoparticles was tested by comparing the $\boldsymbol{J_c}$ performance to the pure YBCO 123 film. Figure 1.13 ploted the $\boldsymbol{J_c}$ values of YBCO 123 films with or without YBCO 211 nanoparticles, in function of applied magnetic field. Obviously, the film with 211 nanoparticles showed slower $\boldsymbol{J_c}$ decrease with increasing applied field, and the self-field $\boldsymbol{J_c}$ increased to 4 MA/cm^2,

compared to 2-3 MA/cm^2 for the pure YBCO film. All these results indicated effective pinning effect was provided by incorporating YBCO 211 nanoparticles.

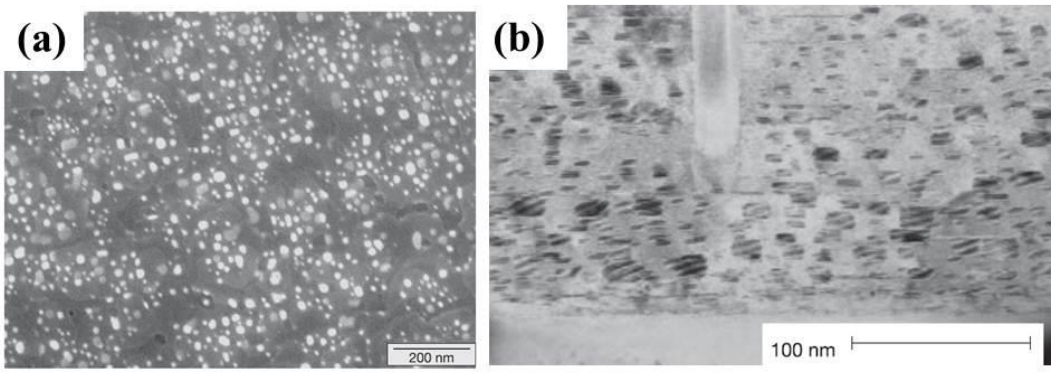

Figure 1.12 (a) Plan-view SEM image and (b) cross-sectional TEM images of YBCO with nanoparticles. [81] Reprinted with permission from "T. Haugan, P. N. Barnes, R. Wheeler, F. Meisenkothen, and M. Sumption, Nature 430, 867 (2004)."

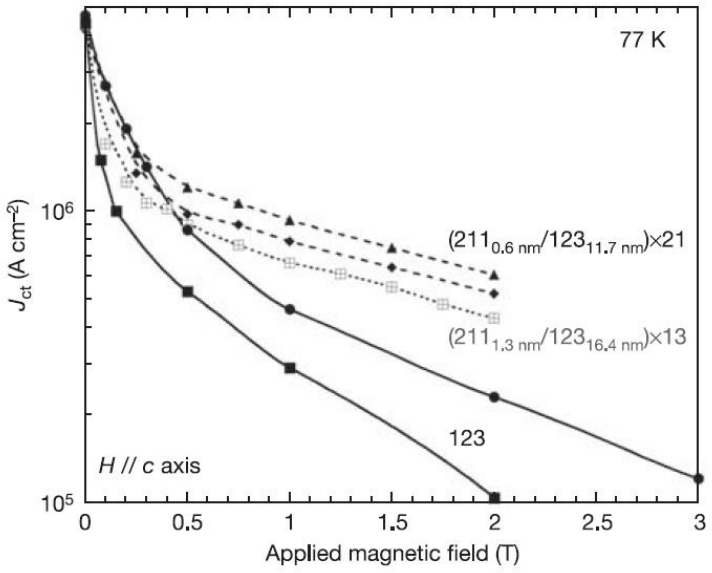

Figure 1.13 In-field $\boldsymbol{J_c}$ comparison of YBCO films with or without nanoparticles. [81] Reprinted with permission from "T. Haugan, P. N. Barnes, R. Wheeler, F. Meisenkothen, and M. Sumption, Nature 430, 867 (2004)."

Another well-studied nanoparticle dopant was $BaZrO_3$ (BZO), which was also first reported in 2004. [83] Different from the multilayer method discussed in the 211 nanoparticle doping, the BZO nanoparticles were generated by a BZO-YBCO mixed target. The films were directly deposited by this 5 mol% BZO doped YBCO target, using PLD. From the cross-sectional TEM images in Figure 1.14(a), (b), nanoparticles could be observed in YBCO matrix, the size of nanoparticles falls in a wide range from 5 nm to 100 nm. The lattice parameter of the nanoparticles could be estimated to be ~4.23 Å from the high resolution TEM image in Figure 1.14(c), which corresponded to $BaZr_{1-x}Y_xO_3$. Furthermore, c-aligned misfit edge dislocations of spacing <50 nm could also be seen, as marked with black arrows in Figure 1.14. These dislocations were correlated defects and might provide pinning effects along the c-direction. The in-field $\boldsymbol{J_c}$ performance of YBCO films with or without BZO addition was compared. Figure 1.15(a), (b) showed significant $\boldsymbol{J_c}$ enhancement of BZO-YBCO film along all the applied magnetic field up to 7 T. The inset of Figure 1.15(a) showed the angular dependence of $\boldsymbol{J_c}$ measured in a magnetic field of 1T, a large up shift of BZO-YBCO could be seen when applied field ***H//c***, which suggested strong pinning along this direction. The large $\boldsymbol{J_c}$ enhancement in c-axis could be correlated to the c-aligned dislocation observed in the microstructure study. Furthermore, the pinning force of the film with BZO nanoparticles was also increased significantly along the measured field, illustrated in the inset of Figure 1.15(b). This study introduced a straightforward way to incorporate BZO nanoparticles into YBCO matrix, by depositing films using a single mixed target.

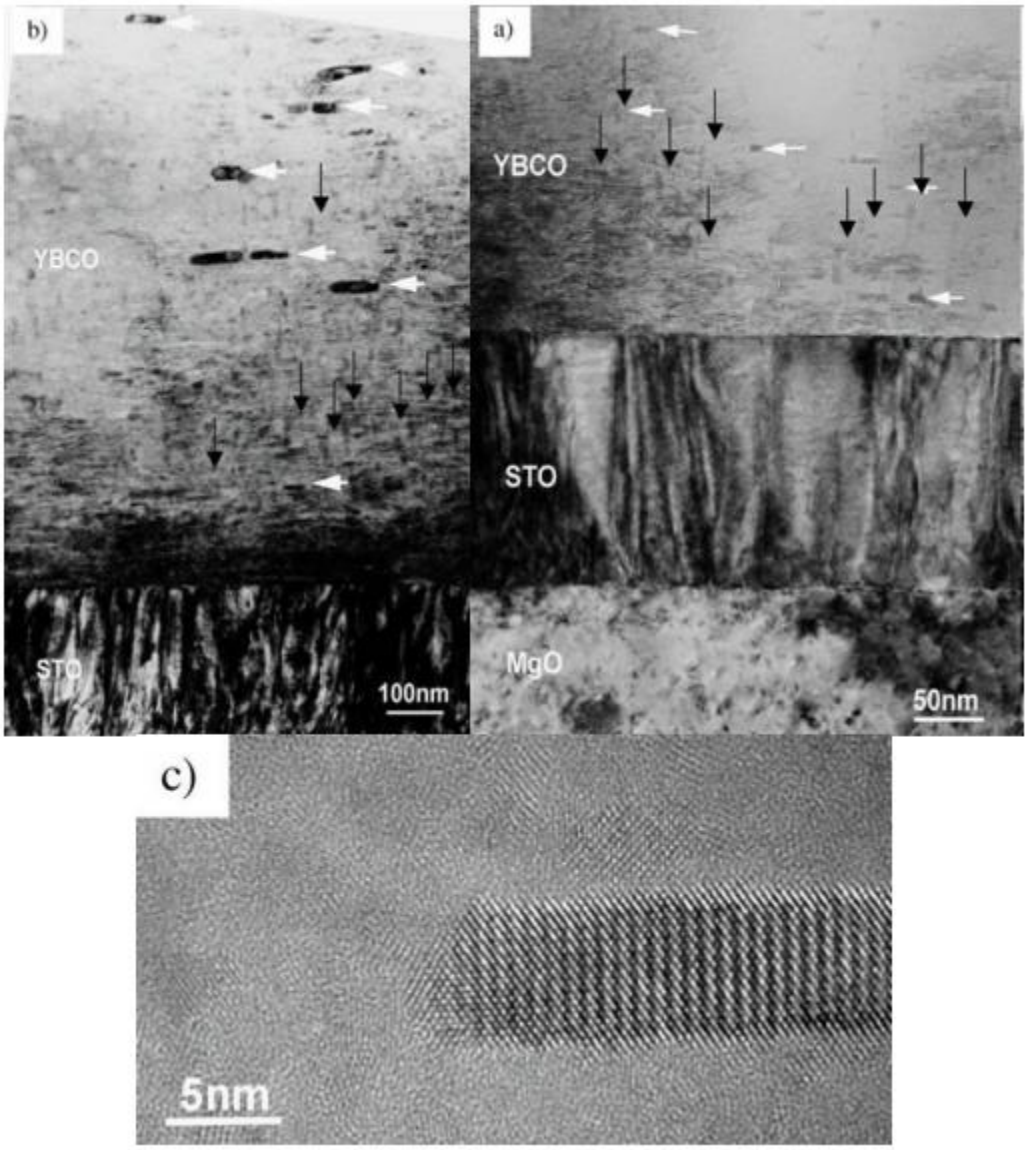

Figure 1.14 (a), (b) Cross-sectional TEM images of YBCO thin film with BZO nanoparticles; (c) High resolution TEM image in a particular area with a BZO nanoparticle. [83] Reprinted with permission from "J. L. Macmanus-Driscoll, S. R. Foltyn, Q. X. Jia, H. Wang, A. Serquis, L. Civale, B. Maiorov, M. E. Hawley, M. P. Maley, and D. E. Peterson, Nat. Mater. **3**, 439 (2004)."

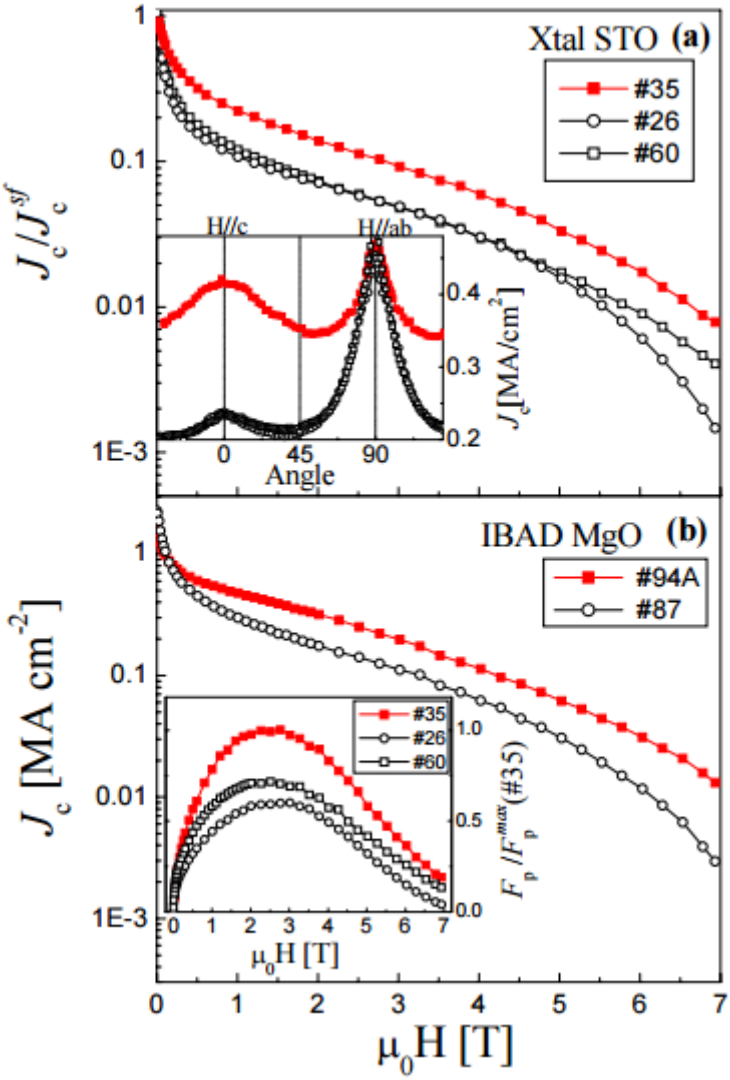

Figure 1.15 In-field J_c comparison of YBCO films with or without BZO nanoparticles on (a) STO, and (b) IBAD-MgO substrates. Inset of (a) shows the the angular dependence of J_c measured in a magnetic field of 1T; Inset of (b) is the pinning force comparison of the films. [83] Reprinted with permission from "J. L. Macmanus-Driscoll, S. R. Foltyn, Q. X. Jia, H. Wang, A. Serquis, L. Civale, B. Maiorov, M. E. Hawley, M. P. Maley, and D. E. Peterson, Nat. Mater. **3**, 439 (2004)."

The relationship between pinning centers and $\boldsymbol{J_c}$ enhancement is complex, generally, the best pinning condition is that the size of the defects close to the coherence length of the superconductor (ξ_{ab}~2 nm, ξ_c~0.5 nm for YBCO), and the areal density of defects is in the order of $(H/2)\times10^{11}$ cm^{-2} (H is the applied magnetic field in tesla). [25, 82] It is really difficult to achieve such perfect condition, as the distribution and size of the dopants are not easy to be controlled. The density of the dopants can be controlled by adding different amount of the doping materials, however, too much doping may deteriorate the film quality itself. Most of the work in this research area is focusing on introducing different doping materials, and pinning effect can be provided by well controlling the process parameters. Not all the dopants show a nanoparticle structure, Table 1.3 summaries some of the reported nanoparticles been incorporated into YBCO thin films, including YBCO 211, $BaZrO_3$, Y_2O_3, $BaSnO_3$, $BaHfO_3$, Ba_2YTaO_6, $BaIrO_3$, $SrZrO_3$, $LaAlO_3$, ZnO and YSZ. Their $\boldsymbol{T_c}$ and $\boldsymbol{J_c^{sf}}$ vaues at 77 K are also concluded in Table 1.3. Most of the YBCO thin films with nanoparticles show self-field and in-field $\boldsymbol{J_c}$ enhancement compared to pure YBCO films, while $\boldsymbol{T_c}$ sustains around 90 K.

Table 1.3 Summary of the 0-D nanoparticle pinning for YBCO.

Dopant	**Authors**	**Ref.**	**substrate**	**T_c (K)**	**J_c^{sf} at 77 K (MA/cm^2)**
YBa_2CuO_5	T. Haugan *et al.*	81	LAO, STO	88.9-90.2	4
$BaZrO_3$	J. L. MacManus-Driscoll *et al.*	83	STO, STO on MgO, IBAD-MgO	87.5-92	>2.6
Y_2O_3	T.A. Campbell *et al.*	68	LAO, STO	88-91.5	3-5
$BZrO_3$+Y_2O_3	F. Ding *et al.*	84	-	90	6.5
$BaZrO_3$	A. Palau *et al.*	85	LAO	-	~6.5
$BaSnO_3$	C. V. Varanasi *et al.*	86	LAO	86-89	1
Y_2O_3	Y. Q. Li *et al.*	87	LAO	86	1.54
$BaHfO_3$	J Hanisch *et al.*	88	STO	89	~4
Ba_2YTaO_6	M. Coll *et al.*	90	LAO	90	1.5
$BaIrO_3$	J Hanisch *et al.*	89	STO	88-91	~3.5
$SrZrO_3$	M. Liu *et al.*	91	LAO	90.2	2.86
$LaAlO_3$	Y. Xu *et al.*	92	LAO	-	~6
Y_2O_3, ZnO	B. Kang *et al.*	93	STO	88	~4
YSZ	S. Ye *et al.*	94	LAO	89	~3.5
$YFeO_3$	S. C. Wimbush *et al.*	124	STO	90	3
RE_3TaO_7, RE=Er, Gd and Yb	S. A. Harrington *et al.*	125	STO	92	0.86 at 1 T,0.38 at 3 T
$CoFe_2O_4$	C. Tsai *et al.*	126	STO	90	5.1 at 65 K
YBa_2NbO_6	G. Ercolano *et al.*	127	STO	89-91.7	~2.2

1.2.3.1.e 1-D nanocolumns (nanorods) for flux pinning

As discussed above, not all the dopants grow in the form of nanoparticle, some of them can grow as nanocolumn or nanorod. One interesting example was BZO, which was grown as nanoparticle by some research groups. [83-85] However, the geometry of the BZO dopants could easily be tuned by changing the deposition temperature or the deposition rate (laser frequency). [95] In this study, 5 mol% BZO- YBCO target was used for growing all the films. The growth temperature was varied from 745 °C to 840 °C, while tuning the frequency from 2 Hz to 15 Hz. $\boldsymbol{J_c}$ angular dependence (at 75.5 K under applied magnetic field of 1 T) of the films grown at different temperatures were first compared, as shown in Figure 1.16(a). As we can see, when the deposition temperature was higher than 800 °C, a large peak centered H//c appears, which indicated that uniaxial pinning by c-axis correlated defects was the main effect. However, when the temperature was lower than 800 °C, a smooth angular dependence was observed, which demonstrated random disordered pinning in this case. Then, films were deposited at different frequencies (2 Hz, 5 Hz, 10 Hz) and kept the temperature fixed at 795 °C, as this temperature was believed to be the optimized temperature. From the $\boldsymbol{J_c}$ angular dependence comparison in Figure 1.16(b), larger c-axis peak could be correlated to lower deposition rate. The increased deposition temperature could increase more mobility of the initially self-assembled BZO nanoparticles, to create more ordered and aligned nanocolumns. In another side, lower deposition rate gave more time for BZO nanoparticles to migrate, and thus also formed aligned nanocolumns. Both of the results indicated that the morphology of BZO dopants was controlled by growth kinetics. To

confirm this conclusion, TEM study was carried out for the samples deposited at 840, 785 and 765 °C, as shown in Figure 1.17. When the temperature was high at 840 °C, parallel BZO nanocolumn array can be observed in Figure 1.17(a), and the mean column length could be estimated to be 44 ± 18 nm. Then, if the growth temperature lowered to 785 °C, both BZO nanaoparticles and nanocolumns could be seen, and the mean column length reduced to 22.3 ± 10 nm. When the temperature further reduced to 765 °C, more BZO nanoparticles appeared and nanocolumns became shorter with a mean length of 10.5 ± 5 nm. These results were consistent with the superconducting property comparison discussed above. This study successfully controlled the morphology of BZO dopant by simply changing the deposition temperature and rate. By controlling the pinning landscape, thick coated film with high current capability isotropic angle dependence was possible to be made.

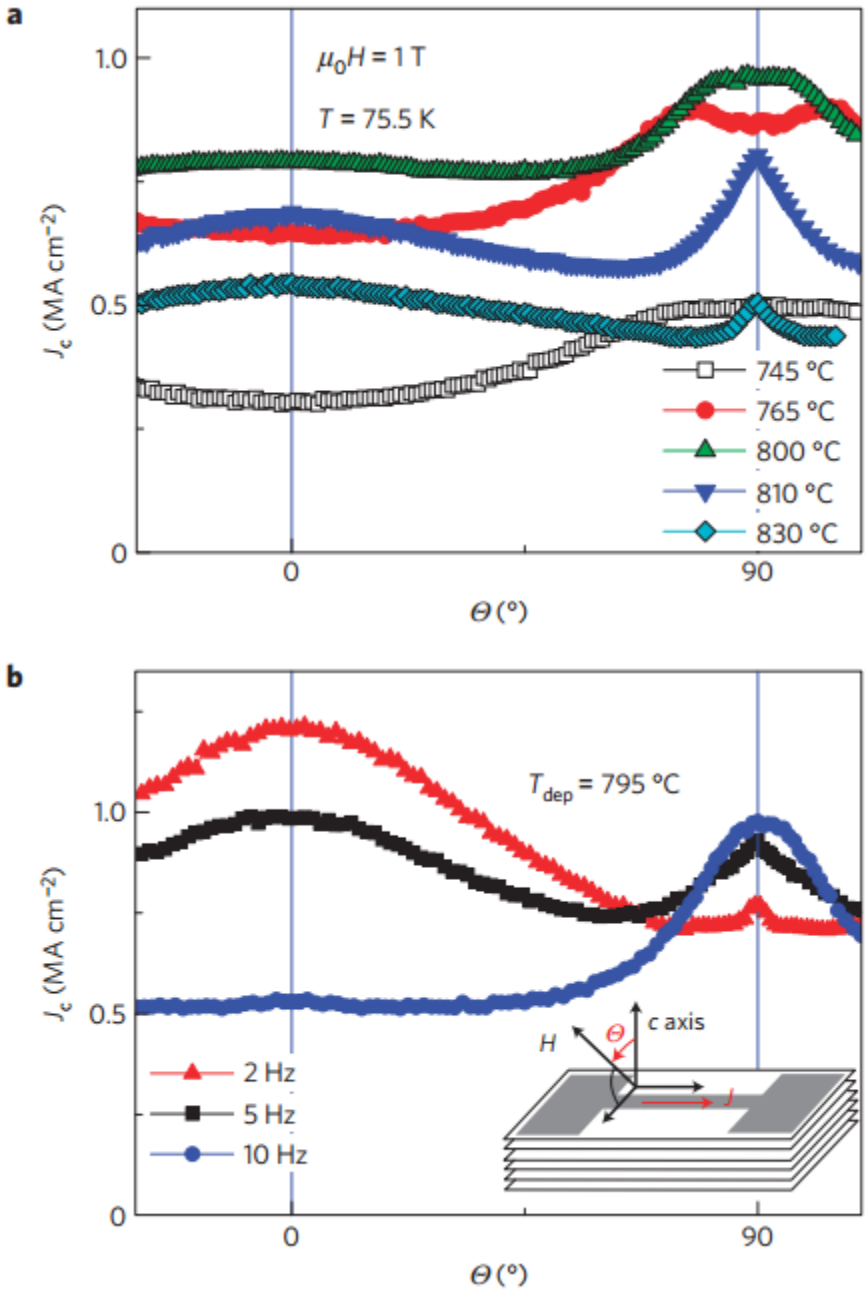

Figure 1.16 Angular dependence of critical current density for the films deposited with different frequencies. [95] Reprinted with permission from "B. Maiorov, S. A. Baily, H. Zhou, O. Ugurlu, J. A. Kennison, P. C. Dowden, T. G. Holesinger, S. R. Foltyn, and L. Civale, Nat. Mater. **8**, 398 (2009)."

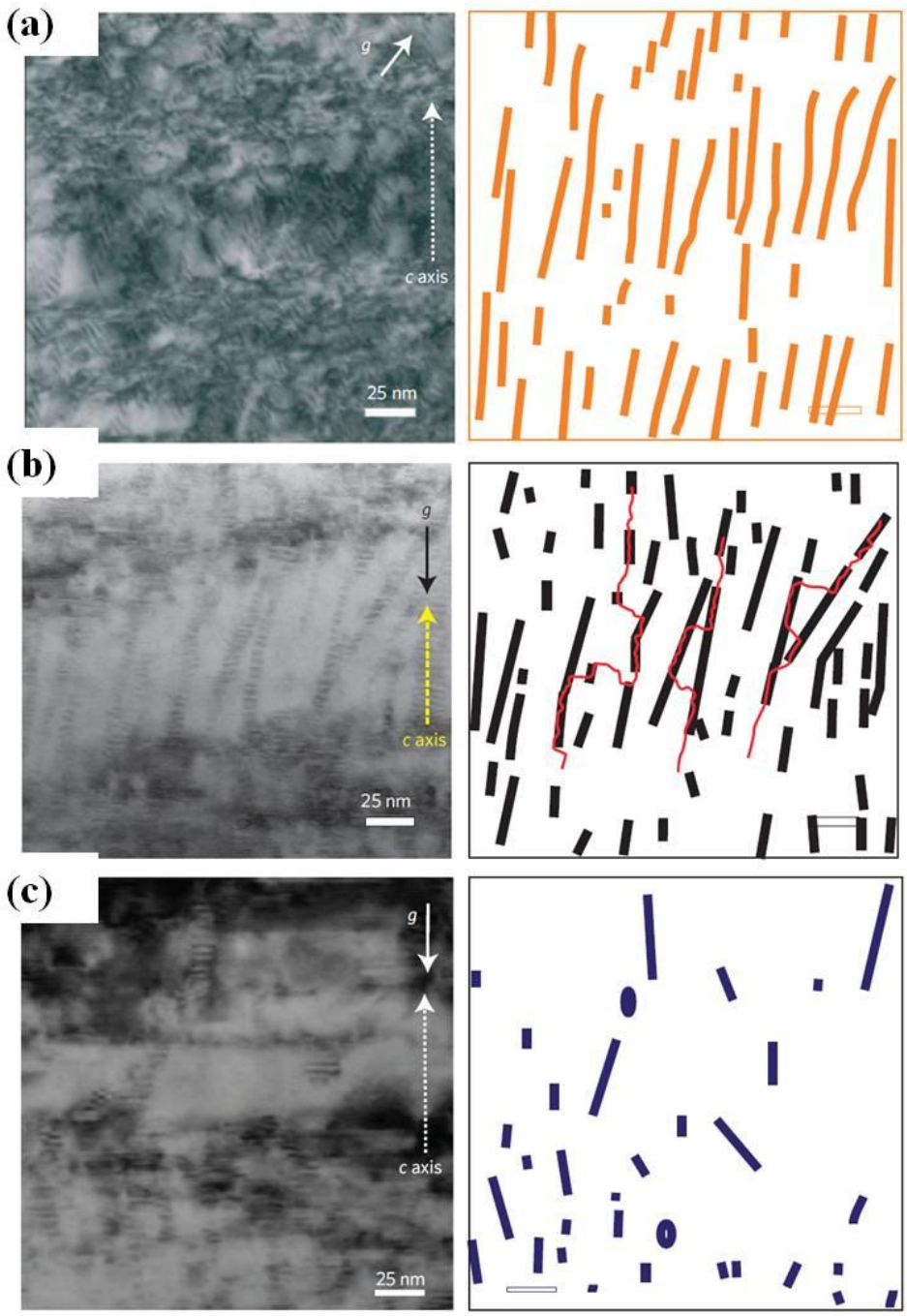

Figure 1.17 TEM images of samples grown at (a) 800 °C, (b) 785 °C and (c) 765 °C. [95] Reprinted with permission from "B. Maiorov, S. A. Baily, H. Zhou, O. Ugurlu, J. A. Kennison, P. C. Dowden, T. G. Holesinger, S. R. Foltyn, and L. Civale, Nat. Mater. **8**, 398 (2009)."

$BaSnO_3$ (BSO) was another well-studied material been doped into YBCO thin films as nanorods. [98-100, 103] Like BZO, BSO nanoparticles have also been achieved for YBCO pinning enhancement. [86] Interestingly, different group reported different structures, although most of them use PLD to grow the films. P. Mele *et al*. conducted a systematic study on BSO doping YBCO thin films, by doping BSO with different levels x wt% (x=2, 3, 4, 5, 6, 8 and 9). [98] This different composition was achieved by making the targets with different amount of BSO. Figure 1.18 exhibited some selected samples with different BSO doping levels: (a) 2 wt%, (b) 4 wt%, (c) 6 wt% and (d) 8 wt%. Obviously, BSO nanorods could be observed in all of the samples, and the density of the nanorods increased with increasing BSO doping, however, the diameters of nanorods were almost the same for all the cases. $\boldsymbol{T_c}$ value decreases with increasing BSO doping level, from 91.5 K for pure YBCO film to 81 K for the highest doping level of 9 wt%. By comparing the in-field $\boldsymbol{J_c}$ performance shown in Figure 1.19(a), 4 wt% could be identified as the optimum doping level. Although the overall pinning force should increase with more BSO nanorods inside the film, as more pinning centers were generated, the film quality would be degraded with more BSO added. Therefore, after the competition between these two effects, the median doping level 4 wt% became the optimum one. The pinning force comparison in Figure 1.19(b) further confirmed and was consistent with the $\boldsymbol{J_c}$ data, the 4 wt% BSO-YBCO sample exhibited the maximum global pinning forces $\boldsymbol{F_P}$ (B//c), and the value achieved 28.3 GN/m^3 near 3 T at 77 K.

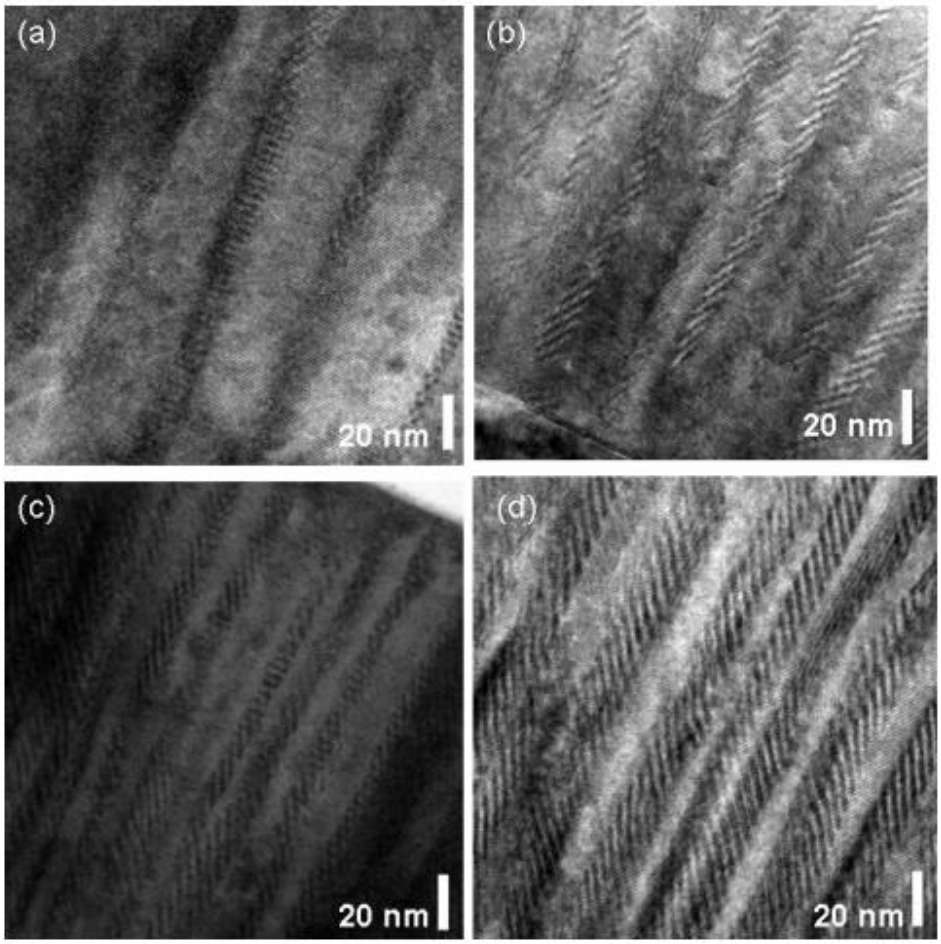

Figure 1.18 Cross-sectional TEM images of YBCO + $BaSnO_3$ samples with different BSO doping levels: (a) 2 wt%, (b) 4 wt%, (c) 6 wt%, and (d) 8 wt%. [98] Reprinted with permission from "P. Mele, K. Matsumoto, A. Ichinose, M. Mukaida, Y. Yoshida, S. Horii, and R. Kita, Supercond. Sci. Technol. **21**, 125017 (2008). © IOP Publishing. Reproduced with permission. All rights reserved. [Ref 98]"

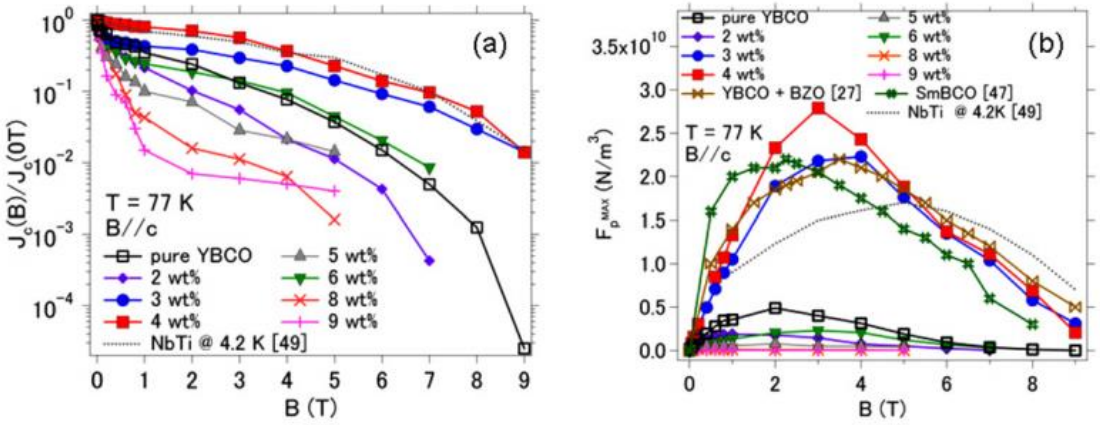

Figure 1.19 (a) Normalized critical current density J_c versus magnetic field B (77 K, B//c) for YBCO films with or without $BaSnO_3$ nanorods. (b) Pinning forces F_P at 77 K as a function of the magnetic field ($F_P = J_c \times B$) applied parallel to the c-axis. [98] Reprinted with permission from "P. Mele, K. Matsumoto, A. Ichinose, M. Mukaida, Y. Yoshida, S. Horii, and R. Kita, Supercond. Sci. Technol. **21**, 125017 (2008). © IOP Publishing. Reproduced with permission. All rights reserved"

It is interesting to see that nanoparticle and nanorod can be achieved for the same material, even by the same method, such like BZO and BSO. The mechanism for this is still not clear, as different groups produce different results. However, most of these dopants show promising pinning effects for YBCO, and people are still trying to find better doping materials or develop better ways to achieve higher in-field performance. Some of the nanorod dopants are reviewed and listed in Table 1.4, beside the discussed BZO and BSO, $BaTiO_3$, Y_2O_3, Ba_2YNbO_6, $CaZrO_3$, YSZ nanorods and nanotube pores were also studied. [95-107]

Table 1.4 Summary of the 1-D nanocolumn (nanorod) pinning for YBCO.

Dopant	**Authors**	**Ref.**	**substrate**	T_c **(K)**	J_c^{sf} **at 77 K (MA/cm^2)**
$BaZrO_3$	B. Maiorov *et al*.	95	STO	-	~3.5
$BaZrO_3$	A. Ichinose *et al*.	96	STO	85.4-88.9	~0.6 at 1 T
$BaTiO_3$	A. K. Jha*et al*.	97	STO	90	6.43
$BaSnO_3$	P. Mele *et al*.	98	STO	81-91	2.4
$BaZrO_3$, $BaSnO_3$	P. Mele *et al*.	99	STO	87.7-93.5	~2
$BaSnO_3$	C. V. Varanasi *et al*.	100	LAO	88.5	1
$BaZrO_3$	M. Peurla *et al*.	101	STO	-	0.1 at 65 K, 22 T
$BaZrO_3$	Y. Yamada *et al*.	102	STO	88.9	1.9
$BaSnO_3$, $BaSnO_3$+Y_2O_3	K. Matsumoto *et al*.	103	STO	-	0.89 under 1 T
Ba_2YNbO_6	D. M. Feldmann *et al*.	104	STO	-	~4.5 at 75.6 K, 1.3-1.5 under 1 T
Nanotube pores	X. Wang *et al*.	105	-	-	5.83
$BaZrO_3$, $CaZrO_3$, YSZ	A. Goyal *et al*.	106	RABiTS	~87	~2.5
$BaSnO_3$	Y. Zhu *et al*.	107	LAO	-	-

In addition, some researchers tried to introduce both nanoparticles and nanorods into YBCO, aim to create more pinning centers for stronger pinning effect. For example, M. A. P. Sebastian *et al*. combined BSO and Y_2O_3 together doping into YBCO thin film. [108] In such work, 3, 5, 10 vol% BSO and 3 vol% Y_2O_3 had been mixed with remaining YBCO to produce targets, and the films were deposited from these targets by

PLD technique. Interestingly, the TEM images showed both Y_2O_3 nanoparticles and BSO nanorods in the film, as shown in Figure 1.20. However, by comparing the in-field $\boldsymbol{J_c}$ performance, no significant improvement could be seen, as shown in Figure 1.21. Some samples even showed worse $\boldsymbol{J_c}$ performance than the reference YBCO thin film, which suggested that pinning effect are not simple addition of all the defects.

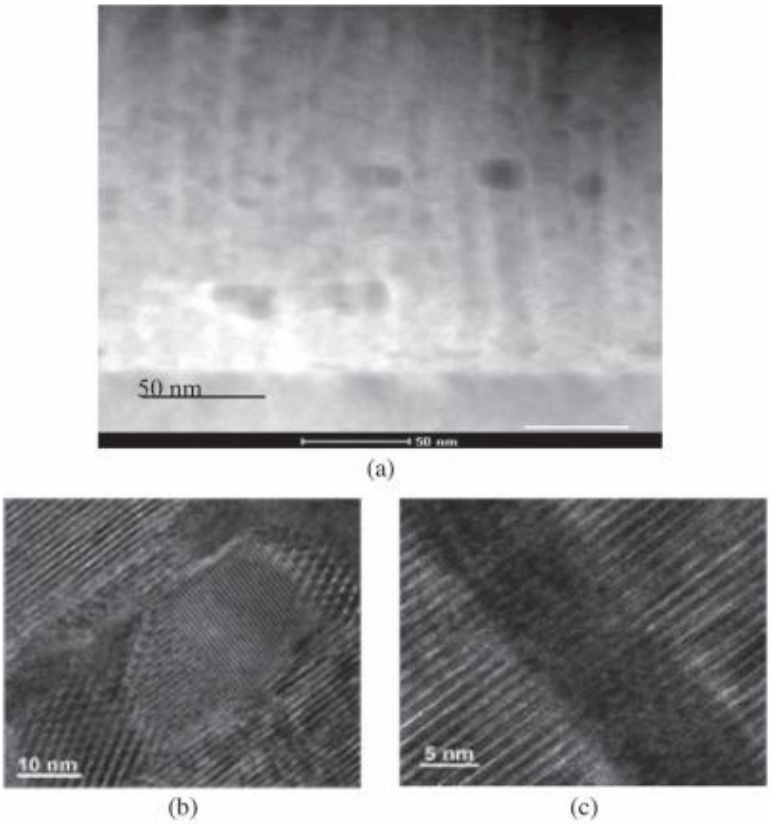

Figure 1.20 TEM images of the sample show both nanoparticles and nanorods. [108]

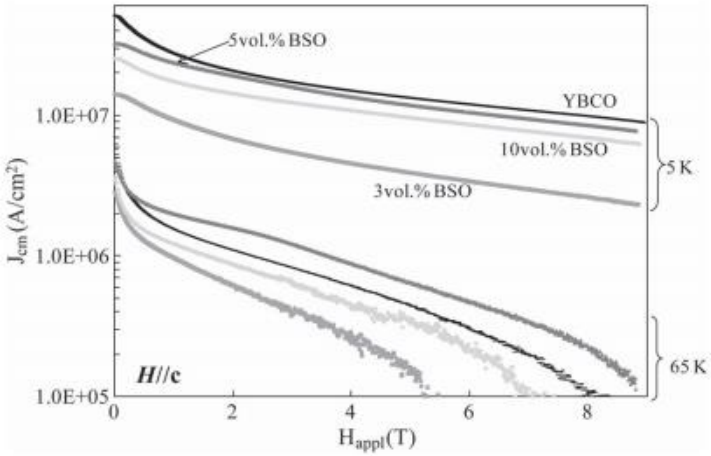

Figure 1.21 In-field $\boldsymbol{J_c}$ comparison at both 5 K and 65 K. [108]

1.2.3.1.f 2-D planar pinning for YBCO

With these defect pinning methods, superconducting performance of YBCO had been significantly improved. However, more work was needed to further enhance its property to satisfy the application requirements. In another side, $\boldsymbol{J_c}$ performance of YBCO thin film always started to drop when the film thickness increases to an optimum value (which is usually in the range of 50-400 nm). [76, 123] Therefore, it was difficult to grow very thick YBCO film with good $\boldsymbol{J_c}$ value, which hindered the application of coated conductor. Multilayered structure was explored to grow thick films, in such scheme designing, YBCO and another material were grown alternatively. This material should have prefect lattice matching and good chemical compatibility with YBCO. In addition, this multilayer was not only for thick film growth, it could also provide pinning effect for YBCO, as a lot of defects could be generated in the interface area. Researchers

selected appropriate materials for the multilayer growth, to achieve pinning enhancement. [109-122]

It is always good to start from a material whose crystal is very close or almost the same to YBCO, such like DyBCO, NdBCO and PrBCO. [109, 110, 118, 119] For example, Pan *et al*. deposited YBCO/NdBCO multilayers with a total thickness of ~1 u m. [110] First, 300 nm YBCO was grown on STO substrate, and then 50 nm NdBCO was deposited on top of YBCO, followed by another 300 nm YBCO, 50 nm NdBCO and a third 300 nm YBCO layer, as shown in the SEM image in Figure 1.22. In such scheme, 300 nm was consider as the optimum thickness for YBCO, and the 50 nm NdBCO could provide a new template for thicker YBCO growth. The film exhibited a $\boldsymbol{T_c}$ value ~90 K with a transition range of <0.5 K. The $\boldsymbol{J_c}$ values of the films in this study were plotted and compared 0.4 u m and 1 u m YBCO films in Figure 1.23. 0.4 u m was considered as the optimum thickness for YBCO, which obtained the best self-field $\boldsymbol{J_c}$ performance of 3.2 MA/cm^2 at 77 K. However, interestingly, the YBCO/NdBCO multilayer started to show high $\boldsymbol{J_c}$ values after the applied field exceeding 0.3 T. This sample also obtained 2-fold and 3-fold higher $\boldsymbol{J_c}$ values under zero field and 1 T, compared to the single layer YBCO with the same thickness of 1 u m. The difference of the ionic radii between Y and Nd will result in a small lattice mismatch between the layers. As a consequence, local stress and edge dislocations were formed near the interface area, which could serve as pinning centers. It was also found that the in-field $\boldsymbol{J_c}$ enhancement was more obvious at low temperature 10 K than high temperature 77 K, which indicated that the pinning effect by the edge dislocations was more effective at lower temperature.

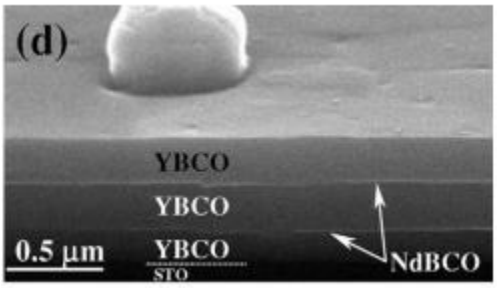

Figure 1.22 Cross-sectional SEM image of the YBCO/NdBCO multilayers. [110]
Reprinted with permission from "A. V. Pan, S. Pysarenko, and S. X. Dou, Appl. Phys. Lett. **88**, 232506 (2006)." With permission from AIP publishing.

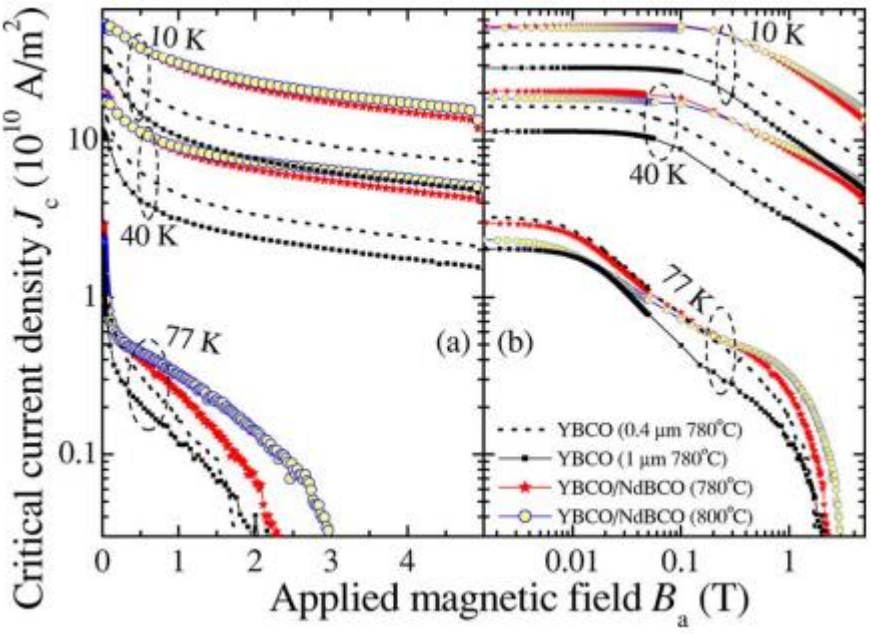

Figure 1.23 Critical current density as a function of applied magnetic field in (a) semilogarithmic and (b) double-logarithmic scales. [110]
Reprinted with permission from "A. V. Pan, S. Pysarenko, and S. X. Dou, Appl. Phys. Lett. **88**, 232506 (2006)." With permission from AIP publishing.

In addition to the advantage of the thick film growth, nanolayer was also widely grown with thin YBCO films for pinning enhancement. CeO_2 was one of the most used materials in the research field of YBCO pinning, which had perfect lattice matching and good chemical compatibility with YBCO. CeO_2 had been grown with YBCO to achieve multilayer structure by different groups. [111, 120, 122] For example, YBCO thin films with 1, 2 and 4 CeO_2 interlayers were successfully grown for pinning enhancement, reported by Tsai *et al*. [122] The multilayer films were produced by alternating ablation of the separate YBCO and CeO_2 targets. By control the deposition time, the whole thickness of the films was fixed at ~500 nm, with each CeO_2 layer of 5 nm. It was believed that defects (mostly dislocations) formed in the interface area, so detailed microstructure study was carried out to explore the defect density as function of different interlayers. Figure 1.24(a), (b) and (c) exhibit high resolution TEM of the interface area of the 1-CeO_2 interlayer sample, its corresponding Fast Fourier Transformation (FFT) image and FFT diffraction pattern, respectively. Very clean interface could be observed and high density misfit dislocation could be identified close to the interface area, which was resulted from the lattice mismatch of the two layers. Figure 1.24(d), (e) and (f) were the same batch of the first interlayer of the 2-CeO_2 interlayer sample. A step of about 1-2 unit cell of YBCO could be see while the majority of the interface was smooth, which produced more dislocations than the 1-CeO_2 interlayer sample. Figure1.24(g), (h) and (i) showed the HRTEM image and corresponding FFT images of the second layer of the 2-CeO_2 interlayer sample. Obviously, more steps appeared in this interface, and more

defects were found consequently. Overall, all the interfaces were relatively clean, however, it became rougher when more interlayers were grown.

From the microstructure study, apparently, 4-CeO_2 interlayer YBCO film obtained the most amount of misfit dislocations, which might provide more pinning centers. However, interestingly, 2-CeO_2 interlayer sample presented the highest self-field and in-field $\boldsymbol{J_c}$ values along the applied field, followed by the 1-CeO_2 interlayer sample, and the 4-CeO_2 interlayer sample was even worse than the pure YBCO film at 65 K. This was opposite to what one may expect. The reason was that when more interlayers being introduced, the film quality itself would be degraded, as shown in the previous microstructure study. When 2 interlayers introduced, pinning effect provided by the misfit dislocation was dominating over the film quality degradation, while reverse result occured with 4 interlayers. Therefore, after the competing of the two opposite effect, 2 interlayers was the optimum. Another interesting finding was that the 4-interlayer sample started to overcome the pure YBCO sample when temperature lowered down to 40 K or 5 K, which suggested that defect pinning was more effective at low temperature. Overall, this study indicated that interfacial defects such as misfit dislocations could act as effective pinning centers for YBCO, and they were more effective at low temperature.

Suitable nanolayer could be template for thick YBCO film growth, and also provided defect pinning effect for YBCO. A brief summary of the 2-D planar pinning effect for YBCO is listed in Table 1.5, the studied materials included DyBCO, NdBCO,

CeO_2, $BaHfO_3$, $(Fe_2O_3)_x(CeO_2)_{1-x}$, $(CoFe_2O_4)_x(CeO_2)_{1-x}$, $BaTiO_3$, $BaSnO_3$, Y_2O_3, PrBCO, $SrTiO_3$ and $BaZrO_3$. [109-122]

Table 1.5 Summary of the 2-D planar pinning for YBCO.

Dopant	**Authors**	**Ref.**	**substrate**	T_c **(K)**	J_c^{sf} **at 77 K (MA/cm^2)**
DyBCO	K. Develos-Bagarinao *et al*.	109	CeO2-buffered sapphire	-	3.04
NdBCO	A. V. Pan *et al*.	110	STO	89.3-91.7	3.2
CeO_2	L. Lei *et al*.	111	STO	90.76	1.59
$BaHfO_3$	E. Backen *et al*.	112	STO	89.5-92.5	1.5
$(Fe_2O_3)_x(CeO_2)_{1-x}$	C. Tsai *et al*.	113	STO	~90	9.1 at 65 K
$(CoFe_2O_4)_x(CeO_2)_{1-x}$	J. Huang *et al*.	114	STO	~90	6.4
$BaTiO_3$	D. Shi *et al*.	115	LAO	-	2.85
$BaSnO_3$	S. Ohshima *et al*.	116	MgO	88	~3.5 at 60 K
Y_2O_3	R. I. Tomov *et al*.	117	NiFe	90	0.06
PrBCO	V. Galindo *et al*.	118	LAO	92.3	~5
PrBCO	X. Qiu *et al*.	119	STO, LAO	~87	0.62 at 50 K
$BaZrO_3$, CeO_2	H. Wang *et al*.	120	STO	88-90	1.4
$SrTiO_3$	Y. Uzun *et al*.	121	STO	92	~1
CeO_2	C. Tsai *et al*.	122	STO	87.8	3.2 at 65 K

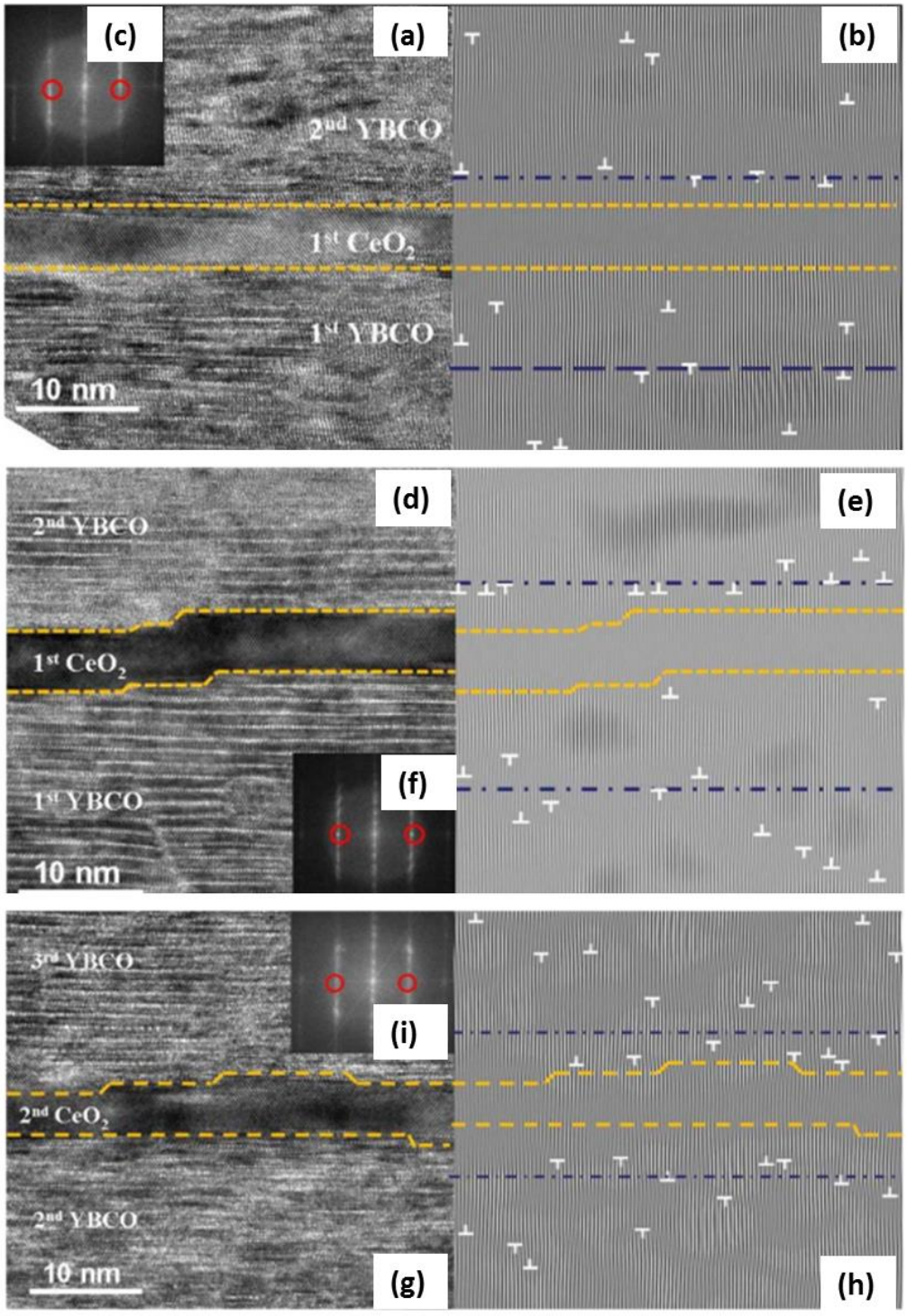

Figure 1.24 HRTEM image and corresponding FFT images of 1-CeO_2 interlayer and 2-CeO_2 interlayer samples. [122]

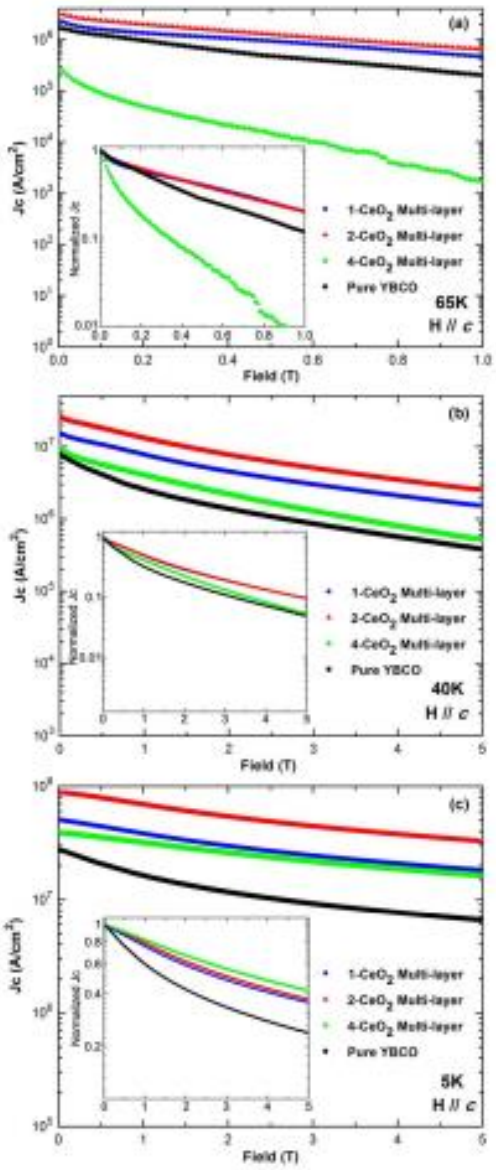

Figure 1.25 In-field J_c performance as a function of applied magnetic field measured at (a) 65 K, (b) 40 K, and (c) 5 K. [122]

1.2.3.2 Magnetic pinning

As mentioned, the perfect defect pinning condition is that the defect size approach the coherence length of the superconductor. For YBCO, its coherence length is very small (ξ_{ab} (0 K) ~1.5 nm, ξ_{ab} (77K) ~ 4nm and ξ_c~0.5 nm), [128] which becomes a major limitation for the defect pinning. The maximum pinning energy equals to the condensation energy of Cooper pairs in the volume of the core (maximum energy per unit length of the vortex), which can be described as:

$$\boldsymbol{U_{cp}} \sim {}^{\boldsymbol{\Phi_0}}\!/_{\boldsymbol{8\pi\lambda_L}} \quad \text{(Equation 1.4)}$$

here $\boldsymbol{\Phi_0}$ is the quantum of magnetic flux and $\boldsymbol{\lambda_L}$ is the London penetration depth. [129] The London penetration depth increases with increasing temperature, which results in the drop of the condensation energy. Thus, defect pinning effect becomes weaker at high temperature. In another side, because of the small volume of the vortex core and layered structure of the high temperature superconductors, the condensation energy is too weak to avoid the depinning by thermal fluctuations. [75] In order to overcome this limitation, magnetic pinning has been proposed. [130] Unlike the defect pinning to pin the normal cores, the proposed magnetic pinning can pin the magnetic flux inside the vortex. The magnetic pinning potential can be estimated by:

$$\boldsymbol{U_{mp}} \sim \boldsymbol{\Phi_0 M(x) d_s} \quad \text{(Equation 1.5)}$$

here $\boldsymbol{M(x)}$ is the magnetization of the ferromagnetic pinning material and $\boldsymbol{d_s}$ is the thickness of the superconducting film. $\boldsymbol{U_{mp}}$ is estimated to be two magnitude larger than $\boldsymbol{U_{cp}}$ from columnar defect. [129] In addition, $\boldsymbol{U_{mp}}$ is not weaken with increasing

temperature, which allows its application at high temperature. Therefore, magnetic pinning is promising for further pinning improvement, especially at high temperature.

Different magnetic materials have been studied for the pinning enhancement for YBCO thin films, in the form of nanoparticle or nanolayer. Wimbush *et al*. introduced ferromagnetic $YFeO_3$ (YFO) into YBCO matrix by a YFO-YBCO composite target. [124] The composition of YFO was controlled at relatively low levels of 1 mol%, 3 mol% and 5 mol%, to avoid the poisoning effect on YBCO. From the low-mag TEM image in Figure 1.26(a), nanoprecipitates with small size less than 5 nm could be observed throughout the whole film. To determine the crystal structure of the nanoprecipitate, high resolution TEM and selected-area diffraction patterns of the selected regions were conducted, as shown in Figure 1.26(b). The results further confirmed that the nanoprecipitates were YFO. Moreover, the orientation matching between YFO and YBCO could be determined as [110]YFeO // [200]YBCO for in-plane and [003]YFeO // [002]YBCO for out-of-plane.

Superconducting properties of these YFO doped YBCO films were measured and compared with the pure YBCO sample, as shown in Figure 1.27. The $\boldsymbol{T_c}$ values of YFO-YBCO slightly decreased with increasing YFO doping, due to poisoning effect. However, even the 5 mol% YFO-YBCO exhibited a reasonably high $\boldsymbol{T_c}$ value of 87 K, compared to 90 K of the pure YBCO film, which indicated that limited poisoning effect introduced with a low level doping. In another side, there was a significant self-field $\boldsymbol{J_c}$ enhancement for the 1 mol% YFO-YBCO compared to pure YBCO film, from 1.5 MA/cm^2 to 3.0 MA/cm^2 at 77 K. This significant self-field $\boldsymbol{J_c}$ enhancement might be

caused by Lorentz force reduction pinning mechanism, as Lorentz force acts on both the vortices and the magnetic pinning sites themselves in this case. However, same as the trend of $\boldsymbol{T_c}$ values, no further enhancement in $\boldsymbol{J_c}$ had been observed with more YFO doping, the 1 mol% YFO-YBCO obtained all the best performance along the applied magnetic field. Furthermore, the angular dependence of $\boldsymbol{J_c}$ in the inset of Figure 1.27 indicated uncorrelated random pinning effect caused by YFO nanoparticles. With such a low level of 1 mol% doping to achieve such a strong pinning effect, the contribution of magnetic pinning was considered as the dominating factor in this case. Tremendous research efforts had been focused on exploring magnetic pinning for YBCO, such as LSMO nanolayer, $La_{2/3}Ca_{1/3}MnO_3$ nanolayer, $CoFe_2O_4$ nanoparticle, $Pr_{0.67}Sr_{0.33}MnO_3$ nanolayer, $(LSMO)_{0.5}$:$(CeO_2)_{0.5}$ nanolayer *etc*. [126, 131-141]

In summary, defect pinning and magnetic pinning are both effective for superconducting property enhancement of YBCO. Some work has also been focusing on combining these two effects together for further improvement. [113, 114, 137, 140, 142] Great pinning enhancement has been observed in these work, however, the mechanism is still not very clear. For example, how much pinning is originated from each pinning effect, which pinning effect is more dominating in different conditions (different temperature, different applied field). As mentioned previously, the pinning effect is not simply additive by different pinning centers. Therefore, there is still a huge space in this research field. One of the most important tasks is how to take advantage of all these different pinning methods, to achieve the most promising pinning scheme.

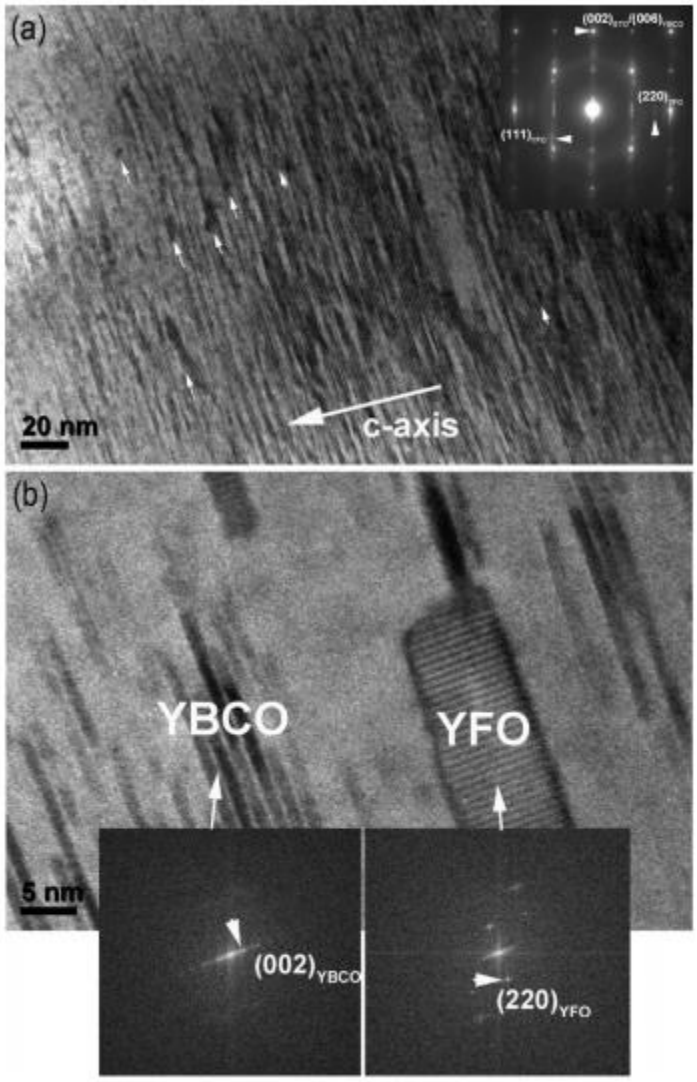

Figure 1.26 (a) Cross-sectional TEM image of the 3 mol% YFO-YBCO film; (b) High resolution TEM image of a single isolated nanoparticle and selected-area diffraction patterns of the indicated regions. [124] Reprinted with permission from "S. C. Wimbush, J. H. Durrell, C. F. Tsai, H. Wang, Q. X. Jia, M. G. Blamire, and J. L. MacManus-Driscoll, Supercond. Sci. Technol. **23**, 045019 (2010). © IOP Publishing. Reproduced with permission. All rights reserved. [Ref 124]"

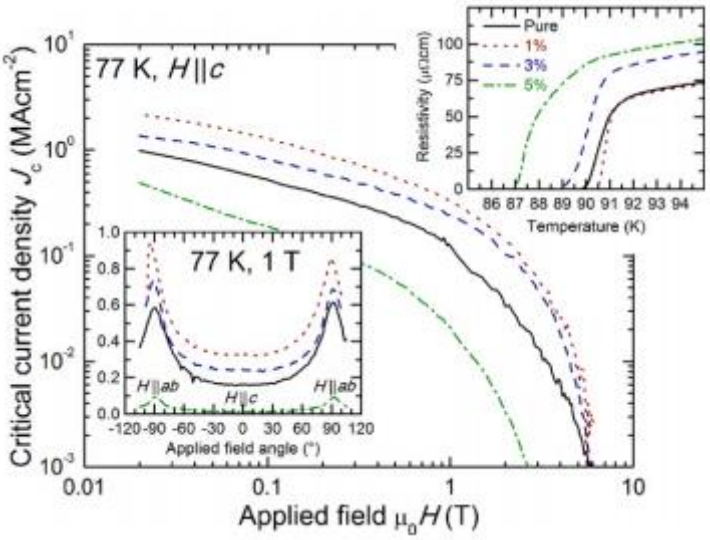

Figure 1.27 In-field J_c comparison of YBCO films with or without YFO doing; Up inset is resistivity-temperature measurement and down inset is the the angular dependence of J_c. [124] Reprinted with permission from "S. C. Wimbush, J. H. Durrell, C. F. Tsai, H. Wang, Q. X. Jia, M. G. Blamire, and J. L. MacManus-Driscoll, Supercond. Sci. Technol. **23**, 045019 (2010).

Table 1.6 Summary of magnetic pinning for YBCO.

Dopant	**Authors**	**Ref.**	**substrate**	T_c **(K)**	J_c^{sf} **at 77 K (MA/cm^2)**
Iron containing oxide nanoparticle	S. C. Wimbush *et al.*	131	STO	87	5
LSMO nanolayer	T. Petrisor Jr. *et al.*	132	STO	88.8	~2 at 70 K
Fe_2O_3 nanolayer	J. Wang *et al.*	133	STO	88	3.98 at 65 K
$YFeO_3$ nanoparticle	S. C. Wimbush *et al.*	124	STO	90	3
$BaFe_{12}O_{19}$ nanolayer	A. G. Santiago *et al.*	134	YSZ	88	-
CoPt nanolayer	D. B. Jan *et al.*	135	LAO	86	4.28 at 75 K
LSMO nanoparticles/layer	A. K. Jha *et al.*	136	STO	88	0.144 at 4 T
$(Fe_2O_3)_{0.5}$:$(CeO_2)_{0.5}$ nanolayer	C. Tsai *et al.*	137	STO	90.1	5.39 at 65 K
$La_{2/3}Ca_{1/3}MnO_3$ nanolayer	J. Albrecht *et al.*	138	STO, LSGO	87	10
LSMO nanolayer	C. Z. Chen *et al.*	139	LAO	~87	~2
$(LSMO)_{0.5}$:$(CeO_2)_{0.5}$ nanolayer	J. Huang *et al.*	140	STO	~90	5.5
$Pr_{0.67}Sr_{0.33}MnO_3$ nanolayer	X. X. Zhang *et al.*	141	STO	88.5	-
$CoFe_2O_4$ nanoparticle	C. Tsai *et al.*	126	STO	90	5.1 at 65 K

1.3 Iron chalcogenide superconducting thin films

1.3.1 Discovery and development of iron chalcogenide superconductor

The high temperature superconductors (with T_c higher than 50 K) were always copper-based materials, including YBCO, until the existence of iron-based superconductor. [143] The first iron-based superconductor was LaOFeP, which was discovered by Kamihara *et al*. in 2006. [144] However, the critical temperature of this superconductor was very low (~4 K) compared to HTS. What made the research community really excited was that the same group reported the superconductivity of F-doped LaFeAsO at 26 K. [145] After that, a lot of iron-based superconductors had been discovered and reported, most of them could be classified into 1111 type ReFeAsO (Re = rare earths), 111-type AFeAs (A = alkali metal), 122-type $AeFe_2As_2$ (Ae = alkaline earths), and 11-type FeX (X = chalcogens). [146-149] Among all of them, 11-type FeSe system has the simplest crystal structure, and it has attracted tremendous research interests since it was first reported in 2008. [149] The crystal structure of FeSe is tetragonal PbO structure (P4/nmm space group) containing Fe-Se planar sub-lattice with an interval of 5.518 Å, as shown in Figure 1.28. The tetrahedral layers of $FeSe_4$ are considered as the key component of this material system, and it plays the similar role like the CuO_2 layers in the copper-based superconductors. Both singles crystals and thin films of FeSe system had been synthesized as superconductors. However, the epitaxial growth of the thin films were relatively difficult in the early stage, thus its superconducting properties were not as good as its single crystal form. Thanks to the great efforts of the community towards optimizing the thin film growth, high epitaxial

films with much better superconducting properties have been grown. The thin film form development is particularly important, since it can be applied into the coated conductor application.

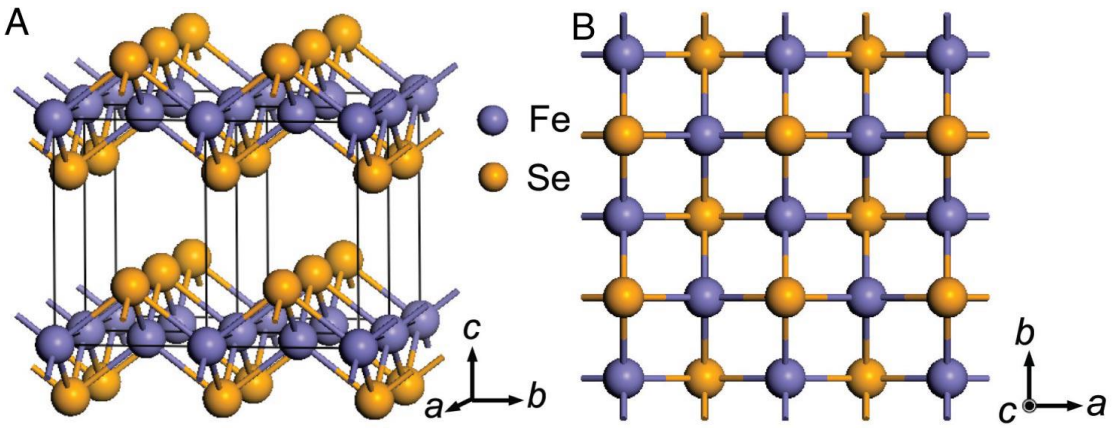

Figure 1.28 Schematic crystal structure of FeSe. (Copyright (2008) National Academy of Sciences, U.S.A.) [149].

As is known, the first discovered FeSe was in the single crystal form. [149] Soon after, thin films had been deposited, mostly by pulsed laser deposition (PLD) technique. [150-155] Wang *et al*. reported the successful grow of $FeSe_{1-x}$ thin films on MgO substrates. [154] The films were deposited at various temperatures, two of them were reported in this study, the one deposited at 320 °C (LT-FeSe) and 500 °C (HT-FeSe). The thickness of both films was controlled at ~140 nm. The XRD results in Figure 1.29(a) showed the (001) peaks of tetragonal phase FeSe for LT-FeSe, however, HT-FeSe obtained (101) peaks. The R-T plots for these two samples were also very different,

as shown in Figure 1.29(b). LT-FeSe only had a slightly resistive drop until the temperature lowered down to 2 K, while HT-FeSe exhibited an obvious transition from 8 K to 4 K. This value was still lower than the discovered single crystal counterpart. [149] The result for the LT-FeSe sample was not as expected, as the film was grown into pure tetragonal phase with nearly epitaxial structure. To explore the reason behind, more LT-FeSe and HT-FeSe films with different thickness (140 nm-1 u m) were prepared. The R-T measurements showed that the $\boldsymbol{T_c}$ value of LT-FeSe was highly related to the thickness, as show in Figure 1.30(a). It was obvious that $\boldsymbol{T_c}$ value of LT-FeSe increases with increasing thickness of the film. However, this trend did not appear for the HT-FeSe films, as shown in Figure 1.30(b), there was no big different of the R-T plots for HT-FeSe films with different thickness. The suppression of $\boldsymbol{T_c}$ in thin LT-FeSe was believed to be caused by the interfacial effect. The atoms from the ab plane in the film-substrate interface area were pinned to the atoms from substrate, which caused a strong lattice strain effect to suppress superconducting property. However, this effect was relaxed with increasing thickness, which explained the thickness dependence of the LT-FeSe samples. In another side, the HT-FeSe films aligned preferably along the (101) orientation and would not be affected by the strain effect. That was why there was no thickness dependence for the HT-FeSe films. This was one typical work for FeSe thin film in its early stage, we could see these early deposited FeSe thin films were not having good property. Therefore, more and more work had been done to improve its superconducting properties since then, until now.

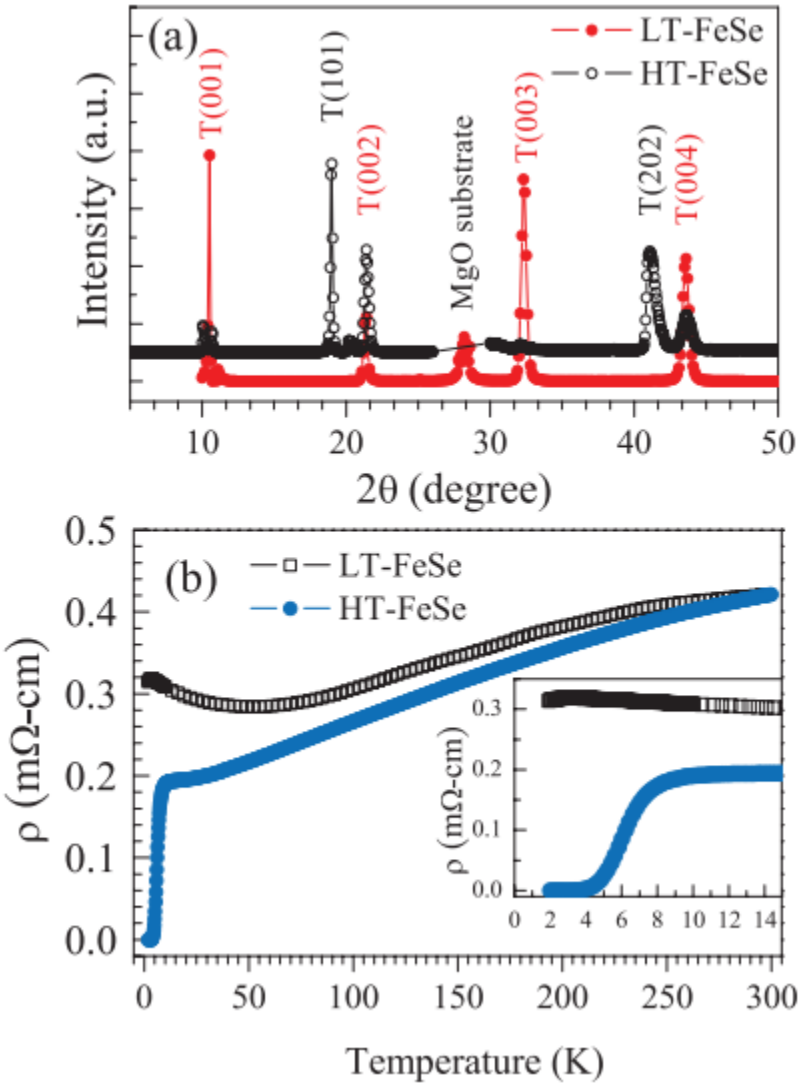

Figure 1.29 (a) XRD scans and (b) R-T plots for both LT- and HT-$FeSe_{1-x}$ films. [154] Reprinted with permission from "M. J. Wang, J. Y. Luo, T. W. Huang, H. H. Chang, T. K. Chen, F. C. Hsu, C. T. Wu, P. M. Wu, A. M. Chang, and M. K. Wu, Phys. Rev. Lett. **103**, 117002 (2009)." Copyright (2009) by the American Physical Society. [Ref 154]

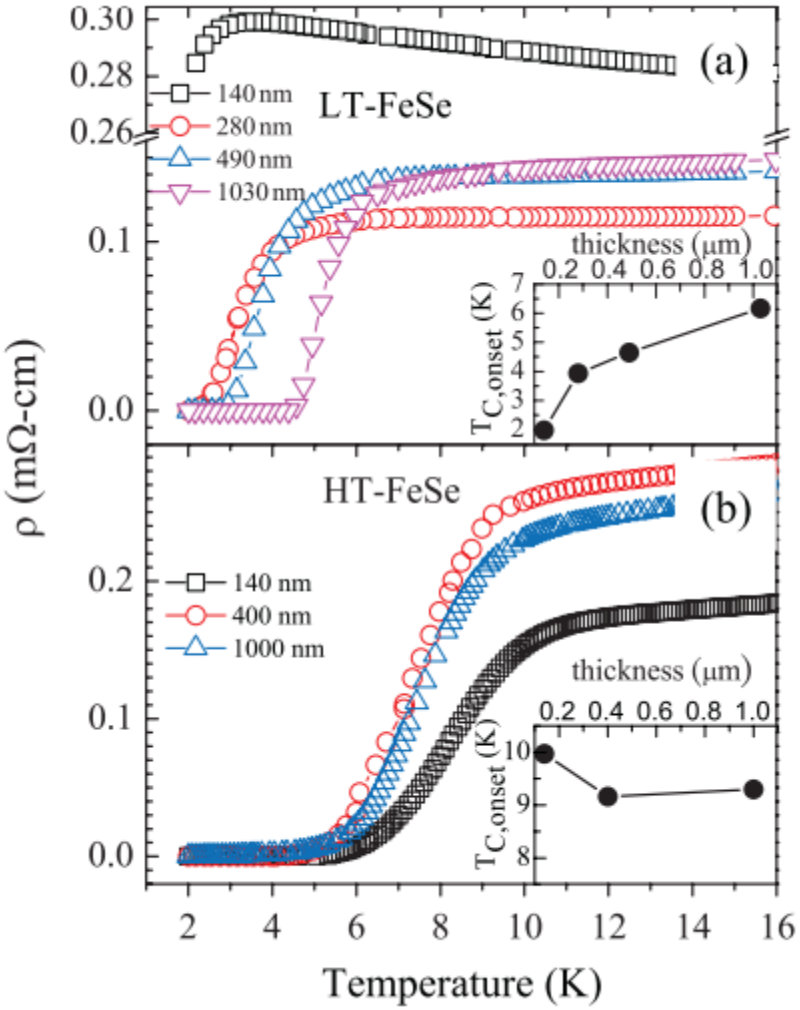

Figure 1.30 R-T plots for (a) LT-FeSe and (b) HT-FeSe thin films with various thicknesses. The insets present the thickness as function of T_c. [154] Reprinted with permission from "M. J. Wang, J. Y. Luo, T. W. Huang, H. H. Chang, T. K. Chen, F. C. Hsu, C. T. Wu, P. M. Wu, A. M. Chang, and M. K. Wu, Phys. Rev. Lett. **103**, 117002 (2009)." Copyright (2009) by the American Physical Society. [Ref 154]

1.3.2 Chalcogens doping of FeSe system

Since the early deposited FeSe films were always having low critical temperature, following work was focusing on improving this value. Doping with the isovalent elements from the same group could be an effective way and worth trying. Therefore, chalcogens doping with different levels of FeSe system was studied by different research groups. However, different groups always reported different results, even for the same film and made by the same technique (mostly by PLD). Some of the results were summarized in Table 1.7.

1.3.2.1 FeSe thin films

As mentioned, FeSe is the first discovered iron chalcogenide superconductor, and some work on FeSe thin film has also been introduced in last section. Beside, FeSe thin film has been grown by other different groups on various substrates. Nie *et al*. deposited FeSe thin films with different thickness of 50 nm, 100 nm and 200 nm on STO, MgO and LAO substrates. [150] It was found that the tetragonal FeSe was the main phase in all the films. Because of the lattice mismatch between the film and substrates, films grown on MgO and STO substrates were with tensile strain. However, this only happened to the 50 nm film, the films on LAO and thicker films (100 nm and 200 nm) are unstrained. The R-T measurements showed that the unstrained films started to show superconductivity at ~8 K, while the films with tensile train did not show any superconductivity sign down to 5 K. These results showed that tensile strain suppress the superconductivity of FeSe thin film.

Therefore, substrate became a critical factor to achieve good superconductivity for FeSe thin film. Chen *et al*. deposited FeSe thin films on different substrates, such as MgO, LAO, STO, Si as well as SiO_x. [152] All the films were grown highly along the c-direction, no matter on which substrate. The transport measurements showed that the films had a low-temperature structural phase transition at 60 K-90 K, and the onset critical temperature varied from 7 K to <2 K. The films on Si and SiO_x showed much worse superconductivity compared to the other films. For Si, a large lattice mismatch of 44% might break the in-plane alignment and suppress its superconductivity consequently. For SiO_x, no template for the film growth was provided, due to the amorphous nature of the substrate. The resistance of these two films even did not go to zero down to 2 K. Because of the close lattice matching, most of the later works were using single crystal STO, LAO or MgO substrates, however, other substrates had also been explored, such as LAST [151], Al_2O_3 [155], $YAlO_3$ [153], and even amorphous glass and stainless steel. [156] Very recently, a very high $\boldsymbol{T_c}$ of above 50 K of one-unit cell FeSe on Se etched STO substrate using MBE method was reported by Wang *et al*. [157] This record had been broken by Ge *et al*. with a surprisingly high value of 100 K, however, the mechanism for this unbelievable value was still under investigation. [158]

1.3.2.2 FeSe0.5Te0.5 thin films

$FeSe_{0.5}Te_{0.5}$ was the most studied composition, as it was reported to obtain the highest $\boldsymbol{T_c}$ value in bulk form. [159] Si *et al*. was one of the earliest researchers who deposited high-quality $FeSe_{0.5}Te_{0.5}$ thin film. [160] They deposited the $FeSe_{0.5}Te_{0.5}$ thin

films using PLD method by a $FeSe_{0.5}Te_{0.5}$ target. The microstructure study showed that the films were well grown on STO and LAO substrates with perfect alignment in both out-of-plane and in-plane directions. Interestingly, the in-plane lattice constant *a* was close to the bulk value, while the out-of-plane lattice constant c was smaller than bulk value. Then, R-T measurement under magnetic field up to 9 T was carried out for the films, as well as its bulk counterpart for comparison, as shown in Figure 1.31. The general transition trend for the film and bulk samples was similar, despite the fact that the normal state resistivity for film was lower. Both $\boldsymbol{T_c^{onset}}$ and $\boldsymbol{T_c^0}$ decreased with increasing applied magnetic field. Furthermore, some of the films shown a 15% higher $\boldsymbol{T_c^{onset}}$ of ~17 K, compared to the bulk sample, as shown in Figure 1.31(c). This increased $\boldsymbol{T_c^{onset}}$ may relate to the 2% smaller unit-cell volume caused by the shrinkage of the c parameter discussed above. With the data plotted in Figure 1.31, upper critical field $\boldsymbol{H_{c2}(T)}$ could be estimated by the Werthamer–Helfand–Hohenberg model: [161]

$$-H_{c2}(0) = 0.7T_c \left. dH_{c2} \right/ _{dT} \mathrm{l}T_c \quad \text{(Equation 1.6)}$$

The $\boldsymbol{H_{c2}(0)}$ value could be estimated to be ~100 T and ~50 T from $\boldsymbol{T_c^{onset}}$ and $\boldsymbol{T_c^0}$, respectively. The $FeSe_{0.5}Te_{0.5}$ thin films in this study were very sensitive to the growth condition, as only some of the samples obtain a higher $\boldsymbol{T_c}$ value, while others have lower value. And the reason behind could not be fully explained based on this work.

Some other works on $FeSe_{0.5}Te_{0.5}$ thin film on various substrates had also been reported. For example, Imai *et al*. deposited $FeSe_{0.5}Te_{0.5}$ thin film on both MgO (001) and $LaSrAlO_4$ (001) substrates. [162] The film on MgO obtained $\boldsymbol{T_c^{onset}}$ of 10.6 K and $\boldsymbol{T_c^0}$ of 9.2 K, while the one on $LaSrAlO_4$ showed much lower values of $\boldsymbol{T_c^{onset}}$ of 5.4 K

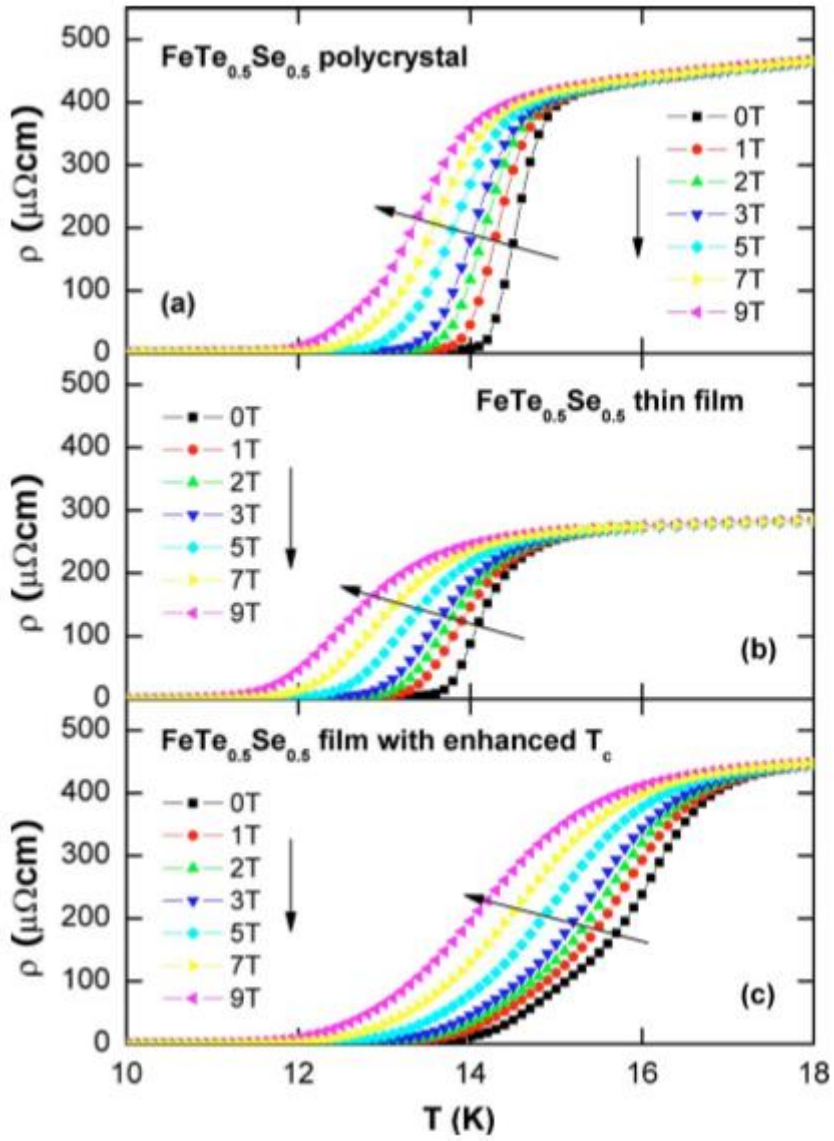

Figure 1.31 R-T measurement under different magnetic fields up to 9 T (H//c) for (a) $FeSe_{0.5}Te_{0.5}$ polycrystal bulk material, (b) $FeSe_{0.5}Te_{0.5}$ thin film and (c) the $FeSe_{0.5}Te_{0.5}$ thin film with enhanced T_c. [160] Reprinted with permission from "W. Si, Z. Lin, Q. Jie, W. Yin, J. Zhou, G. Gu, P. D. Johnson, and Q. Li, Appl. Phys. Lett. **95**, 052504 (2009)." With permission from AIP Publishing.

and T_c^0 of 2.7 K. This again indicated the substrate plays an important role on the superconductivity of iron chalcogenide films. Bellingeri *et al*. deposited epitaxial $FeSe_{0.5}Te_{0.5}$ thin films with different thickness on MgO, STO, LAO and YSZ single crystal substrates. [163] The film with a thickness of 200 nm on LAO shows highest T_c^{onset} value of 21 K. By correlating the T_c value with the in-plane lattice parameter, they concluded that the high T_c value was resulted from compressive strain.

1.3.2.3 FeTe thin films

FeTe was considered to have the highest T_c value among the 11 system with different compositions of Se and Te, predicted by Subedi *et al*. [164] However, no superconductivity was found in FeTe when synthesized as bulk form. Then, people deposited FeTe thin films to see if it is different from its bulk form. Han *et al*. deposited more than 100 FeTe samples on various substrates of LSAT, MgO, STO and LAO by three different targets ($FeTe_{1+x}$, x=0, 0.2, 0.4). [165] The presented samples were all grown using the $FeTe_{1.4}$ target. Different from its bulk form, all the FeTe films exhibited superconductivity, and the one of 90 nm thick on STO obtained the highest T_c^{onset} of 13.0 K and T_c^0 of 9.1 K. Furthermore, the H_{c2} value of this film was estimated as high as 123.0 T, while its critical current density Jc was determined to be 6.7×10^4 A/cm^2 and 3.0×10^4 A/cm^2 at 2 K, 0 T and 2 K, 2 T, respectively. This work demonstrated the superconductivity in FeTe thin film, although it is non-superconducting in bulk form.

Other superconducting FeTe films were achieved by O-doping. Nie *et al*. deposited FeTe thin films on MgO substrates, and then the samples were annealed at 100

°C, in 100 mTorr O_2, N_2, and CO_2 atmosphere and 100 °C, 2×10^{-7} torr vacuum and exposed to 40 °C water. [166] The R-T measurement of the samples were then plotted in Figure 1.32, apparently, only the one treated in O_2 showed a sharp drop from 10 K. And another O_2 annealing could further improve its superconductivity, as revealed in Figure 1.32(g). Therefore, the incorporation of O_2 into FeTe film created the superconductivity. Moreover, X-ray absorption showed that the nominal Fe valence state from 2+ of the nonsuperconducting state changed to mainly 3+ of the superconducting state after introducing O_2.

Si *et al*. presented the similar results and also concluded that O_2 was crucial for FeTe thin film to achieve superconductivity. [167] However, different from the O_2 annealing method in ref. 166, O-doping in this work was achieved by depositing the film in 1×10^{-4} Torr O_2 atmosphere. The FeTe film grown in O_2 showed $\boldsymbol{T_c^{onset}}$ of ~12 K and $\boldsymbol{T_c^0}$ of ~8 K, while the one deposited in vacuum only showed $\boldsymbol{T_c^{onset}}$ and no $\boldsymbol{T_c^0}$ was achieved. The results further emphasized the important role of O_2 for FeTe thin film to be superconducting. Furthermore, this $\boldsymbol{H_{c2}}(0)$ value of this film was estimated to be an extremely high value of ~200 T.

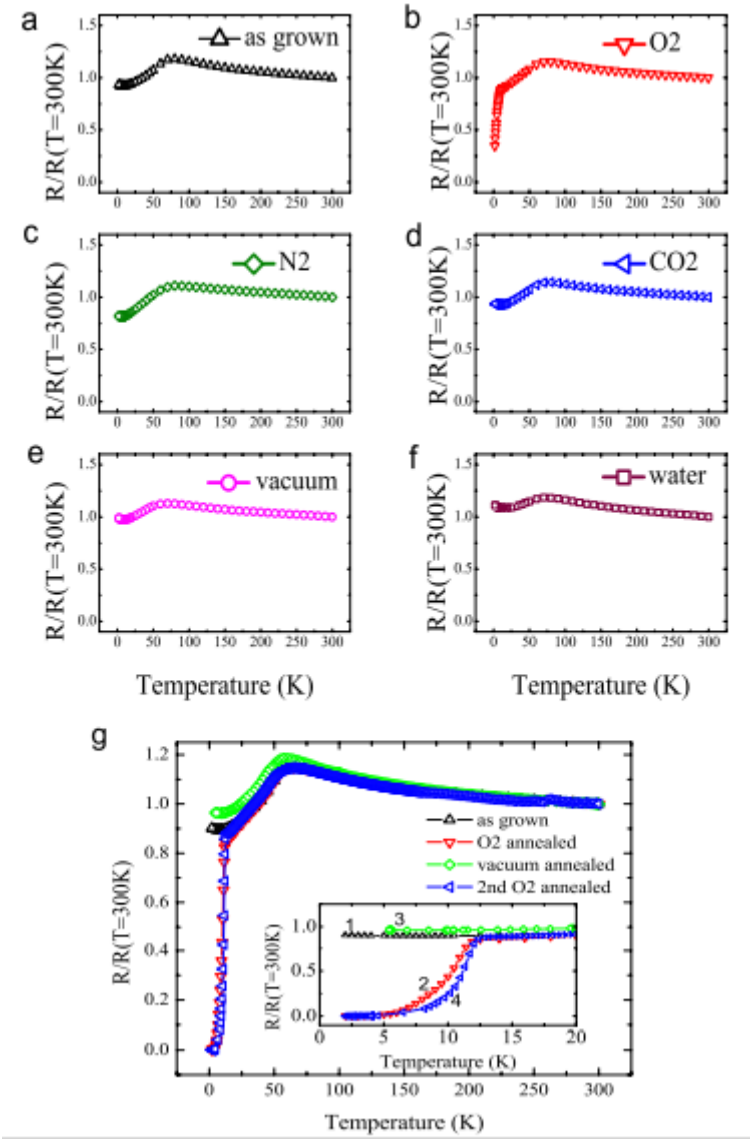

Figure 1.32 Normalized R-T plots for FeTe films after exposure to different elements: (a) as-grown sample, and annealing in (b) O_2, (c) N_2, (d) CO_2, (e) in vacuum, and (f) exposure to water. (g) exhibits the resistivity evolution after repeated oxygen and vacuum anneals. [166] Reprinted with permission from "Y. F. Nie, D. Telesca, J. I. Budnick, B. Sinkovic, and B. O. Wells, Phys. Rev. B **82**, 020508 (2010)." Copyright (2010) by the American Physical Society. [Ref 166]

1.3.2.4 FeSexTe1-x thin films

Beside the three most studied compositions discussed above, other compositions were also reported. Mele *et al*. deposited $FeSe_xTe_{1-x}$ thin films on $SrTiO_3$ (100), MgO (100), $LaAlO_3$ (100) and CaF_2 (100) single crystal substrates using a $FeSe_{0.5}Te_{0.5}$ target. However, according to compositional analysis performed by EDS, the composition of the films was very different from the target of $FeSe_{0.5}Te_{0.5}$. For example, typical compositions were $FeTe_{0.13}Se_{0.57}$ (on MgO, 300 °C), $FeTe_{0.19}Se_{0.6}$ (on STO, 300 °C) and $FeTe_{0.39}Se_{0.76}$ (on LAO, 400 °C). The best sample in this study was grown on CaF_2 substrate, with a composition of $FeTe_{0.35}Se_{0.41}$. By further optimizing, the film on CaF_2 can obtain highest $\boldsymbol{T_c^{onset}}$ of 20.0 K and $\boldsymbol{T_c^0}$ of 16.18 K. Furthermore, its critical current density $\boldsymbol{J_c}$ (T = 4.2 K) was 0.41×10^6 A/cm^2 at 0 T and 0.23×10^6 A/cm^2 at 9 T.

Chen *et al*. also deposited $FeSe_xTe_{1-x}$ thin films with composition variation of Se and Te on STO substrates. Interestingly, they found that the composition of $FeSe_{0.1}Te_{0.9}$ obtained the best performance, not the widely accepted $FeSe_{0.5}Te_{0.5}$. [169] Their $FeSe_{0.1}Te_{0.9}$ presented the highest $\boldsymbol{T_c^{onset}}$ of 13.3 K and $\boldsymbol{T_c^0}$ of 12.5 K. Moreover, this film obtained high $\boldsymbol{J_c^{sf}}$ of 1.3×10^5 A/cm^2 at 4 K, much higher than 2.0×10^4 A/cm^2 of the $FeSe_{0.5}Te_{0.5}$ film. Last but not the least, the $\boldsymbol{H_{c2}}(0)$ value of $FeSe_{0.1}Te_{0.9}$ film was remarkably high of 114 T, compared to 49 T of the $FeSe_{0.5}Te_{0.5}$ film.

1.3.3 Improve the superconductivity of iron chalcogenide thin films

As is known, iron chalcogenide thin films have much lower critical temperature and critical current density than HTS cuprate superconductors, such as YBCO. However, their high upper critical field $\boldsymbol{H_{c2}}(0)$ as well as low anisotropies make this type of superconductor unique for high-field applications. Therefore, most of the work in this research area was on improving its superconducting properties, especially $\boldsymbol{T_c}$ and $\boldsymbol{J_c}$.

1.3.3.1 $\boldsymbol{T_c}$ improvement

As discussed above, the compressive c-axis parameter was considered as the reason for the enhanced $\boldsymbol{T_c}$ value of 21 K. [163] It was possible that a shorter c-axis constant could improve the interlayer coupling of the Cooper pairs by suppressing the superconducting phase fluctuations. [170] In another side, neutron scattering measurements and first principles calculations demonstrated that the magnetic moment of the Fe atoms decreased when the chalcoge atoms moved closer to the Fe plane, which might also relate to the $\boldsymbol{T_c}$ enhancement. [171, 172] Enhanced spin fluctuations under pressure was also considered as the reason for the enhanced $\boldsymbol{T_c}$, indicated by nuclear magnetic resonance study on bulk FeSe. [173] The high $\boldsymbol{T_c}$ value of 21 K in ref. 163 was achieved with a thickness of 200 nm, which was in the middle of their thickness variation. The film growth mode was studied by taking atomic force microscopy (AFM) images of different thickness films. They found that isolated islands formed at the initial stage of the growth and then started to coalesce when grown into 30 nm and finally covered the substrate uniformly. The coalescence was believed to introduce a large

tensile strain by this growth mode. Therefore, the compressive strain in c-direction was considered as the key reason of the enhanced $\boldsymbol{T_c}$ in this case.

The in-plane strain was also considered to play a critical role for the $\boldsymbol{T_c}$ enhancement, reported by Nabeshima *et al*. [174] Instead of depositing films on the most used oxide based substrates, they deposited FeSe thin films with different thickness on CaF_2 substrate. Then, a-axis and c-axis lattice parameters were calculated from their corresponding peaks by XRD measurement. Interestingly, the a-axis lattice constant decreased with increasing thickness up to 150 nm, then, it increased slightly with further thickness increment. This lattice parameter thickness dependence was believed to be caused by the Volmer-Weber type growth of the FeSe film. The a-axis lattice parameter of the film in this studied was smaller than the bulk value, while c-axis is longer. Then, they were trying to find the relationship between the $\boldsymbol{T_c}$ value and c/a value, and plotted it together with single crystal FeSe and FeSe film on oxide STO substrate in Figure 1.33. From the plotting, it was obvious that $\boldsymbol{T_c}$ value of the FeSe films on CaF_2 increases monotonically as c/a increases. However, the results of single crystal FeSe and FeSe film on oxide STO did not follow the same dependence, which could be explained by the effect of disorders.

Therefore, it was highly possible that $\boldsymbol{T_c}$ value of iron chalcogenide thin film was related to both the in-plane a-axis parameter and out-of-plane c-axis parameter. However, it was still unclear how this correlation takes place. For example, the compressive a-parameter and c-parameter and the increasing c/a value were both possible for the

increasing T_c value. Further systematic might needed to find out the exact reason and the relationship between them.

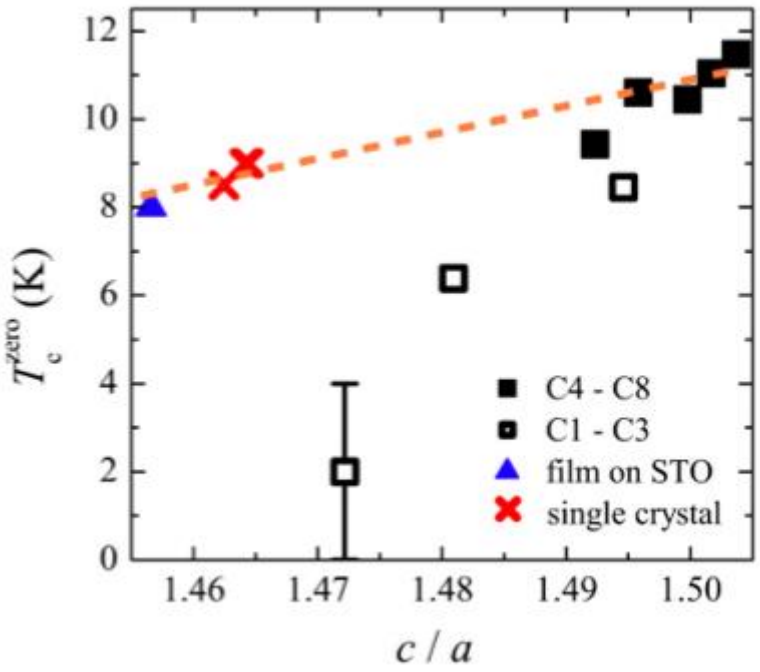

Figure 1.33 T_c^{zero} values for eight FeSe films on CaF_2 (C1–C8) as a function of c/a. [174] Reprinted with permission from "F. Nabeshima, Y. Imai, M. Hanawa, I. Tsukada, and A. Maeda, Appl. Phys. Lett. **103**, 172602 (2013)." With permission from AIP Publishing.

1.3.3.2 Flux pinning for J_c improvement

Critical current density J_c is very critical for commercial applications, especially under magnetic field. As discussed above, flux pinning for J_c improvement of YBCO thin films has been researched a lot, however, there are very limited reports on the flux pinning enhancement for iron chalcogenide thin films. One typical work on improving the J_c value of iron chalcogenide thin film was reported by Si *et al*. [175] Different from the others who directly deposited iron chalcogenide thin films on single crystal

substrates, they put a CeO_2 buffer layer before the superconducting film deposition. With the CeO_2 buffer layer, they found the $\boldsymbol{T_c}$ of the $FeSe_{0.5}Te_{0.5}$ transited from 20 K to 18 K, which was much higher than its bulk counterpart and most reported same films directly on single crystal substrates. Figure 1.34 showed the applied field dependence of the $\boldsymbol{J_c}$ of the $FeSe_{0.5}Te_{0.5}$ films deposited on both CeO_2-buffered single crystalline YSZ and RABiTS substrates at different temperatures. Both of the samples presented a high $\boldsymbol{J_c^{sf}}$ value of $>1\times10^6$ A/cm^2, and remained in the order of 1×10^6 A/cm^2 under applied field up to 31 T, which suggested that these films are suitable for high field applications. Then, they plotted the field as function of the pinning force $\boldsymbol{F_p}$ of the film on CeO_2-buffered RABiTS substrate, together with the reported result of the second-generation YBCO wire, thermos mechanically processed $Nb_{47}Ti$ alloy and Nb_3Sn wire with small grains, for comparison, as shown in Figure 1.35(a). Obviously, the iron chalcogenide film in this study showed much better high field performance than other low temperature superconductors. Although the HTS YBCO still obtained superior performance, the cost for application was the largest disadvantage compared the iron chalcogenide in this work. Figure 1.35(b) exhibited the Kramer's scaling law approximation for the film on CeO_2-buffered RABiTS substrate at various temperatues with the applied field either perpendicular or parallel to the sample surface. The Kramer's scaling law approximation can be described as:

$$f_P \sim h^p (1-h)^q \quad \text{(Equation 1.7)}$$

Here f_p is normalized pinning force density, and h is the reduced magnetic field. The figure shows that all the data almost falls on a single line, which indicates that the

pinning mechanism is independent of the temperature and field direction. In addition, p and q can be fitted to be 2 and ~0.85, and the low-field term demonstrates a point-defect core pinning mechanism in this case. However, it was still unclear what type of defects providing pinning center to achieve the high $\boldsymbol{J_c}$ value. The microstructure study showed some intergrowth at the interface between the $FeSe_{0.5}Te_{0.5}$ film and the CeO_2 buffer layer, which might contribute to the pinning enhancement for the films.

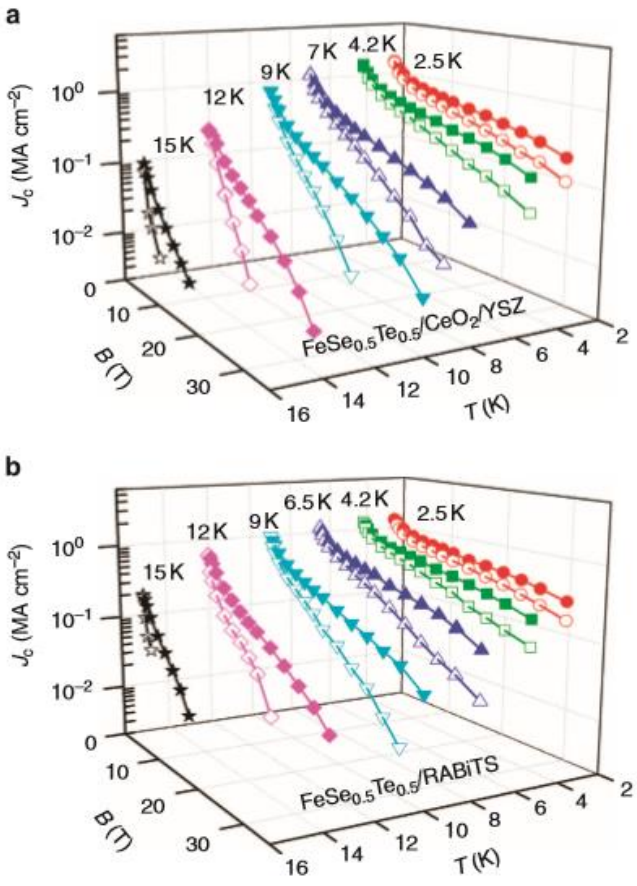

Figure 1.34 Applied field as function of the $\boldsymbol{J_c}$ of the $FeSe_{0.5}Te_{0.5}$ films deposited on (a) single crystalline YSZ with CeO_2 buffer layer and (b) RABiTS substrates at different measured temperatures. [175] Reprinted with permission from "W. Si, S. J. Han, X. Shi, S. N. Ehrlich, J. Jaroszynski, A. Goyal, and Q. Li, Nat. Commun. **4**, 1347 (2013)."

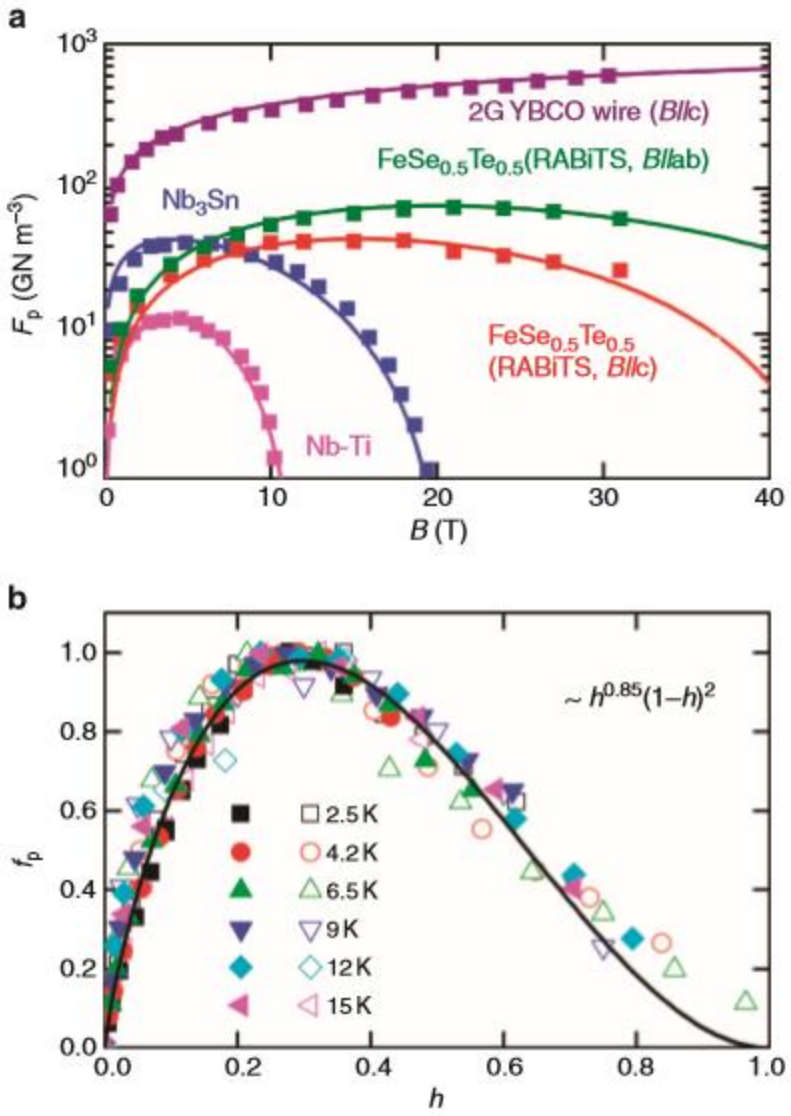

Figure 1.35 (a) $\boldsymbol{F_p}$ at 4.2K of a FST film deposited on a RABiTS substrate, compared with the literature data of YBCO 2G wire, TCP $Nb_{47}Ti$ and Nb_3Sn. The solid lines are Kramer's scaling approximations. (b) Kramer's scaling of pinning force density f_p versus reduced field h for a $FeSe_{0.5}Te_{0.5}$ film deposited on a RABiTS substrate at various temperatures with applied field perpendicular (solid symbols) and parallel (open symbols) to c-axis. [175] Reprinted with permission from "W. Si, S. J. Han, X. Shi, S. N. Ehrlich, J. Jaroszynski, A. Goyal, and Q. Li, Nat. Commun. **4**, 1347 (2013)."

Chen *et al*. also used CeO_2 to introduce flux pinning effect for iron chalcogenide thin film, however, instead of growing it as buffer layer, they made a sandwich like structure with a 7 nm thin CeO_2 nanolayer in between two 75 nm thick $FeSe_{0.5}Te_{0.5}$ layers. [176] For comparison, two single layer of $FeSe_{0.5}Te_{0.5}$ thin films were also grown, one in vacuum and the other in 10^{-4} Torr O_2 condition. R-T measurement showed that the critical temperature of all the three films were very close with $\boldsymbol{T_c^{onset}}$ of ~12 K and $\boldsymbol{T_c^0}$ of ~10 K. However, the $\boldsymbol{J_c}$ performance of the films was very different, the film with CeO_2 nanolayer exhibited higher $\boldsymbol{J_c}$ values along the applied field up to 7 T than the single layer $FeSe_{0.5}Te_{0.5}$ films as shown in Figure 1. 36. This significant $\boldsymbol{J_c}$ performance enhancement suggested effective pinning enhancement by the CeO_2 interlayer. To explore the origin of the pinning effect, microstructure study was conducted. They found that the dislocation density in the $FeSe_{0.5}Te_{0.5}/CeO_2$ interface area was higher than the $FeSe_{0.5}Te_{0.5}$/STO interface area, which indicated more defect pinning centers were introduced. Besides, nanoclusters were seen distributed throughout the film, which might also work as pinning centers for the enhanced $\boldsymbol{J_c}$ performance, although the composition of the nanoclusters were still under investigation. Thus, both the interfacial defects and nanoclusters were considered to contribute to the enhanced pinning performance for the film with CeO_2 interface.

There are several other reports on the flux pinning effect of iron chalcogenide thin films, [177, 178] however, the achieved properties so far are still much lower than HTS. To take the advantage of the high $\boldsymbol{H_{c2}}(0)$ value of the iron chalcogenide thin films, more work is needed to further improve its $\boldsymbol{J_c}$ performance under magnetic field.

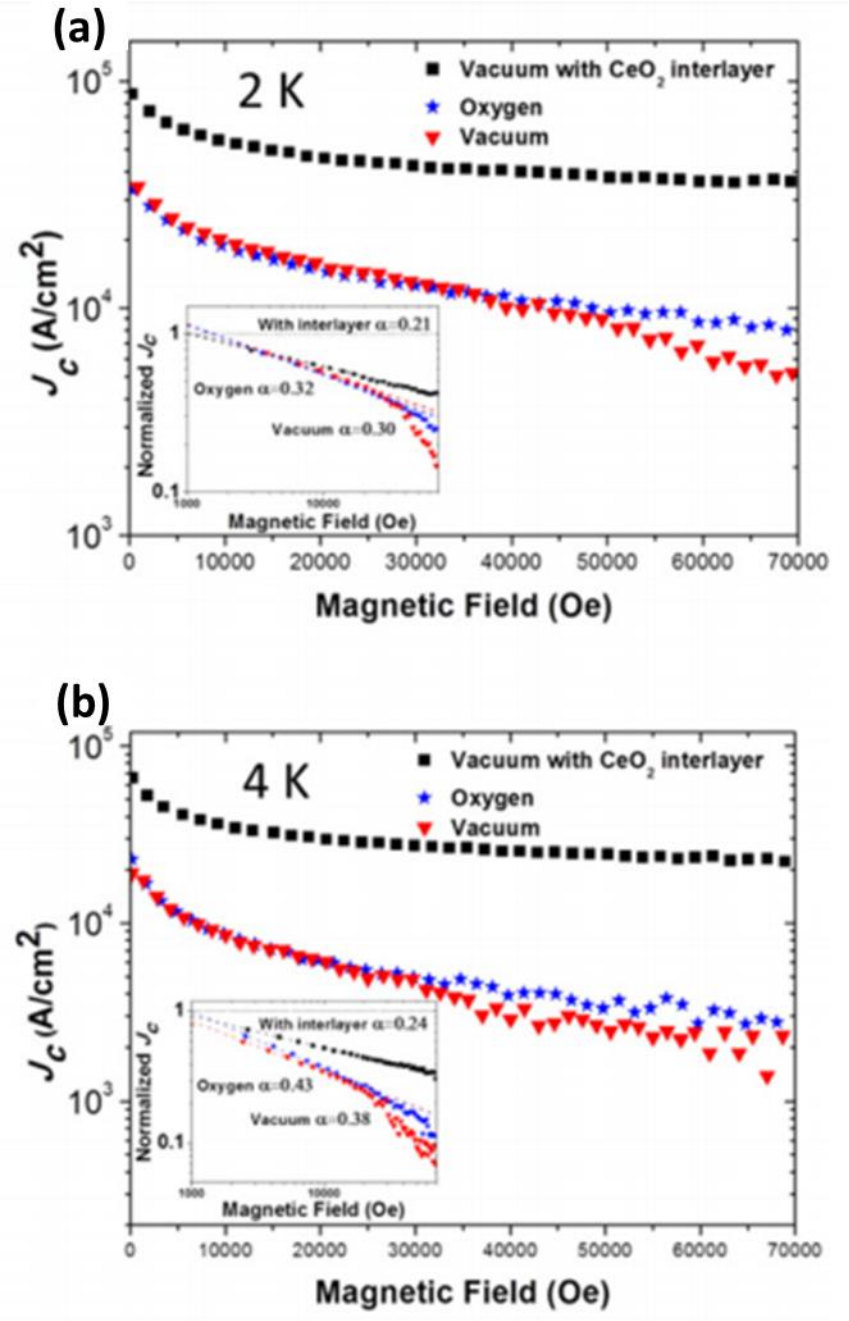

Figure 1.36 Applied field as function of the critical current density for $FeSe_{0.5}Te_{0.5}$ thin films at (a) 2 K and (b) 4 K. [176] Reprinted with permission from "L. Chen, C. Tsai, Y. Zhu, A. Chen, Z. Bi, J. Lee, and H. Wang, Supercond. Sci. Technol. **25**, 025020 (2012).

Table 1.7 Summary of reported iron chalcogenide thin films.

Film	**Authors**	**Ref.**	**substrate**	T_c **(K)**	J_c^{sf} **(MA/cm^2)**	H_{c2} **(T)**
FeSe	Y. F. Nie *et al*.	150	MgO, STO, LAO	8 (onset)	-	-
$FeSe_x$	Y. Han *et al*.	151	STO, LAST, LAO	11.8 (onset), 3.4 (zero)	-	14.0
FeSe	T. K. Chen *et al*.	152	MgO, STO, LAO, Si, SiO_x	~7 (onset)	-	-
FeSe	M. Jourdan *et al*.	153	$YAlO_3$	~7 (onset)	-	25.7
$FeSe_{1-x}$	M. J. Wang *et al*.	154	MgO	10 (onset)	-	-
$FeSe_{1-x}$	S. G. Jung *et al*.	155	Al_2O_3, STO, MgO, LAO	11-12 (onset)	-	56
$FeSe_xTe_{1-x}$	J. Huang *et al*.	156	Galss, stainless steel	12.3 (onset), 10 (zero)	0.02 at 4 K	126
FeSe unit cell	Q. Y. Wang *et al*.	157	Doped STO	53 (onset)	-	-
FeSe unit cell	J.F. Ge *et al*.	158	Doped STO	109 (onset)	-	116±12
$FeSe_{0.5}Te_{0.5}$	W. D. Si *et al*.	160	LAO, STO	~17 (onset)	-	~100
$FeSe_{0.5}Te_{0.5}$	S. X. Huang *et al*.	161	MgO	10.75	-	-
$FeSe_{0.5}Te_{0.5}$	Y. Imai *et al*.	162	MgO, $LaSrAlO_4$	10.6 (onset), 9.2 (zero)	-	-
$FeSe_{0.5}Te_{0.5}$	E. Bellingeri *et al*.	163	MgO, STO, LAO, YSZ	up to 21 (onset)	-	-
FeTe	Y. Han *et al*.	165	LSAT, MgO, STO, LAO	13 (onset),	0.067 at 2 K	123
FeTe	Y. F. Nie *et al*.	166	MgO	~10 (onset)	-	-

Table 1.7 Continued

FeTe	W. D. Si *et al*.	167	STO	12	-	~200
$FeSe_xTe_{1-x}$	P. Mele *et al*.	168	MgO, STO, LAO, CaF_2	up to 20 (onset)	0.41 at 4.2 K	-
$FeSe_xTe_{1-x}$	L. Chen *et al*.	169	STO	up to 13.3 (onset)	0.18 at 2 K	114
FeSe	F. Nabeshima *et al*.	174	CaF_2	up to 12.35 (onset)	-	33
$FeSe_{0.5}Te_{0.5}$	W. D. Si *et al*.	175	LaAlO3, STO, YSZ, and RABiTS with CeO_2 buffer layer	>20 (onset)	>1 at 4.2 K	-
$FeSe_{0.5}Te_{0.5}$	L. Chen *et al*.	176	STO	~12 (onset)	0.1 at 2 K	-
$FeSe_{0.5}Te_{0.5}$	W. D. Si *et al*.	177	LAO, buffered metal	~15 (zero)	~0.5 at ≤4 K	-
$FeSe_{0.5}Te_{0.5}$	L. Chen *et al*.	178	glass	6 (zero)	0.016 at 2 K	-

1.4 Research motivation

Flux pinning is an effective way to improve critical current density $\boldsymbol{J_c}$ for YBCO thin film. Different pinning centers have been introduced into YBCO for pinning enhancement, including 0-D nanoparticles, 1-D nanopillars, 2-D nanolayers, as well as magnetic pinning by incorporating magnetic additions. However, there is very limited work on combining these pinning methods together for further pinning enhancement. For example, different defect pinning centers can be introduced by designing particular structure. In addition, defect pinning and magnetic pinning can be introduced by incorporating a nanolayer with magnetic portion. In this dissertation, $(CoFe_2O_4)_x(CeO_2)_{1-x}$ and $(LSMO)_x(CeO_2)_{1-x}$ nanolayers will be introduced into YBCO for both defect and

magnetic pinning. Both of the nanocomposite films show obvious magnetic properties, and $\boldsymbol{J_c}$ values of YBCO thin films are largely improved by incorporating these nanocomposite layers. As is known, the total pinning effect is not the simple sum of all the pinning landscapes introduced. Further work is needed to explore how to combine these different pinning landscapes in more effective ways.

In another side, significant research efforts have been focused on improving $\boldsymbol{T_c}$ of iron chalcogenide thin films, such as depositing on different substrates and doping with different elements. However, very few reports are focusing on the enhancement of superconducting $\boldsymbol{J_c}$ under either self-field $\boldsymbol{J_c^{sf}}$ or applied magnetic field $\boldsymbol{J_c^{in\text{-}field}}$. Therefore, in this dissertation, $\boldsymbol{J_c}$ enhancement has been achieved by introducing CeO_2 nanolayer for defect pinning. Furthermore, $(CoFe_2O_4)_{0.1}(CeO_2)_{0.9}$ nanocomposite layer has also been incorporated into $FeSe_{0.1}Te_{0.9}$ thin film for both defect and magnetic pinning. In addition, to test the compatibility of iron chalcogenide thin films on metal substrates for coated conductor applications, iron chalcogenide thin films were also grown on amorphous glass and polished stainless steel substrates. The films were successfully deposited on both substrates, and obvious superconducting properties were measured, which indicates the promising iron chalcogenide coated conductor application.

CHAPTER II

EXPERIMENTAL

2.1 Pulsed laser deposition (PLD)

All the films were deposited using pulsed laser deposition (PLD) (Lambda Physik Compex Pro 205, λ=248nm). Different targets were used for different thin film depositions. A typical target making process included materials ratio calculation, powder weighting, powder mixing, pellet pressing and sintering. Then, multilayer structures could be achieved by alternating ablation of different selected targets. The thin films were grown on different substrates, including $SrTiO_3$ (STO) (001) single crystal, Si (001) and SiO_x buffered Si substrates.

PLD is a physical vapor deposition (PVD) method, which is one of the most used techniques for thin film deposition. The first laser deposition of thin film can be traced back to 1965, which was done by Smith and Turner. They suggested that thin film can be generated from materials vaporized by intense laser ablation. [179] For PLD system, the high spatial coherence obtained by lasers allows directional and highly focused irradiation with high energy densities. Some of the advantages of PLD deposition include the reproduction of the material stoichiometry in the targets, as well as vary little contamination and in-situ control of the film properties. Furthermore, almost all metals and complex ceramic materials (except metal has high reflectivity which results in low deposition rate) can be successfully achieved by PLD method. The parameters which influence the film quality include substrate temperature, energy density of the laser,

pulse frequency, gas pressure in the chamber, and the distance between substrate and target.

The setup of the PLD system is very simple, which contains a multiple target holder and a substrate holder in a chamber with high vacuum achieved by a turbo molecular pump, as illustrated in Figure 2.1. A high-power laser is used as an external energy source to vaporize materials from the target and to deposit thin films on the substrates. In addition, a set of optical lens are used to focus and raster the laser beam on the surface of target. For our case, KrF excimer laser (248 nm) is used, with laser power density varied from 3 J/cm^2 to 5 J/cm^2 by adjusting the laser output energy. Before depositions, the base pressure of the chamber was pumped down to ~10^{-6} Torr. The distance between the target and substrate was normally kept at 3-5cm. The substrate temperature precisely controlled up to 840 °C by an external heater. Most of the YBCO related samples were deposited at 780 °C, which the iron chalcogenide thin films were grown at 400 °C.

The process involved in the PLD deposited thin films (laser target interaction) is relatively complex, which combines both nonequilibrium and equilibrium processes. The mechanism that results in material ablation depends on several factors, which includes the laser features, as well as the topological, optical and thermodynamic properties of the target. After the laser radiation has been absorbed by the surface of a target, first, electricomagnetic energy will be transferred into electronic excitation. Then, further be transferred into thermal, chemical, and even mechanical energy, in order to achieve evaporation, ablation, excitation, plasma formation, as well as exfoliation. Then, the

evaporations lead to a ‘plume’, which contains a mixture of energetic species, including atoms, molecules, electrons, ions, clusters, micron-sized solid particulates and molten globules. The collisional mean free path inside the dense plume is very short. Generally,

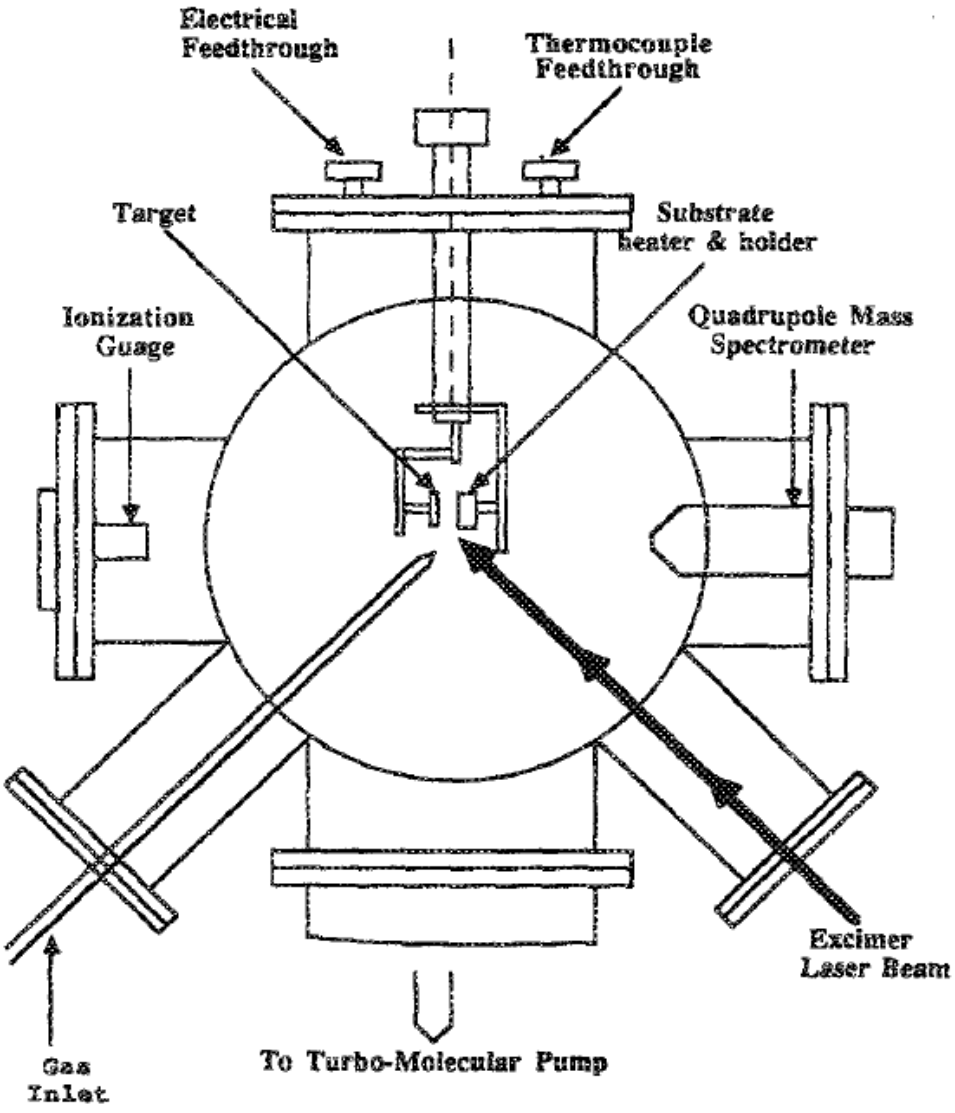

Figure 2.1 Schematic diagram of a pulsed laser deposition system. [180]

the laser target interaction process includes three steps: (1) interaction between the laser beam and the target materials, which leads evaporation of the surface area; (2) interaction between the evaporated material and the incident laser beam, which leads to isothermal plasma formation as well as its expansion; (3) anisotropic adiabatic expansion of the plasma and then the deposition. During the deposition, high deposition temperature is required to provide enough energy for the adatoms to move to preferred lattice sites. The first two steps start with the laser pulse and continue during laser pulse duration. The third regime starts after the ending of the laser pulse. This PLD process mechanism was demonstrated by R. K. Singh and J. Narayan in 1990, and can be illustrated in Figure 2.2. [180]

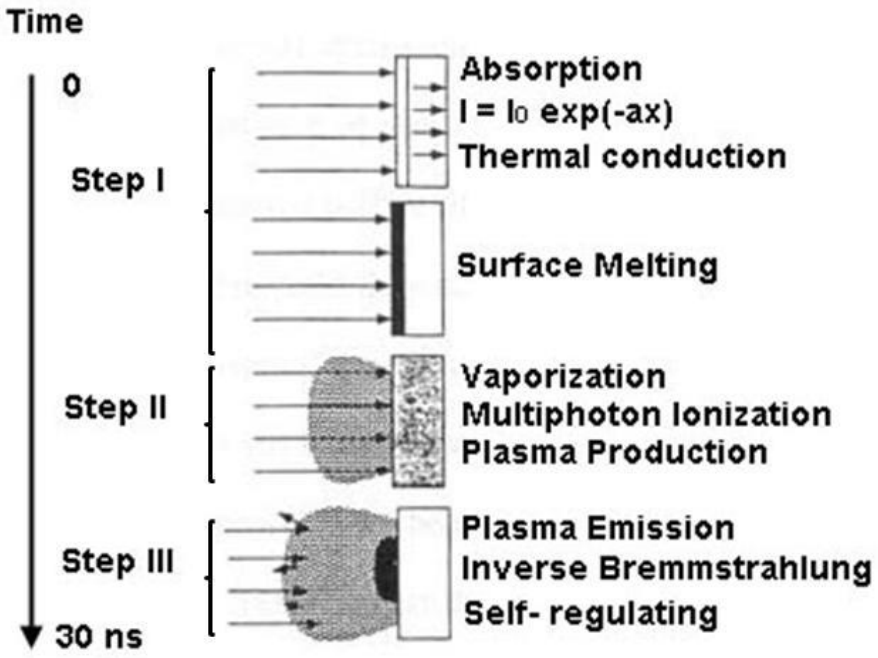

Figure 2.2 Laser target interaction during the short pulsed laser period (stage 1 to 3). [180]

Melting and evaporation of the surface area of the target will be achieved by the heating caused by high-power nanosecond laser pulses. There are various factors affect the heating rate, melting and evaporation through pulsed laser irradiation, such as (1) laser parameters, including pulse energy density, pulse duration, wavelength and the shape of laser pulse, as well as (2) materials properties, including absorption coefficient, reflectivity, density heat capacity and thermal conductivity. During the PLD processing, heat flow through the target can be defined by the following equation:

$$\boldsymbol{\rho_{i(T)}C_{p(T)}}\frac{\boldsymbol{\partial T(x,t)}}{\boldsymbol{\partial t}} = \frac{\boldsymbol{\partial}}{\boldsymbol{\partial t}}\left[\boldsymbol{K_i(T)}\frac{\boldsymbol{\partial T(x,t)}}{\boldsymbol{\partial x}}\right] + \boldsymbol{I_0(t)[1-R(T)]e^{-a(T)x}} \quad \text{(Equation 2.1)}$$

where $\boldsymbol{x}$ and $\boldsymbol{t}$ are the distance normal to the surface of the sample and the time. $\boldsymbol{P_i(T)}$ is density, $\boldsymbol{C_p(T)}$ is thermal heat capacity, $\boldsymbol{R(t)}$ is the reflectivity, $\boldsymbol{a(T)}$ is the absorption coefficient, $\boldsymbol{I_0(t)}$ is the time dependent incident laser intensity and $\boldsymbol{K_i(T)}$ is for the thermal conductivity. The subscript, $\boldsymbol{i}$, indicates the phase where $\boldsymbol{i}$=1 for solid and $\boldsymbol{i}$=2 for liquid phases. And the $\boldsymbol{K}$ value can be varied by the state of the different material phases.

The interaction between the high-power laser beam and the bulk target materials can result in very high temperature, which leads to the emission of positive ions and electrons from the surface of target. The emission of the positive ions and electrons from the free surface presents an exponential increase with temperature. It can be estimated by the Langmuir-Saha equation:

$$\frac{\boldsymbol{i_+}}{\boldsymbol{i_0}} = \frac{\boldsymbol{g_+}}{\boldsymbol{g_0}}\boldsymbol{e^{[(\phi - I)KT]}} \quad \text{(Equation 2.2)}$$

where i_+ and i_0 are fluxes of positive and neutral ions emitted from the surface at a certain temperature of T. g_+ and g_0 are the weights of the ions which are in the ionic and neutral states, f is the work function of the electron and I is the material ionization potential. The absorption and penetration of the laser beam by the plasma depend on several parameters, which includes the electron-ion density, the temperature, as well as the wavelength of laser. Then, the material evaporated from the hot target will be further heated by absorption of laser radiation. The primary absorption mechanism for plasma is the electronion collisions. The absorption takes place mainly by a process, which involves absorption of a photon by free electron.

In conclusion, the PLD thin film deposition process is relatively complicated. PLD has been widely used for growing all kinds of thin films, due to its own advantages, which has been mentioned above. However, there are also some disadvantages for this method, for example, thin film can only be deposited into a relatively small area, which means surface coverage is small. In addition, formation of particulates is another big concern in growing high quality layer-by-layer thin films, although this can be avoided by well controlling the deposition parameters. Therefore, we used PLD to grow all the films, including YBCO, FeSeTe and other composite materials.

2.2 Crystallinity and microstructure characterization

2.2.1 X-ray diffraction (XRD)

X-ray diffraction (XRD) is a tool to identify the atomic and molecular structure of a crystal, which is very widely used for multiple purposes, such as exploring the

composition and crystal structure of the sample and measure the size, shape and internal stress of crystalline materials. For thin films, XRD can be used to determine the epitaxial quality, growth orientation, and strain effect from the substrate. Basically, X-rays are generated from an x-ray tube, in which a focused electron beam is accelerated across a high voltage field and bombards a target. The collision between electrons and atoms in the target results in a continuous spectrum of X-rays. The system we used is Panalytical XPert X-ray diffractometer, and Cu target is used with corresponding wavelengths of 1.54 Å.

The principle mechanism of XRD is mainly based in Bragg's law, which can be expressed as:

$$\boldsymbol{2d\,sin\,\theta = n\lambda} \quad \text{(Equation 2.3)}$$

where λ is the wavelength of X-rays (1.54 Å for Cu in our case), d is the lattice plane spacing, θ is the diffraction angle. The relationship can be described more clearly in Figure 2.3 [181]. Based on the Bragg's law, only certain values of θ and d can satisfy the equation, which will be expressed by peaks of the intensity-2θ plot (θ-2θ scan). From which plot, the width and degree of the intensity peak provides information on the crystallinity of the material and the size of its unit cell, respectively.

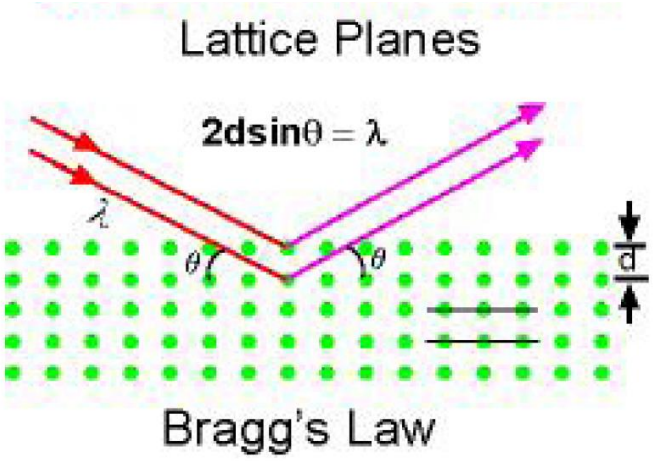

Figure 2.3 2-D illustration of Bragg's law for a set of lattice planes with lattice parameter d. [181]

2.2.2 Transmission electron microscopy (TEM)

Transmission electron microscopy (TEM) is a very widely used tool for microstructure characterization. Different from the conventional optical microscopy, TEM uses electron beam and electromagnetic focal lenses, instead of light and optical lenses in optical microscopy. A typical TEM system contains four parts: the electron source, electromagnetic lens system, sample stage and imaging systems. All of them are combined in a vacuum column backed up by the mechanical pump and turbo pump or diffusion pump, as shown in Figure 2.4. [182] First, the cathode emits electrons when being heated or applied high voltage. Then, electron beam is accelerated towards the anode by the positive voltage, and focused and confined by the condenser lens and apertures. Last, the transmitted beam will be focused by another set of lens after passing through the sample and project the enlarged image on the phosphorescent screen.

Resolution and magnification are the two most important parameters to determine the quality of TEM system. Magnification can be estimated by the product of the magnifying powers for all the lenses refer to the degree of enlargement of the final image compared to the original object. Therefore, it can be adjusted by changing acceleration voltage. The maximum resolution of TEM is defined as the closest spacing of two points. Assuming the ideal condition of no aberration effect, it can be theoretically calculated based on Rayleigh criterion:

$$\boldsymbol{r = \frac{0.612\lambda}{n\,(sin\,\alpha)}}$$ (Equation 2.4)

Where λ is the wavelength, α is the aperture angle and n=1 when the system is operated under vacuum condition. There are several other factors affect maximum resolution of a particular TEM system, such as the spherical aberration, chromatic aberration, as well as astigmatism.

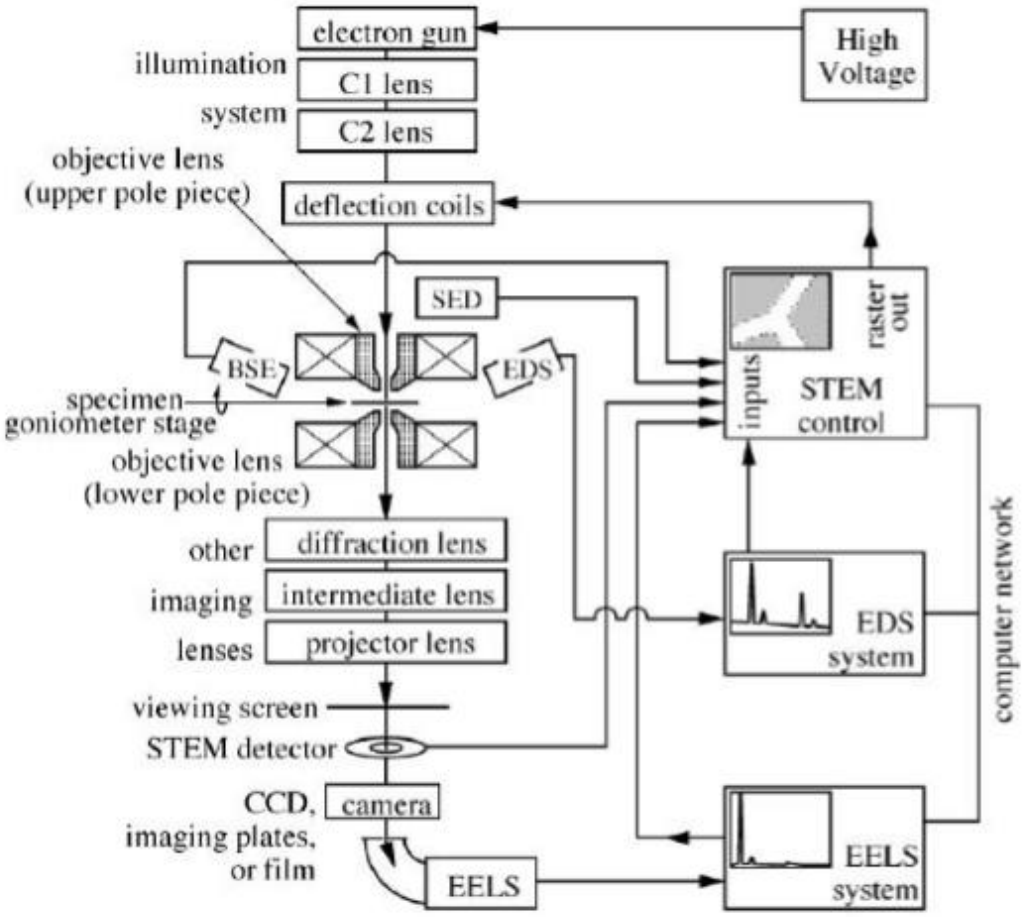

Figure 2.4 The block diagram of a typical TEM system with analytical capabilities. [182]

There are two basic operation modes of the TEM system: the diffraction mode and imaging mode as shown in Figure 2.5. These two modes can be switched back and forth by changing the focal length of the intermediate lens. When in diffraction mode, the image plane coincides with the back focal plane of the objective lens. And, the image plane coincides with the image plane of the objective lens while in imaging mode. Normally, objective apertures are inserted at the back focal plane of the objective lens to

increase the contrast in imaging mode. Bright field (BF) or dark field (DF) images can be obtained depending on the objective aperture configuration and the beam diffraction. When the aperture is positioned to only allow the transmitted (undiffracted) electrons to pass through, a bright-field (BF) image will be generated. In another side, when the aperture is positioned to only allow diffracted electrons to pass through, a dark-field (DF) image will be obtained.

High-resolution TEM (HRTEM) is critical for most of our studies, to explore the microstructure of the thin films in atomic scale. There are several important requirements to achieve HRTEM mode, first, objective lens should be adjusted to obtain the shortest possible focal length and the proper specimen holders has to be used. And, higher accelerating voltages should be applied to achieve higher resolution. The energy spread of electrons generated from field emission guns is much narrower, thus, by using these guns, chromatic aberration may be further reduced. For the selection of the objective lens aperture, larger objective lens aperture minimizes diffraction effects, but with lower contrast. And smaller objective lens aperture cannot achieve high resolution, although with higher contrast. For condenser lens apertures, small ones can be used to reduce the spherical aberration. In order to get high quality HRTEM images, the specimen itself is also very important. Normally, a specimen with thin area without too much ion damage will have a better chance to enhance the resolution capability.

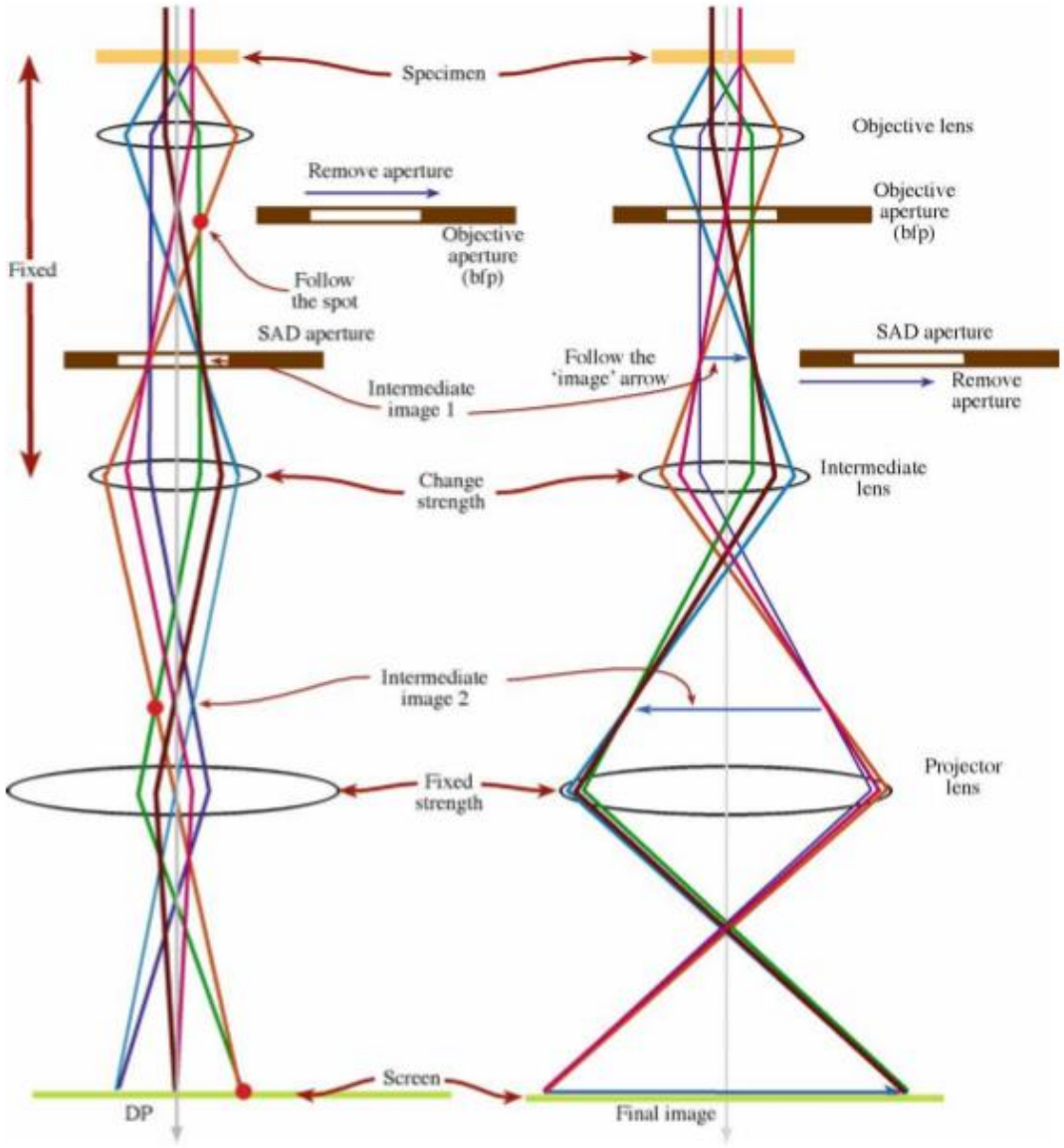

Figure 2.5 Two basic operation modes of TEM system: (a) the diffraction mode and (b) the imaging mode. [183]

Scanning transmission electron microscope (STEM) is also used in our studies, which is one of the working modes of TEM where the beam scans parallel to the optic axis. Multiple signals can be generated by the interaction between the beam and sample.

The signals can be collected for mapping, such as energy dispersive X-ray (EDX) spectroscopy, annular dark-field imaging (ADF), as well as electron energy loss spectroscopy (EELS). Furthermore, these signals can be collected simultaneously, which results in direct correlation of morphology and quantitative data. Finally, for the images obtained by a STEM and a high-angle detector, its contrast is directly related to the atomic number (Z-contrast image).

As discussed above, a good TEM sample is the most important precondition to obtain high quality TEM images, especially HRTEM images. In our studies, both cross-sectional and plan-view TEM samples were prepared by a conventional TEM sample preparation method. The general procedure can be described as: (1) cutting thin slices with length and width from 1 mm-3 mm from the whole large samples; (2) glue two slices together well with heating for 4 hours; (3) pre-thinning one side of the sample with sand paper (600 μm preferred) and followed by diamond papers (15 μm, 6 μm, 3 μm and 1 μm); (4) final thinning and polishing the sample from the other side with a dimpler (better under 25 μm) ; (5) ion milling. By ion milling, a hole will be created in the middle of the sample, and the thin area is around the edge of the hole. Ion milling time is considered to be as short as possible, to avoid the ion damage of the sample. Several parameters can be tuned for ion milling, such as beam energy, angle of incidence, vacuum, initial surface topology and ion orientation.

2.2.3 Scanning electron microscopy (SEM)

Scanning electron microscope (SEM) is another widely used tool for microstructure characterization. The mechanism is that the interaction between focused high energy electrons beam and the surface of solid specimens generates all kinds of signals, including elastically scattered electrons, inelastically scattered electrons, auger electrons, backscattered electrons, secondary electrons and so on, as shown in Figure 2.6. [183] Different signals provide different information, for instance, secondary electrons can show morphology and topography of the sample, and the image generated from backscattered electrons presents composition contrasts in multiphase samples. Furthermore, different elements can be identified by characteristic X-rays, therefore, it can be used to determine the elements in the sample by energy-dispersive X-ray spectroscopy (EDS).

In the work of this dissertation, Quanta 600 FEG analytical microscope (200 V to 30KV, Field emission gun assembly with Schottky emitter source) and JEOL JSM-7500F (100 V to 3 kV, Cold cathode UHV field emission conical anode gun) have been used to explore the different surface morphology of $FeSe_xTe_{1-x}$ thin film with composition variation.

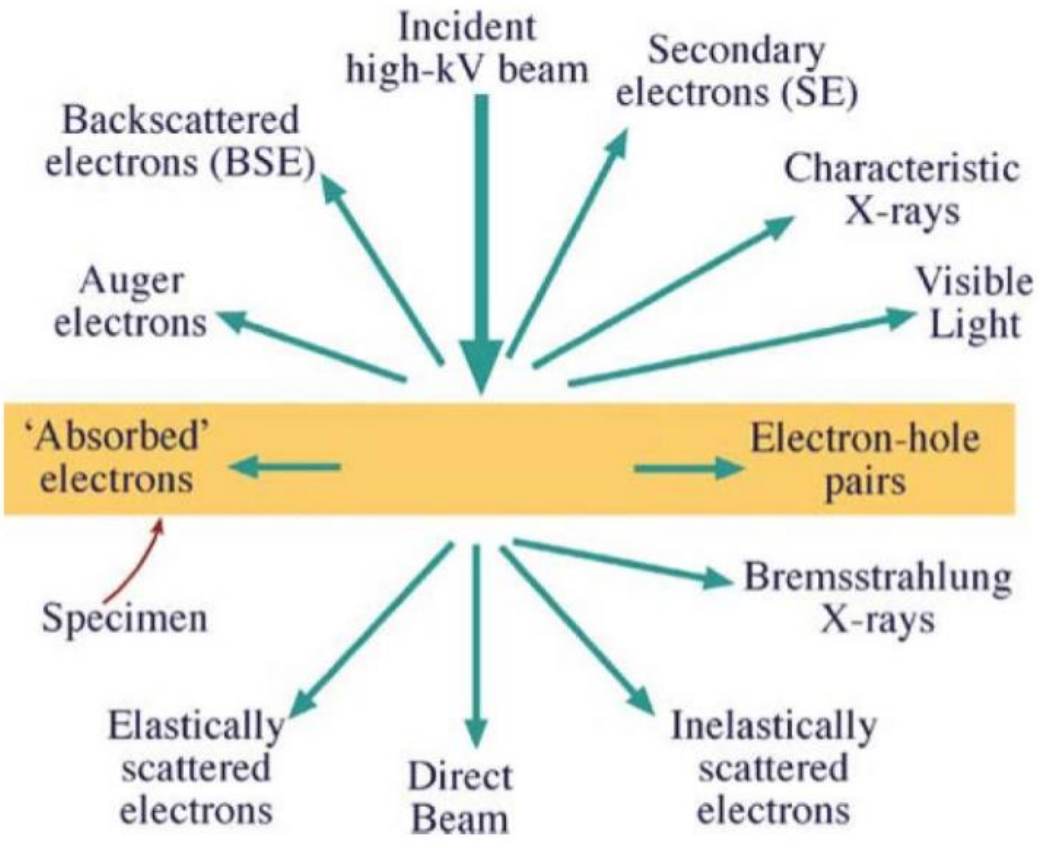

Figure 2.6 Different kinds of electron scattering from a thin specimen in both the forward and back directions. [183]

2.3 Superconducting properties measurement

In this dissertation, superconducting properties (T_c, J_c, H_{c2}) are measured by a Physics Property Measurement System (PPMS) (EverCool, Quantum Design, Inc) combined with a vibrating sample magnetometer (VSM) head, as shown in Figure 2.7 (a). The setup of our PPMS system contains a double-well liquid helium dewar, a sample sleeve, a pumping system including a diaphragm pump and a dry scroll pump, a superconducting magnet coil to generate applied magnetic field and a controller system.

Our PPMS provides a flexible, automated workstation that can conduct different kinds of experiments with precise thermal and applied magnetic field control, which includes magnetization (M-H) and transport resistivity vs. temperature measurements (R-T) measurements. The magnetic field of our PPMS system can be applied up to 9 T, and the temperature can be tuned from 1.9 K to 400 K by the liquid helium and heater. Furthermore, the temperature can be varied with full sweep capability and slew rates from 0.01 K/min up to 12K/min.

First, R-T measurement is used to determine the $\boldsymbol{T_c}$ values of our superconducting thin films, and R-T measurements under applied magnetic field can be used to estimate the $\boldsymbol{H_{c2}}$ values. The DC transport measurement option in PPMS is selected for these measurements, which provides a high precision current source and a high precision voltmeter in the Model 6000 control unit. Four-terminal probe measurements are used, as shown in Figure 2.7(c). Figure 2.7(d) is a typical sample puck used for the R-T measurement. Basically, a known current passes through I^+ and I^-, and the voltage will be measured from V^+ to V^-, then the sample resistivity can be obtained by Ohm's law. Three samples can be mounted on the sample puck and measured at the same time. By applying magnetic field, $\boldsymbol{T_c}$ values under different magnetic field can be obtained to estimate $\boldsymbol{H_{c2}}$ values of the superconducting thin films.

The VSM mode with linear motor to vibrate the sample in PPMS is a fast and sensitive DC magnetometer. The measurement is done by oscillating the sample with or without applied magnetic field near a detection coil and synchronously detecting the voltage induced by the magnetic response in the sample. The sample motor and

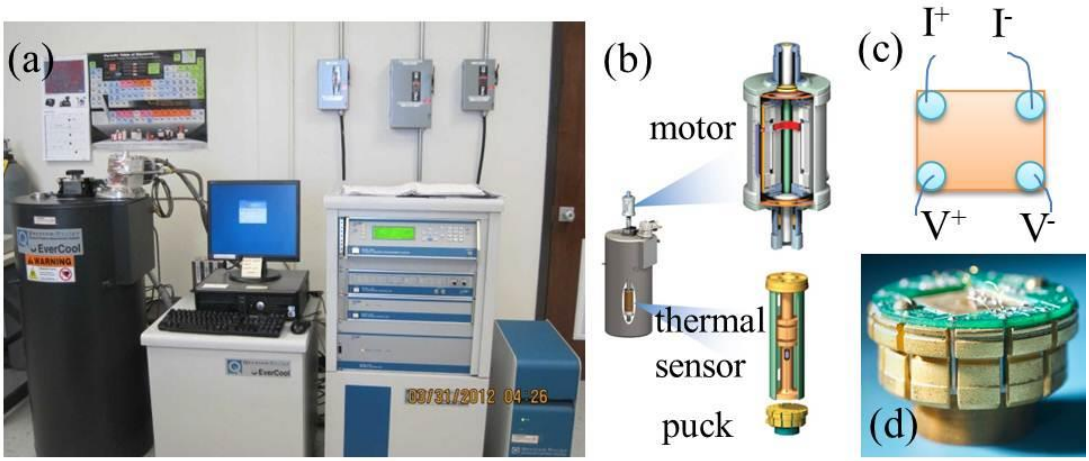

Figure 2.7 (a) The PPMS equipment used in the laboratory, (b) the sample motor drive and detection coil set for VSM option and sample puck for resistivity option and (c) the typical connections for R-T measurement. (d) Sample puck for resistivity option.

detection coil set for VSM option are shown in Figure 2.7(b). The induced voltage can be detected by oscillating the sample near a detection coil. M-H hysteretic loops can be obtained at different temperatures (2 K, 4 K and 8 K for iron chalcogenide thin films, 5 K, 40 K, 65 K and 77 K for YBCO related thin films). Then, $\boldsymbol{J_c}$ values can be calculated by the Bean model: [184]

$$\boldsymbol{J_c = 20\Delta M/a[(1 - a/3b)]}\text{(Equation 2.5)}$$

where ΔM is the opening in the hysteresis loop, and a and b are the sample dimensions.

CHAPTER III

MAGNETIC PROPERTIES OF $(CoFe_2O_4)_x:(CeO_2)_{1-x}$ VERTICALLY ALIGNED NANOCOMPOSITES AND THEIR PINNING PROPERTIES IN $YBa_2Cu_3O_{7-\delta}$ THIN FILMS*

3.1 Overview

Vertically aligned nanocomposites (VAN) combined ferrimagnetic $CoFe_2O_4$ with non-magnetic CeO_2 ($(CoFe_2O_4)_x:(CeO_2)_{1-x}$) in different phase ratios (x=10%, 30% to 50%) have been grown by a pulsed laser deposition (PLD) technique. Various unique magnetic domain structures form based on the VAN compositions and growth conditions. Anisotropic and tunable ferrimagnetic properties have been demonstrated. These ordered ferromagnetic nanostructures have been incorporated into $YBa_2Cu_3O_{7-\delta}$ (YBCO) thin films as both cap and buffer layers to enhance the flux pinning properties of the superconducting thin films. The results suggest that the ordered magnetic VAN provides effective pinning centers by both defect and magnetic nanoinclusions.

3.2 Introduction

$CoFe_2O_4$ is a well-known hard magnetic material with high coercivity and moderate magnetization as well as high chemical and structure stability. It has attracted significant research interests owing to its unique magnetic and electronic properties. [185-187] It has a high Curie temperature ($\boldsymbol{T_c}$) of 793 K and a band gap of 0.8 eV, which

*Reprinted with permission from "Magnetic properties of $(CoFe_2O_4)_x:(CeO_2)_{1-x}$ vertically aligned nanocomposites and their pinning properties in $YBa_2Cu_3O_{7-\delta}$ thin films" by Jijie Huang, Chen-Fong Tsai, Li Chen, Jie Jian, Fauzia Khatkhatay, Kaiyuan Yu, and Haiyan Wang, *Journal of Applied Physics*, **115**, 123902, 2014. With the permission of AIP Publishing

grants it as a promising candidate for room temperature spin filter applications. [188, 189] Furthermore, its highest reported magnetostriction coefficient value makes it possible for mastering the magnetization with strain. [190, 191] A variety of applications such as information storage and drug delivery can also be achieved. [192, 193] $CoFe_2O_4$ has been synthesized into various structures, such as nanoparticles, [194] nanoplatelets, [195] thin films, [196] and even ultrathin films, [185, 197] due to its magnetic properties greatly influenced by different structures. [198] More recently, $CoFe_2O_4$ has also been introduced into nanocomposite thin films to couple with another material/phase and therefore achieve new or multi-functionalities. For example, Zheng *et al.* reported that combine $CoFe_2O_4$ with $BaTiO_3$ can couple magnetic and ferroelectric properties together, which facilitates the interconversion of energy stored in electric and magnetic fields. [199] When both phases are grown into a unique epitaxial vertically aligned nanocomposites (VAN) form, so called VAN structure. [200-202]

For this study, a new VAN system of $(CoFe_2O_4)_x:(CeO_2)_{1-x}$ containing ferrimagnetic $CoFe_2O_4$ and non-magnetic CeO_2 is proposed. Based on the lattice structure, both $CoFe_2O_4$ and CeO_2 can grow epitaxially on $SrTO_3$ (STO) substrates. With the composition of $CoFe_2O_4$ varied as x=0.1, 0.3 and 0.5, one can expect a uniform distribution of $CoFe_2O_4$ magnetic domain structures. Such VAN systems could be incorporated in high temperature superconductor (HTS) $YBa_2Cu_3O_{7-\delta}$ (YBCO) films to explore their impacts on magnetic flux pinning properties. HTS YBCO coated conductors(CCs) are considered as one of the most promising candidate for practical applications such as power transmission lines, generators, magnets, motors, *etc*. [75,

203] However, the critical current density ($\boldsymbol{J_c}$) of CCs under an applied magnetic field needs further improvements [25, 203-205]. In the past decade, a significant amount of work has been focused on incorporating nano-scale defects as flux pinning centers to enhance the superconducting $\boldsymbol{J_c}$. [83, 96, 206, 207] Very recently, various effective magnetic nanoinclusions have also been reported and showed improved in-field $\boldsymbol{J_c}$ performance, by the interactions between the magnetic inclusions and the fluxons [124, 208-212].

By incorporating VAN systems of $(CoFe_2O_4)_x : (CeO_2)_{1-x}$ as both cap and buffer layers in YBCO thin films, one could take advantage of the $CoFe_2O_4$ domains as magnetic pinning centers and the CeO_2 nanopillars as high density defect pinning centers. The unique tunable magnetic properties of the VAN systems were then correlated with the VAN microstructures and the resulted superconducting properties.

3.3 Experimental

$(CoFe_2O_4)_x : (CeO_2)_{1-x}$ VAN layers, as well as $(CoFe_2O_4)_x : (CeO_2)_{1-x}$ VAN doped and undoped YBCO thin films, were deposited on single crystal STO (0 0 1) substrates by a PLD system with a KrF excimer laser (Lambda Physik 201, λ= 248 nm, 300 mJ). The thickness of VAN nanolayer and YBCO matrix were controlled at about 350 nm. The total deposition pulses are 300 and 3000 for the doped nanolayer and single VAN layer, respectively. The architectures of the multilayers thin films were prepared by alternative laser ablation of the nanocomposite and YBCO targets. The deposition recipe was optimized for growing YBCO-123 matrix with the best epitaxial quality, e.g.

200 mTorr (Oxygen) at 780 °C during deposition followed by a post-annealing process under 200 Torr (Oxygen) at 550 °C for 30 min.

Microstructure, and, magnetic and superconducting properties of all the samples were investigated. Microstructure studies were conducted using X-ray diffraction (XRD) (Panalytical XPert X-ray diffractometer), along with high resolution cross-sectional transmission electron microscopy (XTEM) and scanning transmission electron microscopy (STEM) in the FEI Tecnai G2 F20 ST analytical microscopy (a point resolution of 0.24 nm at 200 kV). The magnetization, critical transition temperature (***Tc***) and critical current density (both J_c^{sf} and $J_c^{in\text{-}field}$) were measured by a physical property measurement system (PPMS). $J_c^{in\text{-}field}$ ***(H//c)*** were measured under applied field from 0 to 5T at 75K, 65K, 40K and 5K by the vibrating sample magnetometer (VSM) in PPMS.

3.4 Results and discussion

Figure 3.1 shows the plan-view low mag ((a), (d), (g)) and high resolution ((b), (e), (h)) TEM images for $(CoFe_2O_4)_x : (CeO_2)_{1-x}$ VAN systems on STO substrates with x=0.5, 0.3 and 0.1, respectively. The corresponding schematic diagrams are shown in Figure 3.1(c), (f) and (i). For the case of $(CoFe_2O_4)_{0.5} : (CeO_2)_{0.5}$ in Figure 3.1(a) and (b), it is clearly seen that $CoFe_2O_4$ and CeO_2 domains, shown as dark and bright contrast regions, grow alternately to build up a “nanomaze” structure in-plane. The nanodomains are rectangular ones with an average width of 10 nm and an average length of 60 nm as the schematic illustration in Figure 3.1(c). As x reduces to 0.3 and 0.1 (Figure 3.1(d), (e)

and (g), (h)), the density and size of $CoFe_2O_4$ domains decrease obviously, which are constant with the overall $CoFe_2O_4$ composition trend.

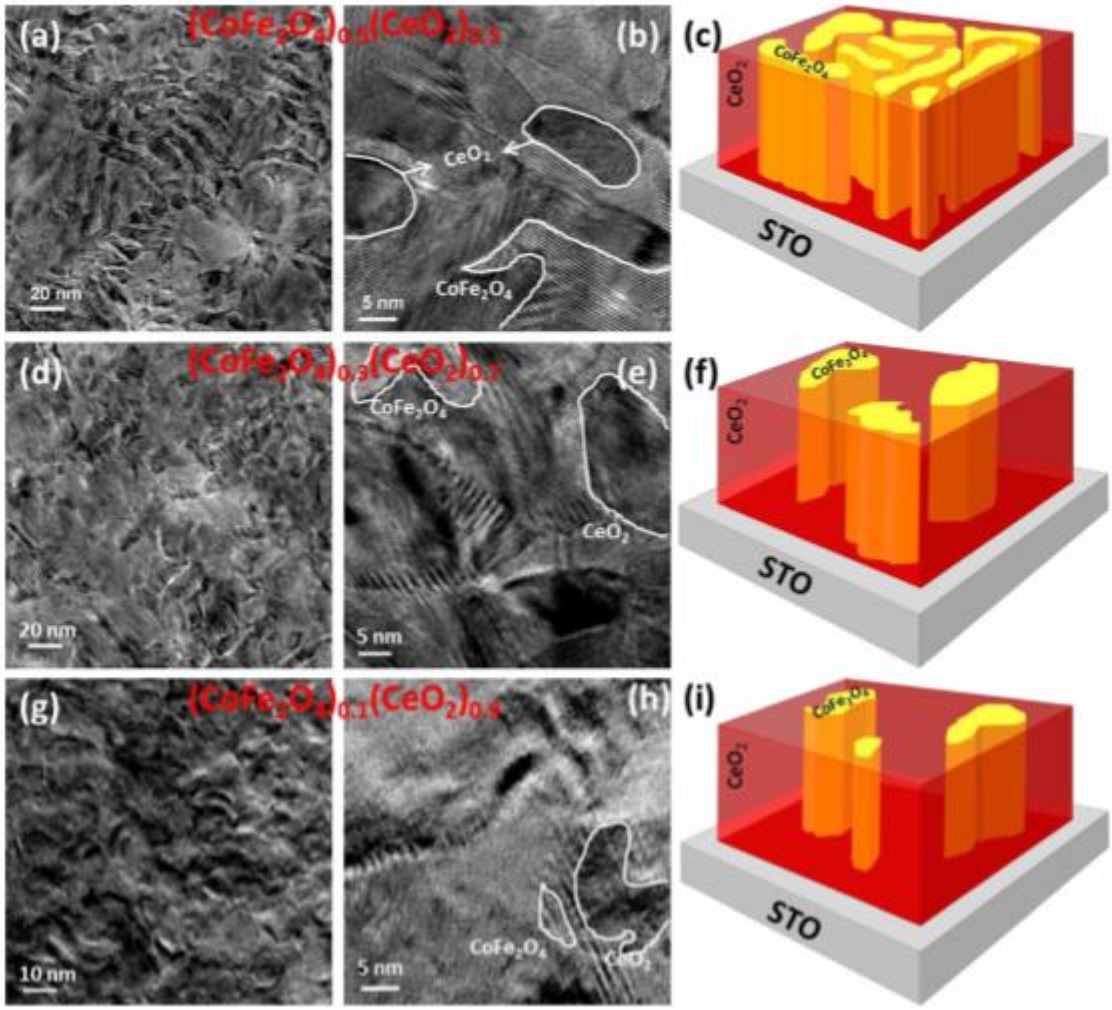

Figure 3.1 (a), (d), and (g) plan view low magnification, (b), (e), and (h) high resolution TEM images, and (c), (f), and (i) the corresponding schematic illustrations for $(CoFe_2O_4)_x$:$(CeO_2)_{1-x}$ VAN systems with x=0.5, 0.3, and 0.1, respectively.

To explore the magnetic properties of the VAN composite films as a function of $CoFe_2O_4$ composition, magnetization measurements (M-H) using VSM were conducted for all the VAN films. Figure 3.2(a) and (b) show the M-H curves for $(CoFe_2O_4)_x$: $(CeO_2)_{1-x}$ VAN systems (x=0.5, 0.3 and 0.1) at 5K with ***H//ab*** and ***H//c***, respectively. There are several major findings: First, all the samples show a similar saturation point as the applied magnetic field increases to around 2.5 T; Second, $(CoFe_2O_4)_{0.5}$: $(CeO_2)_{0.5}$ shows the highest saturation remanence $\boldsymbol{M_{rs}}$ (which is the remaining magnetization when the applied magnetic field is dropped to zero) and coercive field h_c (which is the reverse field needed to drive the magnetization to zero after being saturated). This results in $(CoFe_2O_4)_{0.5}$: $(CeO_2)_{0.5}$ with a much fatter hysteresis loop, compared to the samples with x=0.3 and 0.1. This is because $(CoFe_2O_4)_{0.5}$: $(CeO_2)_{0.5}$ has the most amount of magnetic composition $CoFe_2O_4$; Third, all the samples show an anisotropic magnetic response, i.e., M-H loops are different for the cases for ***H//ab*** and ***H//c***. For example, $(CoFe_2O_4)_{0.5}$: $(CeO_2)_{0.5}$ shows a much stronger magnetization response in ***H//c*** than that in ***H//ab***, however, $(CoFe_2O_4)_{0.3}$: $(CeO_2)_{0.7}$ shows a much stronger magnetization response in ***H//ab*** than that in ***H//c***. This opposite anisotropy property is directly related to the magnetic domain structure and distribution variation in different VAN cases. For examples, interestingly, the sample of $(CoFe_2O_4)_{0.3}$: $(CeO_2)_{0.7}$ shows the highest magnetization with increasing magnetic field when ***H//ab***. This might be because that $CoFe_2O_4$ is more likely to be lateral growth in $(CoFe_2O_4)_{0.3}$: $(CeO_2)_{0.7}$, rather than the vertical growth in the case of x=0.5. In Figure 3.2(c) and (d), M-H loops were measured at 65K, 40K, 5K with ***H//b*** and ***H//c***, respectively, for $(CoFe_2O_4)_{0.5}$: $(CeO_2)_{0.5}$. The M-H

curves are very similar at different temperatures, regardless of the magnetic field orientations, which indicate that the magnetic properties are relatively constant when the temperature decreases from 65K to 5K (this is the temperature range chosen for the following $\boldsymbol{J_c}$ measurement of the doped and undoped YBCO thin films). Overall, all the VAN single layers show an obvious magnetization response, with that $(CoFe_2O_4)_{0.5}$: $(CeO_2)_{0.5}$ shows the strongest and $(CoFe_2O_4)_{0.1}$: $(CeO_2)_{0.9}$ as the least.

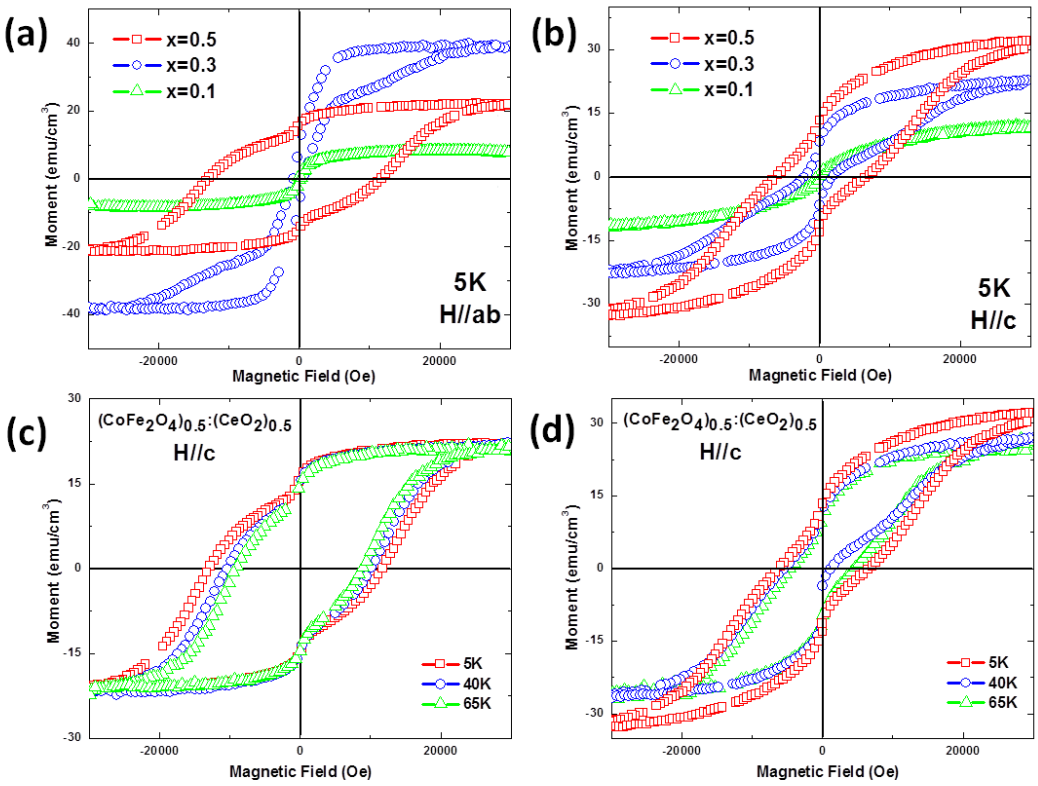

Figure 3.2 M-H curves for $(CoFe_2O_4)_x$: $(CeO_2)_{1-x}$ VAN system at 5K with (a) ***H//ab***, (b) ***H//c*** and for $(CoFe_2O_4)_{0.5}$: $(CeO_2)_{0.5}$ at 65K, 40K, 5K with (c) ***H//ab***, (d) ***H//c***.

$(CoFe_2O_4)_x$: $(CeO_2)_{1-x}$ VAN systems were further introduced into YBCO thin film as both cap and buffer layers to explore the different magnetic response and their effects on YBCO pinning properties. Table 3.1 summarizes the self-field superconducting properties of all the doped samples and a pure YBCO thin film as reference. The $\boldsymbol{T_c}$ value of the VAN doped samples varies from 89.9K to 90.3K, which is pretty close to the reference one of 90.4K. The stable $\boldsymbol{T_c}$ demonstrates that there is very little or even no poisoning effect to the intrinsic YBCO matrix after introducing both cap and buffer $(CoFe_2O_4)_x$: $(CeO_2)_{1-x}$ VAN nanolayers. Furthermore, the $\boldsymbol{J_c^{sf}}$ of all the doped samples has an obvious enhancement compared to the reference YBCO at 75K, 65K, 40K and 5K, especially the one doped with x=0.5 VAN cap layer. It achieves the highest $\boldsymbol{J_c^{sf}}$ values of 5.2, 17.1, 48.3 and 132 MA/cm^2 at all the measured temperature of 75K, 65K, 40K and 5K among all the samples. These results are much higher than the previously reported magnetic doped cases, such as $(Fe_2O_3)_{0.5}(CeO_2)_{0.5}$ VAN doped cases [35]. This result, suggests a much less poisoning effect for the case of $(CoFe_2O_4)_x$: $(CeO_2)_{1-x}$ VAN. Another phenomenon is that most cap layered samples have higher $\boldsymbol{T_c}$ and $\boldsymbol{J_c^{sf}}$ values than the buffer layered one with the same composition of $CoFe_2O_4$. This may be caused by the slight degradation of the surface quality of YBCO growth after introducing buffer layers.

Table 3.1. Summary of self-field superconducting properties of all doped and undoped samples.

Sample	T_c (K)	J_c^{sf} 75K (MA/cm^2)	J_c^{sf} 65K (MA/cm^2)	J_c^{sf} 40K (MA/cm^2)	J_c^{sf} 5K (MA/cm^2)
X=0.1 Cap Buff	90.3 90.1	2.1 1.3	9.5 8.3	26 26	84 106
X=0.3 Cap Buff	90.1 90.0	3.4 3.2	10.0 7.7	27 23.2	73.3 56.1
X=0.5 Cap Buff	90.0 89.9	5.2 3.1	17.1 7.4	48.3 25.4	132 43.3
Ref. YBCO	90.4	1.3	3.1	11.0	35.3

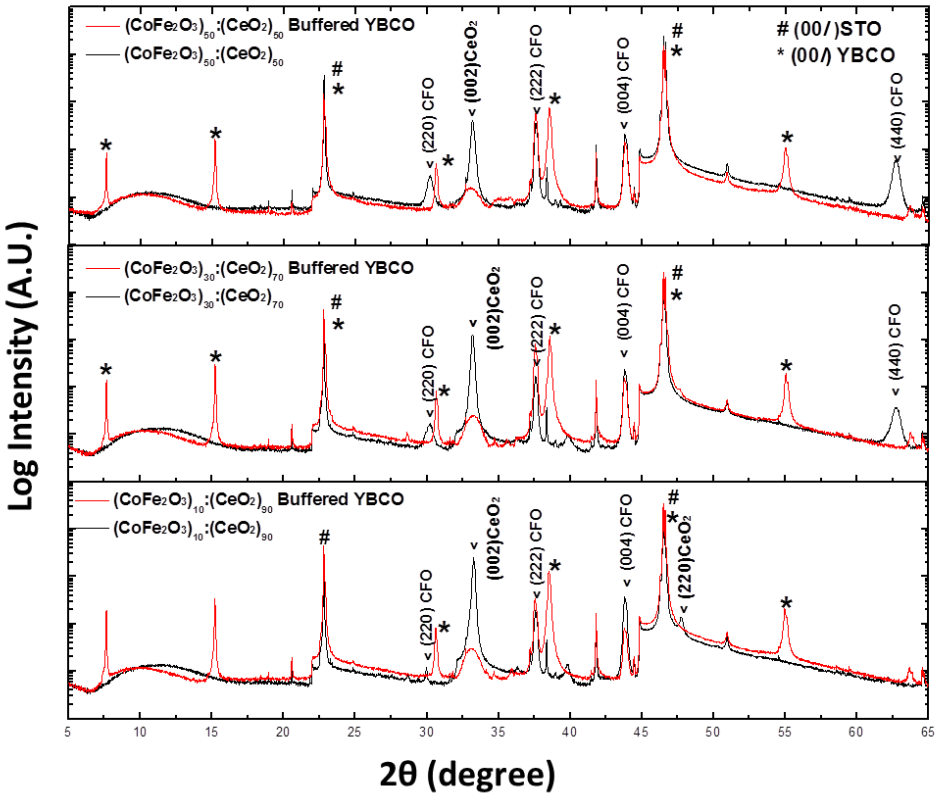

Figure 3.3 XRD patterns of all $(CoFe_2O_4)_x : (CeO_2)_{1-x}$ VAN buffer layered samples (in red) overlapping with pure $(CoFe_2O_4)_x : (CeO_2)_{1-x}$ (in black).

Figure 3.3 shows the θ-2θ X-ray diffraction (XRD) data for all $(CoFe_2O_4)_x$: $(CeO_2)_{1-x}$ VAN buffer layered YBCO samples (Red lines) overlapping with pure $(CoFe_2O_4)_x$: $(CeO_2)_{1-x}$ (Black lines) on STO substrates. Pound (#) and star (*) symbols represent the STO (00*l*) and YBCO (00*l*) peaks, respectively, from which we can see that YBCO (003) and (006) perks (c/3=3.89 Å, PDF#871473) are perfectly overlapped with STO (001) and (002) peaks (c=3.91 Å, PDF#840444), respectively. This confirms that the highly textured YBCO thin films along STO (001). In addition, the peak position of YBCO (002) is pretty close to 15.195° (c=11.68 Å, the value of bulk YBCO), which indicates the high quality YBCO growth even after doped with the VAN buffer layer. Furthermore, several peaks related to $(CoFe_2O_4)_x$: $(CeO_2)_{1-x}$ VAN can be clearly seen, i.e., CeO_2 perks at 33° (d (001)=2.71 Å, PDF#340394) can be identified. The peak intensity slightly decreases compared to the pure VAN. Multiple peaks of $CoFe_2O_4$ (PDF#030864) including $CoFe_2O_4$ (222), (004) and (440) can be seen in the reference VAN samples, but only $CoFe_2O_4$ (004) appears in the buffer layered VAN YBCO thin films, indicating a better textured film for the case of buffered layered VANs.

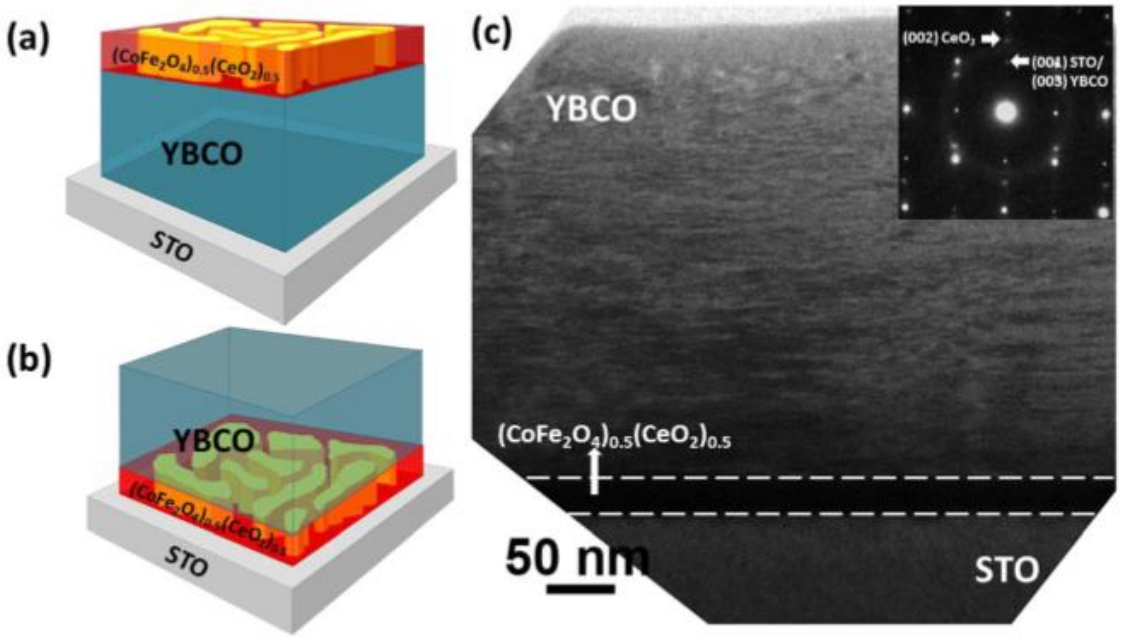

Figure 3.4 Schematical illustrations of the $(CoFe_2O_4)_{0.5}(CeO_2)_{0.5}$ nanolayer doped YBCO thin films as both (a) cap layer and (b) buffer layer, as well as the low magnification XTEM micrograph with the corresponding SAED of the $(CoFe_2O_4)_{0.5}(CeO_2)_{0.5}$ VAN buffered sample.

The schematic diagrams for the cap and buffer doped designs can be seen in Figure 3.4(a) and (b), respectively. Figure 3.4(c) is the low magnification XTEM micrograph with selected area electron diffraction (SAED) pattern for the buffered $(CoFe_2O_4)_{0.5}$: $(CeO_2)_{0.5}$ doped YBCO film (3.4b). It is clear that the total thickness of the YBCO film is about 350 nm with the VAN layer of about 15 nm. The interface between YBCO and VAN layer is very clean, which indicates that there is no or little interdiffusion between the two phases. The SAED pattern shows that YBCO (003) diffraction dot overlaps well with STO (001), which is consistent with the XRD results.

Simultaneously, CeO_2 (002) diffraction dot can also be identified, which suggests the epitaxial growth of the VAN buffer layer.

Figure 3.5(a), (c) and (e) show the cross-sectional high resolution TEM micrographs of the buffered VAN doping samples as well as the corresponding STEM micrographs in Figure 3.5(b), (d) and (f), for x=0.5, 0.3 and 0.1, respectively. In all three cases, the thickness of the VAN layer can be easily identified to be about 15nm, resulted by 300 pulses of deposition. Furthermore, the two phases of $CoFe_2O_4$ and CeO_2 can be distinguished by the different contrast, e.g., $CoFe_2O_4$ gives a brighter contrast and CeO_2 regions are darke. Last, the $(CoFe_2O_4)_{0.1}$: $(CeO_2)_{0.9}$ VAN buffered sample shows the best epitaxial quality for YBCO growth that might be because it contains the most amount of CeO_2 with a minimal lattice mismatch with YBCO. STEM micrographs were taken to further reveal the distribution of $CoFe_2O_4$ and CeO_2 in the VAN layers. The STEM images were taken under a high angle annular dark field mode (HAADF, also called Z-contrast), where the contrast is approximately proportional to Z^2 of the material. Therefore, $CoFe_2O_4$ regions are darker and CeO_2 areas are brighter (note that STEM contrast is opposite to the TEM contrast in general). Figure 3.5(b) shows the STEM image of $(CoFe_2O_4)_{0.5}$: $(CeO_2)_{0.5}$ VAN layer, two phases can be obviously observed with the $CoFe_2O_4$ domains marked by white arrows. In addition, $CoFe_2O_4$ can be observed in Figure 3.5(d), indicated by white arrows. It is obvious that $(CoFe_2O_4)_{0.3}$: $(CeO_2)_{0.7}$ contains less $CoFe_2O_4$ compared to $(CoFe_2O_4)_{0.5}$: $(CeO_2)_{0.5}$ and $CoFe_2O_4$ can be hardly identified from Figure 3.5 (f) for $(CoFe_2O_4)_{0.1}$: $(CeO_2)_{0.9}$ VAN layer, due to the low $CoFe_2O_4$ concentration.

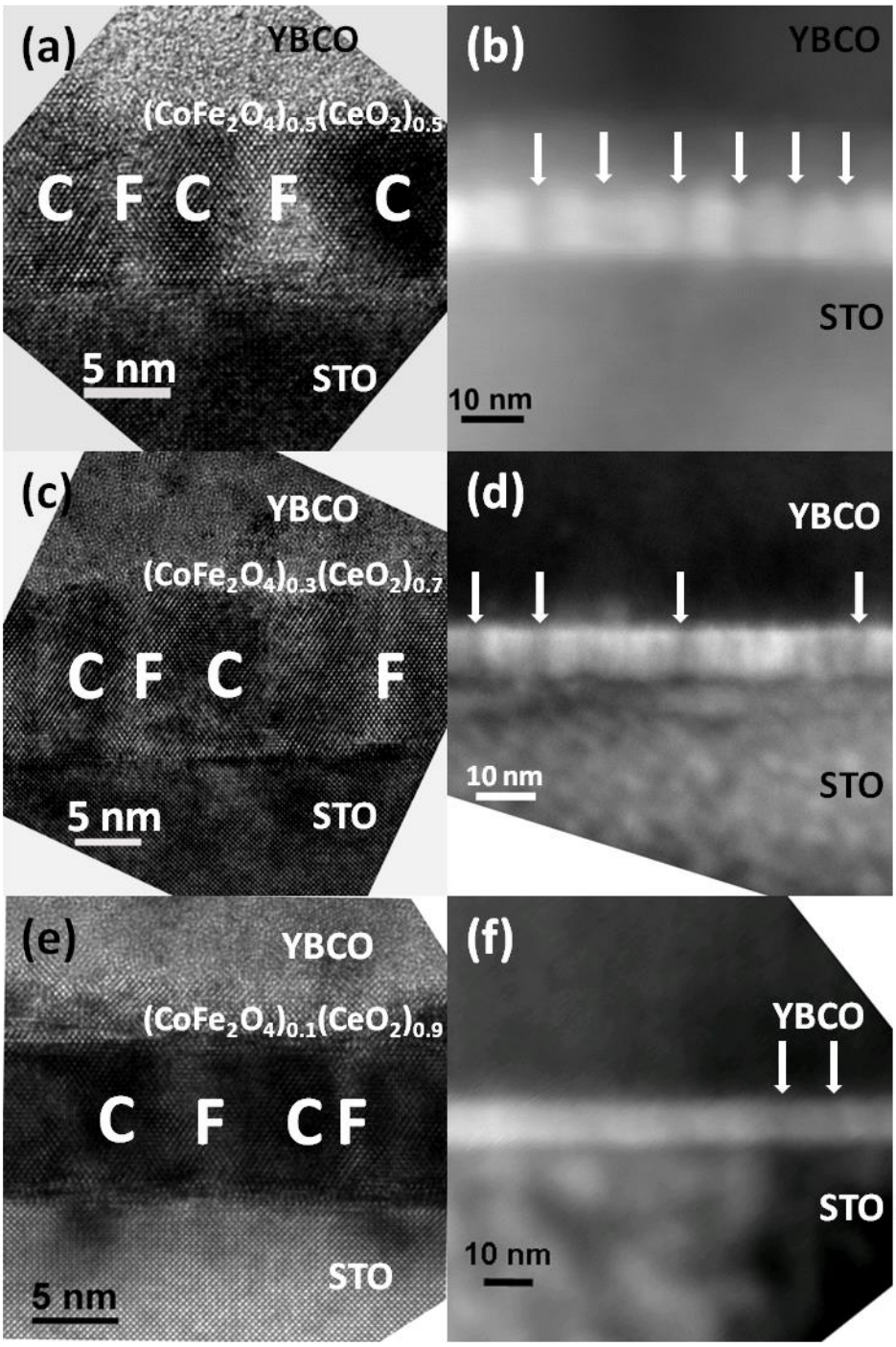

Figure 3.5 Cross-sectional high resolution TEM micrographs of $(CoFe_2O_4)_x:(CeO_2)_{1-x}$ VAN buffered YBCO, with (a) x=0.5, (b) x=0.3, and (c) x=0.1, and their corresponding STEM micrographs in (b), (d), and (f).

The in-field critical current density $\boldsymbol{J_c}$ ***(H//c)*** of all the samples were measured to investigate their superconducting properties and the different pinning properties of different doping architectures. Figure 3.6 plots $\boldsymbol{J_c}$ as a function of applied magnetic field, in both log-linear and log-log scales. All of the samples were measured at three different temperatures of (a) 65K, (b) 40K and (c) 5K to investigate the pinning mechanism in high and low temperature regimes. In the high temperature range of 65K (Figure 3.6(a)), $\boldsymbol{J_c}$ of all the doped samples increase compared to the reference YBCO thin film, and the $(CoFe_2O_4)_{0.5}$: $(CeO_2)_{0.5}$ capped one shows the highest $\boldsymbol{J_c}$ in the entire field regime up to 5 T. Moreover, all the cap layered samples obtain a higher $\boldsymbol{J_c}$ than the corresponding buffered ones, possibly because the buffered layers impact the growth quality of YBCO while the capped ones have remained high YBCO film quality with additional magnetic pinning effects. Another phenomenon is that the samples doped with more magnetic materials of $CoFe_2O_4$ exhibit higher $\boldsymbol{J_c}$, which suggests that magnetic pinning effect is effective at high temperatures for this doping system. However, in a previously reported $(Fe_2O_3)_{0.5}$: $(CeO_2)_{0.5}$ system, magnetic pinning effect is more dominated at low temperatures [35]. This observation, suggests that the dominated pinning mechanism could be quite different in different doping systems.

When the measured temperature lowered to 40K, as seen in Figure 6(b), the $(CoFe_2O_4)_{0.5}$: $(CeO_2)_{0.5}$ capped sample still shows the highest $\boldsymbol{J_c}$ in all the applied magnetic field range and the sequence of pinning performance is similar to that in 65 K. Interestingly, the buffer layer doped specimens start to show better superconducting

properties, and approach the capped ones, especially for the $(CoFe_2O_4)_{0.1}$: $(CeO_2)_{0.9}$ doped ones.

When the measured temperature is further lowered to 5 K, in Figure 6 (c), the $(CoFe_2O_4)_{0.5}$: $(CeO_2)_{0.5}$ capped sample still presents the best pinning performance among all while the $(CoFe_2O_4)_{0.5}$: $(CeO_2)_{0.5}$ buffered one shows the worst. This is mainly due to that the VAN buffer impacts of the YBCO film growth and intrinsic superconducting properties. More interesting, the $\boldsymbol{J_c}$ of $(CoFe_2O_4)_{0.1}$: $(CeO_2)_{0.9}$ doped samples exceeds the $(CoFe_2O_4)_{0.3}$: $(CeO_2)_{0.7}$ doped ones in all the measured field, which demonstrates that defect pinning effect dominates at low temperatures for this case. Another interesting observation is that the $(CoFe_2O_4)_{0.1}$: $(CeO_2)_{0.9}$ buffered one shows higher $\boldsymbol{J_c}$ than its capped one, again related stronger defect pinning effect introduced by the buffered case.

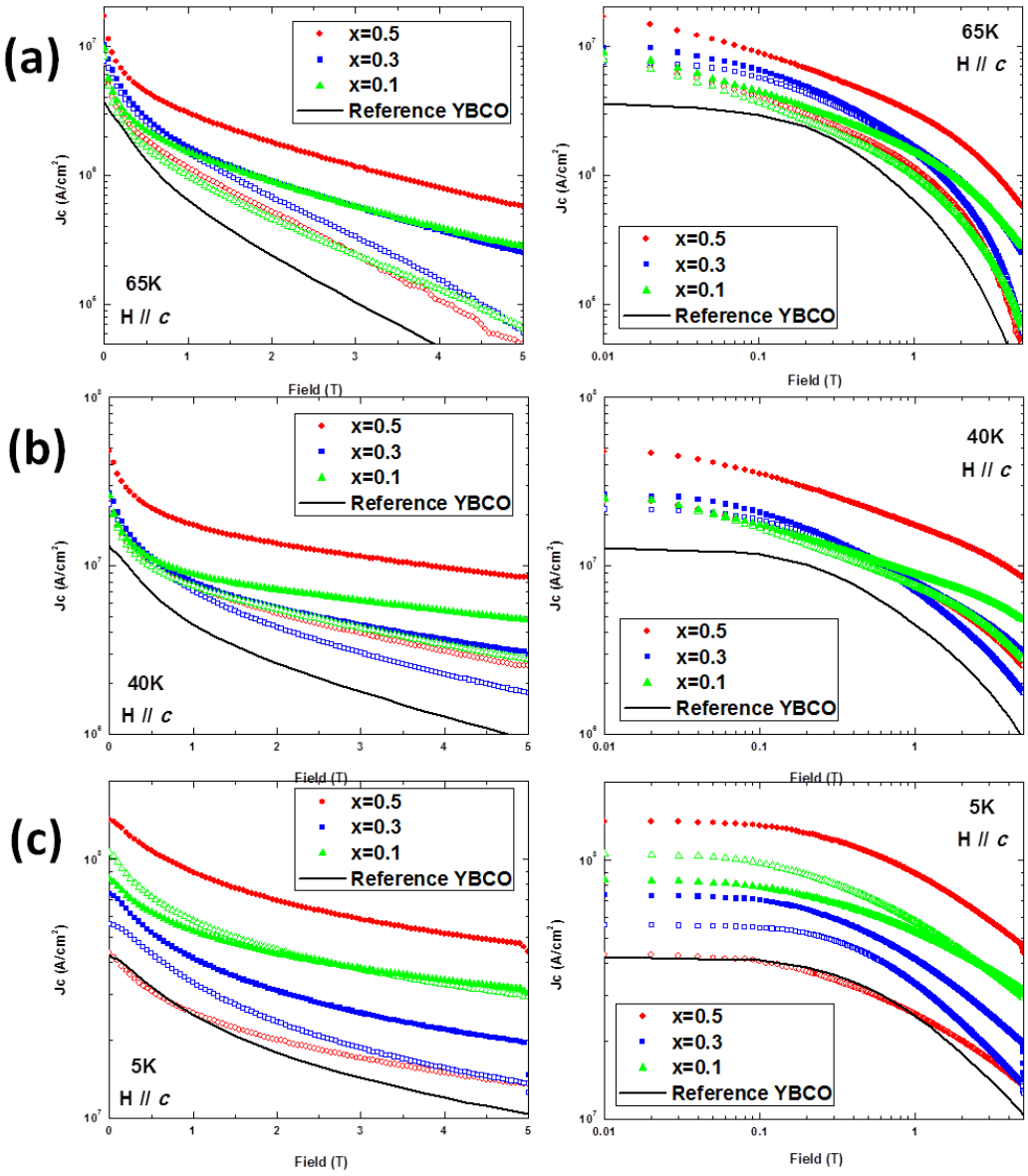

Figure 3.6 ***J_c(H//c))*** plots as a function of applied magnetic field at (a) T=65K, (b) T=40K, and (c) T=5K for the $(CoFe_2O_4)_x$:$(CeO_2)_{1-x}$ VAN doped and undoped samples compared with the reference YBCO sample. The plots are in both log-linear (left) and log-log (right) scales. The solid symbol plots represent cap layer doped samples and the open symbol ones represent buffer layer doped samples.

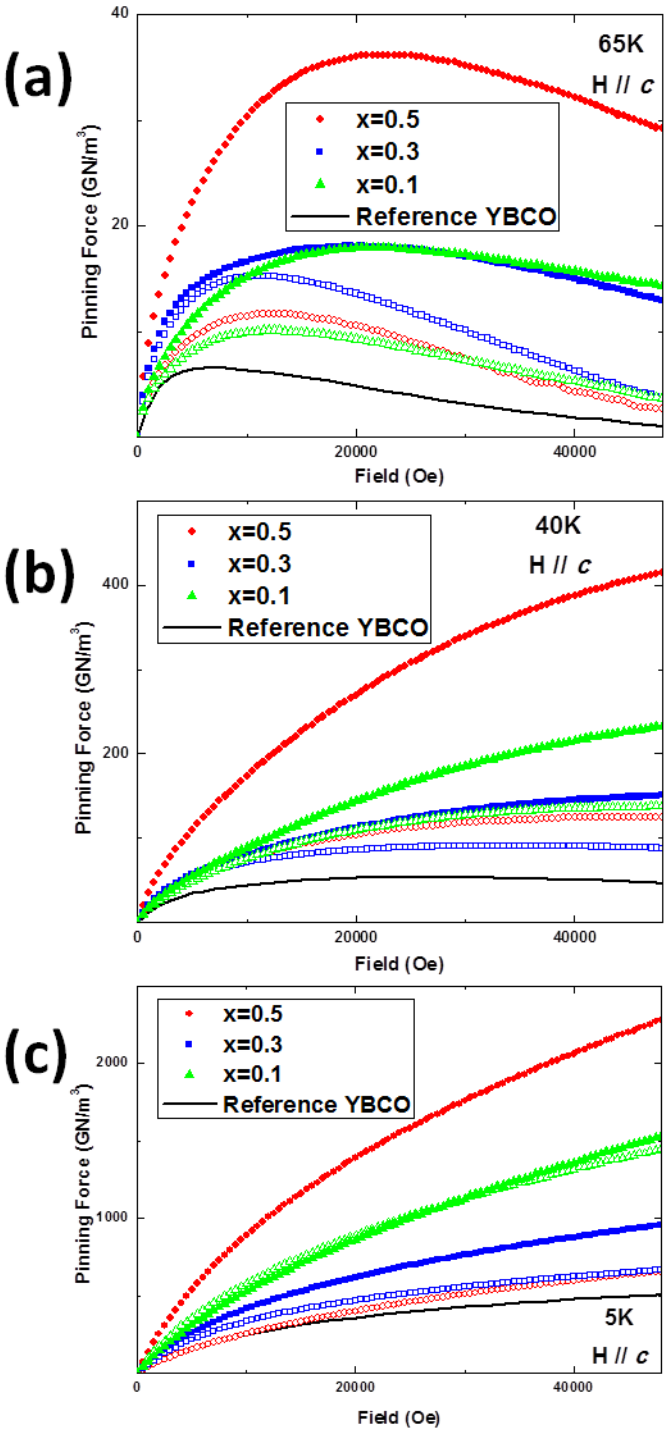

Figure 3.7 Calculated pinning force ***(F_p(H//c))*** plots for all the $(CoFe_2O_4)_x$:$(CeO_2)_{1-x}$ VAN doped and undoped samples as a function of applied magnetic field measured at (a) 65K, (b) 40K, and (c) 5K. The solid symbol lines represent cap layer doped samples and the open lines represent buffer layer doped ones.

To further investigate the pinning effect and matching field of $(CoFe_2O_4)_x$: $(CeO_2)_{1-x}$ VAN system doped YBCO, the calculated pinning force ($\boldsymbol{F_p}$) at (a) 65 K, (b) 40 K and (c) 5 K is plotted in Figure 3.7 for all cases. All the doped samples obviously show a larger $\boldsymbol{F_p}$ value than the reference YBCO at all the three temperatures, and $(CoFe_2O_4)_{0.5}$: $(CeO_2)_{0.5}$ capped sample gives the largest $\boldsymbol{F_p}$, which is consistent with the above $\boldsymbol{J_c}$ results. At 65 K, the matching field at maximum $\boldsymbol{F_p}$ ($\boldsymbol{B_{matching}}$) of $(CoFe_2O_4)_{0.5}$: $(CeO_2)_{0.5}$ capped sample reaches about 2 T, and followed by the other two capped samples and the three buffered ones show a lower $\boldsymbol{B_{matching}}$ of about 1T, all larger than the $\boldsymbol{B_{matching}}$ of YBCO. At 40 K and 5 K, $\boldsymbol{B_{matching}}$ values of all the samples are out-of the field range, and the $\boldsymbol{B_{matching}}$ of $(CoFe_2O_4)_{0.1}$: $(CeO_2)_{0.9}$ doped samples increase faster than the $(CoFe_2O_4)_{0.3}$: $(CeO_2)_{0.7}$ doped ones as the temperature decreases, and surpasses the $(CoFe_2O_4)_{0.3}$: $(CeO_2)_{0.7}$ doped ones at 5 K. This observation again suggests that for $CoFe_2O_4$ case, magnetic pinning effect dominates at higher temperatures when defect pinning effect dominates at lower temperatures. Finally, $(CoFe_2O_4)_{0.5}$: $(CeO_2)_{0.5}$ buffered one shows the lowest $\boldsymbol{F_p}$ at 5 K among all the doped samples, possibly because of the large film quality degradation.

Based on the above discussions, $(CoFe_2O_4)_x$: $(CeO_2)_{1-x}$ VAN system can be effective pinning centers for YBCO thin film, as it can provide both magnetic pinning effect and defect pinning effect, and they dominate at higher and lower temperature regimes, respectively. This phenomenon is opposite to the $(Fe_2O_3)_{0.5}$: $(CeO_2)_{0.5}$ system [35]. One possibility is that in the previous case, Fe_2O_3 provides a weaker magnetic effect and cannot overcome the thermal-induced flux flow in the high temperature

regime. In this case, $CoFe_2O_4$ can provide stronger magnetic pinning centers, and its pinning energy is larger than defect pinning energy for single vortex, therefore the magnetic pinning effects present a stronger impact over defects pinning effects in high temperature regime. This result is also consistent with other reported magnetic pinning effects. [130] For example, Bulaevskii *et al* argued that the estimated magnetic pinning energy for single vortex in their system is about 100 times larger than the defect pinning energy, which can push the critical current density to 10^6-10^7 A/cm^2 at high temperatures. [130] In addition, an optimum pinning effect can be achieved by tuning the composition of the magnetic $CoFe_2O_4$ in VANs. This approach provides a large flexibility in magnetic pinning design scheme for coated conductors as well as the non-magnetic pinning ones.

3.5 Conclusions

$(CoFe_2O_4)_x : (CeO_2)_{1-x}$ VAN systems have been grown and their magnetic properties have been confirmed by the M-H curves. The VAN systems have been introduced into YBCO thin film as both cap layer and buffer layer. All the doped samples show much better $\boldsymbol{J_c^{self\text{-}field}}$ and $\boldsymbol{J_c^{in\text{-}field}(H//c)}$ at all measured temperatures, especially the $(CoFe_2O_4)_{0.5}$: $(CeO_2)_{0.5}$ VAN capped sample, which suggests that $(CoFe_2O_4)_x : (CeO_2)_{1-x}$ VAN system can be effective pinning landscapes by both magnetic pinning effect and defect pinning effect. The results suggest that the magnetic pinning effect is dominant in high temperature regime while defect pinning dominates at low temperature regime for this particular system. Last, the superconducting properties

can be tuned and improved by varying compositions and VAN architectures. This approach provides a large design flexibility in combining magnetic pinning centers with other defect pinning centers to achieve the desired pinning properties for YBCO coated conductors.

CHAPTER IV

ENHANCED FLUX PINNING PROPERTIES IN $YBa_2Cu_3O_{7-\delta}/(CoFe_2O_4)_{0.3}(CeO_2)_{0.7}$ MULTILAYER THIN FILMS*

4.1 Overview

A combined defect and magnetic pinning effect has been demonstrated in this work for improving critical current density ($\boldsymbol{J_c}$) of $YBa_2Cu_3O_{7-\delta}$ (YBCO) thin films. Most of the previous work has focused on either defect pinning or magnetic pinning. In this work, we introduced a unique nanocomposite with two phases, e.g., ferrimagnetic $CoFe_2O_4$ and non-magnetic CeO_2. As a demonstration, the composition of $(CoFe_2O_4)_{0.3}(CeO_2)_{0.7}$ was chosen for this study. The nanocomposite was incorporated into YBCO films as multilayers, i.e., 1-, 2-, and 4-interlayers. A detailed study on the microstructural and superconducting properties was conducted. The results show that the critical temperature remains at ~90 K even after introducing interlayers. More importantly, the films with interlayers show enhanced self-field and in-field $\boldsymbol{J_c}$, especially the 2-interlayer sample with $\boldsymbol{J_c^{sf}}$ of 6.36 MA/cm^2 at 77 K. The enhanced $\boldsymbol{J_c}$ properties are attributed to both magnetic pinning from $CoFe_2O_4$ and defect pinning from CeO_2, as well as the well-designed pinning landscapes.

*Reprinted with permission from "Enhanced Flux Pinning Properties in $YBa_2Cu_3O_{7-\delta}/(CoFe_2O_4)_{0.3}(CeO_2)_{0.7}$ Multilayer Thin Films" by Jijie Huang, Chen-Fong Tsai, Li Chen, Jie Jian, Kaiyuan Yu, Wenrui Zhang, and Haiyan Wang, *IEEE Transitions on Applied Superconductivity*, **25**, 7500404, 2015.

4.2 Introduction

Over the past two decades, $YBa_2Cu_3O_{7-\delta}$ (YBCO) has aroused great research interest, owing to its high transition temperature ($\boldsymbol{T_c}$) of above 90 K and some other advantages. [10] Therefore, YBCO-based coated conductors (CCs) have found many technologically important applications, such as power transmission lines, generators, magnets, motors, and etc. [203, 213] Most of these practical applications require high electrical current transport properties under magnetic field with little or even no losses, which means high in-field critical current density ($\boldsymbol{J_c}$) is needed. Therefore, a significant amount of work has been performed involving various flux pinning approaches for enhancing $\boldsymbol{J_c}$. [102, 214] Commonly, introducing defects into YBCO matrix is adopted to pin the vortices to avoid energy-dissipation. Such effective pinning defects can be generated by 0-D nanoparticles, [81, 83] 1-D nanocolumes [96, 106] as well as 2D nanolayers. [215, 216] These defects were reported to be more effective at low temperatures, because of the temperature dependence of the London penetration length ($\boldsymbol{\lambda_L}$). [132, 213] Later on, magnetic pinning was investigated to overcome this thermal activated flux flow at high temperature regimes, which is crucial for achieving high working temperatures in YBCO. [130] Several successful examples have been demonstrated by introducing magnetic pinning centers into YBCO thin films for superconducting properties enhancement. [138, 211] However, a large lattice mismatch and possible interdiffusion between most of the magnetic materials and YBCO matrix hinders further development of the magnetic doping approaches. To overcome these issues, a unique structure of vertically aligned nanocomposite (VAN) containing both

magnetic and non-magnetic phases has been explored for both defect and magnetic pinning effects. [137, 142]

In this study, ferrimagnetic $CoFe_2O_4$ and non-magnetic CeO_2 have been mixed as $(CoFe_2O_4)_{0.3}(CeO_2)_{0.7}$ and incorporated into YBCO thin films as interlayers. $CoFe_2O_4$ has a spinel structure with 9.03% and 8.85% lattice mismatch with YBCO (with 45° rotation) and CeO_2, respectively. $(CoFe_2O_4)_{0.3}(CeO_2)_{0.7}$ could be an ideal composition that contains enough magnetic materials in an epitaxial CeO_2 matrix with limited quality degradation and inter-diffusion. Furthermore, strong ferrimagnetic properties have been demonstrated in this nanocomposite system. [142] A previous successful demonstration on YBCO/CeO_2 multilayers indicated that the $\boldsymbol{J_c}$ performance achieved the highest value with 2-CeO_2 interlayers. [122] Following that, we designed the pinning landscape with 1-, 2-, and 4-interlayers of $(CoFe_2O_4)_{0.3}(CeO_2)_{0.7}$ into YBCO matrix for ultimate magnetic and defect pinning properties. The superconducting properties as well as microstructure properties were measured and correlated for all the samples for optimum pinning properties.

4.3 Experimental

YBCO thin films with 1-, 2-, and 4-interlayers of $(CoFe_2O_4)_{0.3}$:$(CeO_2)_{0.7}$ nanocomposite interlayers and a pure YBCO sample reference were prepared using pulsed laser deposition (PLD) on $SrTiO_3$(STO) (001) single crystal substrates (KrF excimer laser, Lambda Physik 201, 10 Hz). The multilayer structures were introduced into YBCO matrix by alternating ablation of YBCO and the nanocomposite targets. The

total thickness of YBCO multilayer samples was controlled at ~300 nm, whereas the thickness of each inter-layer was controlled at ~5 nm. An optimized deposition recipe for epitaxial YBCO thin films was used for this study, i.e.,200 mTorr (oxygen pressure) and the substrate temperature of 780°C following by annealing under 200 Torr (oxygen pressure) at 550°C for 30 minutes.

Microstructure studies were conducted using X-ray diffraction (XRD) (Panalytical XPert X-ray diffractometer), along with high resolution cross-sectional transmission electron microscope (XTEM) in the FEI Tecnai G2 F20 ST analytical microscopy (a point resolution of 0.24 nm at 200 kV). The magnetization, critical transition temperature ($\boldsymbol{T_c}$), and critical current density (both $\boldsymbol{J_c^{sf}}$ and $\boldsymbol{J_c^{in\text{-}field}}$) were measured in a physical property measurement system (PPMS). $\boldsymbol{J_c^{in\text{-}field}}$ **(*H//c*)** were measured under applied field from 0 to 5 T at 77 K, 65 K, 40 K, and 5 K using the vibrating sample magnetometer (VSM) in the PPMS.

4.4 Results and discussion

Figure 4.1 shows the θ-2θ XRD patterns for the 1-, 2- and 4-multilayered YBCO thin films on STO (001) substrates. STO (00*l*) and YBCO (00*l*) peaks are represented by pound (#) and star (*) symbols, respectively. YBCO (003) and (006) peaks overlap with STO (001) and (002) peaks very well, which demonstrated the highly textured YBCO thin films along STO (00*l*) for all cases. Peaks from $(CoFe_2O_4)_{0.3}(CeO_2)_{0.7}$ nanolayers were identified, e.g., CeO_2 (002), $CoFe_2O_4$ (220) and $CoFe_2O_4$ (004). The intensity of the peaks increases with more interlayers. Moreover, the full width at half maximum

(FWHM) of the YBCO peaks increased slightly with more interlayers, which indicates slight quality degradation of the YBCO matrix with more interlayers. Some very minor peaks are from the background.

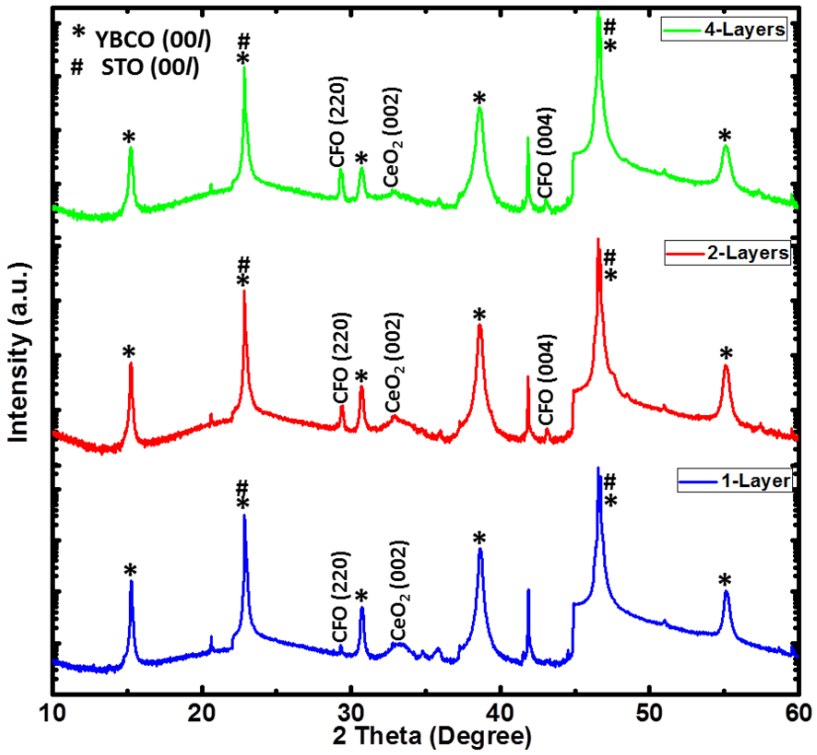

Figure 4.1 θ-2θ XRD patterns of $(CoFe_2O_4)_{0.3}$:$(CeO_2)_{0.7}$ /YBCO multilayered thin films.

Low magnification cross-sectional TEM with selected area electron diffraction (SAED) patterns of the 1-, 2- and 4- interlayered films are shown in Figure 4.2(a), Figure 4.3(a) and Figure 4.4(a), respectively. All the film thicknesses were determined to be ~300 nm. The SAED patterns of all the three samples showed very distinguished diffraction dots, which demonstrate the excellent epitaxial quality for all the interlayered

films. Furthermore, the diffraction dots of YBCO (003) were perfectly overlapped with STO (001) dots, which is consistent with the above XRD results. These results confirm the high epitaxial quality of the interlayer doped YBCO samples without significant quality degradation.

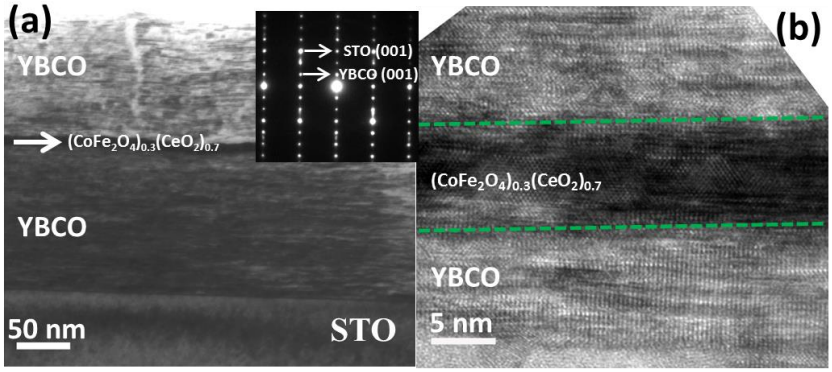

Figure 4.2 (a) Low magnification cross sectional TEM images with corresponding SEAD patterns of 1-interlayered YBCO multilayers; (b) High resolution TEM image of the interlayer area.

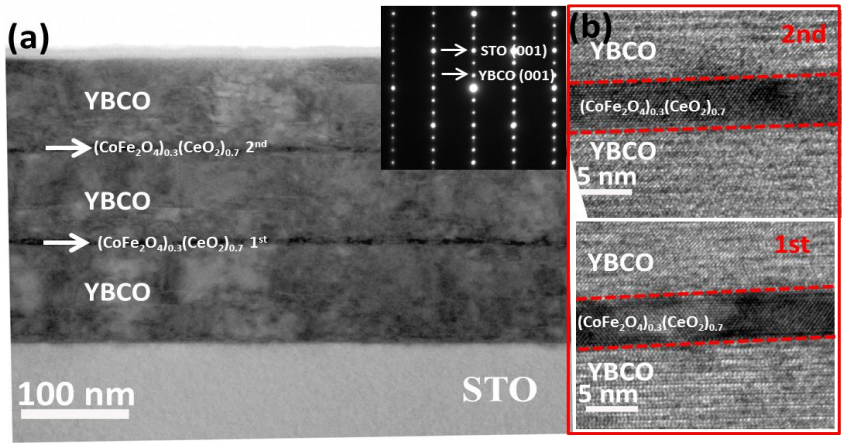

Figure 4.3 (a) Low magnification cross sectional TEM image with corresponding SEAD pattern of the 2-multilayered YBCO thin film; (b) High resolution TEM images of the two interlayers area.

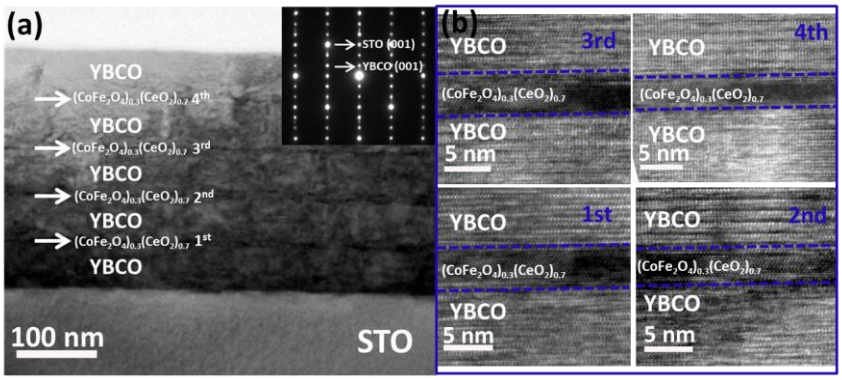

Figure 4.4 (a) Low magnification cross sectional TEM image with corresponding SEAD pattern of the 4-multilayered YBCO thin film; (b) High resolution TEM images of the four interlayers area.

Table 4.1 Summary of self-field superconducting properties of all doped and undoped samples.

Sample	T_c (K)	J_c^{sf} 77K (MA/cm^2)	J_c^{sf} 65K (MA/cm^2)	J_c^{sf} 40K (MA/cm^2)	J_c^{sf} 5K (MA/cm^2)
1-interlayer	90.0	4.4	9.3	26.2	78.5
2-interlaers	90.2	6.4	19.6	49.6	122.2
4-interlayers	90.0	2.4	11.6	35.4	90.9
Ref. YBCO	90.4	1.4	4.1	13.0	46.6

The high resolution TEM images taken from the interlayer areas of the 1-, 2- and 4- interlayered films are shown in Figure 4.2(b), Figure 4.3(b) and Figure 4.4(b), respectively. The thickness of all the interlayers can be identified as ~5 nm and the interfaces between nanolayers and YBCO layers were very clean. The contrast of the YBCO layers was quite uniform, with clear lattice fringes. In the nanocomposite interlayers, the dark and bright contrast areas were determined to be CeO_2 and $CoFe_2O_4$,

respectively. However, due to the very thin layer of 5 nm, it was hard to distinguish the two phases in the ordered distribution. Despite the clean interfaces in these nanolayered samples, high defect density due to the lattice mismatch between $CoFe_2O_4$ and YBCO matrix still existed. The lattice of CeO_2 after an in-plane 45° rotation matches with YBCO matrix very well, which is the primary reason for choosing 70% CeO_2 in the nanocomposite. The high defect density is believed to be a significant factor for pinning enhancement. In addition, $CoFe_2O_4$ is a well-known hard magnetic material with high chemical and structure stability, therefore, magnetic pinning is expected by the introducing of $CoFe_2O_4$. [185, 198]

Superconducting properties of all the multilayered YBCO thin films were investigated and compared with a pure YBCO reference film. The $\boldsymbol{T_c}$ and $\boldsymbol{J_c^{sf}}$ values measured at 77 K, 65 K, 40 K and 5 K are listed in Table 4.1. The $\boldsymbol{T_c}$ results show a minor reduction for the YBCO films with nanocomposite interlayers, compared with the pure one of 90.4 K. However, all the multilayered samples obtained higher $\boldsymbol{J_c^{sf}}$ values compared with the reference one, especially the 2-interlayered one with 6.4 MA/cm^2, 19.6 MA/cm^2, 49.6 MA/cm^2 and 122.2 MA/cm^2 at 77 K, 65 K, 40 K and 5 K, respectively. These values were higher or comparable to some recently reported flux pinning improvement for YBCO thin films. [122, 137]

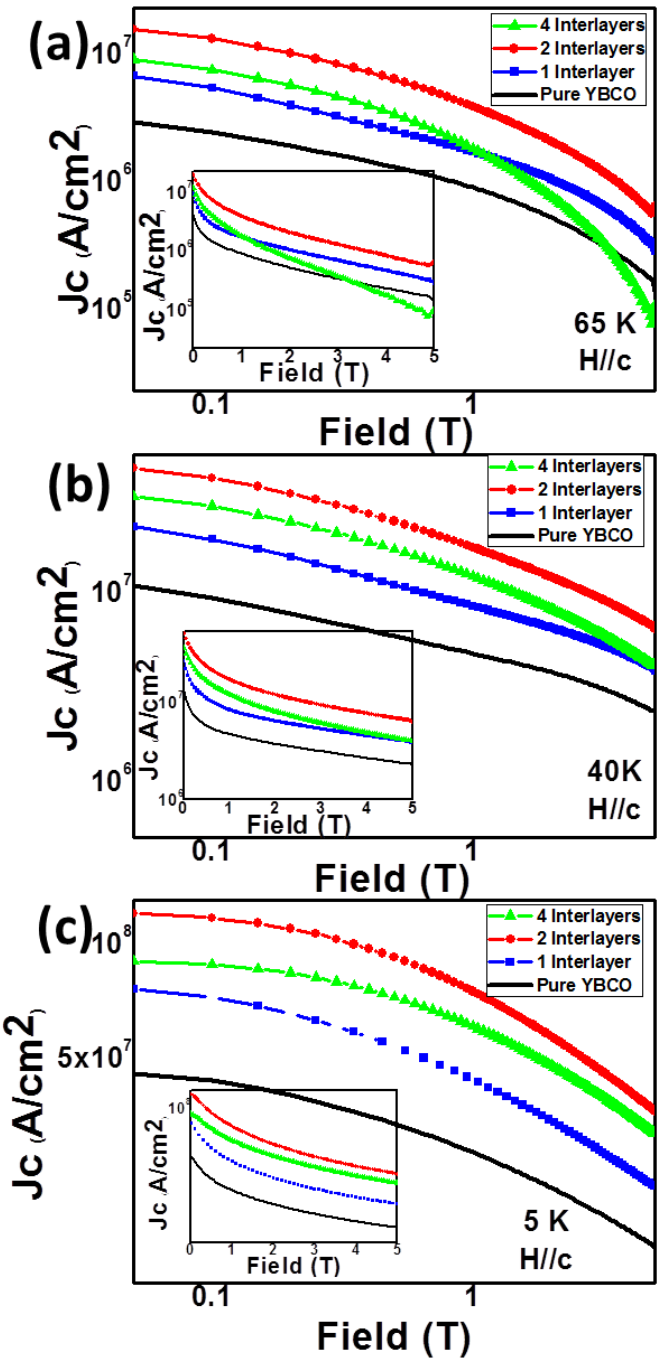

Figure 4.5 In-field performance ($J_c(H//c)$) as a function of applied magnetic field plots in a log-log scale of the 1-, 2-, 4-multilayered samples compared with the reference YBCO sample measured at (a) 65 K, (b) 40 K, and (c) 5 K. The insets are the log-linear scale plots.

The in-field critical current density ($\boldsymbol{J_c^{in\text{-}field}}$) values of the samples were measured to investigate the flux pinning of the nanocomposite interlayer under magnetic field. All the samples were measured at 65 K, 40 K and 5 K with applied magnetic fields up to 5 T. Figure 4.5 shows the in-field performance ($\boldsymbol{J_c(H//c)}$) as a function of applied magnetic field of all the samples plotted in a log-log scale, and the insets are the same data plotted in a log-linear scale. When the measured temperature is 65 K, the 2-interlayered sample shows the best $\boldsymbol{J_c}$ value under the applied magnetic field up to 5 T. All the doped samples show higher $\boldsymbol{J_c}$ than the pure one. This demonstrates apparent flux pinning with the nanocomposite interlayers with the $\boldsymbol{J_c}$ value increasing with more interlayers. However, the 4-interlayered shows clear degraded properties compared to the 2-interlayered one, and even worse than the 1-interlayered one at high field, possiblly because the intrinsic YBCO film quality degraded when the 4 interlayers were introduced.

When the temperature was lowered to 40 K, all the interlayered samples show better pinning properties than the reference one, with the 2-interlayered still showing the best performance. Interestingly, the 4-interlayered sample starts to show better properties in the high field, comparable to the 1-interlayered sample. This indicates that the combination of defect and magnetic pinning generated by the $(CoFe_2O_4)_{0.3}(CeO_2)_{0.7}$ nanolayers also effectively minimize the film quality degradation due to magnetic dopants. When the temperature was further reduced to 5 K, the 2-interlayered sample still showed the highest $\boldsymbol{J_c}$ value in all fields with the 4-interlayered sample exceeded the 1-interlayered one. In this low temperature, the flux pinning of this 4-interlayer sample

was more distinguished. However, the intrinsic film quality degradation still played a role in this case as it was still not able to surpass the 2-interlayered sample.

The calculated pinning force ($\boldsymbol{F_p}$) of all the samples measured at 65 K, 40 K and 5 K are plotted in Figure 4.6 to further investigate the flux pinning effect by introducing the nanocomposite interlayers. At 65 K, the 2-interlayered sample shows the highest $\boldsymbol{F_p}$ value, followed by the pure one. The matching field at maximum $\boldsymbol{F_p}$ ($\boldsymbol{B_{matching}}$) of the 1-interlayered sample was higher than the reference film, close to the 2-interlayered one of about 2 T. And the $\boldsymbol{F_p}$ ($\boldsymbol{B_{matching}}$) value of the 4-interlayered sample was lower than 1 T, which means there was a huge film quality degradation in this case. When the temperature was lowered to 40 K and 5 K, the $\boldsymbol{F_p}$ ($\boldsymbol{B_{matching}}$) of all the samples was out-of- range. However, the 1- and 4-interlayered samples showed a higher $\boldsymbol{F_p}$ than the reference, which demonstrates that the flux pinning effect plays a more important role at low temperatures. More interestingly, the 4-interlayered sample started to catch up with the 2-interlayered one in the high field at 5 K, consistent with the above $\boldsymbol{J_c^{in\text{-}field}}$ results.

In short, $(CoFe_2O_4)_{0.3}(CeO_2)_{0.7}$ nanocomposite interlayers can provide effective pinning centers for YBCO superconducting thin films. Both defect and magnetic pinning are expected in this case. However, the number of the interlayers should be controlled due to the lattice mismatch and interdiffusion between the $CoFe_2O_4$ phase and YBCO film, which could cause the intrinsic film quality degradation. Moreover, as previously mentioned, there is 9.05% lattice mismatch between $CoFe_2O_4$ and YBCO, which will also be a factor for the reduced properties. Two interlayers proved to be the best by balancing the flux pinning effect and the film quality degradation.

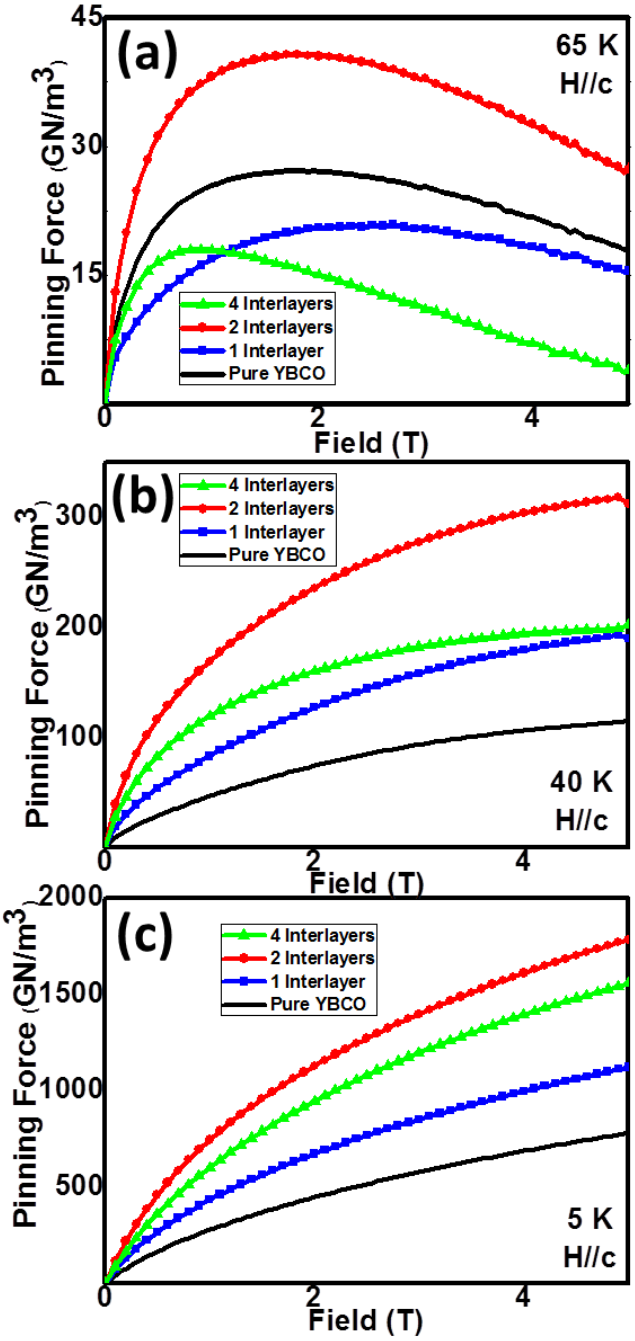

Figure 4.6 Calculated pinning force ***(Fp(H//c))*** plots for all 1-, 2-, 4-multilayered YBCO thin films and the reference sample as a function of applied magnetic field measured at 65 K (a), 40 K (b), and 5 K (c).

4.5 Conclusions

Epitaxial $(CoFe_2O_4)_{0.3}(CeO_2)_{0.7}$ nanocomposites have been introduced into YBCO matrix as 1-, 2- and 4-interlayers for flux pinning enhancement. A strong pinning performance improvement has been observed for the multilayered samples compared to the pure one. The $\boldsymbol{J_c}$ values increase significantly while $\boldsymbol{T_c}$ values are kept the same. The multilayered films showed much pinning enhancement under applied magnetic field. Among all samples, the 2-interlayered sample obtained the best pinning properties, while the 4-interlayered one, with the most amount of defects (caused from the lattice mismatch) and magnetic phase, started to show film quality degradation due to the excess amount of dopants and thus film quality degradation. The study suggests that both defect and magnetic pinning effects can be effectively introduced using this unique $(CoFe_2O_4)_{0.3}(CeO_2)_{0.7}$ nanocomposite system as well as the well-designed pinning landscapes.

CHAPTER V

ENHANCED SUPERCONDUCTING PROPERTIES OF $YBa_2Cu_3O_{7-\delta}$ THIN FILM WITH MAGNETIC NANOLAYER ADDITIONS*

5.1 Overview

Vertically aligned nanocomposite (VAN) **(**$La_{0.7}Sr_{0.3}MnO_3)_{0.5}(CeO_2)_{0.5}$ and pure $La_{0.7}Sr_{0.3}MnO_3$ layers were incorporated into $YBa_2Cu_3O_{7-\delta}$ (YBCO) thin films as bilayer stacks for magnetic flux pinning enhancement. The films show high epitaxial quality, suggested by XRD and TEM study. The critical temperature $\boldsymbol{T_c}$ of the bilayers is about 90 K, which is close to that of pure YBCO films, while both the self-field $\boldsymbol{J_c^{sf}}$ and in-field critical current density $\boldsymbol{J_c^{in\text{-}field}}$ are largely enhanced. Among all samples, the film with VAN cap layer shows the highest $\boldsymbol{J_c}$ values in all field ranges. This study demonstrates an effective way towards the tunable pinning effect for YBCO coated conductors by both defect and magnetic pinning.

5.2 Introduction

Tremendous research efforts have been focused on the development of high temperature superconducting (HTS) coated conductors based on$YBa_2Cu_3O_{7-\delta}$ (YBCO) since it was discovered in 1987. [10, 21, 75, 83, 217] Significant progress has been made first to address the needs on the epitaxial growth of the YBCO coated conductors on flexible metal substrates, and later to address critical issues that limit the performance of

*Reprinted with permission from "Enhanced superconducting properties of $YBa_2Cu_3O_{7-\delta}$ thin film with magnetic nanolayer additions" by Jijie Huang, Meng Fan, Han Wang, Li Chen, Chen-Fong Tsai, Leigang Li, and Haiyan Wang, *Ceramics International*, **42**, 12202, 2016.

YBCO-based coated conductors. To enable the epitaxial growth of YBCO thin films on metal substrate, certain templates are required. The two primary approaches are (1) to involve a textured metal substrate to start with, i.e., rolling-assisted biaxially textured substrates (RABiTS) [21] and (2) to build an epitaxial template on amorphous buffered metal substrates called ion-beam-assisted deposition (IBAD) substrates. [25-27] Moreover, several film growth techniques have been successfully tailored for the deposition of YBCO thin films with high epitaxial quality on these metal substrates, such as metal-organic chemical vapor deposition (MOCVD), [39, 218] pulsed laser deposition (PLD), [113, 219, 220] metal-organic deposition (MOD) [71, 72] as well as magnetron sputtering. [57, 221] With over a decade of development, superconducting properties of YBCO coated conductors have been significantly improved and practical applications have been demonstrated in multiple areas such as HTS coated conductors, superconductor magnets, generators and fault current limiters. [25, 75, 222, 223] However, for most of the above technological applications, high critical current densities ($\boldsymbol{J_c}$) under applied magnetic field, so called in-field performance, is required.

Various flux pinning approaches have been introduced in YBCO HTS coated conductors to better pin flux lines and thus achieve superior $\boldsymbol{J_c}$ performance, in both self-field and in-field. Overall there are two categories, i.e., non-magnetic defect pinning and magnetic pinning. For non-magnetic defect pinning, most of the work has focused on the defect landscape design with various dimensional nanoinclusions, including nanoparticles, [81, 224] nanocolumns, [104, 106] as well as nanolayers. [122] Furthermore, some unique architectures were also designed, for example, Baca et al.

combined Y_2O_3 nanoparticles and $BaZrO_3$ nanorods for overall pinning enhancement. [225] Magnetic pinning is another effective approach, because of the interaction between the magnetic inclusions and the fluxons. [114, 142, 208, 209] Bulaevskiia *et al.* demonstrated that the high value of magnetic pinning potential $\boldsymbol{U_{mp}}$ ($\boldsymbol{U_{mp} \sim \Phi_0 M(x) d_s}$, where $\boldsymbol{M(x)}$ is the magnetization of the magnetic inclusion and $\boldsymbol{d_s}$ the thickness of the YBCO film) can overcome the thermal activated flux flow at high temperatures. [130] Various effective magnetic pinning centers have been demonstrated, including $CoFe_2O_4$ nanoparticle, [126] CoPt layer, [135] as well as $Pr_{0.67}Sr_{0.33}MnO_3$ (PSMO) layer. [141]

In this study, a unique design of vertically aligned nanocomposite (VAN) layer embedding magnetic nanopillars was introduced into YBCO thin films as either cap layer or buffer layer for flux pinning enhancement. For demonstration, a VAN composite of CeO_2 and $La_{0.7}Sr_{0.3}MnO_3$ (LSMO) is selected. The selection of LSMO:CeO_2 VAN as magnetic dopants is based on the excellent magnetic property of the LSMO phase [132, 226] and that the in-plane lattice parameter of both LSMO (3.87Å) and CeO_2 (5.411Å with 45° rotation) is close to orthorhombic YBCO (a=3.82Å, b=3.89Å). Thus, both defect pinning and magnetic pinning effects are expected in this VAN nanolayer doped system. A pure LSMO layer buffered YBCO sample was also introduced for comparison.

5.3 Experimental

$(LSMO)_{0.5}(CeO_2)_{0.5}$ (L5C5)/YBCO and LSMO/YBCO bilayers were deposited by a PLD system with a KrF excimer laser (Lambda Physik 201, λ=248 nm, 300 mJ) on

single crystal STO (001) substrates. The thickness of VAN nanolayer and YBCO matrix were controlled at about 20 nm (2 Hz, 2 min) and 350 nm (10 Hz, 6 min), respectively. The architecture of the bilayers thin films were prepared by alternative laser ablation of the nanocomposite and YBCO targets. The films were deposited with 300 mTorr oxygen in-flow at 780 °C, and followed by a post-annealing process under 300 Torr oxygen at 550 °C for 30 min.

The microstructure of the films was characterized by X-ray diffraction (XRD) (PANalytical X'Pert X-ray diffractometer) and transmission electron microscopy (TEM) (FEI Tecnai G2 F20). The magnetization, critical transition temperature ($\boldsymbol{T_c}$), and critical current density (both $\boldsymbol{J_c^{sf}}$ and $\boldsymbol{J_c^{in\text{-}field}}$) were measured by a physical property measurement system (PPMS). $\boldsymbol{J_c^{in\text{-}field}}$ ($\boldsymbol{H//c}$) were measured under an applied field of 0 to 5 T at 77 K, 65 K, 40 K, and 5 K by the vibrating sample magnetometer (VSM) in PPMS.

5.4 Results and discussion

Prior to incorporating L5C5 VAN and LSMO layers into YBCO, single layers of L5C5 and LSMO were grown on STO substrates for magnetic property measurements. Figure 5.1 (a) and (b) show the M-H curves for the L5C5 and LSMO thin films, respectively, at different temperatures ranging from 20 K to 200 K. It is obvious that the hysteresis loops in both cases remain the same shape at different temperatures, which indicates their magnetic property remains at the superconductor working temperature range. In addition, it is clear that LSMO shows a higher magnetization and saturation

remanence $\boldsymbol{M_{rs}}$ than L5C5 VAN, partly because of the non-magnetic CeO_2 in the L5C5 nanocomposites. By comparing $\boldsymbol{M_{rs}}$ of the two samples, $\boldsymbol{M_{rs}}$ (L5C5) ≈450 emu/cm^3 (here the magnetization of a single LSMO nanocolumn can be estimated to be 2.25×10^{-16} emu based on the volume of one single column as 5×5×20 nm^3), which is lower than half of $\boldsymbol{M_{rs}}$ (LSMO) ≈2000 emu/cm^3. One possible reason is that the incorporation of a second phase (CeO_2) into LSMO may cause the suppression of the double exchange interaction between the neighboring LSMO domains, which could deteriorate the magnetic property of LSMO. [226] Other factors to be considered include the film thickness variations and samples size for VSM measurements among samples. Moreover, interestingly, the L5C5 VAN exhibits higher coercive field $\boldsymbol{h_c}$ than the pure LSMO sample, because of the thin disordered regions at the LSMO|CeO_2 interface areas. [226] This disordered 2-phase boundary may lead to increased pinning effect, [227] as well as larger lattice strain in the films. [228] Overall, both L5C5 VAN and pure LSMO thin films present strong

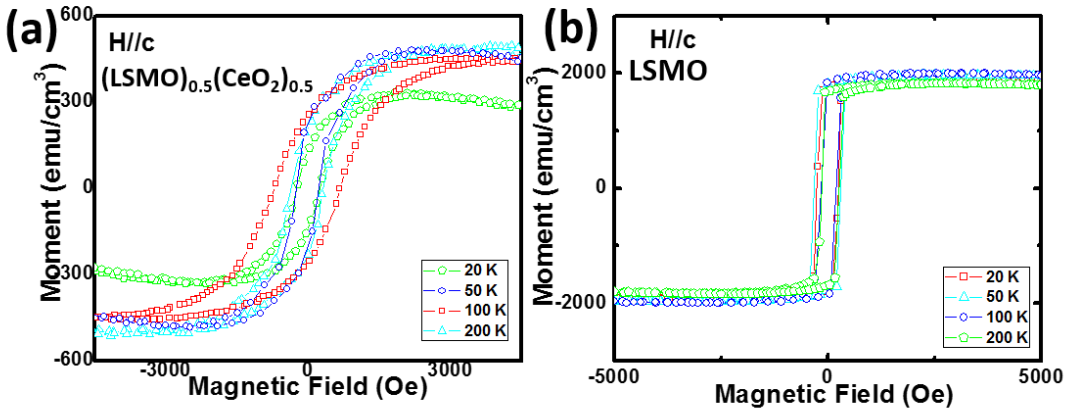

Figure 5.1 M-H curves for (a) $(LSMO)_{0.5}$:$(CeO_2)_{0.5}$ VAN and (b) LSMO at 20 K, 50 K, 100 K and 200 K under magnetic field in the c direction.

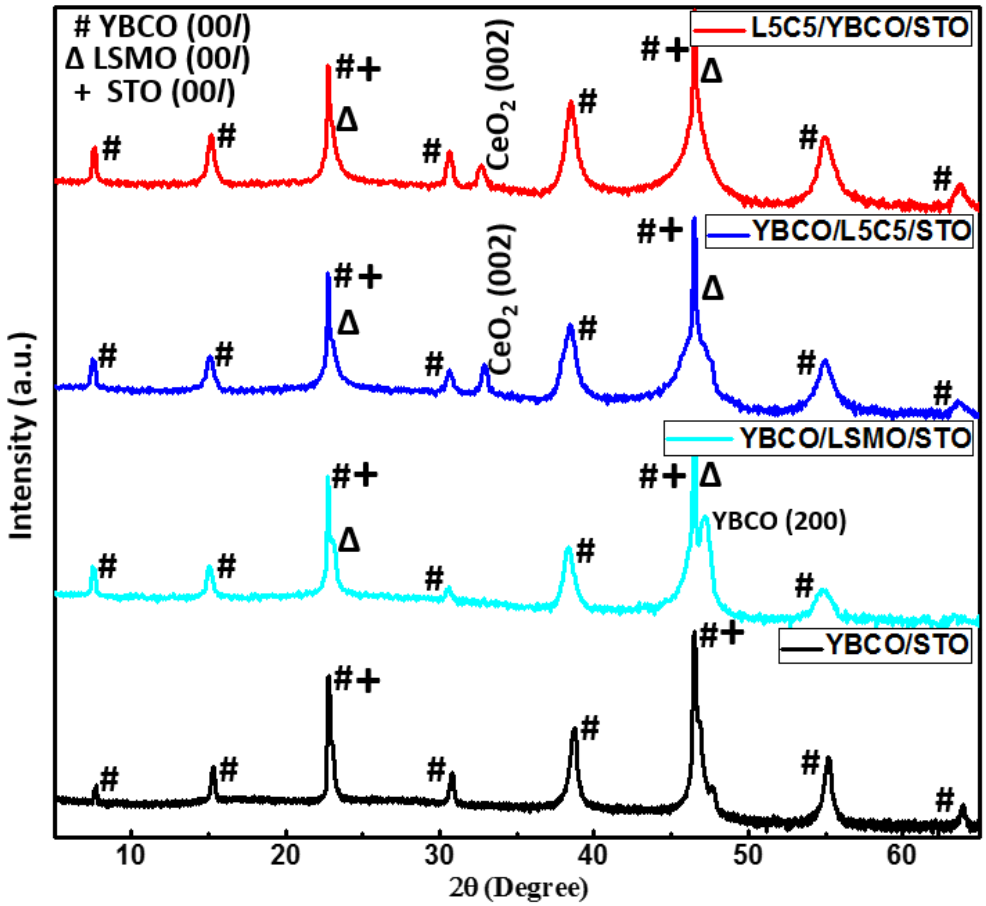

Figure 5.2 θ-2θ XRD patterns of all the bilayer samples compared with the pure YBCO film.

magnetization response under applied magnetic field perpendicular to the sample surface.

L5C5 VAN was then incorporated into YBCO as either cap layer or buffer layer. As a comparison, a YBCO/LSMO bilayer stack was deposited to explore the pinning properties of a pure ferromagnetic LSMO layer. Figure 5.2 shows the standard θ-2θ XRD scans of all the samples, symbols #, Δ and + represent YBCO (00*l*), LSMO (00*l*) and STO (00*l*) peaks, respectively. Apparently, for the L5C5/YBCO/STO and

YBCO/L5C5/STO, YBCO (003) and (006) peaks are perfectly overlapped with STO (001)/LSMO (001) and STO (002)/LSMO (002) peaks, which demonstrates the highly textured growth of the YBCO film, as well as the L5C5 layer. However, for the YBCO/LSMO sample, YBCO (200) peak can be identified, which will be further discussed correlating with the TEM study below. Furthermore, CeO_2 (002) peak can be clearly identified from the L5C5 layer and no other impurity peak was identified. Again this confirms the excellent film quality of both the L5C5 and YBCO layers.

The film quality and microstructural characteristics were explored further using TEM for the L5C5/YBCO/STO and YBCO/LSMO/STO samples. Figure 5.3(a) presents the schematic drawing of the designed L5C5/YBCO bilayer film. Figure 5.3(b) shows the low-magnification cross-sectional TEM (XTEM) micrograph, the different layers can be easily identified as labeled. The thickness of the YBCO layer and L5C5 layer can be estimated to be 350 nm and 20 nm, respectively. Figure 5.3(c) shows the corresponding selected area electron diffraction (SAED) pattern. The distinguished diffraction dots further confirm the high quality epitaxial growth of both YBCO and L5C5 VAN layers. Interestingly, the phase of CeO_2 presents double-epitaxial orientations, as two orthogonal diffraction patterns (red and blue) indicating the two orientation relations for CeO_2. The high resolution TEM image of the enlarged area can be seen in Figure 5.3(d). The two layers can be easily identified with a very sharp interface, which suggests very little or no inter-diffusion between the two layers. For the YBCO layer, the film grows well along c-axis direction. For the L5C5 VAN layer, the two phases of LSMO and CeO_2 grow alternatively on the YBCO layer, with excellent

epitaxial quality. This L5C5 self-assembled VAN structure is of similar quality to the previous reported L5C5 VAN directly on STO substrate. [226]

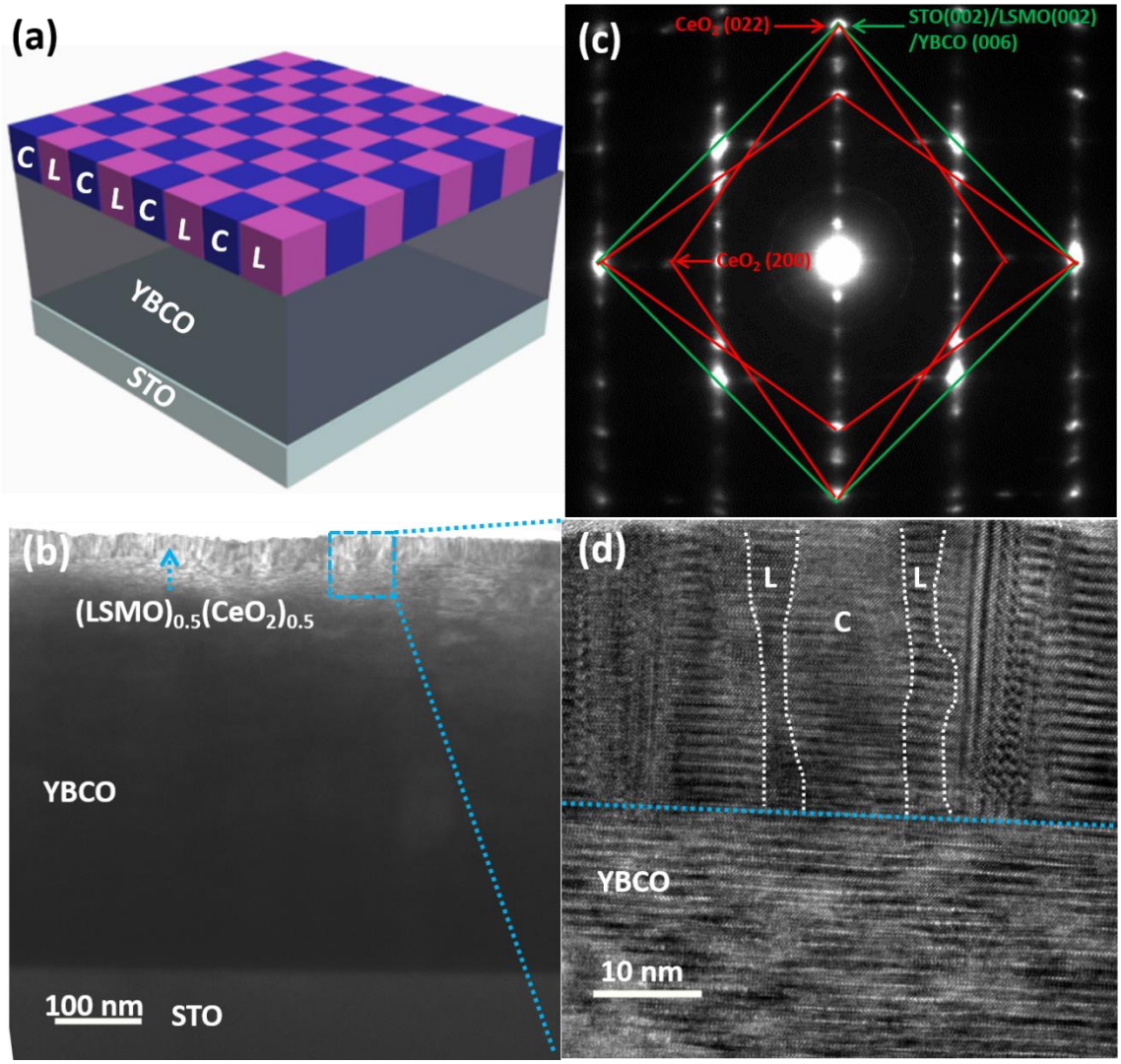

Figure 5.3 Schematic and microstructure images of $(LSMO)_{0.5}(CeO_2)_{0.5}$ capped YBCO thin film, (a) schematic illustration, (b) low-magnification TEM image, (c) the selected area electron diffraction (SAED) pattern, (d) high resolution TEM micrograph in the interface area.

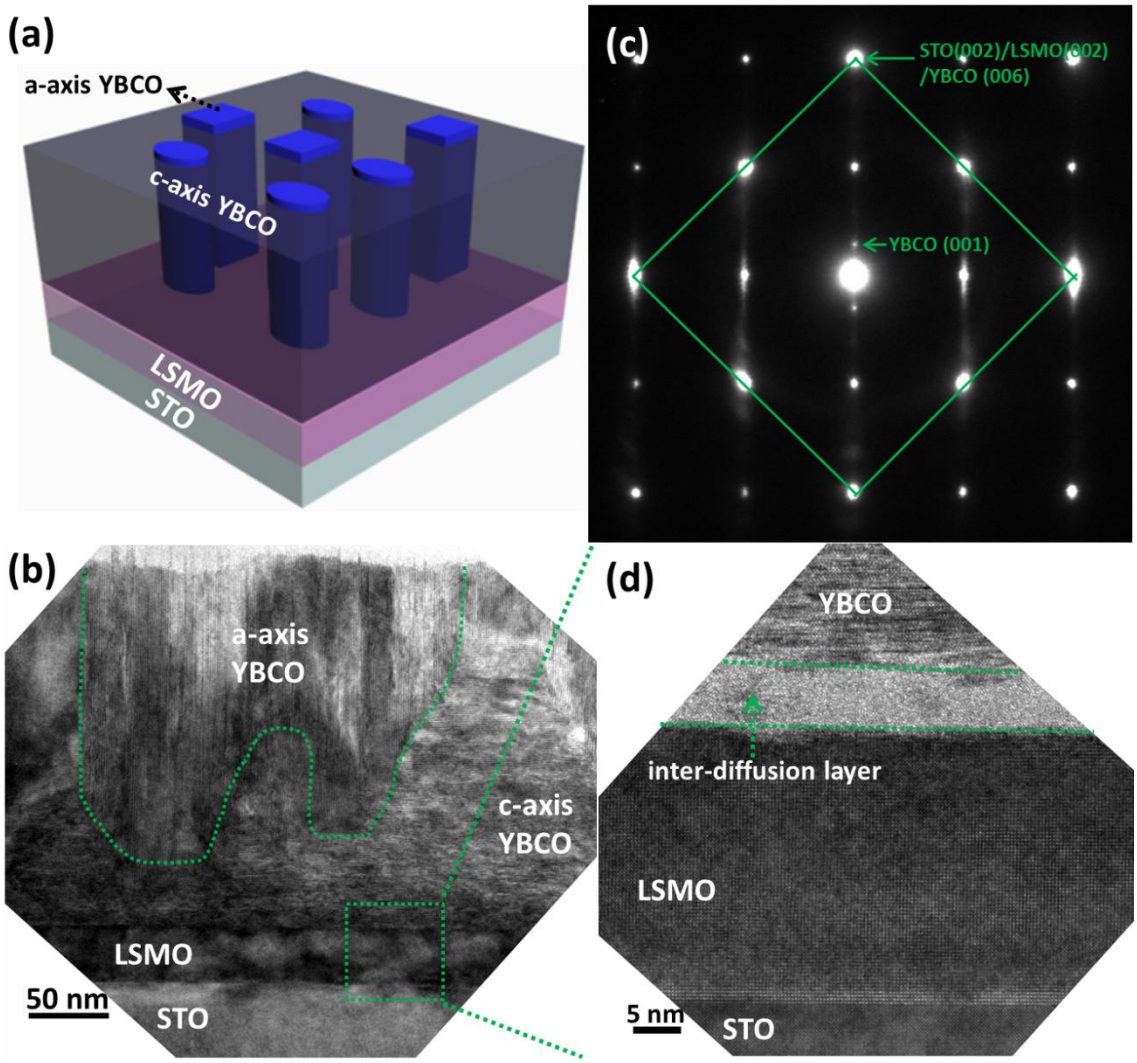

Figure 5.4 Schematic and microstructure images of LSMO buffered YBCO thin film, (a) schematic illustration, (b) low-magnification TEM image, (c) the selected area electron diffraction (SAED) pattern, (d) high resolution TEM micrograph of the selected area.

The microstructure of YBCO/LSMO bilayer has also been explored and its schematic illustration is shown in Figure 5.4(a). However, both a-axis YBCO and c-axis YBCO can be clearly observed in the low mag XTEM image in Figure 5.4(b). From the corresponding SAED pattern in Figure 5.4(b), the orientation relations between the two

layers and substrate can be determined to be YBCO (006) || LSMO (002) || STO (002). The a-axis growth of YBCO is known to be harmful for the overall $\boldsymbol{J_c}$ property of YBCO film, due to the less efficient electrical current transportation and less connectivity of the film. [205] Furthermore, from the high resolution TEM image in Figure 5.4(d), the LSMO layer grow perfectly with high film quality on STO substrate with the YBCO layer on top. However, it is obvious that there is a thin interfacial reaction layer of around 5 nm between LSMO layer and YBCO layer, which can be accounted for the possible inter-diffusion between the two layers. Such interfacial diffusion layer has been reported previously in a LSMO buffered YBCO thin film. [229]

To explore the defect pinning mechanism, detailed high resolution TEM study of the pure YBCO, LSMO buffered YBCO and L5C5 capped YBCO, as well as their corresponding fast Fourier transform (FFT) filtered processing, were carried out. Figure 5.5(a) and (b) show the HRTEM image near the interface area of the pure YBCO sample and its corresponding FFT image, respectively. The dislocations and stacking faults (extra half planes) are represented by "⊥" and "→", respectively. Obvious dislocations and stacking faults can be identified in the image, and most of them are near the interface area. Figure 5.5(c) and (d) show the HRTEM image near the LSMO/YBCO interface area of LSMO buffered sample and the corresponding FFT image. It is obvious that there are more defects compared to the pure YBCO sample, especially close to the interfacial layer area. In addition, there are a lot of defects appear at the L5C5/YBCO interface, as shown in Figure 5.5(e) and (f). These defects could provide strong defect pinning which is discussed in a later section. Furthermore, the defect density reduces in

the area away from the interface, which ensures the high film quality of the main YBCO matrix. Overall, the incorporation of the extra nanolayer produces additional defects in the interface area which could lead to enhanced defect pinning.

Furthermore, the superconducting properties of all the samples were measured and compared with the single layer YBCO film. The $\boldsymbol{T_c}$ and self-field $\boldsymbol{J_c}$ (77 K, 65 K, 40 K and 5 K) values are summarized in Table 5.1. Obviously, the $\boldsymbol{T_c}$ values almost remain the same after introducing the dopant layer, which indicates little or no film quality degradation. Additionally, the $\boldsymbol{J_c^{sf}}$ results show that all the bilayer samples obtain higher values than that of the single YBCO layer at all the measured temperatures, with the best in L5C5/YBCO/STO and followed by YBCO/L5C5/STO. The sample L5C5/YBCO/STO exhibits $\boldsymbol{J_c^{sf}}$ values of 5.5, 18.3, 51.9 and 121.1 MA/cm^2 at 77 K, 65 K, 40 K and 5 K, respectively. YBCO/LSMO presents lower values than the above two cases, probably caused by the inter-diffusion layer shown in the TEM results in Figure 5.4(d), as well as the presence of a-axis YBCO grains (Figure 5.4(b)). Because the inter-diffusion is minimal (the inter-diffusion layer of 5 nm), it did not impact on the main bulk region of the YBCO matrix and thus the film still maintains a higher $\boldsymbol{J_c}$ value than that of the pure YBCO film. In addition, more dislocations in YBCO close to the interface area have been observed for the LSMO buffered case and could contribute to the enhanced $\boldsymbol{J_c}$ performance compared to pure YBCO film. Foltyn *et al.* previously reviewed that a number of defect types can act as pinning centers for superconducting property enhancement. [75] Other prior report also showed similar $\boldsymbol{J_c}$ trend for pure YBCO and LSMO buffered YBCO. [132] In addition, the sample size variation as well

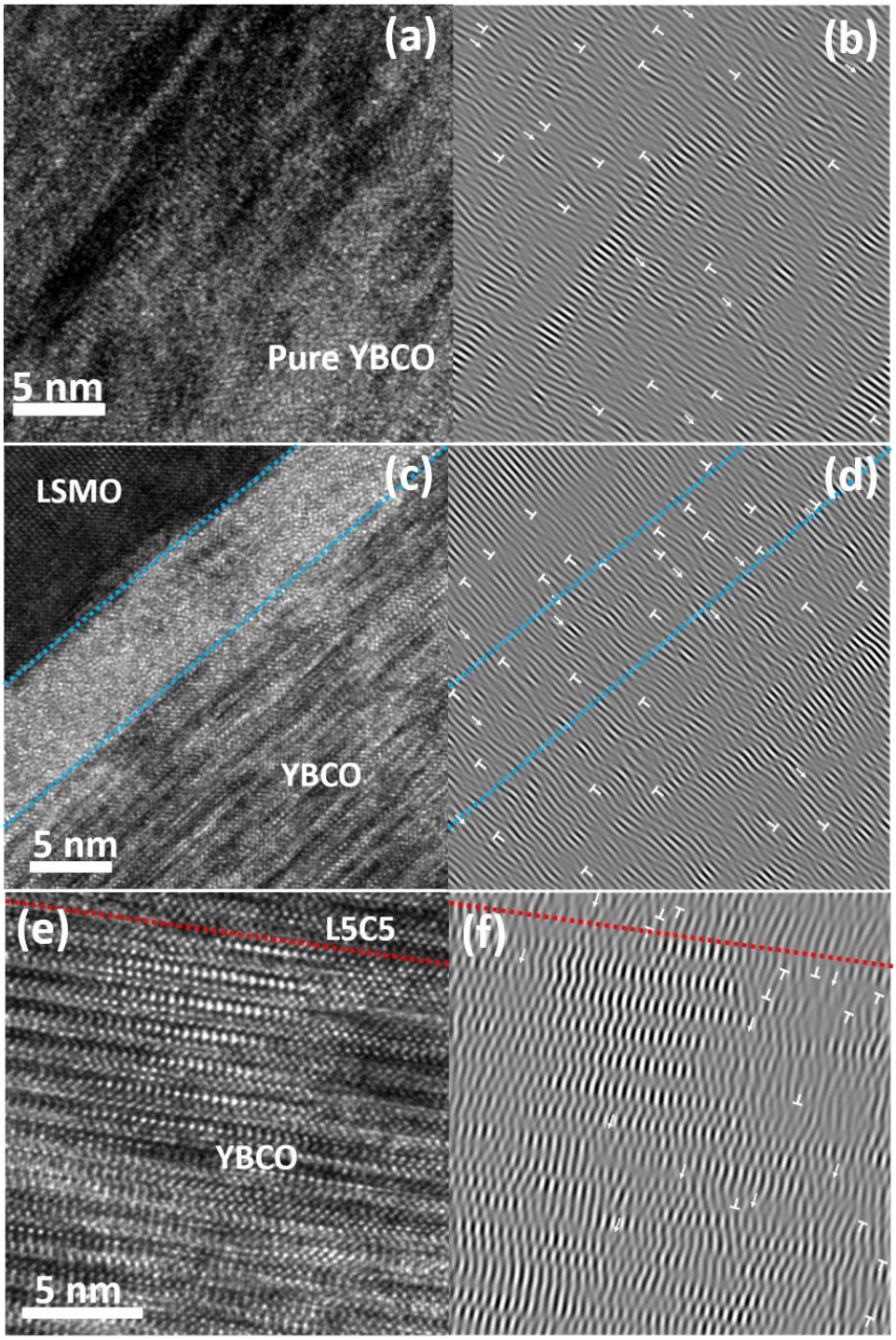

Figure 5.5 Cross-sectional HRTEM image of (a) pure YBCO on STO, (c) LSMO buffered YBCO, (e) L5C5 capped YBCO, and their corresponding representative FFT filtered images (b), (d), (f).

as sample film thickness variation could also cause some minor errors in the final J_c values measured by the VSM. Overall all the doped samples, especially the L5C5 VAN doped cases, have shown enhanced J_c performance compared to pure YBCO. Other nanocomposite systems have also been introduced for pinning enhancement by both defect and magnetic pinning in previous studies. [113, 142] The T_c and J_c^{sf} values of all the samples in this study were summarized and compared with some prior results in Table 5.1. It is obvious that L5C5/YBCO exhibits the highest J_c^{sf} values at all the measured temperatures, followed by $(CoFe_2O_4)_{0.5}(CeO_2)_{0.5}$/YBCO with slightly lower values. Overall, the LSMO:CeO_2 and $CoFe_2O_4$:CeO_2 nanocomposite systems show better performance than Fe_2O_3:CeO_2 system for YBCO pinning enhancement. This is probably because much less inter-diffusion as well as stronger magnetic properties in the cases of the LSMO:CeO_2 and $CoFe_2O_4$:CeO_2 nanocomposite systems compared to the Fe_2O_3:CeO_2 system.

Table 5.1 Comparison of T_c and self-field J_c of all the samples with or without nanolayer.

Property / Sample	T_c (K)	Self-field J_c^{sf} (MA/cm^2)			
		77 K	65 K	40 K	5 K
L5C5/YBCO	90.3	5.5	18.3	51.9	121.1
YBCO/L5C5	90.1	4.9	12.5	33.1	70.7
YBCO/LSMO	89.9	1.7	8.5	26.9	73.9
$(Fe_2O_3)_{0.5}(CeO_2)_{0.5}$/YBCO [11]	90.1	NA	5.4	23.9	81.3
YBCO/$(Fe_2O_3)_{0.5}(CeO_2)_{0.5}$ [11]	89.8	NA	3.5	15.3	52.0
$(CoFe_2O_4)_{0.5}(CeO_2)_{0.5}$/YBCO [26]	90.0	5.2 at 75 K	17.1	48.3	132
YBCO/$(CoFe_2O_4)_{0.5}(CeO_2)_{0.5}$ [26]	89.9	3.1 at 75 K	7.4	25.4	43.3
Pure YBCO	90.4	1.3	3.8	13.2	42.4

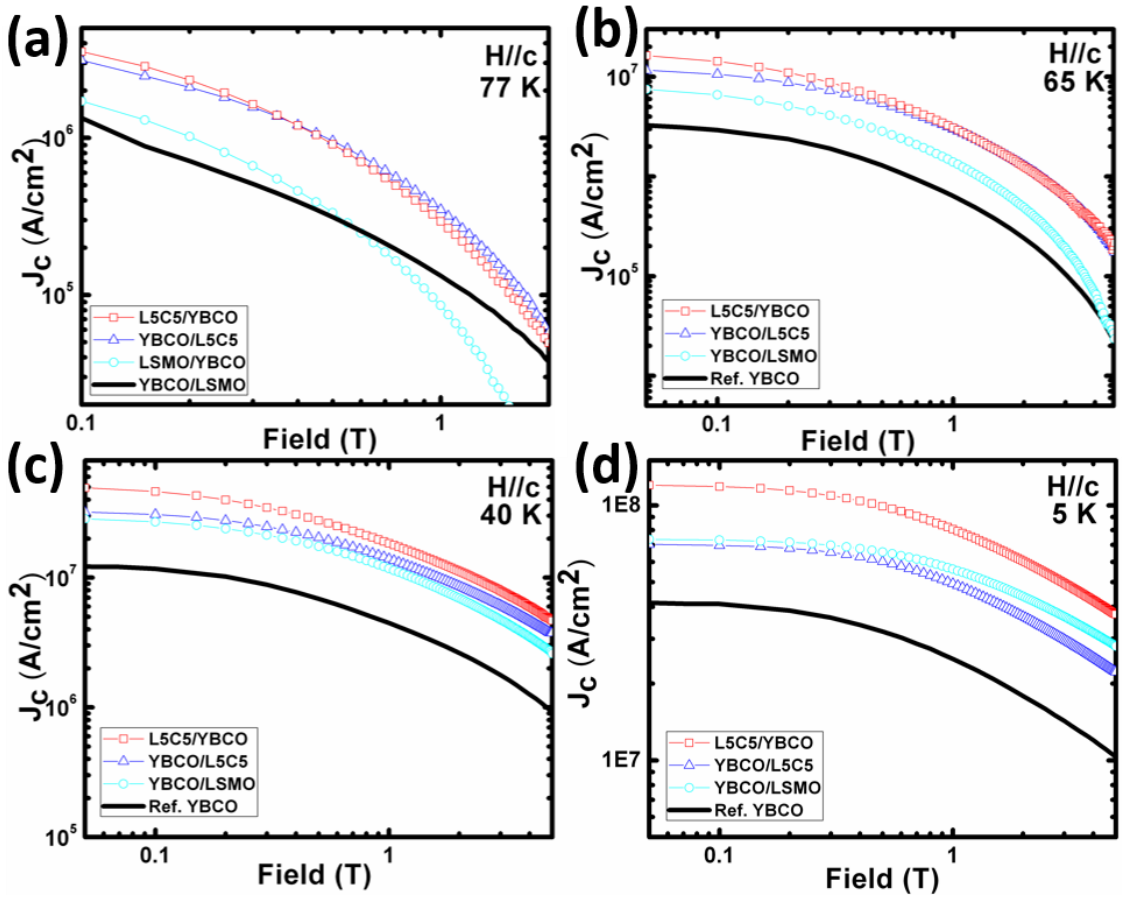

Figure 5.6 In-field J_c (***H//c***) comparison of all the samples in a log-log scale at measured temperature of (a) 77 K, (b) 65 K, (c) 40 K and (d) 5 K.

The in-field (0-5 T, ***H//c***) J_c values were compared in Figure 5.6 at (a) 77 K, (b) 65 K, (c) 40 K and (d) 5 K to investigate the pinning properties in these bilayers. Here, the J_c values were derived by the Bean model: $Jc = 20\Delta M/a(1 - \frac{a}{3b})$, where ΔM is the opening in the hysteresis loop; a and b are the sample dimensions. [184] When the measured temperature is at 77 K, the samples with either L5C5 cap or buffer obtain the highest J_c values under all the measured magnetic fields. And the LSMO buffered sample exhibits higher J_c than the referenced YBCO at low magnetic field, however, J_c

performance depresses faster at higher fields, probably due to the inter-diffusion between LSMO and YBCO. At 65 K, L5C5/YBCO/STO shows the highest $\boldsymbol{J_c^{in\text{-}field}}$ values, especially at low fields, while the YBCO/L5C5/STO catches up at higher fields. The value of YBCO/LSMO/STO is in between the above two and the reference YBCO film. The inter-diffusion as well as the a-axis YBCO growth could hinder its further improvement in pinning properties in this case. It is worth noting that the incorporated CeO_2 confines the inter-diffusion and thus the L5C5 buffered YBCO obtains much higher $\boldsymbol{J_c^{in\text{-}field}}$ values. At 40 K, the plot shows a similar trend as that of 65 K, however, the LSMO buffered sample starts to approach the other two. When the measurement temperature further decreased to 5 K, L5C5/YBCO/STO still shows as the highest in all the applied field regimes. However, interestingly, the performance of LSMO buffered sample exceeds the L5C5 buffered one. One possible reason is that, at this low temperature regime, the magnetic pinning from LSMO is more evident comparing to the superconducting property degradation from the inter-diffusion issue and a-axis YBCO growth, which is consistent with previous report. [122] Overall, all the bilayer samples show pinning enhancement under magnetic field at different measurement temperatures, both defect and magnetic pinning could account for the overall enhanced pinning properties.

To further explore the flux pinning effect from the introduced L5C5 and LSMO, the calculated in-field pinning force $\boldsymbol{F_p}$ values of all the samples were plotted and compared in Figure 5.7(a) 77 K, (b) 65 K, (c) 40 K and (d) 5 K. At high temperature of 77 K, the L5C5 capped and buffered show similar $\boldsymbol{F_p}$ values to each other and higher

values than other samples. At 65 K, both L5C5 capped and buffered YBCO shows the highest F_p values along the applied field, with highest pinning force under the applied field (B_{max}) of ~1 T. At a lower temperature of 40 K, L5C5 buffered starts to show lower F_p value than the capped one, which is possibly due to the minor inter-diffusion and film quality degradation. B_{max} of all the samples are out-of-range at this temperature. Interestingly, the F_p of the LSMO buffered sample surpassed L5C5 buffered YBCO film, which is consistent with the above $J_c^{in\text{-}field}$ results. Here, the defect pinning is caused by the increased density of defects in the interface area, as discussed above based on the TEM results and the corresponding FFT analysis. For the magnetic pinning, it is worth to further discuss the pinning potential of the LSMO magnetic domains in this case. The magnetic pinning in this case can be considered as a "periodic ferromagnetic nanodot array" model, [230] or "ferromagnetic/superconducting multilayer" model. [135] Here, the later model is selected for the discussion as the L5C5 layer can be treated as a ferromagnetic layer, similar to the role of the CoPt layer introduced by Jan *et al* [32]. Thus, the pinning potential for a single vortex line created by the magnetic domain can be estimated to be $U_{mp} \sim \Phi_0 M d_s$, here Φ_0 is the flux quantum, M is the magnetization of the magnetic domain, and d_s is the thickness of the superconductor layer. [130, 135] And the pinning force provided by the magnetic domain is $f_m \sim U_{mp}/\lambda$, where λ is the penetration depth. Hence, the magnetic potential and magnetic pinning force in different temperatures under different applied fields can be estimated, on the basis of the measured magnetization of the LSMO magnetic domain in Figure 5.1.

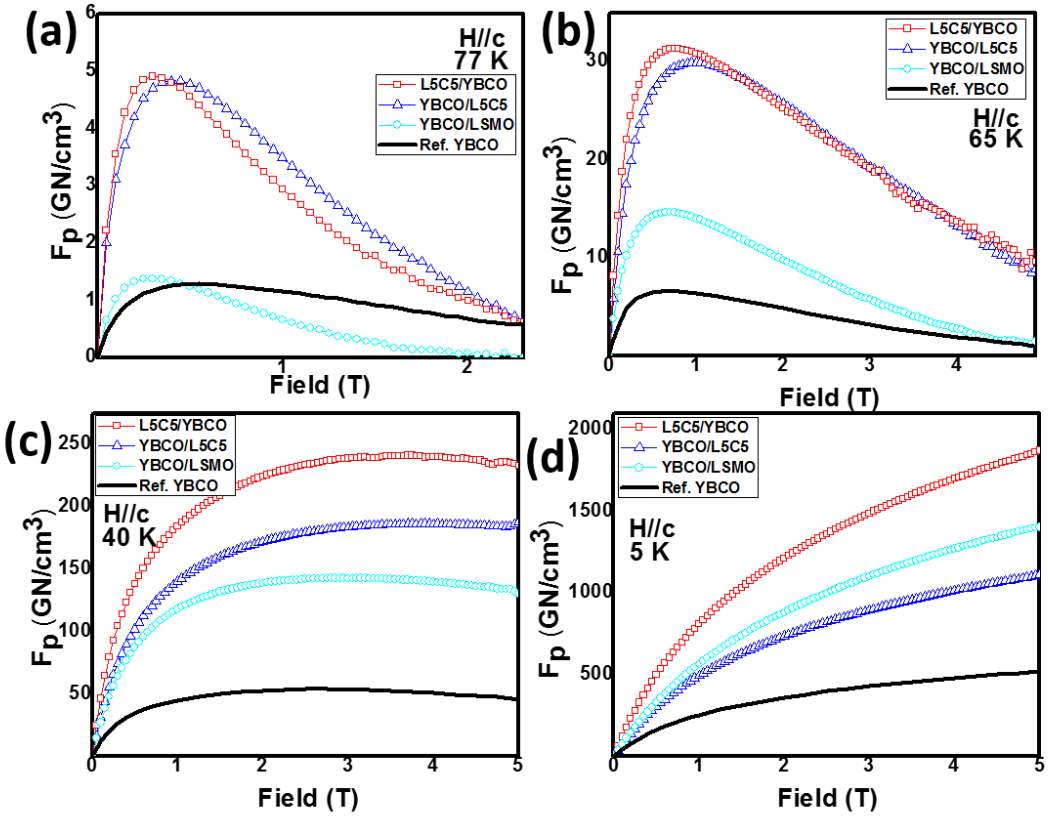

Figure 5.7 Calculated pinning force $\boldsymbol{F_p}$ (***H//c***) plots as a function of applied field (0-5 T) of all the samples measured at (a) 77 K, (b) 65 K, (c) 40 K and (d) 5 K.

Based on the above results, $(LSMO)_{0.5}(CeO_2)_{0.5}$ VAN and LSMO nanolayer can provide effective flux pinning centers for YBCO thin films. Both defect and magnetic pinning effects played a role in the pinning enhancement for all the doped samples. The pinning mechanisms at different measured temperatures are quite different. In this study, magnetic pinning is more obvious at lower temperatures, which is consistent with the previously reported $(Fe_2O_3)_{0.5}(CeO_2)_{0.5}$ [122] system but the trend is opposite to several other systems. [130, 141] To fully understand the flux pinning mechanisms in different cases, future study is needed to focus on the relationship between the pinning energy and

thermal induced flux flow. Moreover, the composition variation study is also important for determining the best composition ratio of LSMO and CeO_2, to achieve the optimum pinning effect for YBCO thin films.

5.5 Conclusions

In summary, $(LSMO)_{0.5}(CeO_2)_{0.5}$ VAN structure and pure LSMO nanolayers were introduced into YBCO thin films, with excellent epitaxial quality. $\boldsymbol{J_c^{sf}}$ and $\boldsymbol{J_c^{in\text{-}field}}$ of the bilayer samples were largely enhanced compared to the pure YBCO film, which illustrates that effective pinning centers are introduced. In this study, L5C5 capped YBCO film shows the best in-field performance than the other cases, because of the minimized inter-diffusion between YBCO and the dopants, as well as limited a-axis YBCO outgrowth compared to the pure LSMO nanolayer doped case. This work demonstrates that the VAN structure is a very flexible and tunable approach for the pinning enhancement for YBCO coated conductors by combining magnetic and defect pinning effects.

CHAPTER VI

NANOSTRUCTURED PINNING CENTERS IN $FeSe_{0.1}Te_{0.9}$ THIN FILMS FOR ENHANCED SUPERCONDUCTING PROPERTIES*

6.1 Overview

$FeSe_{0.1}Te_{0.9}$ thin films were deposited on single crystal $SrTiO_3$ (STO) (100) substrates by a pulse laser deposition (PLD) technique. CeO_2 nanolayer was introduced as either cap layer or buffer layer to investigate its pinning effects in $FeSe_{0.1}Te_{0.9}$ thin films. The results show improved film quality after doping with CeO_2 nanolayers, and no impurity phase was identified. All the samples achieve $\boldsymbol{T_c}$ of 12.5 K, and in-field $\boldsymbol{J_c}$ was greatly enhanced after doping with either cap or buffer CeO_2 nanolayer for the field range up to 7 T. The buffered one shows the best self-field $\boldsymbol{J_c}$ of 0.89 $MAcm^{-2}$ at 4 K and a high upper critical field $\boldsymbol{H_{c2}}$ of 186 T.

6.2 Introduction

Iron-based superconductors have attracted great research interest since the discovery of $LaFeAsO_{1-x}F_x$. [144] Their high upper critical field $\boldsymbol{H_{c2}(0)}$ as well as low anisotropies make this type of superconductor unique for high-field applications, [77, 169, 175, 177, 231-233] even though with low critical transition temperatures (up to 55 K) compared to the cuprates. These superior properties may lead to high-field applications of these iron-based superconductors under liquid helium temperature.

*Reprinted with permission from "Nanostructured pinning centers in $FeSe_{0.1}Te_{0.9}$ thin films for enhanced superconducting properties" by Jijie Huang, Li Chen, Jie Jian, Fauzia Khatkhatay, and Haiyan Wang, *Supercond. Sci. Technol.*, **27**, 105006, 2014. Copyright IOP Publishing

The “11” type iron-based superconductor is one of the most popular research priorities among these, due to its tetragonal PbO structure with only a simple binary composition. [149] A large amount of work has been conducted to further improve its superconducting properties. For example, doping using Chalcogens, [167, 169, 234] alkali metals [163, 235-237] and transition metals, [236] has been achieved for superconducting properties enhancement. Moreover, high external pressure has been demonstrated to effectively enhance their superconducting properties. [163, 237-239] Recently, amorphous substrates such as glass have been used to grow superconducting $FeSe_{0.5}Te_{0.5}$ thin films. [240] However, further work is still needed to improve its superconducting properties, such as the critical current density ($\boldsymbol{J_c}$), for future high field applications. With the advantage of the high $\boldsymbol{H_{c2}}$ value of iron chalcogenide, it is highly possible to enhance its in-field $\boldsymbol{J_c}$ ($\boldsymbol{J_c^{in\text{-}field}}$) values under a high field with proper flux pinning designs. Several previous attempts were demonstrated by different groups, such as introducing nanolayers, [175, 176] as well as irradiation treatment. [241]

Among all the flux pinning enhancement methods in $YBa_2Cu_3O_{7-x}$ (YBCO)-based coated conductors, nanostructured secondary phase doping has been considered as one of the most effective approaches. CeO_2, a possible candidate for secondary phase flux pinning, has been previously applied in YBCO as effective defect pinning centers with little to no poisoning effect because of the excellent lattice matching and chemical compatibilities. [122, 242] The in-plane lattice matching between $FeSe_xTe_{1-x}$ and CeO_2 is also perfect, and CeO_2 doped $FeSe_{0.5}Te_{0.5}$ as interlayer [176] or buffer layer [175] has shown enhanced $\boldsymbol{J_c}$. However, the exact flux pinning mechanism is still unclear.

Recently, an ultrahigh $\boldsymbol{H_{c2}}$ value of 114 T in $FeSe_{0.1}Te_{0.9}$ has been demonstrated along with superior superconducting properties among all different compositions of $FeSe_xTe_{1-x}$. [169] To enable potential applications of the $FeSe_{0.1}Te_{0.9}$ films in high fields, further work to enhance their in-field performance is needed. In this work, we introduce CeO_2 nanolayer into $FeSe_{0.1}Te_{0.9}$ (FST) thin films as either cap layer or buffer layer to explore the pinning effects of the nanolayers with the ultimate goal of achieving high $\boldsymbol{J_c}$ in high field range.

6.3 Experimental

Pure FST thin films, as well as the CeO_2 cap and buffer layered samples were deposited by a PLD system with a KrF excimer laser (Lambda Physik Compex Pro 205, λ=248 nm, 5 Hz) on single crystal STO (001) substrates. The laser energy density was 3 J/cm^2. The deposition temperature was kept at 400 °C, and the target-substrate distance was 4.5 cm for all the depositions. The base pressure for all the depositions reached less than 1×10^{-6} Torr in vacuum. The multilayers thin films were prepared by alternative laser ablation of the CeO_2 and FST targets. The total deposition pulses for the CeO_2 nanolayer and FST layer are 100 pulses and 6000 pulses, respectively. The microstructure of the films was characterized by X-ray diffraction (XRD) (Panalytical X'Pert X-ray diffractometer) and transmission electron microscopy (TEM) (FEI Tecnai G2 F20). The superconducting properties were characterized using resistivity-temperature (R-T) measurement by a four point probe method from 2 to 300 K in a physical properties measurement system (PPMS: Quantum Design). Both the self-field

and in-field critical current densities ($\boldsymbol{J_c^{sf}}$ and $\boldsymbol{J_c^{in\text{-}field}}$: ***H//c***) were measured under an applied magnetic field of 0-7 T at various temperatures (8, 4 and 2 K) by the vibrating sample magnetometer (VSM) in the PPMS. The samples were cut into ~2mm X 2mm in square for VSM measurements.

6.4 Results and discussion

The standard θ-2θ scans for the single FST thin film, as well as CeO_2 capped and buffered bilayer thin films, are shown in Figure 6.1(a). All the three films can be indexed as tetragonal phase without any impurity phase, and are highly textured along FST (00*l*) on STO (00*l*). Figure 6.1(b) is the enlarged local scan around FST (003) peak, which clearly shows that the (003) peaks of both doped samples shift to lower angles compared to the pure film. Accordingly, the ***c***-lattice parameter is calculated to be 6.1922 Å, 6.2295 Å and 6.2243 Å for pure FST, CeO_2 capped FST and CeO_2 buffered FST, respectively. The tensile of the doped films in ***c***-direction will be further discussed in correlation with the micrographs in the following discussion.

Figure 6.1(c) shows the φ scans of the FST (112) peaks, as well as STO (112) peaks for all the three samples. The four sharp peaks of the films match very well with the peaks of STO substrates, which indicate the in-plane texture for the thin films and no in-plane rotation between the films and the STO substrates. The full width at half maximum (FWHM) values for the pure FST film, CeO_2 capped FST film and CeO_2 buffered FST film are 2.75°, 1.52° and 1.10°, respectively. Obviously, the incorporation of CeO_2 nanolayers effectively improves the in-plane alignment for the FST films,

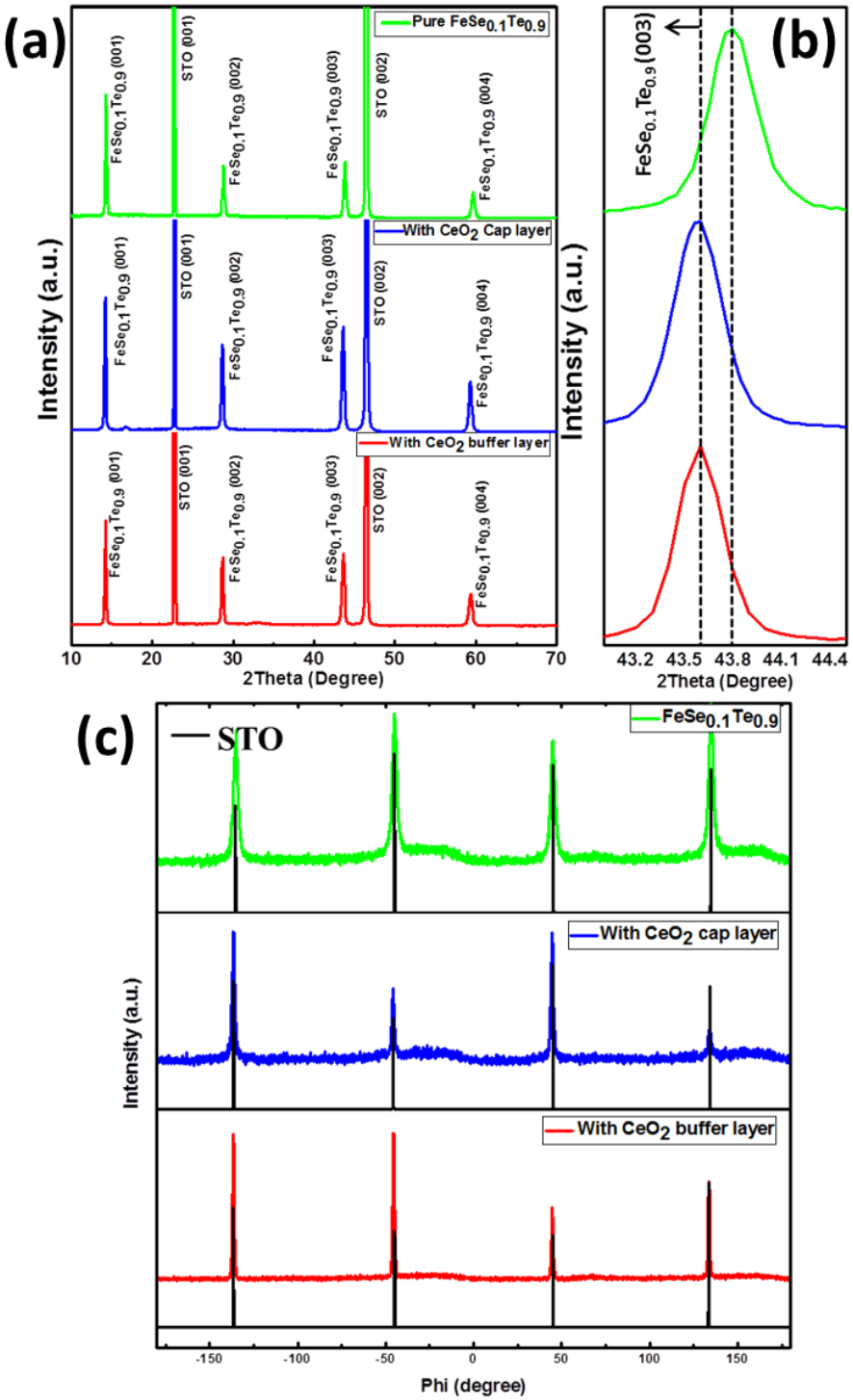

Figure 6.1 (a) θ-2θ XRD patterns of pure $FeSe_{0.1}Te_{0.9}$ and with CeO_2 cap and buffer layers; (b) Enlargement of the area around $FeSe_{0.1}Te_{0.9}$ (001) peak in (a); (c) φ scan of $FeSe_{0.1}Te_{0.9}$ (112) peaks.

especially the buffered one. The improved in-plane alignment could also affect the overall flux pinning properties, e.g., the critical current density under applied magnetic field.

A detailed TEM study was conducted to explore the microstructure characteristics as shown in Figure 6.2. Figure 6.2(a), (c) and (e) are the low magnification cross-section transmission electron microscopy (XTEM) images with the corresponding selected area electron diffraction (SAED) patterns of the pure FST film, CeO_2 buffered film and CeO_2 capped film, respectively. The thickness of the FST and CeO_2 layers can be identified as ~60 nm and ~7 nm, respectively. The distinguished FST (00*l*) diffraction dots in the SAED pattern indicate the perfect out-of-plane alignment of all the films. High resolution XTEM study was also carried out and the high resolution TEM images for the interface area are shown in Figure 6.2(b), (d) and (f). These images demonstrate that the ***c***-planes of all the FST films are perfectly parallel to the substrate lattice with excellent epitaxial film quality. The doped CeO_2 layer does not deteriorate the overall film quality, for the samples with CeO_2 either on the top or bottom. Figure 6.2 (d) represents an an abrupt interface for the buffer CeO_2 layer and the superconductor film layer suggesting excellent chemical compatibility between CeO_2 and FST. Furthermore, the dislocation density in the FST/CeO_2 interface area could be higher than that of the FST/STO interface area due to the large nanoclusters in the CeO_2 layer according to a previous report. [176] This could account for the pinning enhancement in this system. For the CeO_2 cap layered case in Figure 6.2(f), the FST/CeO_2 interface is not as clean as the previous case, which indicates some other

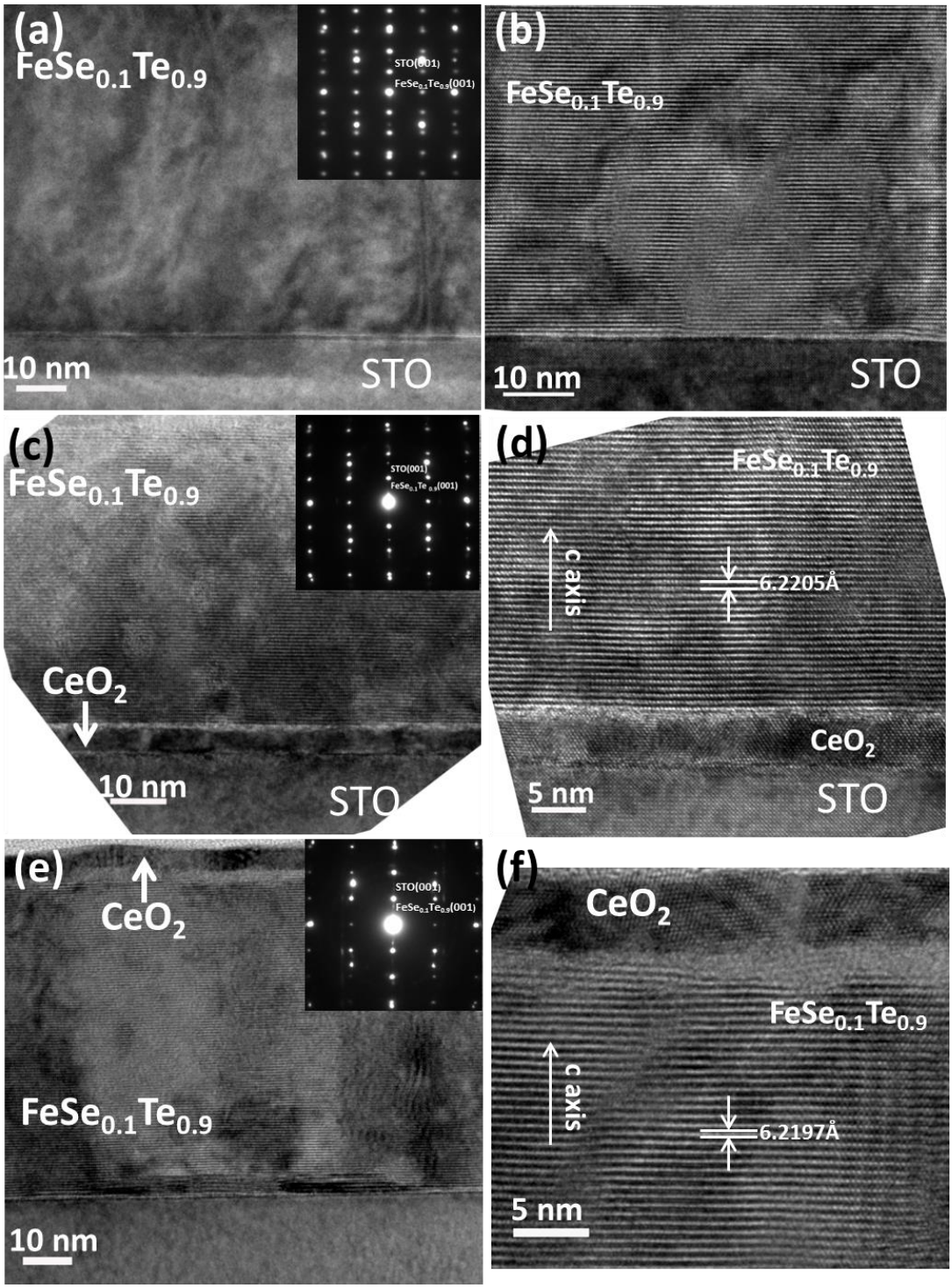

Figure 6.2 Low magnification cross sectional TEM images with the corresponding selected area electron diffraction (SAED) patterns of (a)pure $FeSe_{0.1}Te_{0.9}$, (c) with CeO_2 buffer layer, (e) with CeO_2 cap layer; And their corresponding high resolution TEM images (b), (d) and (f).

phases may appear and a higher defect density is expected. It is possible that some residual oxygen in the chamber diffused into FST through the thin CeO_2 layer during the cooling process. This is ideal for eliminating the excess Fe, since the excess Fe is generally considered harmful for superconducting properties of iron-chalcogenide. [243]

Superconducting properties of the films were measured to explore the pinning properties of these films. Figure 6.3(a) are the R-T plots for all the thin films measured in the range of 2-300 K, and Figure 6.3(b) presents the corresponding enlarged plots from 2-20 K. The results show that all the samples have a similar $\boldsymbol{T_c^{onset}}$ (the point where resistivity starts to sharply decrease) of about 12.5 K, and $\boldsymbol{T_c^{zero}}$ (the point where resistivity starts to be absolutely zero) of about 11.5 K. These results are similar to our previous reports for pure FST films [169, 176] and higher than the reported bulk counterparts. [244, 245]

High upper critical field $\boldsymbol{H_{c2}(T)}$ is essential for high field applications. It can be estimated by the Werthamer-Helfand-Hohenberg model,

$$-H_{c2}(0) = 0.7T_c \, dH_{c2}/dT \,|T_c \quad \text{(Equation 6.1)}$$

The film with CeO_2 buffer layer was selected for R-T measurement under $\boldsymbol{H//c}$ up to 9 T, and plotted in Figure 6.3(c). Figure 6.3(d) shows $\boldsymbol{H_{c2}(T)}$ extrapolated with $\boldsymbol{T_c^{onset}}$ and $\boldsymbol{H_{irr}(T)}$ extrapolated with $\boldsymbol{T_c^{zero}}$. The upper critical field $\boldsymbol{H_{c2}(0)}$ is estimated to be ~186 T (as the test range is only up to 9 T, a ~10% errors are considered for this value).This result is much higher than previous reports of pure iron chalcogenide, [160, 169] and very comparable to the extremely high $\boldsymbol{H_{c2}(0)}$ of $Fe_{1.08}Te{:}O_x$ thin film of ~200 T. [167]

Despite possible errors in the extrapolated $H_{c2}(T)$ values, the results still demonstrate its great potential for high field applications.

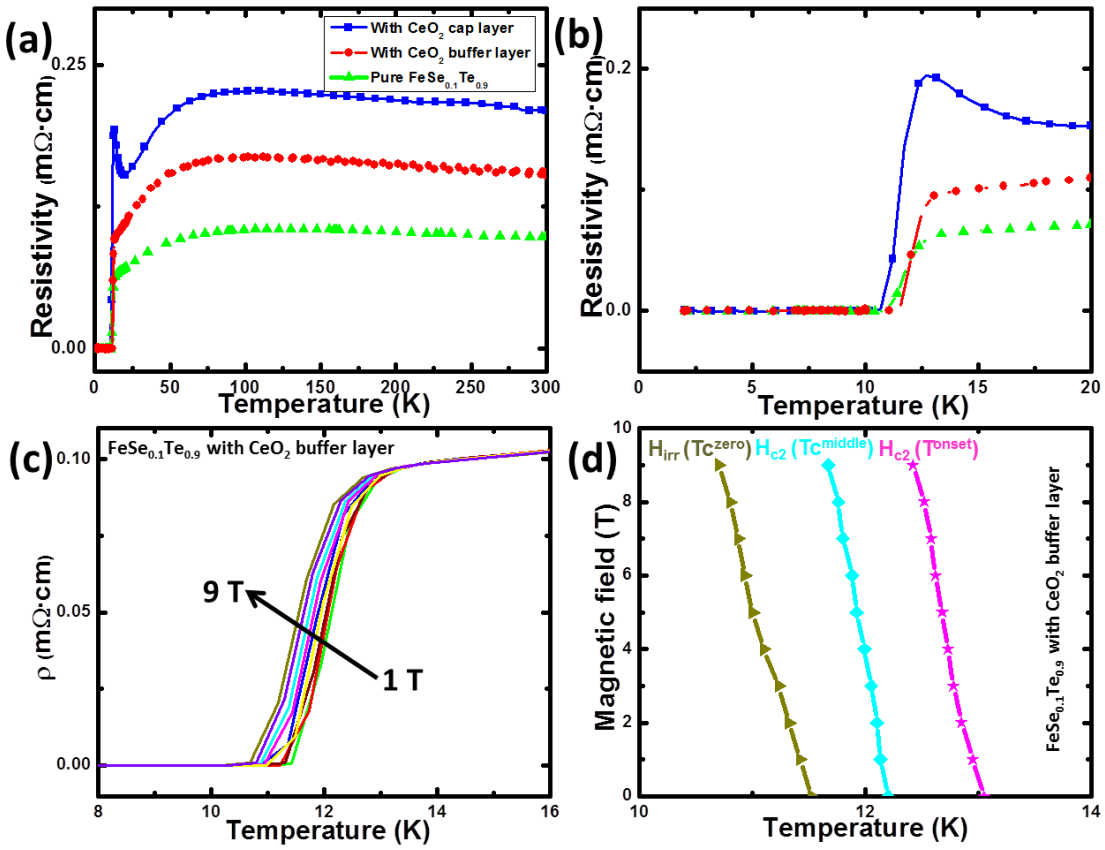

Figure 6.3 R-T plots of $FeSe_{0.1}Te_{0.9}$ thin film, as well as with CeO_2 cap and buffer layers, (a) 2-300 K, (b) 2-20 K; (c) R-T plot of $FeSe_{0.1}Te_{0.9}$ with CeO_2 buffer layer from 8-16 K under magnetic field from 1-9 T; (d) The estimation of H_{irr} and H_{c2} of $FeSe_{0.1}Te_{0.9}$ with CeO_2 buffer layer.

The critical current density (J_c) of the three samples was derived by the Bean model, which can provide a logical estimation of the J_c value for the moderate magnetization variation in the measurement range. The J_c values estimated from the Beam model has been previously compared to the J_c transport measurement results for

pure FST films [242] and the results are very consistent. This suggests that the current circulation in the FST films is quite uniform. Therefore the Beam model is adopted here for the $\boldsymbol{J_c}$ estimation in this case. The in-field $\boldsymbol{J_c}$ of the three samples measured up to 7 T was plotted for Figure 6.4(a) 2 K, (b) 4 K and (c) 8 K, respectively. The applied magnetic field is parallel to ***c***-axis. The self-field $\boldsymbol{J_c}$ of the single FST film, the ones with CeO_2 cap layer and with CeO_2 buffer is estimated as 0.12, 0.23 and 0.89 MA/cm^2 at 4 K, respectively. The $\boldsymbol{J_c}$ value of the buffered sample is very close to that reported in $FeSe_{0.5}Te_{0.5}$ films on both CeO_2-buffered Yttria-stabilized zirconia (YSZ) and RABiTS substrates of ~1 MA/cm^2, [175] and much higher than other reported iron chalcogenide thin films on STO, MgO or LAO substrates. [165, 176, 177] In-field $\boldsymbol{J_c}$ values of the films with CeO_2 nanolayers are much higher than the single FST film at all the measured temperatures, especially the buffered one. The insets of the figures are the normalized $\boldsymbol{J_c}$ vs. applied field, and the power-law exponent $\boldsymbol{\alpha}$ value for the low-field regime were estimated from the log-log plots. The $\boldsymbol{\alpha}$ value is considered as a quantification of the flux pinning property of the samples. Interestingly, the normalized $\boldsymbol{J_c}$ values and the $\boldsymbol{\alpha}$ values for the capped and buffered samples are very close at all the measured temperatures, and are all higher than that of the pure film. This significantly enhanced in-field performance of the doped samples indicates that the introduced CeO_2 nanolayer can provide effective pinning centers, such as the interfacial defects generated at the interface of FST layer and CeO_2 layer. For the case of the absolute in-field $\boldsymbol{J_c}$ of the buffered sample being higher than the capped one, it may be due to the better in-plane lattice matching between FST (3.8462 Å) and CeO_2 (a (220) =3.8264 Å, with a 45° in-plane rotation) than that on

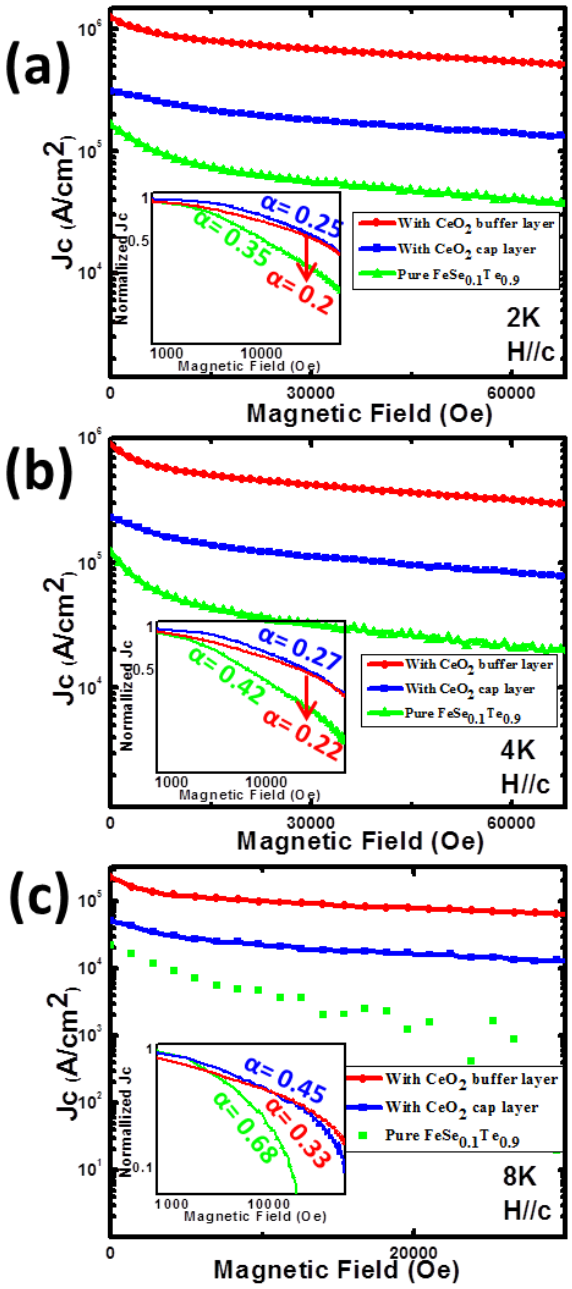

Figure 6.4 The in-field critical current density dependence of applied magnetic field for all three $FeSe_{0.1}Te_{0.9}$ thin films at (a) 2 K, (b) 4 K and (c) 8 K. The insets show the normalized critical current density plots on a log-log scale for calculation of the $\boldsymbol{\alpha}$ value.

STO (3.905 Å). Therefore, the buffered samples may result in a better epitaxial quality and thus the overall enhanced superconducting properties. Interestingly, the pinning properties for both doped cases are very similar, evidenced by the in-field J_c and α values. Currently the $J_c//ab$ measurement is ongoing. Based on the $J_c//c$ results, it is evident that the CeO_2 interlayer significantly improves the overall pinning performance of the FST films. In summary, the above results suggest that both the capped and buffered CeO_2 could introduce similar pinning effects and both could be used as effective pinning centers for FST films.

6.5 Conclusions

Epitaxial $FeSe_{0.1}Te_{0.9}$ films were deposited on STO substrates with or without CeO_2 nanolayer, all with a T_c^{onset} of ~13 K. The sample with buffered CeO_2 shows the highest $J_c^{in\text{-}field}$ among all the measured magnetic field range (0-7 T), with the $J_c^{self\text{-}field}$ as high as 0.89 MA/cm^2 at 4 K. In addition, the $H_{c2}(0)$ value of this sample is estimated to be as high as 186 T, which is very promising for high field applications. More interestingly, the sample with CeO_2 cap layer shows similar values of normalized $J_c^{in\text{-}field}$, $H_{c2}(0)$, and α as the buffered case under all the measured temperatures. Overall, CeO_2 nanolayers can effectively improve the pinning property of $FeSe_{0.1}Te_{0.9}$ thin films and such CeO_2-doped schemes can be used for future Fe-based coated conductors for high field applications.

CHAPTER VII

MAGNETIC $(CoFe_2O_4)_{0.1}(CeO_2)_{0.9}$ NANOCOMPOSITE AS EFFECTIVE PINNING CENTERS IN $FeSe_{0.1}Te_{0.9}$ THIN FILMS*

7.1 Overview

Magnetic epitaxial $(CoFe_2O_4)_{0.1}(CeO_2)_{0.9}$ nanocomposite layers were incorporated into superconducting $FeSe_{0.1}Te_{0.9}$ thin films as either cap layer or buffer layer. Both capped and buffered samples show superconducting property enhancement compared to the reference sample without the incorporated layer, while the capped one shows the best pinning properties among all. Specifically for the capped sample, the critical temperature T_c is ~12.5 K, while the self-field critical current density J_c^{sf} increases to as high as 1.20 MA cm^{-2} at 4 K. Its $J_c^{in-field}$ value shows slower decrease with increasing applied magnetic field, with the lowest power-law exponent $\boldsymbol{\alpha}$ values (derived following $J_c \propto (\mu_0 H)^{-\alpha}$ by the $log(J_c) - log(\mu_0 H)$ plot) of 0.20, 0.23 and 0.33 at 2 K, 4 K and 8 K, respectively. This nanocomposite capped sample also exhibits a high upper critical field $H_{c2}(0)$ of 166 T, which indicates its potentials in high field applications. This pinning method provides an effective way for the superconducting property enhancement of iron chalcogenide thin film.

*Reprinted with permission from "Magnetic $(CoFe_2O_4)_{0.1}(CeO_2)_{0.9}$ nanocomposite as effective pinning centers in $FeSe_{0.1}Te_{0.9}$ thin films" by Jijie Huang, Li Chen, Jie Jian, Kevin Tyler, Leigang Li, and Haiyan Wang, *J. Phys.: Condens. Matter*, **28**, 025702, 2016. Copyright IOP Publishing

7.2 Introduction

Iron chalcogenide superconductor has generated tremendous research interests since its initial discovery in 2008. [149] This "11" type iron-based superconductor has a simple binary composition, which makes this material ideal for composition control during thin film processing. Although with relatively low critical temperature (T_c) compared to other high temperature superconductors (such as $YBa_2Cu_3O_{7-x}$), iron chalcogenide has its advantages. For examples, Si *et al.* reported that the upper critical field $H_{c2}(0)$ of $Fe_{1.08}Te$:O thin film could achieve as high as ~200 T. [167] Several other reports further confirms the high $H_{c2}(0)$ of iron chalcogenide superconductors. [165, 246, 247] Moreover, the iron-based superconductor is considered to have low anisotropy in superconducting properties, e.g., less J_c anisotropy. [77] All of these findings suggest that this material holds promises for high field applications and to substitute the widely used Nb_3Sn nowadays, which is a low T_c superconductor with allowed magnetic field of 20 T at Helium temperature of 4.2 K. [175]

To enable the proposed applications, much effort has been devoted to improve the superconducting properties of the iron chalcogenide superconductors with significant emphasis on improving T_c of this system. For examples, multiple single crystal substrates, such as $SrTiO_3$ (STO), MgO, $LaAlO_3$ (LAO) and CaF_2, have been selected to obtain better superconducting properties. [151, 154, 168, 174, 248] Doping is another effective way for the superconducting property enhancement. For example, dopings of chalcogens, [177, 234, 248] alkali metals [235, 237] and transition metals [236] have been investigated. Furthermore, the onset of the transition temperature T_c^{onset} can reach

to as high as 36.7 K under an applied pressure of around 4 GPa. [238] In addition, Wang *et al.* demonstrated a surprisingly high transition temperature above 50 K of FeSe with an ultrathin layer (as thin as 1 unit cell) on STO substrate. [157] Such record has been replaced recently by a new record of 100 K of the single layer FeSe film on doped STO substrate, [158] despite the fact that the mechanism is still under investigation.

Comparing to T_c improvement, fewer reports have been focusing on superconducting J_c enhancement under both self-field J_c^{sf} and applied magnetic field $J_c^{in-field}$. [165, 247] The methods for flux pinning property in iron chalcogenide superconductor include doping, [169] nanolayers incorporation [175, 246] and irradiation treatment. [241] Much work is still needed for J_c enhancement aiming at future practical applications of Fe-chalcogenides. One approach is to combine doping with incorporating nanolayers, both providing defect pinning centers. On the other hand, magnetic pinning could be another type of effective potential pinning centers, however, has rarely been investigated for iron chalcogenide superconductor.

In this study, $FeSe_{0.1}Te_{0.9}$ (FST) is selected as the thin film matrix, as this typical ratio of Se and Te (10:90) has been demonstrated as the composition with the optimal superconducting properties. [169] A thin layer of epitaxial $(CoFe_2O_4)_{0.1}$:$(CeO_2)_{0.9}$ vertically aligned nanocomposite(VAN) has been introduced as either a cap layer or a buffer layer in the matrix. The schematic illustrations of the designed architectures are shown in Figure 7.1 (a) VAN/FST/STO and (b) FST/VAN/STO. $CoFe_2O_4$ (CFO) is a well-known ferrimagnetic material, which can provide magnetic pinning centers and has been reported for flux pinning for YBCO thin films. [114, 142] The selected

composition of the nanocomposite is 10:90 to minimize the effects of the large lattice mismatch between CFO and FST, and possible inter-diffusion. On the other hand, CeO_2 has perfect lattice matching with FST after an in-plane 45° rotation. It has a high phase compatibility with FST and thus the $(CoFe_2O_4)_{0.1}$:$(CeO_2)_{0.9}$ nanocomposites with much reduced CFO concentration have less inter-diffusion issue with the FST layer comparing to the CFO only case. With this design, both defect and magnetic pinning effects could be incorporated with minimal film quality degradation.

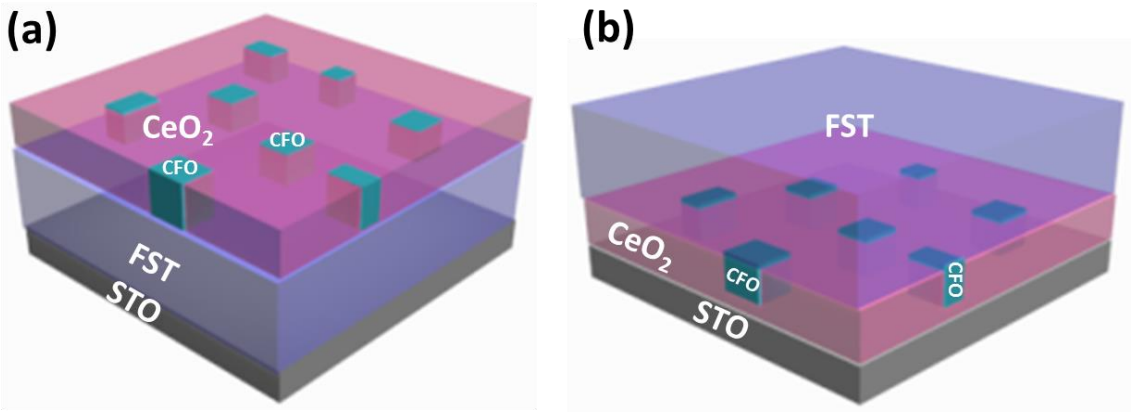

Figure 7.1 Schematic illustrations of the designed film architecture of (a) nanocomposite/FST/STO, and (b) FST/nanocomposite/STO.

7.3 Experimental

Single layer of FST film, as well as the bilayers with $(CoFe_2O_4)_{0.1}$:$(CeO_2)_{0.9}$ nanocomposite layer on top or at the bottom were deposited by a pulsed laser deposition (PLD) system with a KrF excimer laser (Lambda Physik Compex Pro 205, λ=248 nm, 5 Hz) on single crystal STO (001) substrates. The deposition parameters were optimized as follows: the laser energy density was 3 J/cm^2, deposition temperature was 400°C and

target-substrate distance was kept at ~4.5 cm. Before deposition, the base pressure was lower than 1×10^{-6} Torr, and the films were deposited under vacuum condition. The bilayer thin films were prepared by alternative laser ablation of the $(CoFe_2O_4)_{0.1}$:$(CeO_2)_{0.9}$ nanocomposite target and the FST target.

The microstructure of the films was characterized by X-ray diffraction (XRD) (Panalytical X'Pert X-ray diffractometer) and transmission electron microscopy (TEM) (FEI Tecnai G2 F20). The superconducting properties were characterized using resistivity-temperature (R-T) measurement by a four point probe method from 2 to 300 K in a physical properties measurement system (PPMS: Quantum Design). Both the self-field and in-field critical current densities (J_c^{sf} and $J_c^{in-field}$: $H \parallel c$) were measured under an applied magnetic field of 0-7 T at various temperatures (8 K, 4 K and 2 K) by the vibrating sample magnetometer (VSM) in the PPMS.

7.4 Results and discussion

Figure 7.2(a) shows the θ-2θ XRD patterns for all the films from 10° to 70°, with or without nanocomposite doping layer. Here, the pound (#) and star (*) symbols represent the STO (00*l*) and FST (00*l*) peaks, respectively. It is obvious that all the films can be indexed as tetragonal PbO-type structure with the space group of P4/mmm, and no impurity phase was identified. Furthermore, the FST (00*l*) peak intensity of both bilayer samples, especially the buffered sample, is slightly weaker compared to the pure FST film, which indicates that there is some film quality degradation after incorporating the nanocomposite layer. In addition, it is worth noting that there are two minor peaks at

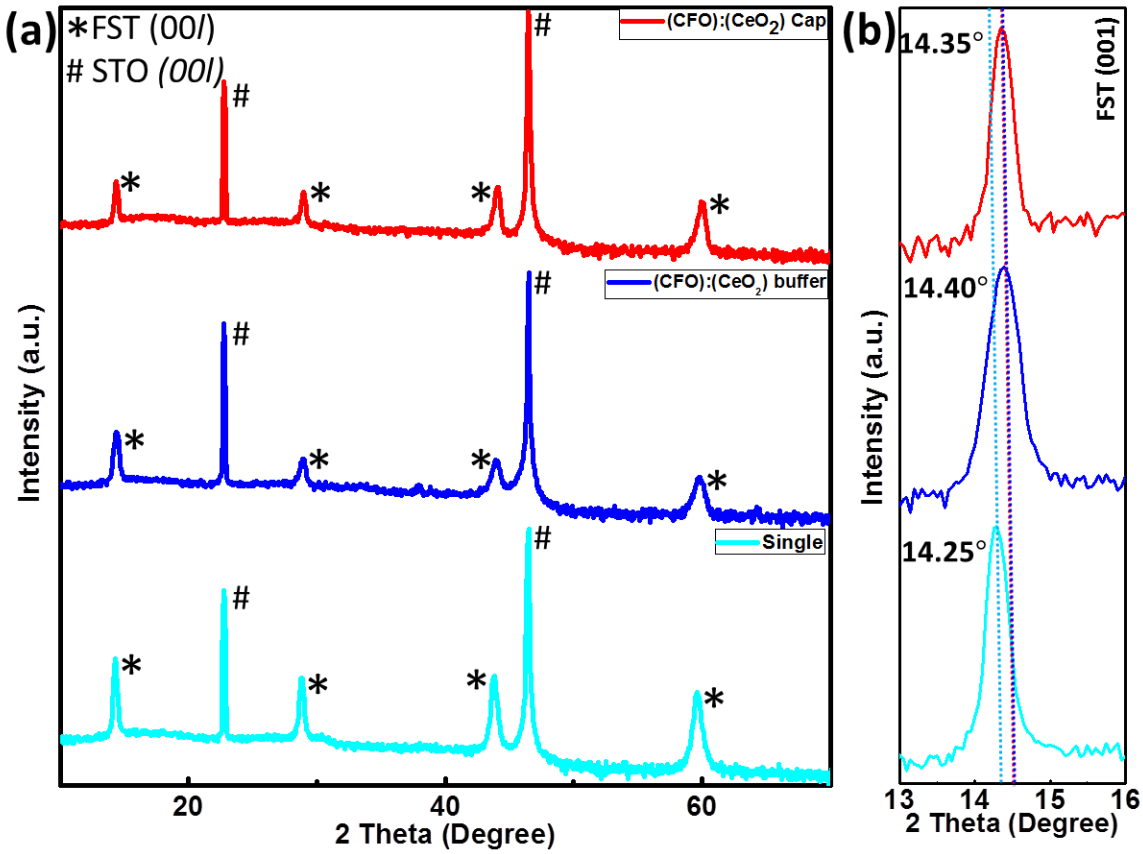

Figure 7.2 (a) Standard θ–2θ XRD scans of single layer $FeSe_{0.1}Te_{0.9}$ thin film and with nanocomposite cap and buffer layers; (b) Local area around $FeSe_{0.1}Te_{0.9}$ (001) peak from 13° to 16°.

38° and 64° in the buffered sample, which is possibly related to Fe_2O_3 (400) and (541), respectively. Figure 7.2(b) shows the enlarged local scan around the FST (001) peak of the films. The 2θ of the FST(001) peak is estimated as 14.35°, 14.40° and 14.25° for nanocomposite layer capped, buffered and single FST layer, respectively, indicating a right shift from the single layer sample. In addition, to minimize measurement errors, the Nelson-Riley extrapolation function $[(\cos\theta^2/\sin\theta) + (\cos\theta^2/\theta)]$ has been used to determine the out-of-plane lattice constant of the films based on all the (00*l*) diffraction peaks. [251] The *c*-axis lattice of the films is calculated to be 6.1650 Å, 6.1669 Å and

6.2004 Å, for nanocomposite layer capped, buffered and single FST layer, respectively. The slightly reduced *c*-axis lattice in the VAN doped samples may account for the superconducting property enhancement to be discussed later.

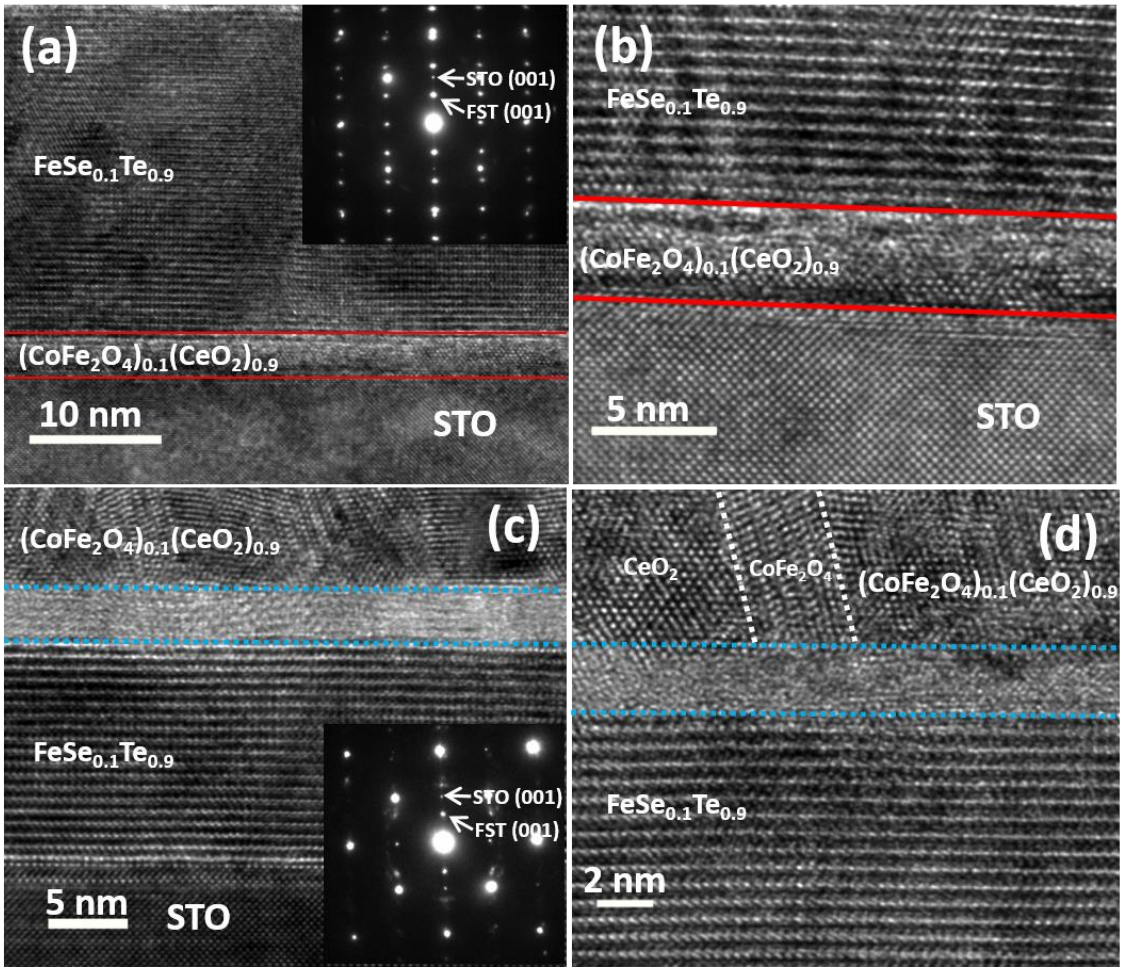

Figure 7.3 Low magnification cross sectional TEM images with the corresponding selected area electron diffraction (SAED) patterns of (a) nanocomposite buffered and (c) capped FST thin films; And their corresponding high resolution TEM images in the interface area (b) and (d). The solid red line marked in (a) and (b) is the nanocomposite layer, while the dash blue line marked layer in (c) and (d) is the transition layer.

To further explore the film quality after incorporating the nanocomposite layer, cross-sectional TEM study was carried out. Figures 7.3(a) and (c) show the low-magnification TEM images of FST film with buffered and capped nanocomposite layer, respectively. The thickness of the FST layer and nanocomposite layer can be identified as ~20 nm and ~5 nm, respectively. Their corresponding selected area electron diffraction (SAED) patterns clearly show the distinguished diffraction dots, which further confirms the high quality epitaxial growth of the films. A closer view at the interface area of both bilayer samples (shown in Figures 7.3(b) and (d)), minor inter-diffusion can be found in both cases. For the nanocomposite buffered sample in Figure 7.3(b), the lattice mismatch between FST layer and the CFO part in the nanocomposite layer may cause some film quality degradation, which is also consistent with the above XRD results. Here, CFO is in the spinel family with a lattice parameter of 8.396 Å, and its lattice mismatch (a/2=4.198 Å) with FST (a=3.826 Å) is around 8.9%. Because of the relatively large lattice mismatch, interfacial defects may generate in this area and provide effective pinning centers, which will be further discussed by correlating with the superconducting properties in the following section. For the nanocomposite capped sample in Figure 7.3(d), a thin transition layer (estimated to be 3-4 nm) appears at the interface area and it is highly possible that some interfacial phases may be generated. This transition layer may be produced by the diffusion of the residue oxygen in the chamber through the thin top layer during the cooling process. [246] However, as $CoFe_2O_4$ has been incorporated into the CeO_2 layer, more inter-diffusion may cause a thicker transition layer, compared the case of pure CeO_2 in the previous report. [246]

Furthermore, from this high-resolution TEM image, the two phases of CFO and CeO_2 can be easily observed. Overall, the majority part of the FST layer is still in good epitaxial quality in both cases.

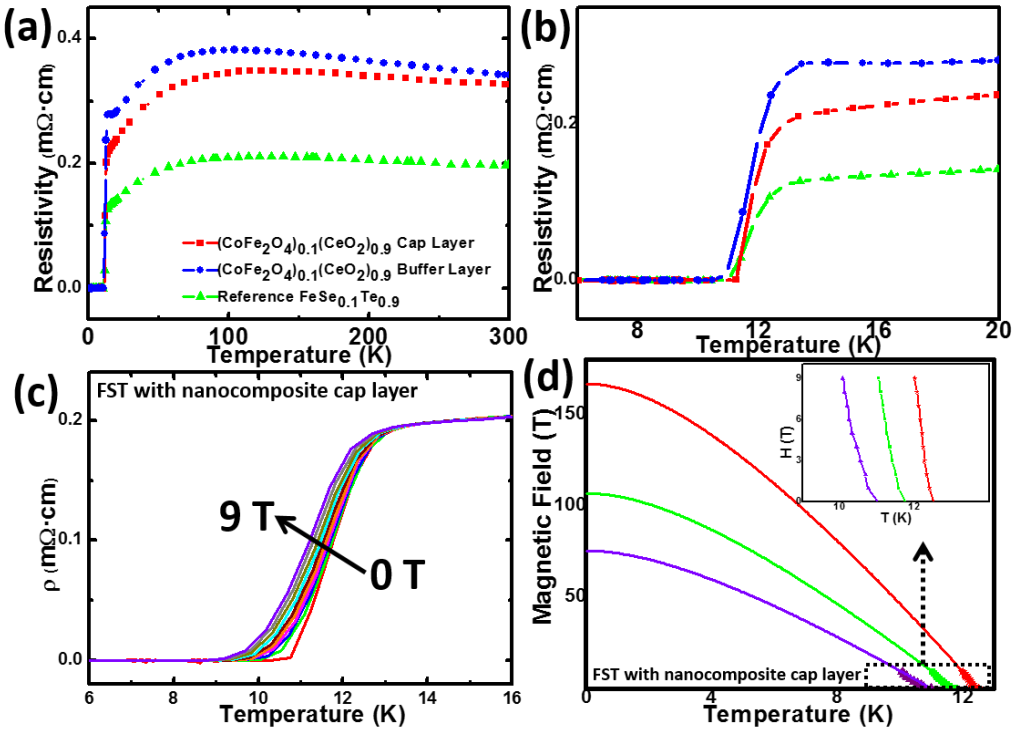

Figure 7.4 R-T plots of single FST film and FST/nanocomposite bilayers, (a) 2-300 K, (b) 2-20 K; (c) R-T plot of nanocomposite capped sample from 6-16 K under magnetic field from 0-9 T; (d) And the estimation of $\boldsymbol{H_{irr}(T)}$ and $\boldsymbol{H_{c2}(T)}$ values.

Figure 7.4(a) presents the temperature dependence of the resistivity in the temperature range of 2-300 K of the as-grown films, with or without the nanocomposite layer. It is obvious that all the films show a sharp R-T transition at around 12 K. By enlarging the transition temperature region, shown in Figure 7.4(b), it is clear that the transition initiates around 12.5 K and ends at ~11.5 K with a slight variation between

samples. Furthermore, the resistivity values in the normal state condition (up to 300 K) increase after incorporating the nanocomposite layer, because that FST is more conductive than the nanocomposite layer in normal state. Another finding is that the metal-semiconductor transition temperature is higher for the nanocomposite layer samples.

Further R-T measurement under applied magnetic field ($H \parallel c$, up to 9 T) was conducted for the sample with nanocomposite cap layer, which is shown in Figure 4(c). Through these results, the upper critical field $H_{c2}(T)$ can be estimated by the Werthamer–Helfand–Hohenberg (WHH) model: $-H_{c2}(0) = 0.7T_c\, dH_{c2}/dT\,|T_c$. [250] Although there may be some deviation of the results derived by this model compared to the real values, it is still a useful way to estimate the $H_{c2}(T)$ value. Figure 7.4(d) inset presents the applied magnetic field dependence of the T_c values, in which the irreversibility line $H_{irr}(T)$ extrapolated with T_c^{zero} (T_c^{zero}: the point where the resistivity is ~10% of the resistivity in normal state), while the upper critical field $H_{c2}(T)$ extrapolated with both T_c^{mid} (T_c^{mid}: the point where the resistivity is ~50% of the resistivity in normal state) and T_c^{onset} (T_c^{onset}:the point where the resistivity is ~90% of the resistivity in normal state) are plotted in Figure 7.4(d). The fitting lines are shown in Figure 7.4(d), which demonstrates that the $H_{c2}(0)$ value can be estimated to be as high as 166 T from T_c^{onset}. This value is higher than some reported $H_{c2}(0)$ of iron chalcogenide $FeSe_xTe_{1-x}$ thin films, [169, 247] which were also derived by WHH model. This high $H_{c2}(0)$ value is critical and further confirms that iron chalcogenide superconductor is promising for high field applications.

Table 7.1 Summary of the J_c^{sf} and α values of all the samples. (Note: FST/CeO_2 bilayer samples are listed for comparison)

Property / Sample	J_c^{sf} (MA cm^{-2})			α value		
	2 K	4 K	8 K	2 K	4 K	8 K
NC Cap	1.67	1.20	0.29	0.20	0.23	0.33
NC Buffer	0.79	0.54	0.08	0.26	0.29	0.50
CeO_2 Cap [246]	0.31	0.23	0.05	0.25	0.27	0.45
CeO_2 Buffer [246]	1.25	0.89	0.22	0.20	0.22	0.33
Reference FST	0.16	0.12	0.02	0.35	0.42	0.68

As above mentioned, critical current density J_c is another important superconducting property, which demonstrates the capability of carrying supercurrent in the superconductor. Here, the J_c values were derived by the Bean model: $Jc = 20\Delta M/a(1-\frac{a}{3b})$, where ΔM is the opening in the hysteresis loop; a and b are the sample dimensions. [184] This method is often used to estimate J_c values for the moderate magnetization variation in the testing range. Here, all the samples were measured under applied magnetic field up to 7 T at 2 K, 4 K and 8 K, and the calculated J_c was compared with that of previous reported CeO_2/FST bilayer thin films, [246] as well as the reference single layer FST. Table 7.1 lists the J_c^{sf} comparison of all the samples, which shows that the nanocomposite capped sample obtains all the highest J_c^{sf} of 1.67 MA cm^{-2}, 1.20 MA cm^{-2} and 0.29 MA cm^{-2} at 2 K, 4 K and 8 K, respectively. These values are higher than most previous reports of iron chalcogenide thin films, [177, 246] as well as the bulk single crystal counterparts. [239, 250] Its J_c^{sf} value is even at a comparable range of ~1 MA cm^{-2} at 4.2 K with that of the $FeSe_{0.5}Te_{0.5}$ film on complicated and costly CeO_2 buffered RABiT substrate. [175]

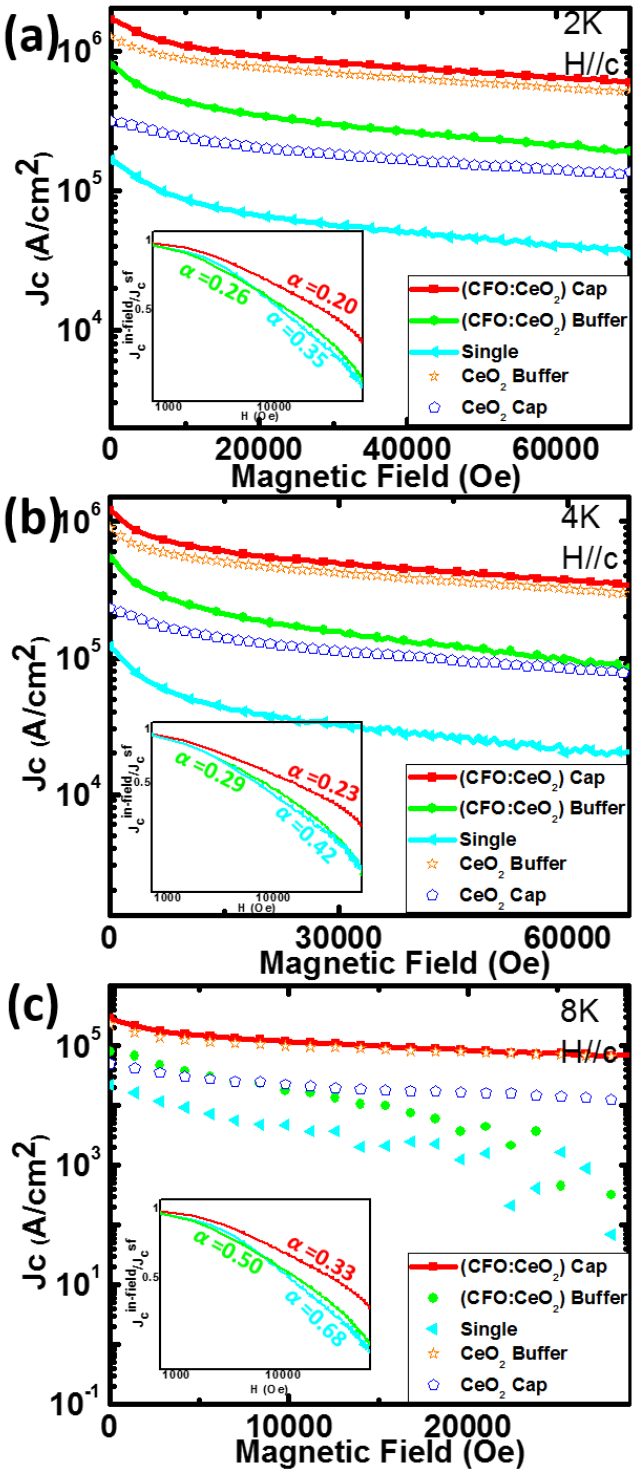

Figure 7.5 The in-field critical current density dependence of applied magnetic field for all the samples at (a) 2 K, (b) 4 K and (c) 8 K. The insets show the normalized critical current density plots on a log-log scale.

Taking into account its potential applications in high field, it is essential to explore the J_c property under applied magnetic field ($J_c^{in-field}$). The J_c dependence of the applied field is plotted in Figure 7.5, and the J_c values of previous reported FST/CeO_2 are also plotted to demonstrate the various pinning mechanisms in different cases. It is obvious that all the bilayer samples (FST/CeO_2 or FST/nanocomposite) show higher J_c values than the reference single FST film along all the measured field regime, which indicates enhanced flux pinning effects by introducing CeO_2 or the CFO:CeO_2 nanocomposite layer. Among all, nanocomposite capped and CeO_2 buffered FST films exhibit the highest J_c values. To better understand the pinning mechanism in all the cases, the capped and buffered samples are compared to each other, respectively. For the capped ones, FST film with nanocomposite cap layer presents much higher J_c^{sf} and $J_c^{in-field}$ values than the one with CeO_2 cap layer. Two factors may be considered: first, the CFO portion in the nanocomposite can produce more defects (such as dislocations and lattice distortions), due to the large lattice mismatch between CFO and FST. Second and more importantly, it is the magnetic pinning effect introduced by the additional magnetic material CFO. For the buffered cases, conversely, CeO_2 buffered sample shows better properties than the nanocomposite buffered one. This is because the FST film quality degrades with nanocomposite layer underneath, while the CeO_2 layer can improve the overall film epitaxy quality. Although the magnetic pinning caused by CFO can lead to better superconducting properties, the film quality degradation dominates in this case. Therefore, CeO_2 is more favorable than nanocomposite as buffer layer. In addition, the power-law exponent $\boldsymbol{\alpha}$ value is also estimated from the normalized J_c *vs.*

applied field as $J_c \propto (\mu_0 H)^{-\alpha}$ (Figure 7.5 inset), which can be considered as a reasonable quantification of the flux pinning property. Table 1 lists the α values of all the samples. It is evident that the nanocomposite capped sample obtains all the lowest values of 0.20, 0.23 and 0.33 at 2 K, 4 K and 8 K, respectively. This further confirms the strongest pinning effects in the nanocomposite capped sample, both in absolute J_c and normalized J_c forms. Last, it is obvious that all the J_c values decrease with increasing temperatures, compared the J_c values from Figure 7.5(a) (low temperature 2 K) to Figure 7.5(c) (high temperature 8 K), due to the thermally activated flux flow. With a closer look at Figures 7.5(a), (b), (c), the J_c values of the CeO_2/FST bilayers start to narrow the gap from nanocomposite/FST bilayers with increasing temperature, one possibility is that magnetic pining plays a greater role at lower temperature in this case.

Overall, the incorporation of $(CFO)_{0.1}(CeO_2)_{0.9}$ nanocomposite layer can provide effective pinning centers. The pinning mechanism is different from that of FST/CeO_2 bilayer, as both defect and magnetic pinning take place in this study. Further work is needed in the follows: First, searching for other magnetic materials with better lattice match and chemical compatibility with FST could be essential, especially for the buffer layer structure cases; Second, more complicated architectures such as incorporation of multilayers of $(CFO)_{0.1}(CeO_2)_{0.9}$ VAN in the FST matrix to further enhance the overall defects and magnetic pinning properties. However more attentions should be paid during growth since such multilayer structure will require prolonged deposition time and thus lead to a higher chance of inter-diffusion between the dopants and the matrix; Third, magnetic pinning centers with good chemical compatibility can be doped uniformly into

the FST matrix for flux pinning, with the goal of forming nanostructures with size in the similar range of the coherence length of FST thin films.

7.5 Conclusions

In summary, a $(CFO)_{0.1}(CeO_2)_{0.9}$ nanocomposite layer has been incorporated into epitaxial FST films as either a cap layer or a buffer layer for enhanced flux pinning properties. Both samples show effective pinning enhancement compared to the pure FST films, while the capped one shows the highest J_c^{sf} of 1.20 $MAcm^{-2}$ at 4 K with an estimated $H_{c2}(0)$ value of 166 T. The pinning mechanism of the nanocomposite layer combines the defect pinning from the CeO_2 and the magnetic pinning from the additional magnetic CFO in the nanolayer. Overall, the incorporation of magnetic pinning centers in a matrix in the form of VAN structure demonstrates an effective approach for the pinning enhancement of iron chalcogenide superconductors.

CHAPTER VIII

A SIMPLIFIED SUPERCONDUCTING COATED CONDUCTOR DESIGNED WITH Fe-BASED SUPERCONDUCTOR ON GLASS AND FLEXIBLE METALLIC SUBSTRATES*

8.1 Overview

Iron-based superconductors have attracted great research interests from both the intriguing fundamental superconducting mechanism aspects and their potential applications in high fields owing to their high critical field $\boldsymbol{H_{c2}}$ and low field anisotropy. However, one critical factor limiting the commercial applications of superconducting coated conductors is the significant manufacturing costs involved in the processing of the complex layered buffers and the subsequent epitaxial growth of superconducting coated conductors. Here we demonstrate a much simplified superconducting coated conductor design for Fe-based superconductor on glass and metallic substrates without bi-axial texturing buffers. Using this design, $FeSe_{0.1}Te_{0.9}$ thin films on glass show superconducting properties of critical temperatures $\boldsymbol{T_c^{zero}}$ of 10 K, and $\boldsymbol{T_c^{onset}}$ of 12.5 K, self-field critical current density ($\boldsymbol{J_c}$) of 2.1×10^4 A/cm^2 at 4 K, and upper critical field ($\boldsymbol{H_{c2}}$) as high as 126 T. This work could lay a critical foundation toward future practical applications of Fe-based superconductor coated conductors.

*Reprinted with permission from "A simplified superconducting coated conductor design with Fe-based superconductors on glass and flexible metallic substrates" by Jijie Huang, Li Chen, Jie Jian, Fauzia Khatkhatay, Clement Jacob, and Haiyan Wang, *Journal of Alloys and Compounds*, **647**, 380, 2015.

8.2 Introduction

Since the discovery of high temperature superconductor (HTS) in the late 1980s, it has raised great research interests. [10, 75, 83, 252] Especially in the past two decades, $YBa_2Cu_3O_{7-\delta}$ (YBCO)-based HTS coated conductors (CCs) have gone through a significant development. It was considered as one of the most promising candidates for practical applications, owing to its high critical temperature ($\boldsymbol{T_c}$) up to 93 K and high critical current density ($\boldsymbol{J_c}$: the maximum supercurrent density that the superconductor can sustain). However, its large scale commercial applications have been greatly hindered by its complicated CCs processing methods and associated high processing cost. Several successful methods were developed for YBCO CCs, including ion-beam-assisted deposition (IBAD), the rolling-assisted biaxially textured substrate (RABiTS) process and others. [21, 26, 253, 254] However, various fundamental scientific questions still exist, including the self-field critical current density ($\boldsymbol{J_c^{sf}}$: $\boldsymbol{J_c}$ without applied magnetic field) thickness dependence and the in-field critical current density ($\boldsymbol{J_c^{in\text{-}field}}$: $\boldsymbol{J_c}$ under certain applied magnetic field) dependence. [255, 256]

The '11' compounds of $FeSe_xTe_{1-x}$ could be a desired candidate for coated conductors, owing to its relatively low anisotropies (i.e., the ratio of upper critical field $\boldsymbol{H_{c2}^{ab}/H_{c2}^{c}}$ is 1~8) and extremely high $\boldsymbol{H_{c2}}$ (close to 200 T). [177, 257] These sensational properties make it promising in high-field applications, to substitute Nb_3Sn-the most widely used in the high field nowadays [258, 259]. Iron chalcogenide is one sub-class of the Fe-based superconductors with the simplest structure with binary composition. [149] A large amount of work has been conducted to improve their superconducting

properties. For example, by doping with isovalent (such as S and Te), the superconducting properties can be enhanced effectively, [163, 260, 261] as well as doping with Sn. [266] In addition, the $\boldsymbol{T_c}$ of FeSe thin film reaches to as high as 36.7 K under applied pressure. [238] The self-field critical current density $\boldsymbol{J_c^{sf}}$ of $FeSe_{0.5}Te_{0.5}$ grown on single-crystal lanthanum aluminate (LAO) (001) substrate can achieve 8×10^5 A/cm^2 at 4.2 K. [241] Very recently, $FeSe_{0.1}Te_{0.9}$, a composition close to the antiferromagnetic ordering, has been reported to reach the best superconducting properties among all the different compositions of $FeSe_xTe_{1-X}$. [169] Furthermore, $\boldsymbol{J_c}$ values of $FeSe_{0.1}Te_{0.9}$ thin film can be further improved by introducing a thin CeO_2 nanolayer as effective pinning centers. [246] Si *et al.* recently incorporated $FeSe_{0.5}Te_{0.5}$ thin films on textured metal template made by IBAD method, and these tapes can achieve high $\boldsymbol{J_c}$ $>1\times10^4$ A/cm^2 at about 4.2 K under a magnetic field as high as 25 T. [177] All above studies demonstrate a great promise for Fe-based superconductor coated conductors for potential high field applications.

Different from YBCO-coated conductors that require perfect epitaxial template with multiple buffer layers, iron chalcogenide thin films can be directly grown on amorphous glass substrates with good c-axis texturing and certain in-plane texturing. The $FeSe_{0.5}Te_{0.5}$ films have been reported to have comparable superconducting properties as that of the ones on single crystal $SrTiO_3$ (STO) substrates. [240] This encouraging result clearly suggests that $FeSe_xTe_{1-x}$ system could have a unique self-texturing mechanism and thus be adapted as coated conductors without extensive epitaxial buffer processing. In this work, we demonstrate a much simplified coated

conductor scheme for $FeSe_xTe_{1-x}$ system by directly growing the films on polished stainless steel substrates with a thin amorphous Al_2O_3 layer. The results are also compared with the $FeSe_xTe_{1-x}$ films directly on amorphous glass substrates. Detailed superconducting property studies are correlated with the film texturing nature/mechanisms on glass and amorphous buffered metal substrates. Such a simplified coated conductor scheme could provide a promising route to process cost-effective Fe-based superconductor coated conductor for future high field applications. In addition, this work explores the fundamental texturing mechanisms on amorphous substrates which could be of interests to the Fe-based materials community as well as other thin film community in general.

8.3 Experimental

All the thin films were deposited by a pulsed laser deposition (PLD) system with a KrF excimer laser (Lambda Physik Compex Pro 205, λ=248 nm, 5 Hz) on either glass (double sides polished plain microscope glass slide with thickness of 1.0 mm from Fisher Scientific) or polycrystalline metallic substrates (stainless steel 316 with thickness of 0.175 mm from Maudlin products, polished with SiC sandpapers and finished with 1 um alumina polishing abrasives). The laser energy density was kept around 3 J/cm^2. The deposition temperature (i.e., substrate temperature) was kept at 400°C, while the target-substrate distance was 4.5 cm. The base pressure for all the depositions reached 1×10^{-6} Torr or better vacuum conditions. The thickness of the films was kept about 80 nm.

The microstructural properties of the films were characterized using X-ray diffraction (XRD) (PANalytical X'Pert x-ray diffractometer), scanning electron microscopy (SEM) (JEOL JSM-7500F with a field emission gun) and transmission electron microscopy (TEM) (FEI Tecnai G2 F20) techniques. The superconducting properties were characterized by a resistivity–temperature (R-T) measurement using a four point probe system with temperature ranging from 2 to 300 K in a physical properties measurement system (PPMS; Quantum Design). Both the self-field and in-field critical current densities ($\boldsymbol{J_c^{sf}}$ and $\boldsymbol{J_c^{in\text{-}field}}$ ($\boldsymbol{H//c}$) were measured under an applied magnetic field of 0-9 T at various temperatures (8, 4 and 2 K) by the vibrating sample magnetometer (VSM) option in the PPMS.

8.4 Results and discussion

Figure 8.1 shows the standard θ-2θ XRD scans for the $FeSe_{0.5}Te_{0.5}$, $FeSe_{0.1}Te_{0.9}$ and FeTe thin films grown on glass substrates. The peaks are indexed as $FeSe_xTe_{1-x}$ (00*l*), which indicates the (00*l*) preferred c-axis texturing directly on amorphous substrates. Since there is no preferred orientation in this amorphous substrate, the preferred c-axis texturing of the film is resulted from its growth characteristics, so-called self-texturing. In addition, all three films can be identified as tetragonal phase without any obvious impurity phase, and only the pattern of FeTe shows an extra peak possibly from the compound of Fe_2TeO_5. The estimated c-axis lattice parameter gradually increases from 5.8847Å for $FeSe_{0.5}Te_{0.5}$, to 6.1549Å for $FeSe_{0.1}Te_{0.9}$ to 6.2208Å for FeTe, as Te concentration increases. The increased *c*-lattice parameter may lead to better

superconducting properties as *c/a* ratio may increase, [174] but not necessary as *a* may also increase. These results are also consistent to that of $FeSe_xTe_{1-x}$ thin films on STO substrates. [169]

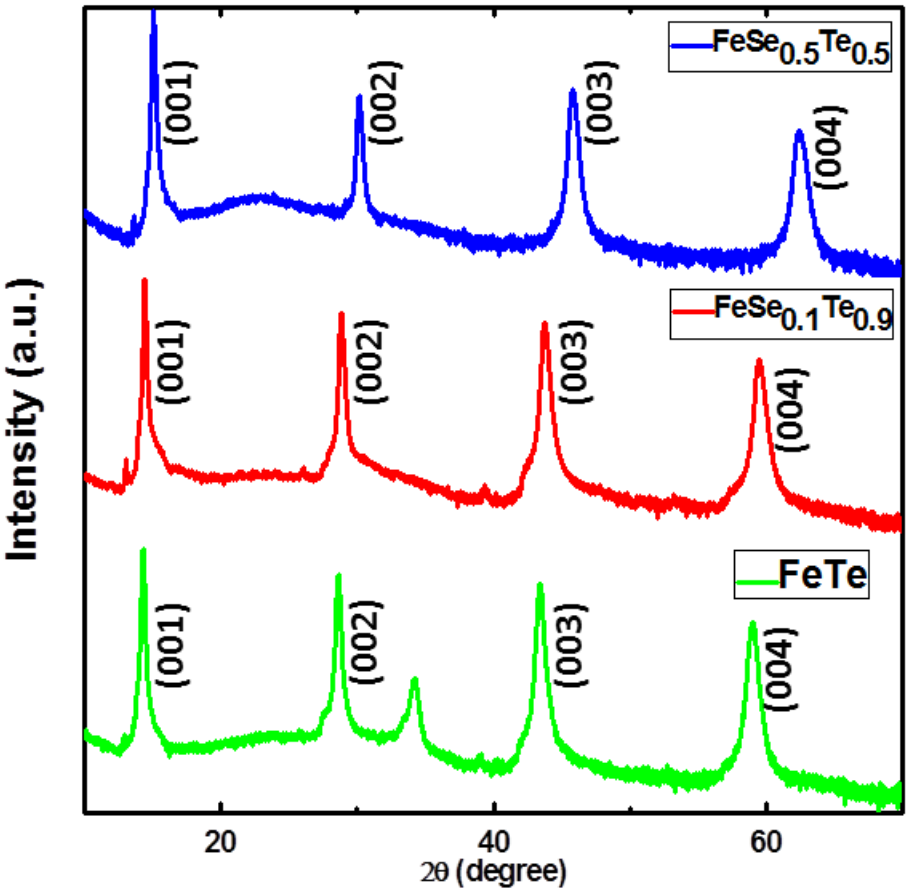

Figure 8.1 θ-2θ XRD scans of $FeSe_{0.5}Te_{0.5}$, $FeSe_{0.1}Te_{0.9}$ and FeTe thin films on glass.

To further explore the microstructural variation of the samples as a function of the film composition, SEM and cross-sectional TEM were conducted. Figure 8.2(a), (b) and (c) show the SEM images of $FeSe_{0.5}Te_{0.5}$, $FeSe_{0.1}Te_{0.9}$ and FeTe thin films, respectively. The surface morphologies of the three samples are significantly different.

$FeSe_{0.5}Te_{0.5}$ and $FeSe_{0.1}Te_{0.9}$ display much smoother surface than that of FeTe, where some spherical particles are obvious on the surface. This suggests that $FeSe_{0.5}Te_{0.5}$ and $FeSe_{0.1}Te_{0.9}$ grow laterally and the grains coalesce well. On the other hand, much rougher surface of FeTe indicates poor nucleation and incomplete grain coalescence, which may account for the lower superconducting properties discussed in the following sections.

Figure 8.2(d) and (e) show the low-magnification cross-sectional TEM image with the corresponding selected area electron diffraction (SAED) and the high resolution TEM image of $FeSe_{0.1}Te_{0.9}$ film on glass, respectively. The film thickness is about 80 nm, which is estimated based on Figure 8.2(d). Furthermore, the obvious and bright diffraction dots of $FeSe_{0.1}Te_{0.9}$ (00*l*) along the out-of-plane direction can be observed from the SAED pattern, which reveals the excellent out-of-plane alignment. From Figure 8.2(e), the clear lattices also demonstrate excellent film growth quality even on amorphous substrates without any preferred crystallographic orientation. In addition, the c-lattice planes can be clearly determined to be parallel to the surface of the glass substrate, which further confirms its preferred c-axis texturing (self-texturing), consistent with the XRD results above.

FeTe thin film deposited on glass substrate shows obvious transition temperature from the resistivity-temperature (R-T) measurement (Figure 8.3(a)). The resistivity reaches to zero at 8 K. This $\boldsymbol{T_c}$ value is slightly lower than that of $FeSe_{0.1}Te_{0.9}$ thin film on glass. The microstructural properties of FeTe are shown in the low magnification 8.3(b) and high resolution 8.3(c) cross-section TEM images. The film thickness is about

80 nm. However, the high resolution TEM image and the corresponding SAED show that the film was grown as polycrystalline in most of the areas. This is very different from the highly textured c-axis growth of $FeSe_{0.1}Te_{0.9}$, which may be the main reason account for the T_c degradation of FeTe.

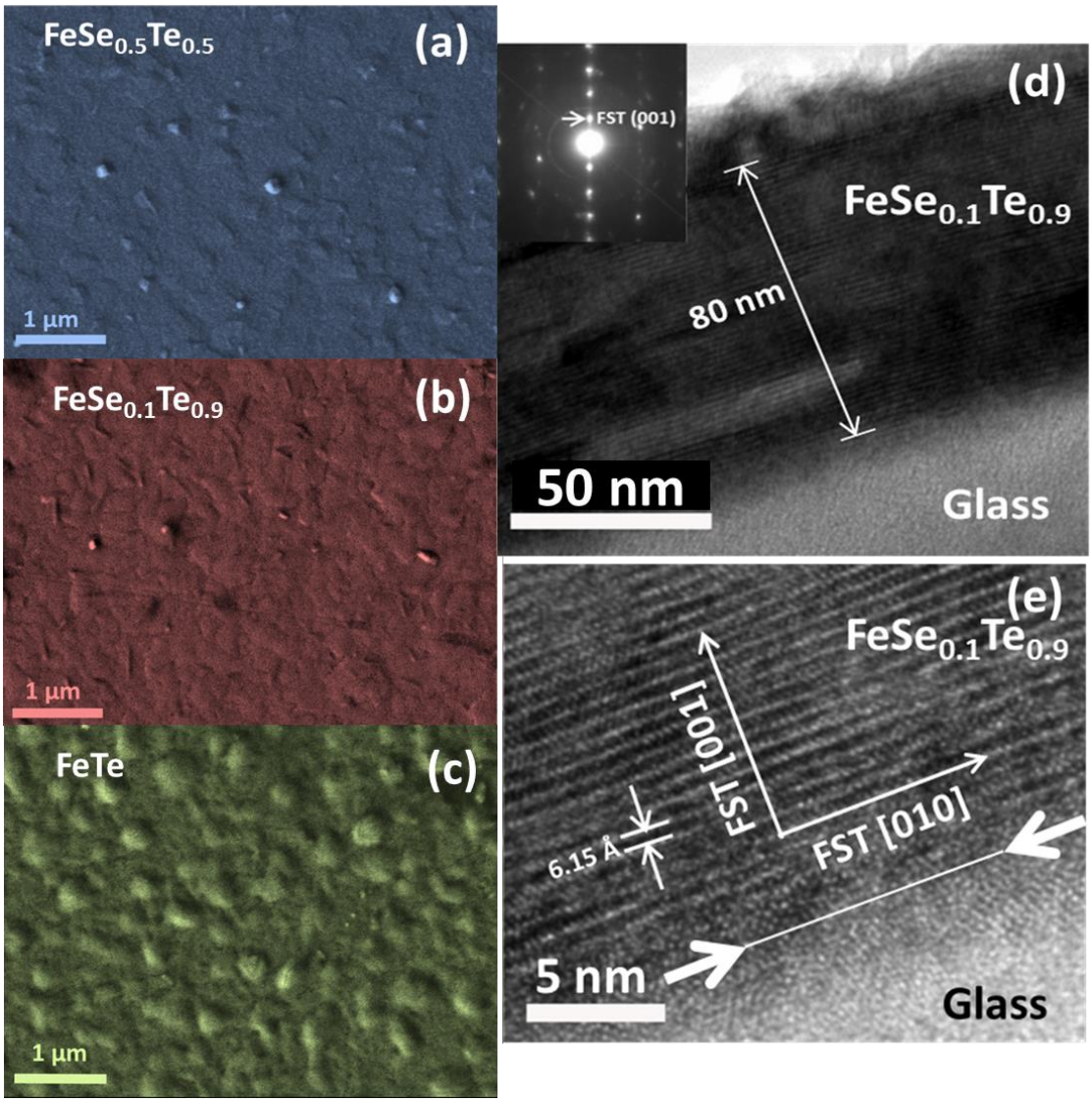

Figure 8.2 Plan-view SEM images of (a) $FeSe_{0.5}Te_{0.5}$, (b) $FeSe_{0.1}Te_{0.9}$, (c) FeTe thin films on glass substrates; Cross-section TEM image with corresponding SAED of $FeSe_{0.1}Te_{0.9}$ film on glass (d) Low magnification; (e) High resolution.

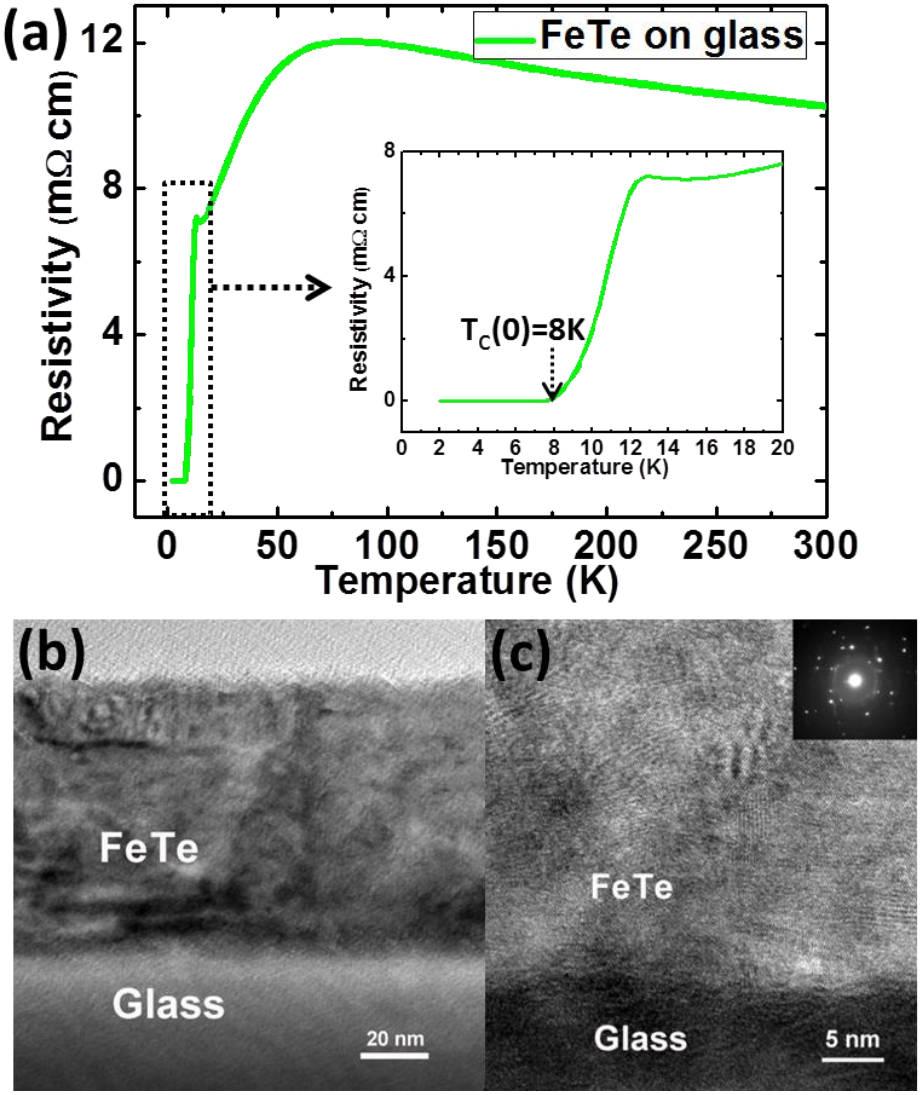

Figure 8.3 (a) R-T plot of FeTe thin film on glass substrate; XTEM images with corresponding SEAD of FeTe thin film (b) Low magnification; (c) High resolution.

The superconducting properties of the films, including T_c, J_c and H_{c2}, were measured and compared. Figure 8.4(a) shows the R-T plot of the $FeSe_{0.1}Te_{0.9}$ film on glass, and the inset is the in-field (0-9 T, ***H//c***) transport measurement. The superconducting transition starts from 12.3 K (T_c^{onset}) and reaches zero resistance at 10 K (T_c^{zero}), which is comparable to the results on single crystal substrates [161, 169] and some bulk counterparts, [262, 263, 267] and better than $FeSe_{0.5}Te_{0.5}$ film on glass. [240] From the R-T plot in Figure 8.3(a), T_c^{zero} of FeTe thin film can be identified as about 8 K, while T_c^{onset} is about 12 K. This is also comparable to the reported values for the counterparts deposited on single crystal substrate. [165, 166] The irreversibility field $H_{irr}(T)$ and upper critical field $H_{c2}(T)$ have been extrapolated using T_c^{zero} and T_c^{onset} values under different fields, respectively, and plotted in Figure 8.4(b). The Werthamer-Helfand-Hohenberg(WHH) model was applied to estimate the upper critical filed, as follows:

$$-H_{c2}(0) = 0.7T_c \, dH_{c2}/dT \,|T_c \quad \text{(Equation 8.1)}$$

By this model, H_{c2} of $FeSe_{0.1}Te_{0.9}$ film on glass can be estimated to be around 126 T. Although there could be some over estimation in the H_{c2} by the WHH model, this method is still useful and has been widely used to obtain H_{c2} values for various systems. [169, 175, 267] And H_{c2} of $FeSe_{0.1}Te_{0.9}$ film on glass (126 T) is even higher than some reported $FeSe_xTe_{1-x}$ films on single crystal substrates, [169, 247] as well as $FeSe_{0.5}Te_{0.5}$ film on glass, [240] which were also estimated by WHH model. The extremely high H_{c2} grants its potential applications in high field regimes.

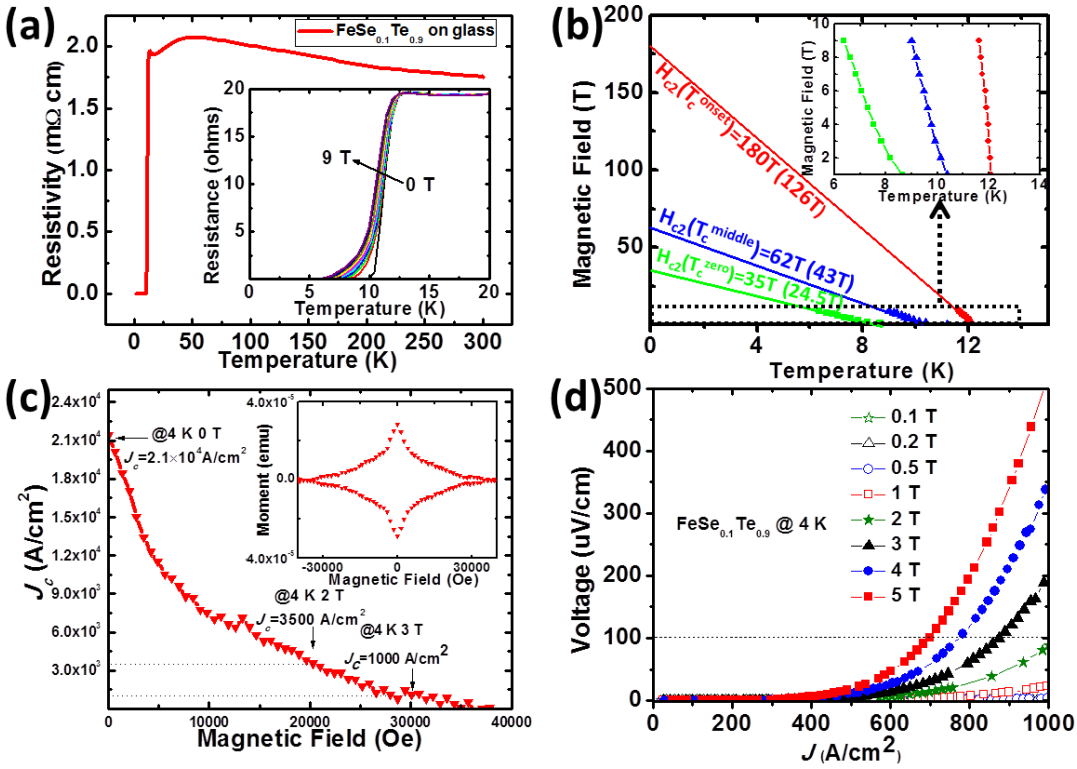

Figure 8.4 (a) R-T plot of $FeSe_{0.1}Te_{0.9}$ thin film on glass from 2-300 K, inset is R-T plot from 2-20 K under magnetic fields; (b) The irreversibility line $\boldsymbol{H_{irr}}$ (T) and upper critical field $\boldsymbol{H_{c2}}$ (T); (c) The field dependence critical current density with corresponding magnetic hysteresis loop at 4 K; (d) The transport measurement at 4 K under magnetic fields.

Self-field critical current density $\boldsymbol{J_c^{sf}}$ and in-field $\boldsymbol{J_c^{in\text{-}field}}$ (up to 4 T, ***H//c***) were measured at 4 K by VSM in PPMS. Figure 8.4(c) shows the field dependence of the critical current density at 4 K, which is calculated from the moment versus magnetic field (M-H) hysteresis loop (inset), by the Bean model : $Jc = 20\Delta M/a(1 - \frac{a}{3b})$, where ΔM is the opening in the hysteresis loop; a and b are the sample dimensions. [184] From the results, $\boldsymbol{J_c^{sf}}$ at 4 K for $FeSe_{0.1}Te_{0.9}$ film can be determined to be about 2.1×10^4 A/cm^2, which is higher than that of $FeSe_{0.5}Te_{0.5}$ film on glass, [240] as well as that of

$FeSe_xTe_{1-x}$ wires fabricated by the powder-in-tube (PIT) method. [264, 265] Transport measurement was also conducted as a comparison. Figure 8.4(d) presents the results measured at 4 K and up to 5 T. 1 μV/cm criterion was used for the $\boldsymbol{J_c}$ measurement. $\boldsymbol{J_c}$ at 4 K, 3 T can be estimated to about 900 A/cm^2, which is close to 1000 A/cm^2 measured by VSM. In Table 8.1, superconducting properties are compared to the previous reported $FeSe_{0.5}Te_{0.5}$ film on glass. [240] Overall, all the superconducting properties of $FeSe_{0.1}Te_{0.9}$ film on glass are better than that of $FeSe_{0.5}Te_{0.5}$. Comparing to the samples on STO substrates, the $\boldsymbol{J_c}$ values are relatively low. It is believed that the relatively lower $\boldsymbol{J_c}$ values are related to the relatively weak in-plane texture and high density defects at the grain boundaries which could be scattering factors. For example, the in-plane lattice matching between $FeSe_{0.1}Te_{0.9}$ (3.8462 Å) and STO (3.905 Å) allows the films growing as cube-on-cube relation on single crystalline STO substrates. However, for the film on glass, high c-axis texture is formed out-of-plane with very limited in-plane alignment because of the amorphous glass for the film growth. The $\boldsymbol{J_c}$ values could be further improved by optimizing the growth parameters, substrate surface treatments, as well as incorporating appropriate cap layer for pinning enhancement.

With these promising results for the films on glass substrates, a natural step forward is to demonstrate $FeSe_{0.1}Te_{0.9}$ on metal substrates. Here we deposited iron chalcogenide thin films on a polished stainless steel substrate with a thin Al_2O_3 buffer layer, shown in Figure 8.5(a). The low magnification TEM image shows that the thickness of $FeSe_{0.1}Te_{0.9}$ and Al_2O_3 layer can be estimated to be around 150 nm and 50 nm, respectively. The high resolution TEM image of a representative interface area

shows that $FeSe_{0.1}Te_{0.9}$ film has grown highly c-axis textured with c-plane parallel to the Al_2O_3 buffered metal substrate. The standard θ-2θ XRD scan of $FeSe_{0.1}Te_{0.9}$ film on Al_2O_3 buffered metal substrate is shown in Figure 8.5(c). The four (00*l*) peaks confirm the c-axis preferred texturing, and no impurity phase has been observed. The R-T plot in Figure 8.5(d) shows the superconducting transition initiates from $\boldsymbol{T_c^{onset}}$ of 10 K and reaches zero resistance at $\boldsymbol{T_c^{zero}}$ of 5 K. Figure 8.6(a) presents the field dependence critical current density of iron chalcogenide thin film on Al_2O_3 buffered metal substrate, which can be derived from its corresponding magnetic hysteresis loop (Figure 8.6(b)) using the Bean model. The result shows that this film exhibits a $\boldsymbol{J_c^{self\text{-}field}}$ value of 1.34×10^4 A/cm^2 at 4 K. These results are slightly lower than that of the film on glass substrates, however, presents great potential for future optimization of the deposition process.

Table 8.1 Comparison of superconducting properties of $FeSe_{0.1}Te_{0.9}$ and $FeSe_{0.5}Te_{0.5}$ thin films on glass substrates.

	$FeSe_{0.1}Te_{0.9}$ on glass	$FeSe_{0.5}Te_{0.5}$ on glass [240]
$\boldsymbol{T_c^{onset}}$ (K)	**12.3**	10
$\boldsymbol{T_c^{zero}}$ (K)	**10**	8
$\boldsymbol{H_{c2}}$ (T)	**126**	77
$\boldsymbol{J_c^{self\text{-}field}}$ @4 K (A/cm^2)	**2.1×10^4**	1.4×10^4
$\boldsymbol{J_c^{in\text{-}field}}$ @4 K 2 T (A/cm^2)	**3500**	900
$\boldsymbol{J_c^{in\text{-}field}}$ @4 K 3 T (A/cm^2)	**1000**	500

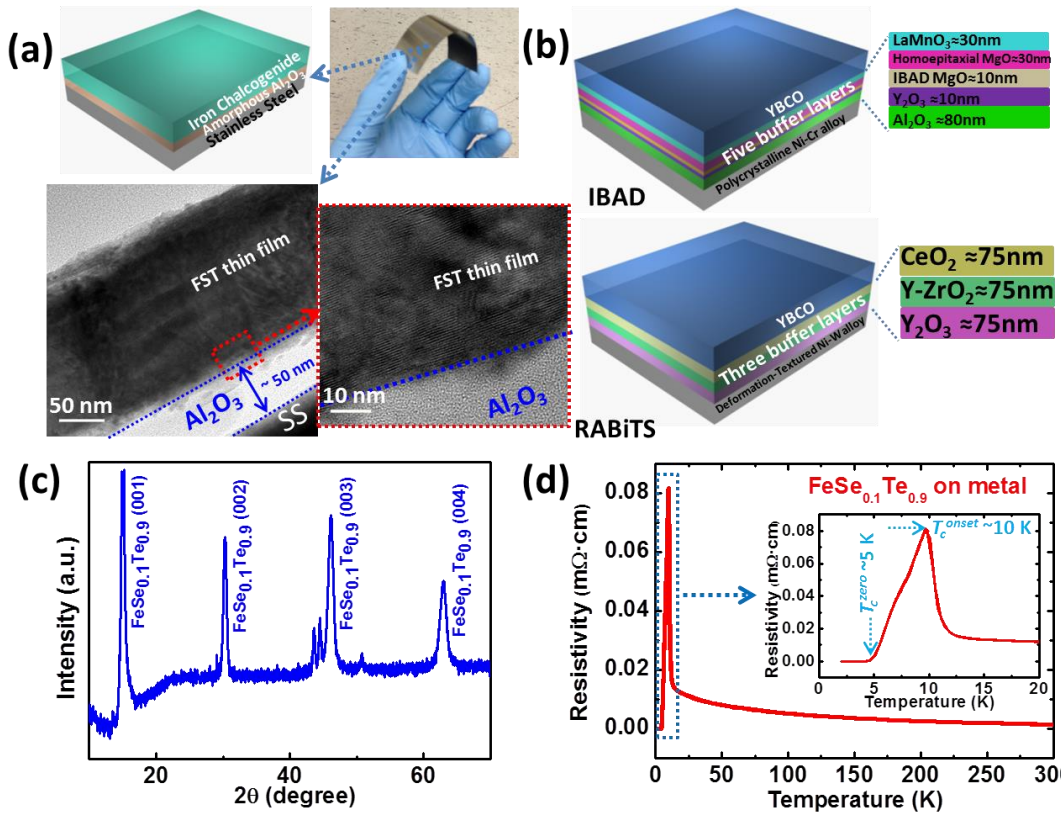

Figure 8.5 (a) Schematic illustration and TEM images of iron chalcogenide thin film on Al_2O_3 buffered metal substrate, inset is the real sample; (b) Schematic illustrations of coated-conductor tapes based on IBAD and RABiTS technique; (c) XRD pattern of $FeSe_{0.1}Te_{0.9}$ thin film on metal substrate; (d) R-T plot from 2-300 K.

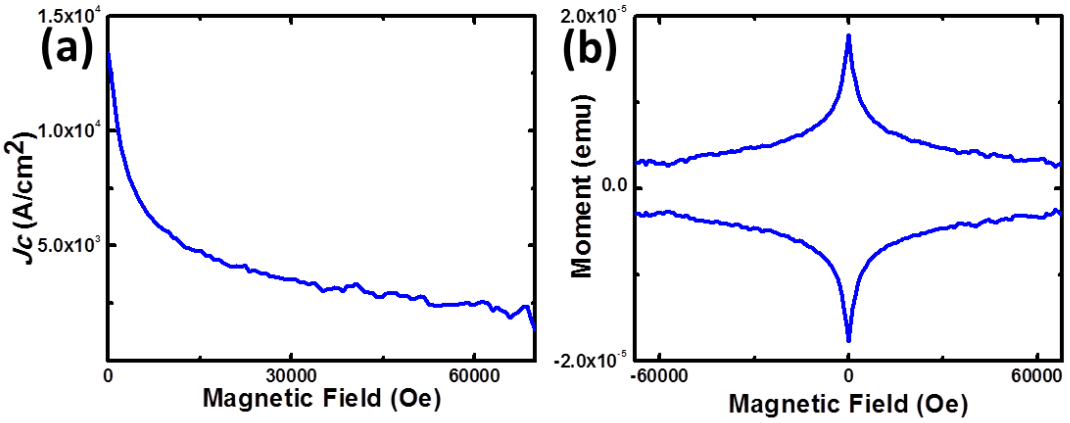

Figure 8.6 (a) The field dependence critical current density of iron chalcogenide thin film on Al_2O_3 buffered substrate, and (b) corresponding magnetic hysteresis loop at 4 K.

As discussed above in the introduction, for YBCO coated conductors, a set of textured buffers are required for the epitaxial growth of superconducting YBCO films. Two major coated conductor techniques have been developed, i.e., IBAD and RABiTS, as illustrated in Figure 8.4(b). Both require either several layers of buffers as template or complicated substrate texturing treatment, which results in high processing cost and limits large-scale commercial applications. Compared to the multilayer buffer scheme, the self-textured $FeSe_{0.1}Te_{0.9}$ films on metal substrate (Figure 8.4(a)), i.e., preferred c-axis growth in the out-of-plane orientation instead of random polycrystalline growth, [268, 269] present a much simplified and cost-effective approach. The intriguing self-texturing of iron chalcogenide films could be attributed to the preferred c-axis growth of the system (i.e., preferred layered growth along c-axis) and underlying amorphous template provided by glass or the amorphous buffered metallic substrates. Thus, the films grow layer by layer without preferred template orientation. However, we also observed the minor preferred in-plane texturing of the films on both glass and the amorphous buffered metallic substrates, which is surprising and still under investigation. Furthermore, the film is also tested to be robust with excellent mechanical integrity after preliminary bending tests. Overall this simplified Fe-based superconductor coated conductor scheme presents a promising route towards cost-effective coated conductors for high field applications.

8.5 Conclusions

In summary, $FeSe_xTe_{1-x}$ thin films have been deposited on amorphous glass substrates. Surprisingly, all the samples with different film compositions on glass show obvious superconducting properties comparable to that on single crystal substrates. $FeSe_{0.1}Te_{0.9}$ obtains the superconducting properties with $\boldsymbol{T_c^{zero}}$ of 10 K, $\boldsymbol{J_c^{sf}}$ of 2.1×10^4 A/cm^2 at 4 K, and $\boldsymbol{H_{c2}}$ as high as 126 T. $FeSe_{0.1}Te_{0.9}$ thin film has also been grown on a simple and cost-effective metallic substrate with a thin amorphous Al_2O_3 buffer layer. The film shows promising superconducting properties with further optimization underway. This demonstration of highly textured Fe-based superconductors grown on glass and metallic substrates opens a new route for processing cost-effective Fe-based superconductor coated conductors for high filed applications as well as many other layered materials on cost-effective substrates.

CHAPTER IX

SUMMARY AND FUTURE PLAN

In this dissertation, a systematic research has been done to improve the superconducting properties of YBCO and iron chalcogenide thin films. In particular, critical current density $\boldsymbol{J_c}$ has been enhanced by introducing designed nanostructures, with a similar $\boldsymbol{T_c}$ value.

For YBCO, based on previous reported work either on defect or magnetic pinning enhancement, both defect and magnetic pinning have been achieved in this dissertation, by introducing a unique magnetic vertically aligned nanocomposite (VAN) layer. First, $(CoFe_2O_4)_x(CeO_2)_{1-x}$ nanocomposite has been incorporated into YBCO thin film as either cap layer or buffer layer. The ordered ferrimagnetic $CoFe_2O_4$ nanopillars along with high density interfacial defects can work as effective pinning centers. Furthermore, by controlling the composition of the nanocomposite and deposition parameters, the density and size of the $CoFe_2O_4$ nanopillars can be tuned. Consequently, the best pinning landscape for YBCO at different conditions can be achieved for different application requirements. Then, YBCO/$(CoFe_2O_4)_{0.3}(CeO_2)_{0.7}$ multilayers have been successfully deposited to explore another pinning architecture for YBCO. And the 2-interlayer sample exhibits the best performance, as a lot of pinning centers have been introduced in this sample with very little film quality degradation and inter-diffusion. Last, another VAN system $(LSMO)_x(CeO_2)_{1-x}$ has also been studied, as LSMO has better lattice matching with YBCO. The results indeed show better performance by incorporating this system than the previous $(CoFe_2O_4)_x(CeO_2)_{1-x}$ VAN system.

For iron chalcogenide thin film, most of previous work in this field is on the $\boldsymbol{T_c}$ improvement, and very limited work has been done on the pinning enhancement for iron chalcogenide thin film. In this dissertation, pinning property is studied for $FeSe_xTe_{1-x}$ thin film. First, CeO_2 nanolayer has been selected to grow into $FeSe_{0.1}Te_{0.9}$ thin film, because of its perfect lattice matching and their good chemical compatibility. Large pinning enhancement has been achieved, mainly caused by the interfacial defects introduced by the heterogeneous interface. Then, $(CoFe_2O_4)_{0.1}(CeO_2)_{0.9}$ VAN has also been introduced for both defect and magnetic pinning, to further improve the $\boldsymbol{J_c}$ value. Finally, to test the compatibility of iron chalcogenide for future coated conductor application, $FeSe_xTe_{1-x}$ thin films have been grown amorphous glass and polished stainless steel substrates. Surprisingly, the films are well grown along the c-direction with comparable superconducting properties with the films on single-crystal substrates.

There is still space remaining in this research field, some future research directions can be towards the following:

(1) Search for other VAN system and optimize the deposition recipe to develop better pinning landscapes, which can combine all the pinning effects in a more effective way;

(2) Design thin film architecture to introduced more pinning centers, for example, BZO-YBCO/VAN can be grown to have BZO nanoparticles or nanopillars doped in YBCO and the VAN layer can provide interfacial defect as well as magnetic pinning centers;

(3) To take the advantage of the high $\boldsymbol{T_c}$, $\boldsymbol{J_c}$ of YBCO and high $\boldsymbol{H_{c2}}$ of iron chalcogenide, $FeSe_xTe_{1-x}$/YBCO multilayer can be achieved to couple all these three important properties;

(4) Josephson junction based on both YBCO and $FeSe_xTe_{1-x}$ can be made for further quantum computing applications.

REFERENCES

[1] C. P. Poole, H. A. Farach, and R. J. Creswick, Academic Press: San Diego, CA, USA, (1995).

[2] M. Tinkham, Second Edition., McGraw Hill New York, NY, USA, (1996).

[3] J. D. Doss, Engineer's guide to high-temperature superconductivity, John Wiley & Sons New York, NY, USA, (1989).

[4] H. K. Onnes and P K Akad, Wet-Amsterd **14**, 113 (1911).

[5] W. Meissner and R. Ochsenfeld, Naturwissenschaften **21**, 787 (1933).

[6] L. V. Shubnikov, Zh. Eksp. Teor. Fiz. **7,** 221 (1937).

[7] J. Bardeen, L. N. Cooper, and J. R. Schrieffer, Phys. Rev. **108**, 1175 (1957).

[8] A. A. Abrikosov, Sov Phys Jetp-Ussr **5**, 1174 (1957).

[9] J. G. Bednorz and K. A. Muller, Z Phys. B Con. Mat. **64**, 189 (1986).

[10] M. K. Wu, J. R. Ashburn, C. J. Torng, P. H. Hor, R. L. Meng, L. Gao, Z. J. Huang, Y. Q. Wang, and C. W. Chu, Phys. Rev. Lett. **58**, 908 (1987).

[11] A. Maeda, K. Noda, K. Uchinokura, and S. Tanaka, Jpn. J. Appl. Phys. **28**, L576 (1989).

[12] Z. Z. Sheng and A. M. Hermann, Nature **332**, 138 (1988).

[13] A. Schilling, M. Cantoni, J. D. Guo, and H. R. Ott, Nature **363**, 56 (1993).

[14] C. W. Chu, L. Gao, F. Chen, Z. J. Huang, R. L. Meng, and Y. Y. Xue, Nature **365**, 323 (1993).

[15] J. Nagamatsu, N. Nakagawa, T. Muranaka, Y. Zenitani, and J. Akimitsu, Nature **410**, 63 (2001).

[16] Y. Kamihara, H. Hiramatsu, M. Hirano, R. Kawamura, H. Yanagi, T. Kamiya, and H. Hosono, J. Am. Chem. Soc. **128**, 10012 (2006).

[17] I. Guillamon, H. Suderow, A. Fernandez-Pacheco, J. Sese, R. Cordoba, J. M. De Teresa, M. R. Ibarra, and S. Vieira, Nat. Phys. **5**, 651 (2009).

[18] C. Tsai, PhD Dissertation, Texas A&M University, College Station, (2013).

[19] R. Alexandrov, IOP, Philadelphia, PA, USA, (2003).

[20] K. Brodt, H. Fuess, E. F. Paulus, W. Assmus, and J. Kowalewski, Acta Crystallogr C **46**, 354 (1990).

[21] A. Goyal, P. M. Paranthaman, and U. Schoop, MRS Bulletin **29(8),** 552 (2004).

[22] B.W. Kang, A. Goyal, D.F. Lee, J.E. Mathis, E.D. Specht, P.M. Martin, and D.M. Kroeger, J. Mater. Res. **17(7)**, 1750 (2002).

[23] J. Eickemeyer, D. Selbmann, R. Opitz, H. Wendrock, E. Maher, U. Miller, and W. Prusseit, Physica C **372-376**, 814 (2002).

[24] T. Caroff1, S. Morlens, A. Abrutis, M. Decroux, P. Chaudouët, L. Porcar, Z. Saltyte, C. Jiménez, P. Odier, and F Weiss, Supercond. Sci. Tech. **21(7)**, 075007 (2008).

[25] D. Larbalestier, A. Gurevich, D. M. Feldmann, and A. Polyanskii, Nature **414**, 368 (2001).

[26] P. N. Arendt and S. R. Foltyn, MRS Bulletin **29(8),** 543 (2004).

[27] M. Inoue, T. Kiss, D. Mitsui, T. Nakamura, T. Fujiwara, S. Awaji, K. Watanabe, A. Ibi, S. Miyata, Y. Yamada, and Y. Shiohara, IEEE Tran. Appl. Supercond. **17(2),** 3207 (2007).

[28] P.N. Arendt, S.R. Foltyn, L. Civale, R.F. DePaula, P.C. Dowden, J.R. Groves, T.G. Holesinger, Q.X. Jia, S. Kreiskott, L. Stan, I. Usov, H. Wang, and J.Y. Coulter, Physica C **412-414**, 795 (2004).

[29] A. Ibi, H. Iwai, K. Takahashi, T. Muroga, S. Miyata, T. Watanabe, Y. Yamada, and Y. Shiohara, Physica C **426-431**, 910 (2005).

[30] D. Peng, G. Meng, C. Cao, C. Wang, Q. Fang, Y. Wu, and Y. Zhang, Journal de Physique Colloques **50(C5)**, 149 (1989).

[31] C. S. Chern, J. Zhao, Y. Q. Li, P. Norris, B. Kear, and B. Gallois, Appl. Phys. Lett. **57**, 721 (1990).

[32] R. J. Betsch, A. J. Panson, R. G. Charles, and W. Cifone, Jounal of Electronic Materials **19(7)**, 51 (1990).

[33] V.Selvamanickam, Y.Xie, J.Reeves, and Y.Chen, MRS Bulletin **29(8)**, 579 (2004).

[34] H. Yamane, H. Masumoto, T. Hirai, H. Iwasaki, K. Watanabe, N. Kobayashi, Y. Muto, and H. Kurosawa, Appl. Phys. Lett. **53**, 1548 (1988).

[35] H. Nagai, Y. Yoshida, Y. Ito, S. Taniguchi, I. Hirabayashi, N. Matsunami, and Y. Takai, Supercond. Sci. Technol. **10**, 213 (1997).

[36] H. Busch, A. Fink, A. Müller, and K. Samwer, Supercond. Sci. Technol. **6**, 42 (1993).

[37] V. Burtman, M. Schieber, I. Brodsky, H. Hermon, and Y. Yaroslavsky, J. Cryst. Growth **166**, 832 (1996).

[38] B.C. Richards, S.L. Cook, D.L. Pinch, G.W. Andrews, G. Lengeling, B, Schulte, H. Jürgensen, Y.Q. Shen, P. Vase, T. Freltoft, A. Spee, J.L. Linden, M.L. Hitchman, S.H. Shamlian, and A. Brown, Physica C **252**, 229 (1995).

[39] T Aytug, M Paranthaman, E D Specht, Y Zhang, K Kim, Y L Zuev, C Cantoni, A Goyal, D K Christen, V A Maroni, Y Chen, and V Selvamanickam, Supercond. Sci. Technol. **23**, 014005 (2010).

[40] A.A. Voevodin, M.A. Capano, S.J.P. Laube, M.S. Donley, and J.S. Zabinski, Thin Solid Films **298**, 107 (1997).

[41] R.C. Hugo, H. Kung, J.R. Weertman, R. Mitra, J.A. Knapp, and D.M. Follstaedt, Acta Materialia **51**, 1937 (2003).

[42] J. Musil, P. Zeman, H. Hruby´, and P.H. Mayrhofer, Surface and Coatings Technology **120-121**, 179 (1999).

[43] J.F. Piersona, D. Wiederkehra, and A. Billard, Thin Solid Films **478**, 196 (2005).

[44] W. J. Meng and B. A. Gillispie, J. Appl. Phys. **84**, 4314 (1998).

[45] M. Buchanan, J. B. Webb, and D. F. Williams, Appl. Phys. Lett. **37**, 213 (1980).

[46] J. Huang, Y. Wang, J. Lu, L. Gong, and Z. Ye, Chinese Phys. Lett. **28**, 127306 (2011).

[47] T. Minami, Semicond. Sci. Technol. **20**, S35 (2005).

[48] O. Klutha, B. Recha, L. Houbena, S. Wiedera, G. SchoÈpea, C. Benekinga, H. Wagnera, A. LoÈf, and H.W. Schock, Thin Solid Films **351**, 247 (1999).

[49] H. Q. Chiang, J. F. Wager, R. L. Hoffman, J. Jeong, and D. A. Keszler, Appl. Phys. Lett. **86**, 013503 (2005).

[50] P. F. Carcia, R. S. McLean, M. H. Reilly, and G. Nunes Jr, Appl. Phys. Lett. **82**, 1117 (2003).

[51] S. PalDey and S.C. Deevi, Materials Science and Engineering A **342**, 58 (2003).

[52] L. Hultman, Vacuum **57**, 1 (2000).

[53] M. Dubois and P. Muralt, J. Appl. Phys. **89**, 6389 (2001).

[54] M. Stavrev, D. Fischer, C. Wenzel, K. Drescher, and N. Mattern, Thin Solid Films **307**, 79 (1997).

[55] B. Viala, M. K. Minor, and J. A. Barnard, J. Appl. Phys. **80**, 3941 (1996).

[56] C.E. Caley, J.P. Collman, and W.A. Little, Physica C **162-164**, 651 (1989).

[57] E. Yin, M. Rubin, and M. Dixon, J. Mater. Res. **7(7),** 1636 (1992).

[58] W. Ito, A. Oishi, S. Okayama, Y. Yoshida, N. Homma, and T. Morishita, Physica C **204**, 295 (1993).

[59] A. Cassinese, A. Di Chiara, F. Miletto Granozio, S. Saiello, U. Scotti di Uccio, and M. Valentino, J. Mater. Res. **10(1)**, 11 (1995).

[60] V. Pan, Y. Cherpak, V. Komashko, S. Pozigun, and C. Tretiatchenko, Phys. Rev. B **73**, 054508 (2006).

[61] H. Kim, C. M. Gilmore, A. Piqué, J. S. Horwitz, H. Mattoussi, H. Murata, Z. H. Kafafi, and D. B. Chrisey, J. Appl. Phys. **86**, 6451 (1999).

[62] E. M. Kaidashev, M. Lorenz, H. von Wenckstern, A. Rahm, H.-C. Semmelhack, K.-H. Han, G. Benndorf, C. Bundesmann, H. Hochmuth, and M. Grundmann, Appl. Phys. Lett. **82**, 3901 (2003).

[63] X.M. Fan, J.S. Lian, Z.X. Guo, and H.J. Lu, Applied Surface Science **239**, 176 (2005).

[64] S. L. Jones, D. Kumar, Rajiv K. Singh, and P. H. Holloway, Appl. Phys. Lett. **71**, 404 (1997).

[65] F. K. Shan and Y. S. Yu, Journal of the European Ceramic Society **24**, 1869 (2004).

[66] M. Lorenz, H. Hochmuth, D. Natusch, H. Börner, G. Lippold, K. Kreher, and W. Schmitz, Appl. Phys. Lett. **68**, 3332 (1996).

[67] M. Peurla, P. Paturi, Y. P. Stepanov, H. Huhtinen, Y. Y. Tse, A. C. Bodi, J. Raittila, and R. Laiho, Supercond. Sci. Technol. **19**, 767 (2006).

[68] T. A. Campbell, T. J. Haugan, I. Maartense, J. Murphy, L. Brunke, and P.N. Barnes, Physica C **423**, 1 (2005).

[69] P. Mele, K. Matsumoto, T. Horide, A. Ichinose, M. Mukaida, Y. Yoshida, and S. Horii, Supercond. Sci. Technol. **20**, 244 (2007).

[70] K. Develos-Bagarinao, H. Yamasaki, J. C. Nie, and Y. Nakagawa, Supercond. Sci. Technol. **18**, 667 (2005).

[71] S. Ghalsasi, Y. X. Zhou, J. Chen, B. Lv, and K. Salama, *Supercond. Sci. Technol.* **21,** 045015 (2008).

[72] M. Sohma, K. Tsukada, I. Yamaguchi, K. Kamiya, W. Kondo, S. Mizuta, T. Manabe, and T. Kumagai, J. Phys.: Conf. Ser. **43,** 349 (2006).

[73] D. T. Verebelyi, U. Schoop,C. Thieme, X. Li, W. Zhang, T. Kodenkandath, A. P. Malozemoff, N. Nguyen, E. Siegal, D. Buczek, J. Lynch, J. Scudiere, M. Rupich, A. Goyal, E. D. Specht, P. Martin, and M. Paranthaman, Supercond. Sci. Technol. **16**, L19 (2003).

[74] T. Puig, J. C. Gonzalez, A. Pomar, N. Mestres, O. Castano, M. Coll, J. Gazquez, F. Sandiumenge, S. Pinol, and X. Obradors, Supercond. Sci. Technol. **18**, 1141 (2005).

[75] S. R. Foltyn, L. Civale, J. L. Macmanus-Driscoll, Q. X. Jia, B. Maiorov, H. Wang, and M. Maley, Nat. Mater. **6**, 631 (2007).

[76] S. R. Foltyn, Q. X. Jia, P. N. Arendt, L. Kinder, Y. Fan, and J. F. Smith, Appl. Phys. Lett. **75**, 3692 (1999).

[77] A. Gurevich, Nat. Mater. 10, 255 (2011).

[78] L. Civale, A. D. Marwick, M. W. Mcelfresh, T. K. Worthington, A. P. Malozemoff, F. H. Holtzberg, J. R. Thompson, and M. A. Kirk, Phys. Rev. Lett.

65, 1164 (1990).

[79] F. M. Sauerzopf, H. P. Wiesinger, W. Kritscha, H. W. Weber, G. W. Crabtree, and J. Z. Liu, Phys. Rev. B **43**, 3091 (1991).

[80] J. Giapintzakis, W. C. Lee, J. P. Rice, D. M. Ginsberg, I. M. Robertson, R. Wheeler, M. A. Kirk, and M. O. Ruault, Phys. Rev. B **45**, 10677 (1992).

[81] T. Haugan, P. N. Barnes, R. Wheeler, F. Meisenkothen, and M. Sumption, Nature **430**, 867 (2004).

[82] T. Matsushita, Supercond. Sci. Technol. **13**, 730 (2000).

[83] J. L. Macmanus-Driscoll, S. R. Foltyn, Q. X. Jia, H. Wang, A. Serquis, L. Civale, B. Maiorov, M. E. Hawley, M. P. Maley, and D. E. Peterson, Nat. Mater. **3**, 439 (2004).

[84] F. Z. Ding, H. W. Gu, T. Zhang, H. Y. Wang, F. Qu, S. T. Dai, X. Y. Peng, and J. L. Cao, J. Alloy. Compd. **513**, 277 (2012).

[85] A. Palau, E. Bartolome, A. Llordes, T. Puig, and X. Obradors, Supercond. Sci. Tech. **24**, 125010 (2011).

[86] C. V. Varanasi, P. N. Barnes, J. Burke, L. Brunke, I. Maartense, T. J. Haugan, E. A. Stinzianni, K. A. Dunn, and P. Haldar, Supercond. Sci. Technol. **19**, L37 (2006).

[87] Y. Q. Li, J. Zhao, C. S. Chern, P. Lu, T. R. Chien, B. Gallois, P. Norris, B. Kear, and F. Cosandey, Appl. Phys. Lett. **60**, 2430 (1992).

[88] J. Hanisch, C. Cai, V. Stehr,R. Huhne, J. Lyubina, K. Nenkov, G. Fuchs, L. Schultz, and B. Holzapfel, Supercond. Sci. Technol. **19**, 534 (2006).

[89] J. Hänisch, C. Cai, R. Hühne, L. Schultz, and B. Holzapfel, Appl. Phys. Lett. **86**, 122508 (2005).

[90] M. Coll, R. Guzman, P. Garcés, J. Gazquez, V. Rouco, A. Palau, S. Ye, C. Magen, H. Suo, H. Castro, T. Puig, and X. Obradors, Supercond. Sci. Technol. **27**, 044008 (2014).

[91] M. Liu, D. Shi, Q. Li, L. Wang, S. Ye, H. Suo, and S. Dou, Int. J. Mod. Phys. B **23**, 3532 (2009).

[92] Y. Xu, H. Suo, Z. Yue, J. Grivel, and M. Liu, IEEE Trans. Appl. Supercon. **26(3)**, 6602804 (2016).

[93] B. Kang, C. H. Wie, D. H. Tran, W. B. K. Putri, T. J. Hwang, and D. H. Kim, Journal of the Korean Physical Society **60(11)**, 1911 (2012).

[94] S. Ye, H. L. Suo, M. Liu, X. Tang, Z. P. Wu, Y. Zhao, and M. L. Zhou, Mod. Phys. Lett. B **25**, 2371 (2011).

[95] B. Maiorov, S. A. Baily, H. Zhou, O. Ugurlu, J. A. Kennison, P. C. Dowden, T. G. Holesinger, S. R. Foltyn, and L. Civale, Nat. Mater. **8**, 398 (2009).

[96] A. Ichinose, K. Naoe, T. Horide, K. Matsumoto, R. Kita, M. Mukaida, Y. Yoshida, and S. Horii, Supercond. Sci. Technol. **20**, 1144 (2007).

[97] A. K. Jha, N. Khare, and R. Pinto, Solid State Communications **151**, 1447 (2011).

[98] P. Mele, K. Matsumoto, A. Ichinose, M. Mukaida, Y. Yoshida, S. Horii, and R. Kita, Supercond. Sci. Technol. **21**, 125017 (2008).

[99] P. Mele, K. Matsumoto, T. Horide, A. Ichinose, M. Mukaida, Y. Yoshida, S. Horii, and R. Kita, Supercond. Sci. Technol. **21**, 032002 (2008).

[100] C. V. Varanasi, J. Burke, L. Brunke, H. Wang, M. Sumption, and P. N. Barnes, J. Appl. Phys. **102**, 063909 (2007).

[101] M. Peurla, H. Huhtinen, M. A. Shakhov, K. Traito, Yu. P. Stepanov, M. Safonchik, P. Paturi, Y. Y. Tse, R. Palai, and R. Laiho, Phys. Rev. B **75**, 184524 (2007).

[102] Y. Yamada, K. Takahashi, H. Kobayashi, M. Konishi, T. Watanabe, A. Ibi, T. Muroga, S. Miyata, T. Kato, T. Hirayama, and Y. Shiohara, Appl. Phys. Lett. **87**, 132502 (2005).

[103] K. Matsumoto, T. Horide, A. K. Jha, P. Mele, Y. Yoshida, and S. Awaji, IEEE Trans. Appl. Supercon. **25(3)**, 8001106 (2015).

[104] D. M. Feldmann, T. G. Holesinger, B. Maiorov, S. R. Foltyn, J. Y. Coulter, and I. Apodaca, Supercond. Sci. Technol. **23**, 095004 (2010).

[105] X. Wang, A. Dibos, and J. Z. Wu, Phys. Rev. B **77**, 144525 (2008).

[106] A. Goyal1, S. Kang, K. J. Leonard, P. M. Martin, A. A. Gapud, M. Varela, M. Paranthaman, A. O. Ijaduola, E. D. Specht, J. R. Thompson, D. K. Christen, S. J. Pennycook, and F. A. List, Supercond. Sci. Technol. **18**, 1533 (2005).

[107] Y. Zhu, C. Tsai, J. Wang, J. Kwon, H. Wang, C. V. Varanasi, J. Burke, L. Brunke, and P. N. Barnes, J. Mater. Res. **27(13)**, 1763 (2012).

[108] M. A. P. Sebastian, J. N. Reichart, J. L. Burke, L. B. Brunke, T. J. Haugan, . Tsai, and H. Wang, IEEE Trans. Appl. Supercon. **23(3)**, 8002104 (2013).

[109] K. Develos-Bagarinao, H. Yamasaki, K. Ohki, and Y. Nakagawa, Supercond. Sci. Technol. **20**, L25 (2007).

[110] A. V. Pan, S. Pysarenko, and S. X. Dou, Appl. Phys. Lett. **88**, 232506 (2006).

[111] L. Lei, Y. Bai, C. Wu, and G. Zhao, J. Sol-Gel Sci. Technol. **69**, 21 (2014).

[112] E. Backen, J. Hänisch, R. Hühne, K. Tscharntke, S. Engel, T. Thersleff, L. Schultz, and Bernhard Holzapfel, IEEE Trans. Appl. Supercon. **17(2)**, 3733 (2007).

[113] C. Tsai, J. Huang, J. Lee, F. Khatkhatay, L. Chen, A. Chen, Q. Su, and H. Wang, Physica C **510**, 13 (2015).

[114] J. Huang, C. Tsai, L. Chen, J. Jian, K. Yu, W. Zhang, and H. Wang, IEEE Trans. Appl. Supercon. **25(3)**, 7500404 (2015).

[115] D. Q. Shi, Q. Li, L. Wang, X. B. Zhu, J. G. Kim, T. Yamashita, and S. Cooper, IEEE Trans. Appl. Supercon. **21**, 2900 (2011).

[116] S. Ohshima, S. Oikawa, T. Noguchi, M. Inadomaru, M. Kusunoki, M. Mukaida, H. Yamasaki, and Y. Nakagawa, Physica C **372**, 671 (2002).

[117] R. I. Tomov, A. Kursumovic, M. Majoros, D. J. Kang, B. A. Glowacki, and J. E. Evetts, Supercond. Sci. Tech. **15**, 598 (2002).

[118] V. Galindo, J.P. SeHnateur, A. Abrutis, A. Teiserskis, and F. Weiss, Journal of Crystal Growth **208**, 357 (2000).

[119] X. G. Qiu, L. Li, B. R. Zhao, Y. Y. Zhao, P. Xu, C. A. Wang, and H. C. Li, J. Appl. Phys. **72**, 2072 (1992).

[120] H. Y. Wang, and J. Wang, IEEE Trans. Appl. Supercon. **19**, 3395 (2009).

[121] Y. Uzun, and I. Avci, Thin Solid Films **566**, 9 (2014).

[122] C. Tsai, Y. Zhu, L. Chen, and H. Wang, IEEE Trans. Appl. Supercon. **21(3)**, 2758 (2011).

[123] B. Utz, R. Semerad, M. Bauer, W. Prusseit, P. Berberich, and H. Kinder, IEEE Trans. Appl. Supercond. **7**, 1272 (1997).

[124] S. C. Wimbush, J. H. Durrell, C. F. Tsai, H. Wang, Q. X. Jia, M. G. Blamire, and J. L. MacManus-Driscoll, Supercond. Sci. Technol. **23**, 045019 (2010).

[125] S. A. Harrington, J. H. Durrell, B. Maiorov, H. Wang, S. C. Wimbush, A. Kursumovic, J. H. Lee, and J. L. MacManus-Driscoll, Supercond. Sci. Technol. **22**, 022001 (2009).

[126] C. Tsai, L. Chen, A. Chen, F. Khatkhatay, W. Zhang, and H. Wang, IEEE Trans. Appl. Supercond. **23(3)**, 8001204 (2013).

[127] G. Ercolano, S. A. Harrington, H. Wang, C. F. Tsai, and J. L. MacManus-Driscoll, Supercond. Sci. Technol. **23**, 022003 (2010).

[128] J. M. Triscone and O. Fischer, Rep. Prog. Phys. **60**, 1673 (1997).

[129] M. Baert, V. V. Metlushko, R. Jonckheere, V. V. Moshchalkov, and Y. Bruynseraede, Phys. Rev. Lett. **74**, 3269 (1995).

[130] L. N. Bulaevskii, E. M. Chudnovsky, and A. P. Maley, Appl. Phys. Lett. **76**, 2594 (2000).

[131] S. C. Wimbush, J. H. Durrell, R. Bali, R. Yu, H. Wang, S. A. Harrington, and J. L. MacManus-Driscoll, IEEE Trans. Appl. Supercond. **19(3)**, 3148 (2009).

[132] T. Petrisor Jr., M. S. Gabor, C. Tiusan, V. Galluzzi, G. Celentano, S. Popa, A. Boulle, and T. Petrisor, J. Appl. Phys. **112**, 053919 (2012).

[133] J. Wang, C. F. Tsai, Z. X. Bi, D. G. Naugle, and H. Y. Wang, IEEE Trans. Appl. Supercon. **19**, 3503 (2009).

[134] A. García-Santiago, F. Sánchez, M. Varela, and J. Tejada, Appl. Phys. Lett. **77**, 2900 (2000).

[135] D. B. Jan, J. Y. Coulter, M. E. Hawley, L. N. Bulaevskii, M. P. Maley, Q. X. Jia, B. B. Maranville, F. Hellman, and X. Q. Pan, Appl. Phys. Lett. **82**, 778 (2003).

[136] A. K. Jha, N. Khare, and R. Pinto, J. Supercond. Nov. Magn. **27**, 1021 (2014).

[137] C. Tsai, J. Lee, and H. Wang, Supercond. Sci. Technol. **25**, 075016 (2012).

[138] J. Albrecht, S. Soltan, and H.-U. Habermeier, Phys. Rev. B **72**, 092502 (2005).

[139] C. Z. Chen, Z. Y. Liu, Y. M. Lu, L. Zeng, C. B. Cai, R. Zeng, and S. X. Dou, J. Appl. Phys. **109**, 073921 (2011).

[140] J. Huang, M. Fan, H. Wang, L. Chen, C. Tsai, L. Li, and H. Wang, Ceramics International **42**, 12202 (2016).

[141] X. X. Zhang, G. H. Wen, R. K. Zheng, G. C. Xiong, and G. J. Lian, Europhys. Lett. **56**, 119 (2001).

[142] J. Huang, C. Tsai, L. Chen, J. Jian, F. Khatkhatay, K. Yu, and H. Wang, J. Appl. Phys. **115**, 123902 (2014).

[143] Z. A. Ren, W. Lu, J. Yang, W. Yi, X. Shen, Z. Li, G. Che, X. Dong, L. Sun, F. Zhou, and Z. Zhao, Chin. Phys. Lett. **25**, 2215 (2008).

[144] Y. Kamihara, H. Hiramatsu, M. Hirano, R. Kawamura, H. Yanagi, T. Kamiya, and H. Hosono, J. Am. Chem. Soc. **128**, 10012 (2006).

[145] Y. Kamihara, T. Watanabe, M. Hirano, and H. Hosono, J. Am. Chem. Soc. **130**, 3296 (2008).

[146] X. H. Chen, T. Wu, G. Wu, R. H. Liu, H. Chen, and D. F. Fang, Nature **453**, 761762 (2008).

[147] X. C. Wang, Q. Q. Liu, Y. X. Lv, W. B. Gao, L. X. Yang, R. C. Yu, F. Y. Li, and C. Q. Jin, Solid State Commun. **148**, 538 (2008).

[148] M. Rotter, M. Tegel, and D. Johrendt, Phys. Rev. Lett. **101**, 107006 (2008).

[149] F. C. Hsu, J. Y. Luo, K. W. Yeh, T. K. Chen, T. W. Huang, P. M. Wu, Y. C. Lee, Y. L. Huang, Y. Y. Chu, D. C. Yan, and M. K. Wu, Proc. Natl. Acad. Sci. U. S. A. **105**, 14262 (2008).

[150] Y. F. Nie, E. Brahimi, J. I. Budnick, W. A. Hines, M. Jain, and B. O. Wells, Appl. Phys. Lett. **94**, 242505 (2009).

[151] Y. Han, W. Y. Li, L. X. Cao, S. Zhang, B. Xu, and B. R. Zhao, J. Phys.: Condens. Matter **21**, 235702 (2009).

[152] T. Chen, J. Luo, C. Ke, H. Chang, T. Huang, K. Yeh, C. Chang, P. Hsu, C. Wu, M. Wang, and M. Wu, Thin Solid Films **519**, 1540 (2010).

[153] M. Jourdana and S. ten Haaf, J. Appl. Phys. **108**, 023913 (2010).

[154] M. J. Wang, J. Y. Luo, T. W. Huang, H. H. Chang, T. K. Chen, F. C. Hsu, C. T. Wu, P. M. Wu, A. M. Chang, and M. K. Wu, Phys. Rev. Lett. **103**, 117002 (2009).

[155] S. Jung, N. H. Lee, E. Choi, W. N. Kang, S. Lee, T. Hwang, and D. H. Kim, Physica C **470**, 1977 (2010).

[156] J. Huang, L. Chen, J. Jian, F. Khatkhatay, C. Jacob, and H. Wang, J. Alloy. Compd. **647**, 380 (2015).

[157] Q. Wang, Z. Li, W. Zhang, Z. Zhang, J. Zhang, W. Li, H. Ding, Y. Ou, P. Deng, K. Chang, J. Wen, C. Song, K. He, J. Jia, S. Ji, Y. Wang, L. Wang, X. Chen, X. Ma, and Q. Xue, Chin. Phys. Lett. **29**, 037402 (2012).

[158] J. Ge, Z. Liu, C. Liu, C. Gao, D. Qian, Q. Xue, Y. Liu, and J. Jia, Nat. Mater. **14**, 285 (2015).

[159] M. K. Wu, F. C. Hsu, K. W. Yeh, T. W. Huang, J. Y. Luo, M. J. Wang, H. H. Chang, T. K. Chen, S. M. Rao, B. H. Mok, C. L. Chen, Y. L. Huang, C. T. Ke, P. M. Wu, A. M. Chang, C. T. Wu, and T. P. Perng, Physica C **469**, 340 (2009).

[160] W. Si, Z. Lin, Q. Jie, W. Yin, J. Zhou, G. Gu, P. D. Johnson, and Q. Li, Appl. Phys. Lett. **95**, 052504 (2009).

[161] S. X. Huang, C. L. Chien, V. Thampy, and C. Broholm, Phys. Rev. Lett. **104**, 217002 (2010).

[162] Y. Imai, T. Akiike, R. Tanaka, H. Takahashi, M. Hanawa, I. Tsukada, and A. Maeda, Physica C **470**, 1038 (2010).

[163] E. Bellingeri, I. Pallecchi, R. Buzio, A. Gerbi, D. Marr`e, M. R. Cimberle, M. Tropeano, M. Putti, A. Palenzona, and C. Ferdeghini, Appl. Phys. Lett. **96**, 102512 (2010).

[164] A. Subedi, L. Zhang, D. J. Singh, and M. H. Du, Phys. Rev. B **78**, 134514 (2008).

[165] Y. Han, W. Y. Li, L. X. Cao, X. Y. Wang, B. Xu, B. R. Zhao, Y. Q. Guo, and J. L. Yang, Phys. Rev. Lett. **104**, 017003 (2010).

[166] Y. F. Nie, D. Telesca, J. I. Budnick, B. Sinkovic, and B. O. Wells, Phys. Rev. B **82**, 020508 (2010).

[167] W. Si, Q. Jie, L. Wu, J. Zhou, G. Gu, P. D. Johnson, and Q. Li, Phys. Rev. B **81**, 092506 (2010).

[168] P. Mele, K. Matsumoto, K. Fujita, Y. Yoshida, T. Kiss, A. Ichinose, and M. Mukaida, Supercond. Sci. Technol. **25**, 084021 (2012).

[169] L. Chen, J. Huang, C. Tsai, Y. Zhu, J. Jian, A. Chen, Z. Bi, F. Khatkhatay, N. Cornell, A. Zakhidov, and H. Wang, Supercond. Sci. Technol. **26**, 112001 (2013).

[170] Q. Li, W. Si, and I. K Dimitrov, Rep. Prog. Phys. **74**, 124510 (2011).

[171] A. Kreyssig, M. A. Green, Y. Lee, G. D. Samolyuk, P. Zajde J. W. Lynn, S. L. Budko, M. S. Torikachvili, N. Ni, S. Nandi, J. B. Leão, S. J. Poulton, D. N. Argyriou, B. N. Harmon, R. J. McQueeney, P. C. Canfield, and A. I. Goldman, Phys. Rev. B **78**, 184517 (2008).

[172] T. Yildirim, Phys. Rev. Lett. **102**, 037003 (2009).

[173] T. Imai, K. Ahilan, F. L. Ning, T. M. McQueen, and R. J. Cava, Phys. Rev. Lett. **102**, 177005 (2009).

[174] F. Nabeshima, Y. Imai, M. Hanawa, I. Tsukada, and A. Maeda, Appl. Phys. Lett. **103**, 172602 (2013).

[175] W. Si, S. J. Han, X. Shi, S. N. Ehrlich, J. Jaroszynski, A. Goyal, and Q. Li, Nat. Commun. **4**, 1347 (2013).

[176] L. Chen, C. Tsai, Y. Zhu, A. Chen, Z. Bi, J. Lee, and H. Wang, Supercond. Sci. Technol. **25**, 025020 (2012).

[177] W. Si, J. Zhou, Q. Jie, I. Dimitrov, V. Solovyov, P. D. Johnson, J. Jaroszynski, V. Matias, C. Sheehan, and Q. Li, Appl. Phys. Lett. **98**, 262509 (2011).

[178] L. Chen, C. Tsai, A. Chen, Q. Su, and H. Wang, IEEE Trans. Appl. Supercond., **23(3)**, 7500904 (2013).

[179] H. M. Smith and A. F. Turner, Appl. Optics **4**, 147 (1965).

[180] R. K. Singh, O. W. Holland, and J. Narayan, J. Appl. Phys. **68**, 233 (1990).

[181] D. McMorrow and J. Als-Nielsen, John Wiley & Sons Ltd, West Sussex UK., (2001).

[182] B. Fultz and J.M. Howe, Springer Berlin Heidelberg, Berlin, Germany, (2013).

[183] D.B. Williams and C.B. Carter, Springer London, Limited, (2009).

[184] C. P. Bean, Phys. Rev. Lett. **8**, 250 (1962).

[185] C. Gatel, B. Warot-Fonrose, S. Matzen, and J. B. Moussy, Appl. Phys. Lett. **103**, 092405 (2013).

[186] E. S. Murdock, B. R. Natarajan, and R. G. Walmsley, IEEE Trans. Magn. **28**, 3078 (1992).

[187] Q. Song and Z. J. Zhang, J. Phys. Chem. B **110**, 11205 (2006).

[188] A. V. Ramos, M. J. Guittet, J. B. Moussy, R. Mattana, C. Deranlot, F. Petroff, and C. Gatel, Appl. Phys. Lett. **91**, 122107 (2007).

[189] Z. Szotek, W. M. Temmerman, D. Ködderitzsch, A. Svane, L. Petit, and H. Winter, Phys. Rev. B **74**, 174431 (2006).

[190] G. Hu, J.H. Choi, C.B. Eom, and Y. Suzuki, Mater. Res. Soc. Symp. Proc. **603**, 201 (2000).

[191] G. Hu, J. H. Choi, C. B. Eom, V. G. Harris, and Y. Suzuki, Phys. Rev. B **62**, R779 (2000).

[192] S. Laurent, D. Forge, M. Port, A. Roch, C. Robic, L. V. Elst, and R. N. Muller, Chem. Rev. **108**, 2064 (2008).

[193] S. Odenbach, J. Phys.: Condens. Matter **16**, R1135 (2004).

[194] W.B. Shi, X.D. Zhang, S.H. He, and Y.M. Huang, Chem. Commun. **47(38)**, 10785 (2011).

[195] W.C. Liu, Y.K. Chan, J.Z. Cai, C.W. Leung, C. Mak, K.H. Wong, F.M. Zhang, X.S. Wu, and X. D. Qi, J. Appl. Phys. **112**, 104306 (2012).

[196] W. Huang, J. Zhu, H. Z. Zeng, X. H. Wei, Y. Zhang, and Y. R. Lia, Appl. Phys. Lett. **89**, 262506 (2006).

[197] S. Matzen, J. B. Moussy, R. Mattana, F. Petroff, C. Gatel, B. Warot-Fonrose, C. Cezar, A. Barbier, M. A. Arrio, and P. Sainctavit, Appl. Phys. Lett. **99**, 052514 (2011).

[198] K. Vasundhara, S. N. Achary, S. K. Deshpande, P. D. Babu, S. S. Meena, and A. K. Tyagi, J. Appl. Phys. **113**, 194101 (2013).

[199] H. Zheng, J. Wang, S. E. Lofland, Z. Ma, L. Mohaddes-Ardabili, T. Zhao, L. Salamanca-Riba, S. R. Shinde, S. B. Ogale, F. Bai, D. Viehland, Y. Jia, D. G. Schlom, M. Wuttig, A. Roytburd, and R. Ramesh, Science **303**, 661 (2004).

[200] J. L. MacManus-Driscoll, P. Zerrer, H. Wang, H. Yang, J. Yoon, A. Fouchet, R. Yu, M. G. Blamire, and Q. Jia, Nat. Mater. **7**, 314 (2008).

[201] A. Chen, Z. Bi, Q. Jia, J. L. MacManus-Driscoll, and H. Wang, Acta Materialia **61**, 2783 (2013).

[202] Z. Bi, E. Weal, H. Luo, A. Chen, J. L. MacManus-Driscoll, Q. Jia, and H. Wang, J. Appl. Phys. **109**, 054302 (2011).

[203] D. Christem, Nat. Mater. **3**, 421-422, 2004.

[204] J. L. MacManus-Driscoll and S. C. Wimbush, IEEE Trans. Appl. Supercond. **21**, 2495 (2011).

[205] A. Goyal, Kluwer Academic, Boston, MA, USA, (2004).

[206] N. M. Strickland, N. J. Long, E. F. Talantseva, P. Hoefakker, J. A. Xia, M. W. Rupich, W. Zhang, X. Li, T. Kodenkandath, and Y. Huang, Current Applied Physics **8**, 372 (2008).

[207] P. N. Barnes, R. M. Nekkanti, T. J. Haugan, T. A. Campbell, N. A. Yust, and J. M. Evans, Supercond. Sci. Technol. **17**, 957 (2004).

[208] K. Develos-Bagarinao, and H. Yamasaki, Supercond. Sci. Technol. **24**, 065017 (2011).

[209] M. G. Blamire, R. B. Dinner, S. C. Wimbush, and J. L. MacManus-Driscoll, Supercond. Sci. Technol. **22**, 025017 (2009).

[210] N. H. Babu , K. Iida, and D.A. Cardwell, Physica C **445**, 353 (2006).

[211] C. Tsai, Y. Zhu, L. Chen, and H. Wang, IEEE Trans. Appl. Supercond. **21**, 2749 (2011).

[212] S. C. Wimbush, R. Yu, R. Bali, J. H. Durrell, and J. L. MacManus-Driscoll, Physica C **470**, 223 (2010).

[213] G. Eason, B. Noble,and I. N. Sneddon, Phil. Trans. R. Soc. London **247(935)**, 529 (1955).

[214] S. Kang, Science **311**, 1911 (2006).

[215] S. R. Foltyn, Appl. Phys. Lett. **87(16)**, 162505 (2005).

[216] S. H. Wee, Supercond. Sci. Technol. **23(1)**, 014007 (2010).

[217] X. Obradors, T. Puig, A. Pomar, F. Sandiumenge, N. Mestres, M. Coll, A. Cavallaro, N. Roma, J. Gazquez, J. C. Gonzalez, O. Castano, J. Gutierrez, A. Palau, K. Zalamova, S. Morlens, A. Hassini, M. Gibert, S. Ricart, J. M. Moreto, S. Pinol, D. Isfort, and J. Bock, Supercond. Sci. Technol. **19,** S13 (2006).

[218] A. Molodyk, M. Novozhilov, S. Bitkowsky, S. Street, A. Delaney, L. Castellani, and A.Ignatiev, IEEE Tran. Appl. Supercond. **19(3),** 3196 (2009).

[219] M. Lorenz, H. Hochmuth, D. Natusch, M. Kusunoki, V. L. Svetchnikov, V. Riede, I. Stanca, G. Klstner, and D. Hesse, IEEE Tran. Appl. Supercond. **11,** 3209 (2001).

[220] J. Yang, H. Zhang, X. L. Feng, H. Z. Liu, and Q. Zhou, J. Phys.: Conf. Ser. **234**, 022043 (2010).

[221] B. Blagoev, E. Mateev, V. Strbik, T. Nurgaliev, and L. S. Uspenskaya, J. Phys.: Conf. Ser. **223,** 012015 (2010).

[222] R. F. Service, Science **308(5720)**, 348 (2005).

[223] D. Christen, Nat. Mater. **3**, 421 (2004).

[224] I. Birlik, M. Erbe, T. Freudenberg, E. Celik, L. Schultz, and B. Holzapfel, J. Phys.: Conf. Ser. **234**, 012004 (2010).

[225] F. J. Baca, T. Haugan, P. Barnes, T. Holesinger, B. Maiorov, R. Lu, X. Wang, J. Reichart, and J. Wu, Adv. Funct. Mater. **23**, 4826 (2013).

[226] A. Chen, Z. Bi, H. Hazariwala, X. Zhang, Q. Su, L. Chen, Q. X. Jia, J. L. MacManus-Driscoll, and H. Wang, Nanotechnology **22**, 315712 (2011).

[227] L. M. Berndt, V. Balbarin, and Y. Suzuki, Appl. Phys. Lett. **77,** 2903 (2000).

[228] Y. C. Wang, J. Ding, J. B. Yi, B. H. Liu, T. Yu, and Z. X. Shen, Appl. Phys. Lett. **84,** 2596 (2004).

[229] T. Aytug, M. Paranthaman, H. Y. Christen, S. Saathyamurthy, D. K. Christen, and R. E. Ericson, J. Mater. Res. **17(09),** 2193 (2002).

[230] W. J. Yeh, B. Cheng, and T. Ragsdale, Journal of Modern Physics **1,** 364 (2010).

[231] C. Tarantini, A. Gurevich, J. Jaroszynski, F. Balakirev, E. Bellingeri, I. Pallecchi, C. Ferdeghini, B. Shen, H. H. Wen, and D. C. Larbalestier, Phys. Rev. B **84**, 184522 (2011).

[232] P. J. W. Moll, R. Puzniak, F. Balakirev, K. Rogacki, J. Karpinski, N. D. Zhigadlo, and B. Batlogg, Nat. Mater. **9**, 628 (2010).

[233] T. Katase, H. Hiramatsu, V. Matias, C. Sheehan, Y. Ishimaru, T. Kamiya, K. Tanabe, and H. Hosono, Appl. Phys. Lett. **98**, 242510 (2011).

[234] J. Janaki, T. G. Kumary, A. Mani, S. Kalavathi, G. V. R. Reddy, G. V. N. Rao, and A. Bharathi, J. Alloys Compounds **486,** 37 (2009).

[235] Z. Shermadini, A. Krzton-Maziopa, M. Bendele, R. Khasanov, H. Luetkens, K. Conder, E. Pomjakushina, S. Weyeneth, V. Pomjakushin, O. Bossen, and A. Amato, Phys. Rev. Lett. **106**, 117602 (2011).

[236] T. W. Huang, T. K. Chen, K. W. Yeh, C. T. Ke, C. L. Chen, Y. L. Huang, F. C. Hsu, M. K. Wu, P. M. Wu, M. Avdeev, and A. J. Studer, Phys. Rev. B **82**, 104502 (2010).

[237] Y. Mizuguchi, F. Tomioka, S. Tsuda, T. Yamaguchi, and Y. Takano, Appl. Phys. Lett. **93**, 152505 (2008).

[238] S. Medvedev, T. M. McQueen, I. A. Troyan, T. Palasyuk, M. I. Eremets, R. J. Cava, S. Naghavi, F. Casper, V. Ksenofontov, G. Wortmann, and C. Felser, Nat. Mater. **8**, 630 (2009).

[239] C. S. Yadav and P. L. Paulose, Solid State Communications **151**, 216 (2011).

[240] L. Chen, C. Tsai, J. Lee, X. Zhang, and H. Wang, Jpn. J. Appl. Phys. **52**, 020201 (2013).

[241] M. Eisterer, R. Raunicher, H. W. Weber, E. Bellingeri, M. R. Cimberle, I. Pallecchi, M. Putti, and C. Ferdeghini, Supercond. Sci. Technol. 24, 065016 (2011).

[242] T. Muroga, H. Iwai, Y. Yamada, T. Izumi, Y. Shiohara, Y. Iijima, T. Saito, T. Kato, Y. Sugawara, and T. Hirayama, Physica C **392-396**, 796 (2003).

[243] T. M. McQueen, Q. Huang, V. Ksenofontov, C. Felser, C. Q. Xu, H. Zandbergen, Y. S. Hor, J. Allred, A. J. Williams, D. Qu, J. Checkelsky, N. P. Ong, and R. J. Cava, Phys. Rev. B **79**, 014522 (2009).

[244] K. W. Yeh, T. W. Huang, Y. L. Huang, T. K. Chen, F. C. Hsu, P. M. Wu, Y. C. Lee, Y. Y. Chu, C. L. Chen, J. Y. Luo, D. C. Yan, and M. K. Wu, Eur. Phys. Lett. **84**, 37002 (2008).

[245] M. H. Fang, H. M. Pham, B. Qian, T. J. Liu, E. K. Vehstedt, Y. Liu, L. Spinu, and Z. Q. Mao, Phys. Rev. B **78**, 224503 (2008).

[246] J. Huang, L. Chen, J. Jian, F. Khatkhatay, and H. Wang, Supercond. Sci. Technol. **27**, 105006 (2014).

[247] I. Tsukada, M. Hanawa, T. Akiike, F. Nabeshima, Y. Imai, A. Ichinose, S. Komiya, T. Hikage, T. Kawaguchi, H. Ikuta, and A. Maeda, Appl. Phys. Express **4**, 053101 (2011).

[248] E. Bellingeri, S. Kawale, V. Braccini, R. Buzio, A. Gerbi, A. Martinelli, M. Putti, I. Pallecchi, G. Balestrino, A. Tebano, and C. Ferdeghini, Supercond. Sci. Technol. **25**, 084022 (2012).

[249] N. R. Werthamer, E. Helfand, and P. C. Hohenberg, Phys. Rev. **147**, 295 (1966).

[250] V. Tsurkan, J. Deisenhofer, A. Gunther, Ch. Kant, M. Klemm, H. A. Krug von Nidda, F. Schrettle, and A. Loidl, Eur. Phys. J. B **79**, 289 (2011).

[251] J. B. Nelson and D. P. Riley, Proceedings of the Physical Society **57(3)**, 160 (1945).

[252] A. Goyal, D. P. Norton, J. D. Budai, M. Paranthaman, E. D. Specht, D. M. Kroeger, D. K. Christen, Q. He, B. Saffian, F. A. List, D. F. Lee, P. M. Martin, C. E. Klabunde, E. Hartfield, and V. K. Sikka, Appl. Phys. Lett. **69**, 1795 (1996).

[253] M. S. Bhuiyan, M. Paranthaman, S. Sathyamurthy, T. Aytug, S. Kang, D. F. Lee, A. Goyal, E. A. Payzant, and K. Salama, Supercond. Sci. Technol. **16**, 1305 (2003).

[254] A. P. Malozemoff, S. Annavarapu, L. Fritzemeier, Q. Li, V. Prunier, M. Rupich, C. Thieme, W. Zhang, A. Goyal, M. Paranthaman, and D. F. Lee, Supercond. Sci. Technol. **13**, 473 (2000).

[255] K. Ohki, K. Develos-Bagarinao, H. Yamasaki, and Y. Nakagawa, J. Phys.: Conference Series **97**, 012142 (2008).

[256] Q. Li, M. Suenaga, Z. Ye, S. R. Foltyn, and H. Wang, Appl. Phys. Lett. **84**, 18 (2004).

[257] J. Jaroszynski, F. Hunte, L. Balicas, Youn-jung Jo, I. Raičević, A. Gurevich, D. C. Larbalestier, F. F. Balakirev, L. Fang, P. Cheng, Y. Jia, and H. H. Wen, Phys. Rev. B **78**, 174523 (2008).

[258] J. A. Parrell, Y. Zhang, M. B. Field, P. Cisek, and S. Hong, IEEE Trans. Appl. Supercond. **13**, 2 (2003).

[259] A. Godeke, M. C. Jewell, C. M. Fischer, A. A. Squitieri, P.J. Lee, and D. C. Larbalestier, J. Appl. Phys. **97**, 093909 (2005).

[260] Y. Mizuguchi, F. Tomioka, S. Tsuda, T. Yamaguchi, and Y. Takano, Appl. Phys. Lett. **94**, 012503 (2009).

[261] Y. Mizuguchi, Y. Hara, K. Deguchi, S. Tsuda, T. Yamaguchi, K. Takeda, H. Kotegawa, H. Tou, and Y. Takano, Supercond. Sci. Technol. **23**, 054013 (2010).

[262] K. W. Yeh, C. T. Ke, T. W. Huang, T. K. Chen, Y. L. Huang, P. M. Wu, and M. K. Wu, Cryst. Growth Des. **9 (11)**,4847 (2009).

[263] J. Ge, S. Cao, S. Yuan, B. Kang, and J. Zhang, J. Appl. Phys. **108**, 053903 (2010).

[264] T. Ozaki, K. Deguchi, Y. Mizuguchi, Y. Kawasaki, T. Tanaka, T. Yamaguchi, S. Tsuda, H. Kumakura, and Y. Takano, Supercond. Sci. Technol. **24**, 105002 (2011).

[265] Y. Mizuguchi, H. Izawa, T. Ozaki, Y. Takano, and O. Miura, Supercond. Sci. Technol. **24**, 125003 (2011).

[266] N. Chen, Z. Ma, Y. Liu, X. Li, Q.i Cai, H. Li, and L. Yu, J. Alloys Comp. **588**, 418 (2014).

[267] K. Onar and M. E. Yakinci, J. Alloys Comp. **620**, 210 (2015).

[268] S. Yu, P. Ho, C. Lee, C. Bi, C. Yeh, and C. Chang, Appl. Phys. Express **6**, 022301 (2013).

[269] J. R. R. Bortoletoa, M. Chavesa, A. M. Rosab, E. P. da Silvaa, S. F. Durranta, L. D. Trinoc, and P. N. Lisboa-Filho, Applied Surface Science **334**, 210 (2015).